Amperometric Gas Sensing

A thesis submitted for the degree of Doctor of Philosophy
in Physical and Theoretical Chemistry

Linhongjia Xiong
St John's College

Trinity Term 2014

Abstract

Amperometric gas sensors are widely used for environmental and industrial monitoring. They are sensitive and cheap but suffer from some significant limitations. The aim of the work undertaken in this thesis is the development of 'intelligent' gas sensors to overcome some of these limitations. Overall the thesis shows the value of ionic liquids as potential solvents for gas sensors, overcoming issues of solvent volatility and providing a wide potential range for electrochemical measurements. Methods have been developed for sensitive amperometry, the tuning of potentials and especially proof-of-concept (patents Publication numbers: WO2013140140 A3 and WO2014020347 A1) in respect of the intelligent self-monitoring of temperature and humidity by RTIL based sensors. Designs for practical electrodes are also proposed. The specific content is as follows.

Chapter 1 outlines the fundamental principles of electrochemistry which are of importance for the reading of this thesis. Chapter 2 reviews the history and modern amperometric gas sensors. Limitations of present electrochemical approaches are critically established. Micro-electrodes and Room Temperature Ionic Liquids (RTILs) are also introduced in this chapter.

Chapter 4 is focused on the study of analysing chronoamperometry using the Shoup and Szabo equation to simultaneously determine the values of concentration and diffusion coefficient of dissolved analytes in both non-aqueous and RTIL media. A method to optimise the chronoamperometric conditions is demonstrated. This provides an essential experimental basis for IL based gas sensor.

Chapter 5 demonstrates how the oxidation potential of ferrocene can be tuned by changing the anionic component of room temperature ionic liquids. This ability to tune

redox potentials has genetic value in gas sensing.

Chapters 6 and 7 describe two novel patented approaches to monitor the local environment for amperometric gas detection. In Chapter 6, an in-situ voltammetric 'thermometer' is incorporated into an amperometric oxygen sensing system. The local temperature is measured by the formal potential difference of two redox couples. A simultaneous temperature and humidity sensor is reported in Chapter 7. This sensor shows advantageous features where the temperature sensor is humidity independent and vice versa.

The Shoup and Szabo analysis (Chapter 4) requires 'simple' electron transfer and as such the reduction of oxygen in wet RTILs can be complicated by dissolved water. Chapter 8 proposes a method to stop oxygen reduction at the one electron transfer stage under humid conditions by using phosphonium based RTILs to 'trap' the intermediate superoxide ions.

Chapters 9 and 10 report the fabrication of low cost disposable electrodes of various geometries and of different materials. The suitability of these electrode for use as working electrodes for electrochemical experiments in aqueous, non-aqueous and RTIL media is demonstrated. Their capability to be used as working probes for amperometric gas sensing systems is discussed.

Acknowledgements

First and foremost, I would like to express my deep gratitude to Professor Richard Compton for his patient guidance and enthusiastic encouragement throughout my D.Phil., my Part II year and summer projects. Thank him for his great support through my difficult time and for always understanding and trusting me.

I wish to thank all of the post-docs, especially Professor Leigh Aldous, who generously shared his ionic liquids knowledge, Dr. Sven Ernst who always helped me, Dr. Qian Li, who gave me good advices in both my life and projects, and Dr. Chris Batchelor-McAuley, who was my Part II supervisor and still gave me useful advice through my D.Phil.. Also to Dr. Blake Plowman, Dr. Wei Cheng, Dr. Kristina Tschulik and Dr. Friedrich Kaetelhoen for always being on hand to help.

I would like to acknowledge Prof. Chris Hardacre and Dr. Sarah Norman who provided clean and neat RTILs for my project.

Many thanks to Honeywell for funding my D.Phil. research. Great thanks go to Dr. John Chapples, Dr. Keith Pratt, Dr. Martin Jones and Dr. Lei Xiao for their very useful discussion and input throughout the three-year of my D.Phil and for their hospitality and kindness during the internship in Portsmouth.

Special thanks to my 'First Year' friends, Ying, Emma, Min and Eddy, for precious memories throughout the this three years. Thanks to Ying for always being there for me, to Emma for being very sweet and kind the whole time, to Min for her companionship and good food over the past four years and to Eddy for his endless help and patience when I bothered him with the IT stuff. Thank every member in the RGC group for laughters and encouragement. Thanks Patty for emergency chocolate.

I would like to thank all of my friends, especially Ivana and Hao for being are very considerate, Y for being very supportive, NeiNei for helping me through my difficult time. I cannot express my gratitude enough. I am sure all of you are my lifelong friends.

Finally, I would like to thank those special people in my life, my Mum, for her on-going support, and Bin, for being extremely patient with me.

Glossary

Symbol	Definition	Unit
E	Electrode potential	V
ϕ	Electrostatic potential	V
I	Current	A
R_S	Resistance	Ω
E^0	Standard electrode potential (vs standard hydrogen electrode)	V
E^0_f	Formal potential	V
a	Activity of electro-active species	$mol \cdot cm^{-3}$
c/[]	Concentration	$mol \cdot cm^{-3}$
$[]_0$	Solution concentration at electrode surface	$mol \cdot cm^{-3}$
c^*	Bulk solution concentration	$mol \cdot cm^{-3}$
C_d	Double layer capacitance	F/m^2
D	Diffusion coefficient	$cm^2 \cdot s^{-1}$
j	Flux	$mol \cdot cm^{-2} \cdot s^{-1}$
ε	permittivity	F/m
z	Charge on electroactive species	
k_0	Heterogeneous rate constant	
K	Homogeneous rate constant	s^{-1}
n	Number of electron transferred	
α	Butler-Volmer transfer coefficient for electro-reduction	
k^0	Standard heterogeneous rate constant	$cm \cdot s^{-1}$
G	Gibbs free energy	$J \cdot mol^{-1}$
$G^{\ddagger}$	Gibbs free energy at transfer state	$J \cdot mol^{-1}$
F	The faraday constant = 96485.3	$C \cdot mol^{-1}$
A	Surface area of electrode	cm^2
R	Universal gas constant = 8.31447	$J \cdot K^{-1} \cdot mol^{-1}$
ν	Scan rate	$V \cdot s^{-1}$
Λ	the Matsuda and Ayabe parameter	
r	radius of a electrode	m

Contents

Chapter 1

Fundamentals of Electrochemistry

This thesis is concerned with the development of amperometric gas sensors. The first chapter presents the theoretical fundamental electrochemistry underpinning the work reported in the thesis. Fuller discussion appears in the later chapters.

1.1 The Electrochemical Cell

In an electrochemical experiment, a potential difference is applied to an electrode to induce electron transfer.[1, 2] Consider a simple one-electron oxidation,

$$A_{(aq)} \underset{k_b}{\overset{k_f}{\rightleftharpoons}} B_{(aq)} + e \tag{1.1}$$

where $A_{(aq)}$ and $B_{(aq)}$ are electro-active species in solution and e is the electron transferred from/to a working electrode (normally a metal or carbon electrode). It is impossible to pass a current or measure/apply a potential difference using a single electrode; hence, the simplest electrochemical cell includes a reference electrode as well as the ('working') electrode of interest to complete a circuit. The potential is applied to the working electrode relative to the reference electrode, and the latter is designed so that the potential at the reference electrode is constant, provided no current is passed through it. The applied potential is [1, 2]:

$$E = (\phi_M - \phi_S)_{working} - (\phi_M - \phi_S)_{reference} + IR \tag{1.2}$$

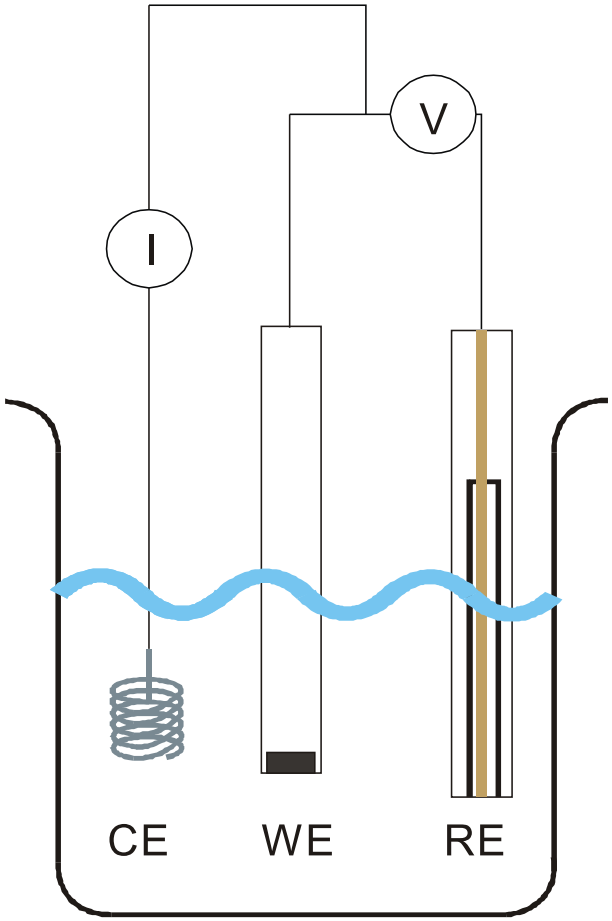

Figure 1.1: Diagram for a three-electrode cell. WE, RE, CE indicate the working, reference and counter electrodes respectively.

where E is the potential applied between the working and reference electrode, (ϕ_M - ϕ_S)$_{working}$ is the potential difference at the working electrode interface, (ϕ_M - ϕ_S)$_{reference}$ is the interfacial potential difference at the reference electrode and IR is the ohmic drop due to the current passed through the bulk solution.

It is essential to maintain a known value of $(\phi_M - \phi_S)_{working}$ since this is the 'driving force' for the electron transfer. For experiments involving electrodes of large surface (see, for example, in Chapter 9), a large current is passed. The ohmic drop in the solutions is no longer negligible and varies with the experimental time. Further the potential

difference at the reference electrode is not constant since the large current can change the surface and the chemical composition of the reference electrode. Consequently, the applied potential in a two-electrode system sometimes does not reflect that applied at the working electrode/solution interface. A third electrode, a counter electrode, is introduced to solve this problem in which the current is only passed through the working and counter electrodes but no current flows through the working and reference electrodes. Note that the counter electrode is required to be highly conductive with a sufficient surface area to ensure easy passage of electrons without limiting the electrochemical reaction. This three electrode set-up is shown schematically in Figure 1.1. With no current passed through the reference electrode, $(\phi_M$ - $\phi_S)_{reference}$ becomes constant, and the value of IR falls to zero. Therefore, changes in the applied potential, E, directly reflect changes in $(\phi_M$ - $\phi_S)_{working}$. A three-electrode system is commonly applied with the use of macro-electrodes, whereas a two-electrode system can often be employed with a micro-electrode,[3–7] but not with a macro-electrode. Even though micro-electrodes are mainly used in this thesis, a three-electrode set-up is utilised for all systems studied to minimise potential shifts from ohmic drop.

The next section discusses how current generated during electrochemical process is interpreted.

1.2 Electrode Kinetics

For an electrochemical reaction to take place, it must overcome an energy barrier to oxidise A to B (see Figure 1.2). The minimum energy needed is the activation energy, which is associated with the reaction kinetic constant, k, as below:

$$k = Ae^{\frac{-\Delta G^{\ddagger}}{RT}} \tag{1.3}$$

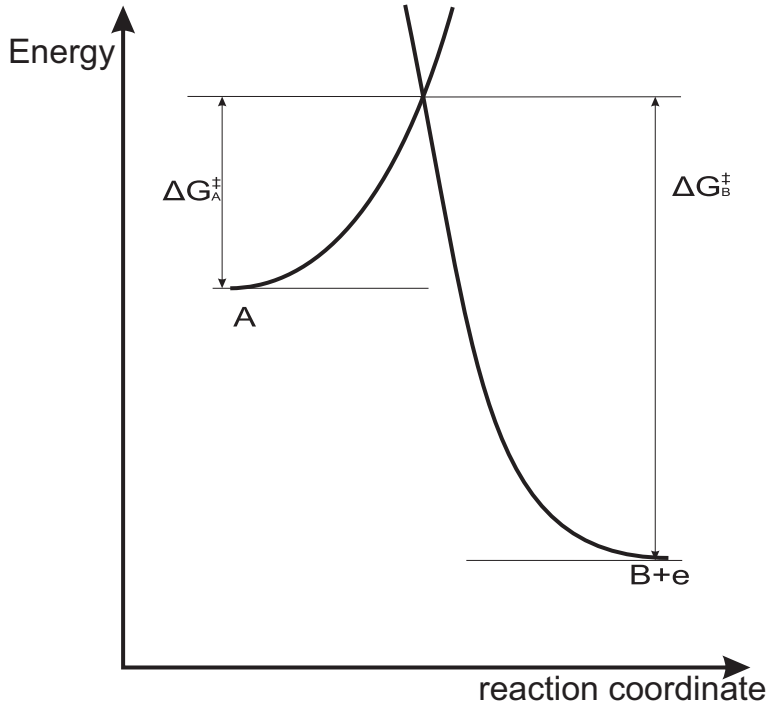

Figure 1.2: Energy profile of Reaction 1.1

where A is the frequency factor for the reaction, describing the number of collisions per second, R is the universal gas constant and T is the temperature.

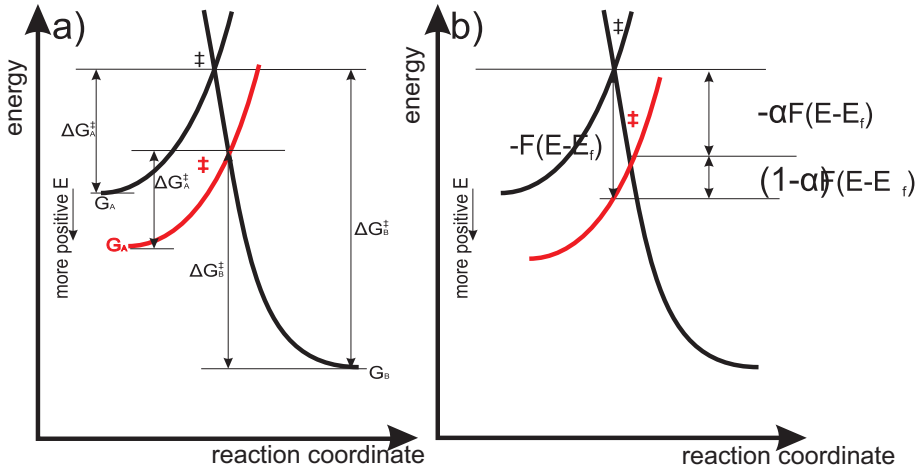

Figure 1.3: Effect of a more positive potential applied to the working electrode on the activation energy.

In a metal electrode, there are continuous bands of energy filled by electrons. The highest energy level is the Fermi level. The Fermi level of the electrode can be altered by changing the applied potential. When a positive potential is applied, the Fermi level is

decreased. If this more matches the energy of highest occupied molecular orbital (E_{HOMO}) of A, Reaction 1.1 can be facilitated. The influence of the potential applied to the electrode on the energy is shown in Figure 1.3. Such reactions are governed by Faraday's law, which states that the amount of chemical reaction caused by the flow of current is proportional to the amount of electricity passed.[8, 9]

$$I = nFAj \tag{1.4}$$

where A is the electrode area, F is Faraday constant, indicating that the charge passed per mole of electrons transferred is equal to 96485 C mol^{-1} and j is the heterogeneous reaction flux at the interface:

$$j = k_b[B]_0 - k_f[A]_0 \tag{1.5}$$

Here, k_f and k_b are heterogeneous electron transfer rates of the forward and backward reactions respectively, $[A]_0$ and $[B]_0$ indicate the concentrations of A and B at the electrode surface. Note that the electron transfer process between the electrode and the reactant, A, occurs via quantum tunnelling and so A must be located within the distance of 10 $\sim$ 20 Å of the electrode, since it requires the electron wavefunctions of A and electrode to overlap. Equation 1.5 suggests that the concentration that is important to the reaction is that close to the electrode surface rather than remotely in the bulk solution. The reactant is oxidised to the product via a transition state ‡ as shown in Figure 1.3. In this state, an 'active complex' is formed via the activation of A, likely involving bond stretching and changes in solvation.[10] The rates of forward reaction and backward reaction depend on the energy difference between the transition state and the initial/final energy. The rate of electron transferred can be defined as:

$$k_f = A_f exp\frac{-(G^{\ddagger} - G_A)}{RT} \quad and \quad k_b = A_b exp\frac{-(G^{\ddagger} - G_B)}{RT} \tag{1.6}$$

The relation between the activation energy before ($\Delta G_0^{\ddagger}$) and after the applied potential ($\Delta G_0^{\ddagger}$) is shown in Figure 1.3 b) and can be expressed as,

$$\Delta G_A^{\ddagger} = \Delta G_{0,A}^{\ddagger} - (-\alpha)(E - E_f^0) \tag{1.7}$$

$$\Delta G_B^{\ddagger} = \Delta G_{0,B}^{\ddagger} - (1 - \alpha)(E - E_f^0) \tag{1.8}$$

Here, $E - E_f$ is also known as the over-potential. Therefore, the reaction kinetic coefficients can be further expressed as,

$$k_f = A_f exp\frac{-\Delta G_{0,A}^{\ddagger}}{RT} exp[\frac{(-\alpha)(E - E_f^0)}{RT}] \quad and \quad k_b = A_b exp\frac{-\Delta G_{0,B}^{\ddagger}}{RT} exp[\frac{(1 - \alpha)(E - E_f^0)}{RT}] \tag{1.9}$$

By assuming the oxidation reaction is at equilibrium where $[A]_0$=$[B]_0$ and $E = E_f^0$, leading to k_f=k_b, the reaction rate coefficient, k_0, can be resolved via the Butler-Volmer Equation as,[11]

$$j = k_0[exp(\frac{-\alpha F}{RT}(E - E_f^0))[B]_0 - exp(\frac{(1 - \alpha)F}{RT}(E - E_f^0))[A]_0] \tag{1.10}$$

where k_0 is the standard electrochemical rate constant and α is the transfer coefficient. The transfer coefficient indicates the position of transition state relative to the reactants and products, α lies in the range of 0 to 1 for one electron system. If α is close to 0, the transition state is product-like for an oxidation, whereas if α is near 1, the transition state is reactant-like.

The transfer coefficient can be evaluated by the following approach: An extreme over-

potential $(E - E_0)$ is applied at the working electrode, resulting in only oxidation or reduction taking place. Therefore one term in Equation 1.10 can be neglected. The current is evaluated through the use of the Tafel law:[2]

$$I_{red} = AFk_0 exp(\frac{-\alpha F}{RT}(E - E_f^0))[B]_0 \quad and \quad I_{ox} = AFk_0 exp(\frac{(1-\alpha)F}{RT}(E - E_f^0))[A]_0 \tag{1.11}$$

Here I_{red} and I_{ox} are the reduction and oxidation current respectively. Taking natural logarithms of the above equations gives,

$$\alpha = -\frac{RT}{F}\frac{\partial ln|I_{red}|}{\partial E} \quad and \quad 1 - \alpha = \frac{RT}{F}\frac{\partial ln|I_{ox}|}{\partial E} \tag{1.12}$$

α can be obtained via a plot of $ln\ I$ against E where the gradient of this straight line is diretly proportional to α, assuming $[A]_0$ and $[B]_0$ are approximately constant. The data can be simply measured from cyclic voltmmetry (see Section 1.5.1). Despite the simple operation of Butler-Volmer theory in modelling a variety of experimental results, it exhibits some limitations that are likely due to the lack of physical insight. The Butler-Volmer model suggests that the rate constant can infinitely increase when the applied potential tends toward infinity which is physically impossible since excess energy may be lost to heat or other forms. Therefore a better model is proposed by Marcus that provides better physical insights into the electrochemical reactions.[12]

1.3 The Electrical Double Layer

Two types of charge transfer processeses dominate at electrodes. One type is that previously discussed in which the charge transfer across the electrode/solution interface causes electrochemical reactions, leading to a current that follows Faraday's law. The other pro-

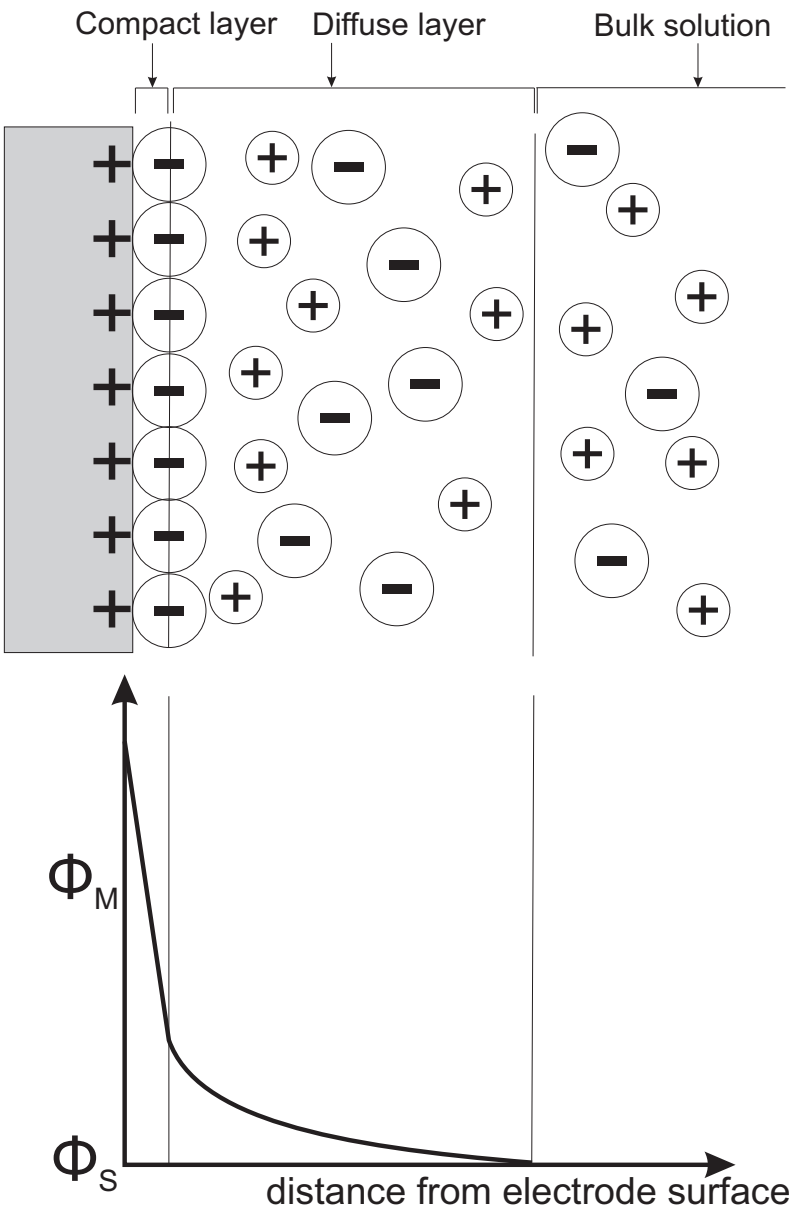

Figure 1.4: Model of the electrical double layer.

cess is a non-Faradaic process in which the structure of the electrode/solution interface can vary with the change of applied potentials, again leading to a flow of current.

This section introduces the simplest case of a system in which only non-Faradaic current occurs due to charging and discharging of the electrical double layer capacitance.[1]

When a potential difference is established at an electrode/solution interface, an electric double layer capacitance is formed. At the charged electrode, ions of opposite charge to that of the electrode are built up in the solution at close proximity to the electrode so

as to maintain charge neutrality. This layer partly comprises a compact layer of ions at the electrode surface, as shown in Figure 1.4. Within the compact layer, the potential decreases linearly with the distance away from the electrode surface. Beyond the compact layer, a diffuse layer exists. The potential drops less rapidly in the diffuse layer, where the ions undergo Brownian motion due to thermal forces. The charging current, I, caused by redistribution of ions in forming the double layer is given by,

$$I = \frac{dQ}{dt} = C_d \frac{dE}{dt} = C_d A \upsilon \tag{1.13}$$

where Q is the charge and C_d is the double layer capacitance. Since electrode processes take place within the double layer, it is important to compresses the diffuse layer thickness within the electron tunnelling distance of $10 \sim 20$ Å so the full drop in potential at the electrode/solution interface is available to 'drive' the reaction. The diffuse thickness can be compressed by adding an excess of salt ('supporting electrolyte'). The Debye length is defined as the distance in which the charged particles can screen external electric field. By definition, the Debye length is also the double layer thickness. Its value can be shown via the following equation:

$$\kappa^{-1} = \sqrt{\frac{\varepsilon_0 \varepsilon_r kBT}{2NAe^2 I}} \tag{1.14}$$

where κ^{-1} is the Debye length, ε_0 is the electric constant, ε_r is the permittivity of free space, N_A is the Avogadro constant, e is the elementary charge and I is the ionic strength. Ionic strength is a measure of the concentration of ions in the solutions; it is related to concentration via

$$I = 1/2 \sum_{i=1}^{n} (2cz) \tag{1.15}$$

where c is the concentration and z is the charge. The excess of supporting electrolytes will increase the ionic strength via the increase of concentration. As a result of higher ionic strength, the Debye length will decrease as will the double layer thickness. In ionic

liquids, the high concentration of ions ensures the desired, rapid fall-off of potential within distance.

1.4 Mass Transport

In practice, electron transfer only occurs at a working electrode when the electro-active species is within a few molecules distance of the electrode surface. Hence, the overall reaction rate is governed by both the electron transfer rate for a given reaction and the rate at which electro-active species is replenished at the electrode surface from the bulk solution (mass transport). There are three types of mass transport: diffusion, convection and migration.

1.4.1 Diffusion

Diffusion occurs when a concentration gradient exists in the system. When electro-active species close to electrode surface are consumed, the concentration of the species at the electrode decreases, forming a depletion layer ('diffusion layer') near the electrode surface. The analytes are drawn to the electrode surface in order to maximise entropy. The rate of diffusion depends on the concentration gradient as given by Fick's first law:[13]

$$j = -D\frac{\partial c}{\partial x} \tag{1.16}$$

where D is the diffusion coefficient, c is the concentration and x is the distance away from the electrode. Fick's second law is derived from Fick's first law, via mass conservation, and describes the rate of concentration change at point x:

$$\frac{\partial c}{\partial t} = D\frac{\partial^2 c}{\partial x^2} \tag{1.17}$$

There are two types of diffusion to an electrode, linear and convergent. These two

limiting cases are determined by comparing the sizes of the electrode radius, r, and the diffusion layer, d. The latter describes the thickness of the depletion region near the electrode through which electro-active material diffuses to reach the electrode. The diffusion layer is a result of a charge transfer reaction, and d is a function of time given by the following equation,

$$d = \sqrt{6Dt} \tag{1.18}$$

in which t is the experimental time. Linear diffusion dominates if $d<<r$, where r is the radius of the electrode.[1] Examples for linear diffusion include experiments at short experimental durations and/or using a macro-electrode. A macro-electrode normally has dimensions of millimeters. Convergent diffusion occurs when $d>>r$. This type of diffusion takes place at longer experimental times or at micro-electrodes (with one dimension in micrometers). These two limits are schematically shown in Figure 1.5.

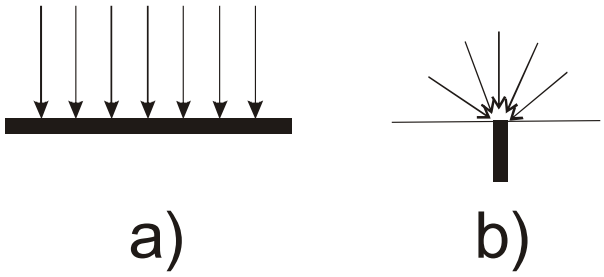

Figure 1.5: Diffusion to an electrode; a) linear diffusion and b) convergent diffusion.

1.4.2 Convection

Convection is the movement of particles due to mechanical forces exerted in a solution. There are two types of convection: natural convection, due to thermal or density gradient, and forced convection, produced by external forces such as stirring and vibrations. Flows caused by natural convection tend to mix the solution in an unpredictable manner. Natural convection often occurs if the experimental time of a voltammetric experiment is

longer than ca. 10 seconds with the use of a macro-electrode.[14] Forced convection can be introduced in a well controlled way, for example by using rotating disc or a chemical flow cell.[1, 2, 15] The convective flux is expressed as

$$j = cv(x) \tag{1.19}$$

Here *v(x)* is the solution velocity at point x.

1.4.3 Migration

Migration arises due to the motion of a charged particle down a potential gradient (electric field).[16–19] This type of mass transport takes place for all charged species in solution when a potential is applied to a working electrode relative to a solution, leading to a potential gradient and resulting in a flow of charged species electro-statically attracted to or repelled from the electrode.[20] The flux j, down a potential gradient, $\frac{\partial \phi}{\partial x}$, is given by the following equation:

$$j = -\frac{zF}{RT} Dc \frac{\partial \phi}{\partial x} \tag{1.20}$$

in which z is the charge of species migrating. To simplify the interpretation of electrochemistry, it is convenient to eliminate migration. This is done by adding supporting electrolytes to the solvent. The excess salt compresses the electrical double layer (discussed in Section 1.3), and hence, the electric field is confined to a very close region to the electrode. Consequently, mass transport to and from the electrode can be simplified to diffusion only. For experiments in room temperature ionic liquids, the solution is already self-supported.

High concentration of supporting electrolyte also offers several other advantages[14]. First, the solution conductivity is increased and therefore ohmic drop can be minimised. Second, the presence of electrolyte maintains a near constant ionic strength in solution,

fixing the formal potentials of redox couples. Third, excess supporting electrolyte compresses the diffuse layer to within a distance of 10 $\sim$ 20 Å from the electrode,[21] across which the electron quantum tunnelling can take place (see Section 1.2).

1.5 Analytical Techniques

This section introduces the major electrochemical techniques for analysing and studying electrochemical reactions. Information such as analyte concentrations, diffusion coefficients, and reaction rates can be obtained from voltammetry or amprometry.

1.5.1 Cyclic Voltammetry

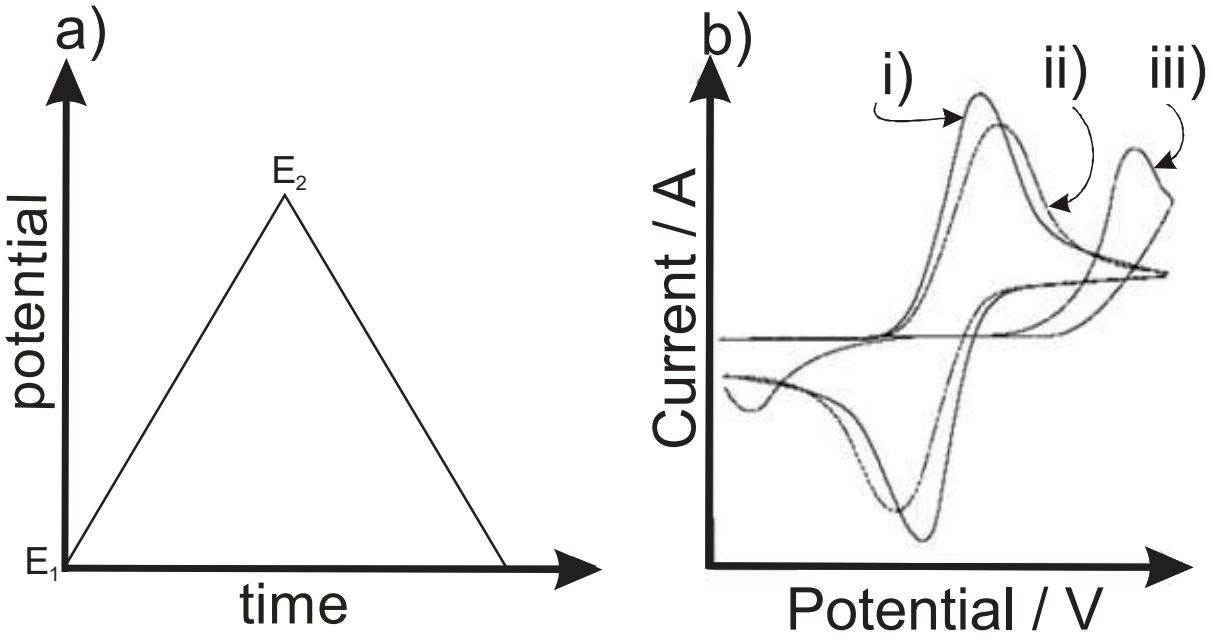

Figure 1.6: a) Potential waveform of cyclic voltammetry and b) Cyclic voltammetric responses for i) reversible, ii) quasi reversible and iii) irreversible electrochemical reactions at a macro-electrode.

In a cyclic voltammetry experiment, the potential is swept from an initial value, E_1, where no reaction takes place to a final value, E_2, where reaction is 'fully driven', then back to E_1 at a scan rate, ν(Equation 1.21). Figure 5.1 a) shows the potential waveform

of cyclic voltammetry.

$$\nu = \frac{\partial E}{\partial t} \tag{1.21}$$

The resultant current is plotted as a function of the sweeping potential as can be seen from Figure 5.1 b). The current - potential wave shape can be understood by considering the rates of electron transfer and mass transport. Initially, the applied potential is less than the oxidation potential of A (see Equation 1.1) and hence no current passes. When the potential increases to the oxidation potential of A, electrons pass from A to the electrode. This current is a function of the reaction rate and the concentration of A (see Equation 1.10) since the electron transfer rate is smaller than the rate of mass transport at this point. As potential increases further, the current reaches a peak at which the electron rate transfer is balanced by the diffusion rate of A. At larger potentials, the current decreases because the electron transfer is faster in comparison to mass transport. Therefore, the rate of diffusion of A is not sufficient to replenish the material consumed at the electrode surface. In the reverse scan, an analogous process takes place for the reduction of B back to A.

There are two extremes of electrochemical process: 'reversible' and 'irreversible'. These limits can be explained in terms of electron kinetics, measured by standard electrochemicl rate constant, k_0, and the rate of mass transport, measured by the mass transport coefficient m_T where

$$m_T = \frac{D}{\delta} \tag{1.22}$$

where δ is the diffusion layer thickness, given by Equation 1.18. The experimental time in Equation 1.18 can be related to the scan rate via,

$$t \sim \frac{RT}{F\nu} \tag{1.23}$$

Therefore m_T can be estimated from the following equation,

$$m_T \sim \sqrt{\frac{DF\nu}{RT}} \tag{1.24}$$

For $k_0 >> m_T$, the process is 'reversible' whilst for $k_0 << m_T$, it is 'irreversible'. The limits of reversible and irreversible systems have been rigorously mathematically evaluated by Matsuda and Ayabe via a parameter, Λ, where[22]:

$$\Lambda = \frac{k_0}{(FD\nu/RT)^{\frac{1}{2}}} \tag{1.25}$$

The boundaries were found to be:

$$Reversible \quad \Lambda \geq 15 \quad k_0 \geq 0.3\ \nu^{\frac{1}{2}}\ cm \cdot s^{-1} \tag{1.26}$$

$$Irreversible \quad \Lambda \leq 10^{-3} \quad k_0 \leq 2 \times 10^{-5}\ \nu^{\frac{1}{2}}\ cm \cdot s^{-1} \tag{1.27}$$

These results assume the experiments at 298 K and a transfer coefficient, α, of 0.5.

These two limiting cases can also be explored via cyclic voltammetry. In the reversible limit for one electron transfer at 298 K, the peak to peak separation (i) in Figure 5.1 b)), ΔE, is 57 mV and the peak current, i_p, can be given by the Randles-Ševčík equation[23, 24].

$$i_{p,\mathrm{rev}} = 0.446FAc^*_{\mathrm{A}}\sqrt{\frac{FD\nu}{RT}} \tag{1.28}$$

The cyclic voltammogram of irreversible limit is shown in Figure 5.1 b) iii). An

overpotential much larger than the formal potential is required to overcome the kinetic barrier and to drive the electrochemical reaction.[20] Therefore, a large ΔE (> 200 mV) is normally expected. The peak current resulting from a one-electron transfer irreversible reaction is given by:[1, 2]

$$I_{p,\text{irrev}} = 0.496\sqrt{\alpha}FA[A]\sqrt{\frac{FD\nu}{RT}} \tag{1.29}$$

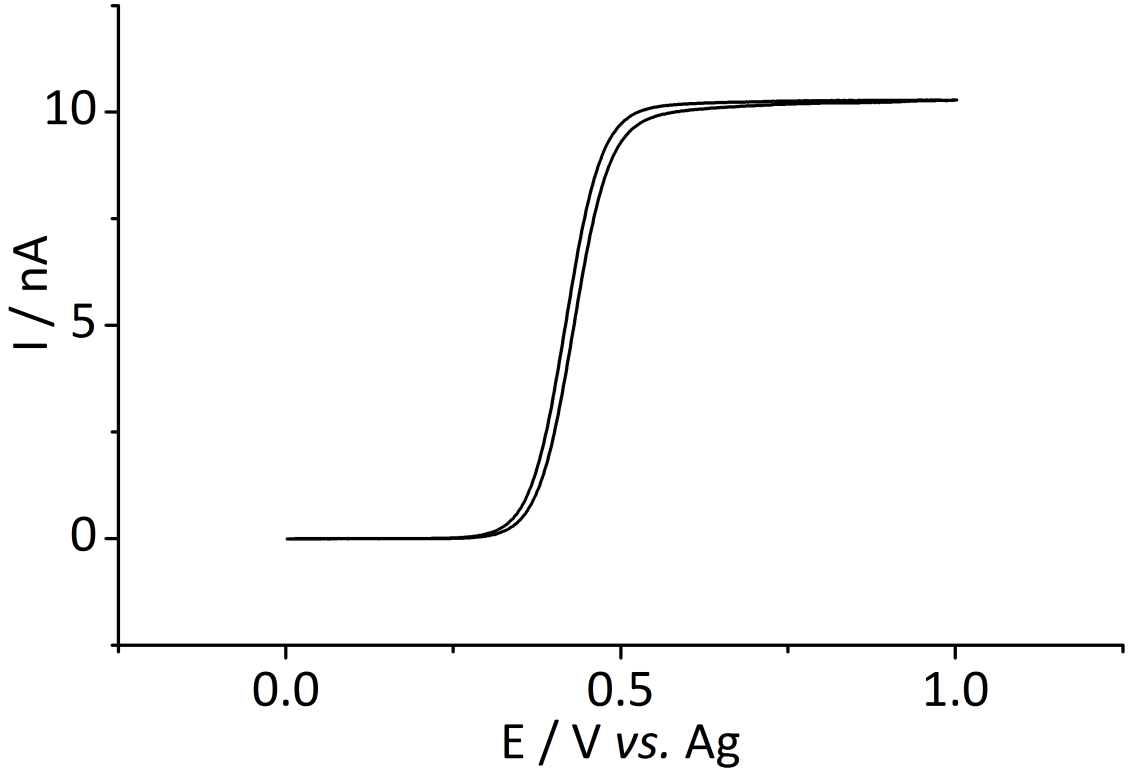

Figure 1.7: Typical cyclic voltammetric response at a micro-disc electrode.

The cyclic voltammetric response of an electrochemical experiment at a micro-disc electrode is significantly different from that at a macro-disc electrode. Normally, no peak is observed with a micro-disc electrode. This is due to a more effective 'convergent diffusion' at a micro-disc electrode at an experimental time when $r << d$, leading to a steady state current, i_{ss}, given by:

$$I_{ss} = 4nFrDc \tag{1.30}$$

However at a vary fast scan rate, a peak will appear because the linear diffusion occurs at a short experimental time (see Equation 1.18).

1.5.2 Square Wave Voltammetry

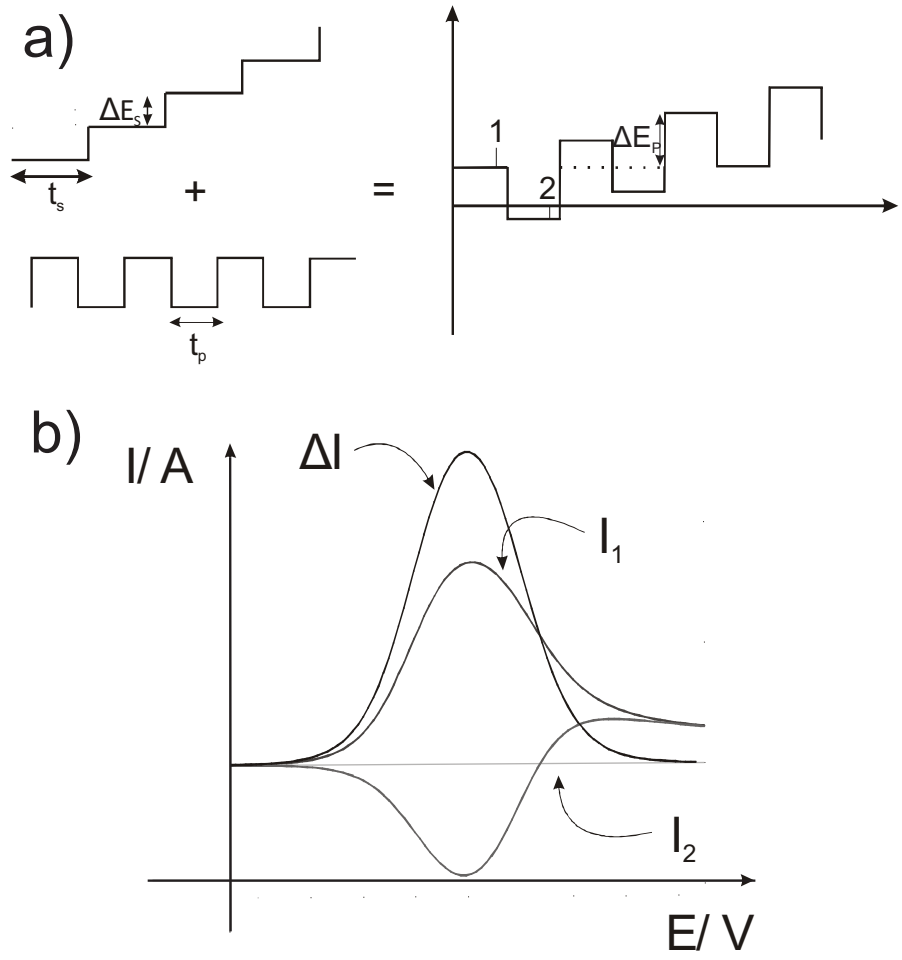

Figure 1.8: Square wave voltammetry a)Potential - time profile and b) resultant current - time response.

Square wave voltammetry is a technique commonly used to enhance the sensitivity of the voltammetry of an electrochemical process [25] due to its ability to reduce capacitative currents. In square wave voltammetry, a square potential is superimposed on a staircase waveform as shown in Figure 1.8 a). The current is measured at positions 1 and 2. The

square wave voltammetric response is characterised by a pulse height, ΔE_P, the staircase height, ΔE_P, the pulse time, t_P, and the cycle period, t_S. The voltage scan rate is given by,

$$\frac{\Delta E_S}{2t_P} = f\Delta E_S \tag{1.31}$$

where ΔE_S is defined in Figure 1.8 a).

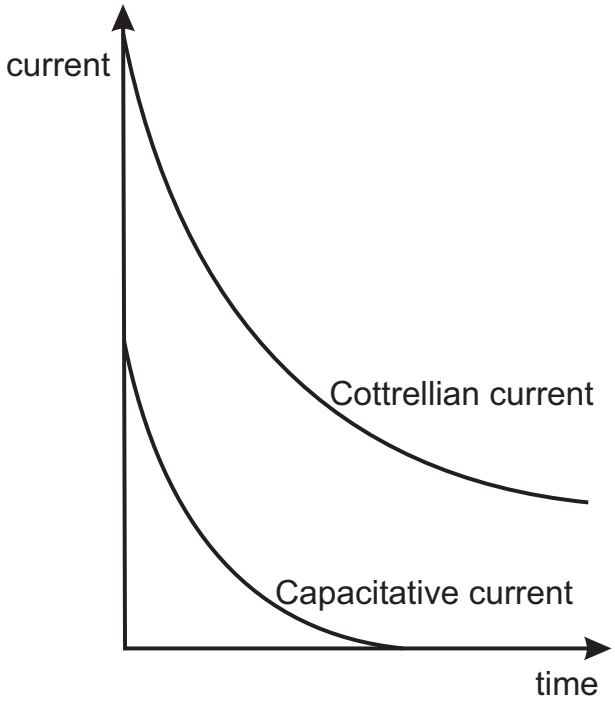

Figure 1.9: Faradaic and capacitive current versus time.

The capacitative component decays much faster than the Faradaic current because capacitative current falls as a function of e^{-t} whilst the Faradaic current decreases by $t^{-\frac{1}{2}}$. The current time responses of the Faradaic current (Cottrellian current) and the capacitative current are shown in Figure 1.9. The Faradaic current is expressed as,

$$I(t) = \frac{nFAcD^{\frac{1}{2}}}{t^{\frac{1}{2}}\pi^{\frac{1}{2}}} \tag{1.32}$$

The capacitative current, I_c, decays exponentially as,

$$I_c(t) = I_0 exp\left(\frac{-t}{RC_d}\right) \tag{1.33}$$

Here, I_0 is the initial current and R is the resistance. Therefore it is possible to minimise the capacitive contribution by sampling the current at the end of each step.

The resultant current, ΔI is the difference of I_1 and I_2 (see Figure 1.8 b)) and is plotted against applied potential as shown in Figure 1.8 b). Assuming the capacitative currents at 1 and 2 are approximately equal, the current due to the non-Faradaic process is reduced. Due to these features, the square wave technique provides higher sensitivity, easily reaching detection limits of 1×10^{-8} M.

1.5.3 Potential Step Chronoamperometry at A Micro-electrode

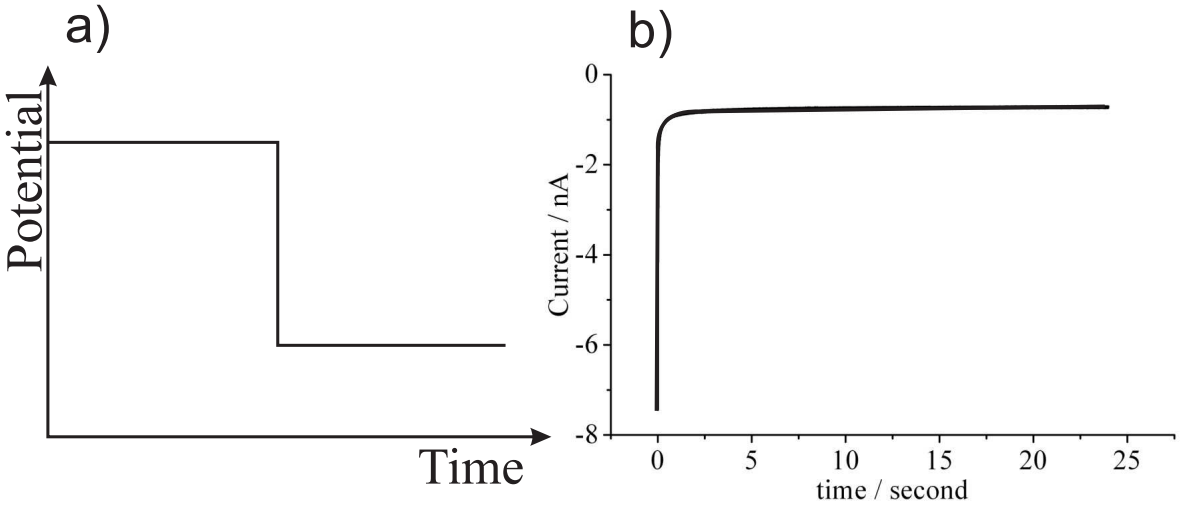

Figure 1.10: a) Potential - time profile, b) resultant current - time response at a micro-electrode.

Chronoamperometry at a micro-electrode, with the aid of relevant theory, is a commonly used technique for simultaneous measurement of concentration and diffusion coefficients[2, 4, 26–28] whereby a potential is stepped from a value where no reaction takes place to a potential where reaction is fully driven in a diffusion controlled way (Figure 1.10 a). The resulting current is plotted against time as shown in Figure 1.10 b).

The current is initially very large, resulting from a steep concentration gradient close to the electrode surface. Then the Faradaic current decays rapidly because it is limited by the depletion of the electro-active species near the electrode surface. Such a current-time relationship resulting from a potential step to a planar macro electrode is described under diffusion controlled conditions by the Cottrell equation. [1, 2, 29]

At a long experimental time, I_{ss} is recorded at a micro-disc electrode as discussed in Section 1.5.1.

Several numerical models have been developed to describe the chronoamperometric responses observed at a microelectrodes.[26, 27, 30–35] The Shoup and Szabo equation is most widely used, and has been reported to describe the current response over all time values to within an error of 0.5 %[26]. Chapter 4 gives more details of the Shoup and Szabo analysis. Chronoamperometry is also used in conjunction with standard addition of analytes to observe analytical responses.[36].

References

[1] Compton, R. G.; Banks, C. E. *Understanding Voltammetry*; Imperial College Press, 2011, 2nd Edition.

[2] Bard, A. J.; Faulkner, L. R. *Electrochemical Methods: Fundamentals and Applications*; Wiley, 2001.

[3] Fleischmann, M.; Lasserre, F.; Robinson, J.; Swan, D. *Journal of Electroanalytical Chemistry and Interfacial Electrochemistry* **1984**, *177*, 97 – 114.

[4] Rogers, E. I.; Silvester, D. S.; Poole, D. L.; Aldous, L.; Hardacre, C.; Compton, R. G. *Journal of Physical Chemistry C* **2008**, *112*, 2729–2735.

[5] Faure, M.; Pallandre, A.; Chebil, S.; Le Potier, I.; Taverna, M.; Tribollet, B.; Deslouis, C.; Haghiri-Gosnet, A.-M.; Gamby, J. *Lab on a Chip - Miniaturisation for Chemistry and Biology* **2014**, *14*, 2800–2805.

[6] Meng, Y.; Aldous, L.; Belding, S.; Compton, R. *Physical Chemistry Chemical Physics* **2012**, *14*, 5222–5228.

[7] Evans, R. G.; Klymenko, O. V.; Saddoughi, S. A.; Hardacre, C.; Compton, R. G. *Journal of Physical Chemistry B* **2004**, *108*, 7878–7886.

[8] Strong, F. C. *Journal of Chemical Education* **1961**, *38*, 98.

[9] Ehl, R. G.; Ihde, A. J. *Journal of Chemical Education* **1954**, *31*, 226.

[10] Atkins, P.; De Paula, J. *Atkins' Physical Chemistry*; Macmillan Higher Education, 2006.

[11] Butler, J. A. V. *Transactions of the Faraday Society* **1924**, *19*, 729 – 733.

[12] Marcus, R. A.; Sutin, N. *Biochimica et Biophysica Acta - Reviews on Bioenergetics* **1985**, *811*, 265–322.

[13] Fick, A. *Annal. Phys. Chem.* **1855**, *94*, 59 – 86.

[14] Bamford, C. H.; Tipper, C. F. H.; Compton, R. G. *Electrode Kinetics: Principles and Methodology: Principles and Methodology*; Comprehensive Chemical Kinetics; Elsevier Science, 1986.

[15] Montenegro, M. I.; Montenegro, I.; Queirós, A.; Daschbach, J. L.; Division, N. A. T. O. S. A. *Microelectrodes: Theory and Applications: Theory and Applications*; NATO ASI series / E: NATO ASI series; Springer Netherlands, 1991.

[16] Belding, S. R.; Limon-Petersen, J. G.; Dickinson, E. J. F.; Compton, R. G. *Angewandte Chemie International Edition* **2010**, *49*, 9242–9245.

[17] Barnes, E. O.; Wang, Y.; Limon-Petersen, J. G.; Belding, S. R.; Compton, R. G. *Journal of Electroanalytical Chemistry* **2011**, *659*, 25 – 35.

[18] Barnes, E. O.; Belding, S. R.; Compton, R. G. *Journal of Electroanalytical Chemistry* **2011**, *660*, 185 – 194.

[19] Barnes, E. O.; Wang, Y.; Belding, S. R.; Compton, R. G. *ChemPhysChem* **2012**, *13*, 92 – 95.

[20] Pletcher, D.; of Chemistry (Great Britain), R. S. *A First Course in Electrode Processes*; A First Course in Electrode Processes; Royal Society of Chemistry, 2009.

[21] Sakata, T.; Azuma, M. *Bulletin of the Chemical Society of Japan* **2013**, *86*, 1158–1173.

[22] Matsuda, H.; Ayabe, Y. *Zeitschrift fr Elektrochemie* **1955**, *59*, 494.

[23] Randles, J. E. B. *Transactions of the Faraday Society* **1948**, *44*, 327–338.

[24] Sevcik, A. *Collection of Czechoslovak Chemical Communications* **1948**, *13*, 349–377.

[25] Xiong, L.; Batchelor-Mcauley, C.; Compton, R. G. *Sensors and Actuators, B: Chemical* **2011**, *159*, 251–255.

[26] Shoup, D.; Szabo, A. *Journal of Electroanalytical Chemistry and Interfacial Electrochemistry* **1982**, *140*, 237 – 245.

[27] Klymenko, O. V.; Evans, R. G.; Hardacre, C.; Svir, I. B.; Compton, R. G. *Journal of Electroanalytical Chemistry* **2004**, *571*, 211–221.

[28] Paddon, C. A.; Silvester, D. S.; Bhatti, F. L.; Donohoe, T. J.; Compton, R. G. *Electroanalysis* **2007**, *19*, 11–22.

[29] Cottrell, F. G. *Z. Physik. Chem.* **1903**, *42*, 385 – 431.

[30] Heinze, J. *Journal of Electroanalytical Chemistry* **1981**, *124*, 73–86.

[31] Gavaghan, D. J.; Rollett, J. S. *Journal of Electroanalytical Chemistry* **1990**, *295*, 1–14.

[32] Oldham, K. B. *Journal of Electroanalytical Chemistry* **1981**, *122*, 1–17.

[33] Aoki, K.; Osteryoung, J. *Journal of Electroanalytical Chemistry* **1981**, *122*, 19–35.

[34] Aoki, K.; Osteryoung, J. *Journal of Electroanalytical Chemistry* **1984**, *160*, 335–339.

[35] Fleischmann, M.; Pons, S. *Journal of Electroanalytical Chemistry* **1988**, *250*, 257–267.

[36] Panchompoo, J.; Aldous, L.; Downing, C.; Crossley, A.; Compton, R. G. *Electroanalysis* **2011**, *23*, 1568–1578.

Chapter 2

Introduction to Amperometric Gas Sensors

This chapter provides an introduction to history and recent progress in amperometric electrochemical gas sensing. Topics covered include the use of room temperature ionic liquids (RTILs) as solvents in gas sensors, the advantageous use of micro-electrodes rather than macro-electrodes and membrane free devices. The work presented here has been published in *International Journal of Electrochemical Science.*[1]

2.1 Introduction

Gas detection plays an important, even essential role in many areas, ranging from food safety to environmental monitoring, with one of the best known examples being fire alarms based on CO[2–4] detection. Quantitative measurement of gases is based on a variety of physical or chemical principles[5]. Examples of commercialised sensors include techniques using spectrometry[6–10], luminescence[11–15] and electrochemistry[16–20] as a basis of sensing. Table 2.1 summaries different types of sensors and their operational principles. Amongst the various techniques, the electrochemical approach often shows significant advantages over the others. First and second, an electrochemical gas sensor provides high sensitivity at low cost. Third, their compact sizes allow for high portability. Fourth, only a small amount of energy is required to run the detector. On the other hand, the selectivity of electrochemical sensors is rarely perfect.

Type	Principle	Some examples
Photoionisation sensor	Detection of the charge generated from the ionised gas molecules produced by UV light	OV[5, 21–23], NO_2[24]
IR sensor	Comparison of IR intensity before and after being absorbed by the target gas	CO_2[25], CO[26], CH_4[27]
Fluorescence sensor [28]	Detection of the wavelength change of the fluorescence	CO[29],H_2S[30],HCN[31]
Metal oxide semiconductor	Measurement of changes in resistance after gas absorbed on the semiconductor surface	H_2[32–34], NH_3[35, 36],NO_2[37], CO[38]
Catalytic gas sensor	Measurement of resistance change on the sensor surface after reactions of target gas with the catalytic bead	OV[39], SO_2[40], CH_4[41, 42]
Electrochemical sensor	Detection of electron transferred during electrochemical reaction	O_2[43–45], NO_2[46], H_2S[47, 48], OV[49]

OV = Organic Vapour

Table 2.1: Table comparing of the principles of different gas sensing techniques.

Electrochemical gas sensors are categorised as being either potentiometric or amperometric in nature. In the former, a potential, $E.$ is established on a suitable electrode and related to the concentrations of the species giving rise to the potential via the concentrations of the Nernst equation[50]. Accordingly potentiometric sensors respond to the logarithm of the concentrations. Figure 2.1 depicts the structure of one type of potentiometric gas sensing electrode. Note the presence of two reference electrodes and an internal solution. Gases like carbon dioxide[51–56], sulphur dioxide[57, 58] and ammonia[59–61] are detected potentiometrically where the gas concentrations can be read as shifts in the measured potential. Often the gases are not measured directly but indirectly via their equilibration with protons in aqueous solution (as in Figure 2.1) to give concentration via pH measurements. Nonetheless, most gas sensors are amperometrically based where the concentrations of gas are monitored by current measurements with the latter arising from electrolysis (oxidation or reduction) of a target gas at a working electrode. Amperometric

sensors mostly originate from the design of the 'Clark oxygen electrode'[62] developed first for medical experiments. The Clark type gas sensor has a history of over five decades. In the immediately following sections, the classic and modern Clark type sensors are reviewed along with their advantages and drawbacks in the practical gas detection. Subsequantly we address recent advances in the area of amperometric gas sensing including the use of room temperature ionic liquids(RTILs) as solvents and micro-electrodes as detectors.

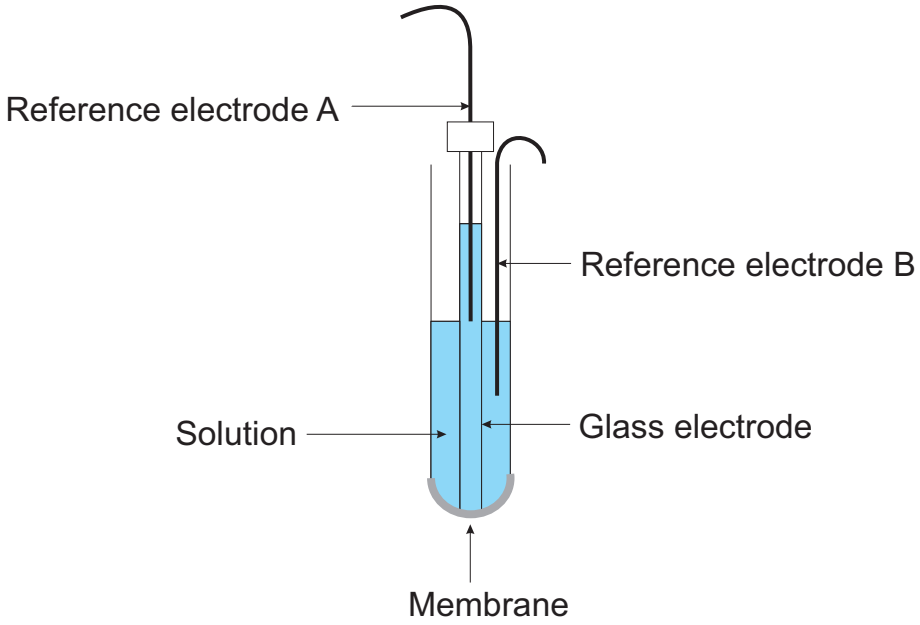

Figure 2.1: A potentiometric gas sensor electrode. The concentration of gas is recorded as the shift of potential. Gases, like CO_2, first diffuse through the membrane then dissolve in the internal solution. The pH of the solution is changed due to the formation of acidic compounds, like H_2CO_3. A potential shift of 59 mV with every one unit of pH is predicted by the Nernst equation.[63]

2.2 Clark Type Sensors

2.2.1 History of the Clark Oxygen Electrode

The Clark oxygen electrode made its first appearance in 1956. It was invented by Professor Leland Clark [62], often considered to be the 'father of biosensors', and was designed to measure the 'tension'(concentration) of oxygen in blood and tested first on dogs. The

device supported the publication of another Clark invention, an oxygen generator for cardiac surgery.[64]

The original design consisted of a power supply, a platinum cathode, a potassium chloride-calomel anode (which was later replaced with a silver wire) and a cellophane membrane. All the electrodes were placed inside a glass tube and were wrapped with cotton soaked with saline solutions. The cellophane membrane was used to separate the internal and external environment in order to avert the influence of red blood cells in the oxygen measurements. To realise the detection, oxygen first diffuses through the membrane and enters the internal solution. The reduction of oxygen then takes place at the platinum cathode (see Equation 2.1) when the power supply applies a potential of 0.6 V (vs. anode) to the cathode.

$$O_2 + 2H^+ + 2e \rightarrow H_2O_2 \tag{2.1}$$

The current of the reduction of oxygen was recorded using a galvanometer. The measured current was proportional to the concentration of O_2. This linear dependence of current on the concentration of dissolved oxygen was first discovered by Heinrich L. Danneel[65] as long ago as the nineteenth century as part of a study on dissolved oxygen in Nernst's laboratory. Experiments were performed by applying - 0.2 V vs. platinum at a platinum macro-electrode in a water solution containing dissolved oxygen. In experiments with blood the biosensor failed since the platinum was blocked by adsorbed blood cells.[66]

Experiments were carried out by Clark to optimise experimental conditions such as temperature, cathode voltage and choice of membrane material.[62] The current reading was observed to increase with the temperature due to the fact that oxygen diffuses faster at higher temperatures. The optimised voltage was within the range of 0.6 to 0.8 V against the anode but 0.6 V was deliberately chosen to reduce blood clot formation *in vivo*. It was found that the response time was largely limited by the time taken for oxygen

diffusion through the membrane reflecting both the diffusion coefficient and solubility of oxygen in the membrane as compared to the aqueous electrolyte of the sensor as well as their relative thickness. The best membrane materials in order to decrease the response times were identified. A collection of polymers was investigated, including cellophane[62], dialysis tubing, condom rubber, condom skin and polyethylene. The time taken to reach steady state reading decreased in the following order:[62] condom skin > condom rubber > polyethylene = dialysis tubing > cellophane. The best response time ($\sim$ 20 s) was seen with cellophane membranes. However, the cellophane membrane slowed the response time by half as compared to what was observed without using a membrane ($\sim$ 10 s).[62]

After the conditions were optimised, experiments for oxygen detection were carried out on blood both *in vitro* and *in vivo*. *In vivo* oxygen sensing was achieved through inserting the Clark type electrode into the aorta of a heparinised[1], Nembutalized[2] dog. The oxygen responses were recorded by a galvanometer. The first experiment was performed under different levels of oxygen where readings[3] on the galvanometer of 74 and 96 indicated partial pressure of O_2 of 95 mm Hg and 700 mm Hg respectively. This design was proved to accurately reflect the oxygen content. The sensing stability using the Clark type electrode was determined under a constant air supply (3 hours) where identical signals were observed throughout the experiment.[62]

The development of the Clark type oxygen electrode is deemed to be the birth of at-point-of-care measurements. Clark cells subsequently allowed applications in gaseous oxygen monitoring, direct blood oxygen measurements and much later even the development of early glucose sensors.[53] This great invention has inspired numerous scientists of later generations to develop other gas sensors using the Clark oxygen electrode as the basis. These are discussed in the next section.

[1]Heparin is an anticoagulant, preventing the formation of clots within blood.
[2]Nembutal is used as a veterinary anesthetic agent.
[3]Full scale = 100

2.2.2 Modern Clark Type Gas Sensors

Figure 2.2: Electrochemical gas sensors produced by Honeywell Analytics (www.honeywell.com). A electrochemical cell consists of electrodes, membrane and insulate seperators(to keep electrodes away from each other). A detector case has a complete electronic circuit which allows the gas concentration to be read. A data recorder can contineously record the gas concentrations.

Modern gas sensors are typically derived from the original design of the Clark type electrode where the gas of interest first passes through a suitable permeable membrane and then dissolves in an internal solution where the electrochemical reaction takes place. Despite the diverse designs for different target gases, Clark type gas sensors share some common features where at least two electrodes are required and a gas selective membrane is used to retain the solvents. This basic design is the one used by companies such as Honeywell, Draeger, Alphasense, etc. to produce gas sensors for the market today. The general form of commercialised gas sensors is shown in Figure 2.2. As can be seen in Figure 2.2, a gas sensor consists of a electrochemical cell that contains electrodes, membrane and insulating separators(to keep electrodes away from each other), a detector case, which gives digital readings of gas concentrations, and a data recorder, which exports the gas concentrations into a computer. A summary of some gases that can be detected electrochemically using sensors supplied by different companies is shown in Table 2.2. Some companies focus on independently manufacturing and developing gas sensors for a full range of applications. Others may specialise in health and safety or environmental

monitoring. The products are divided into small portable devices for field work and larger fixed devices used, for example, in ships or in the laboratory. It is noted that the sensors normally experience a lifetime of around 2 years, limited mainly due to the failure of the membrane and/or loss of the solvent (see next section). More details of gas sensing products in different companies can be found in the websites of the corresponding companies given in Table 2.2.

The value of a gas sensor depends on four properties: selectivity, sensitivity, response time and sensor lifetime. Selectivity allows the detection of a specific gas as other gases are either filtered out physically or chemically. Sensitivity indicates the dependence of the measured current on the concentration of gas. Factors influencing the sensitivity are not restricted to the electrode but reflect the sensing environment. Response times are also of vital importance since the sensor needs to reflect promptly the changing gas concentrations. This is normally measured by the time taken to reach 90% of the steady state response(t_{90}).

The sensor lifespan is controlled by the electrode materials, solutions and membranes. A sensor case (see Figure 2.2) lasts for a long time ($>$ 100 years). An electrochemical sensor normally has a shelf life of 6 months to a year. In standard sensing environments (- 40 to 50 ^{0}C, 20 - 90 % RH, $\sim$ 1 atm)[67], the membrane lasts for ca. 3 years and the sensing probe can run more than several thousand detections.[4] Lifetime limiting factors include the extreme temperature and pressures, low humidity environment and involvement of toxic gases.[68] These directly lead to consumed or contaminated filling solutions or electrode surfaces, resulting in electrode expiration.

[4]Information summarised from the user's manuals

	O_2	CO_2	CO	PH_3	CH	NH_3	H_2S	HCN	SO_2	ClO_2	HX	Halogens	NO	NO_2	O_3	OV	H_2O_2	H_2
https://www.honeywellanalytics.com/ Honeywell	✓	✓	✓	✓	✓	✓	✓	✓	✓	✓	✓	✓	✓	✓	✓	✓	✓	✓
http://www.alphasense.com/ Alphasense	✓	✓	✓	✓		✓	✓	✓	✓	✓	✓	✓	✓	✓		✓	✓	✓
http://www.casellasolutions.com/ Casella	✓		✓	✓		✓	✓	✓	✓	✓	✓	✓		✓		✓	✓	✓
http://www.alphasense.com/ Draeger	✓		✓	✓		✓	✓	✓		✓	✓	✓		✓	✓	✓	✓	✓
http://www.geotechuk.com/ Geotech	✓			✓		✓	✓	✓	✓	✓		✓		✓		✓	✓	✓
http://www.indsci.com/ Industrial Scientific	✓		✓	✓		✓	✓	✓	✓	✓	✓	✓		✓		✓	✓	✓
http://www.ionscience.com/ Ion Science Ltd	✓		✓				✓											
http://www.magusintl.com/ Magus International	✓		✓				✓											
http://www.MSAsafety.com MSA	✓		✓	✓		✓	✓	✓	✓	✓		✓					✓	
http://www.castlegroup.co.uk/ Castle Group Ltd	✓		✓	✓		✓	✓	✓	✓	✓		✓	✓			✓	✓	
http://www.emersonprocess.com/ Net Safety	✓		✓			✓	✓		✓								✓	

CH = hydrocarbon compounds; HX = hydrogen halide

Table 2.2: Table of available gas sensors from different sensing companies.(as at May 2014)

2.2.3 Limitations

Despite the popular application of Clark type electrodes for gas detection, they suffer from some significant limitations. Lifespan, response time and sensitivity are greatly influenced by the use of membranes and conventional solvents as is next discussed.

Gas	t_{90}
O_2	< 11 s
NH_3	< 90 s
H_2S	< 15 s
SO_2	< 25 s
NO_2	< 25 s

Table 2.3: Table of t_{90} of some of the gases. Information is summaried from user's manuals of different gas sensing companies. Solutions for toxic gas sensor (H_2S, NH_3, SO_2, NO_2) sensor are concentrated H_2SO_4 and that of O2 sensor is an aqueous solution of potassium acetate ($KC_2H_3O_2$). The membrane is one type of gas permeable solid polymer membranes.

One of the major drawbacks of Clark type electrodes in gas detection lies in the use of a membrane as the response time is largely limited by the time taken for diffusion through the membrane. It can be easily understood by comparing the diffusion coefficient of O_2 in air, water and in polymer membranes. The diffusion coefficient of O_2 in air[69] is 0.179 $cm^2\ s^{-1}$ (298 K) and in water[69] is 2.10×10^{-5} $cm^2\ s^{-1}$ (298 K) whereas in polymer membranes[70, 71] this value decreases to the order of magnitude of 10^{-6} $cm^2\ s^{-1}$. The decreased diffusion coefficient of oxygen in a membrane reflects the low gas permeability of polymer membranes.[5] In a typical Clark cell, the oxygen permeability in a membrane is 8×10^{-11} mol $m^{-1}\ s^{-1}\ atm^{-1}$ and in water is 2.7×10^{-9} mol $m^{-1}\ s^{-1}\ atm^{-1}$.[72] Note that the response time depends on both the membrane material and the thickness of the membrane. The original work on the Clark electrode showed that the response time rose from 20 seconds to 30 seconds when the thickness of cellophane doubled. Table 2.3 summarises typical values of t_{90} for commonly detected gases using commercial sensors. Toxic gas sensors(H_2S, NH_3, SO_2 and NO_2) contain filling solutions of concentrated H_2SO_4

[5]Permeability describes the diffusion of molecules, called the permeant, through a membrane or interface

whilst that of O_2 sensors is an aqueous solution of potassium acetate.[73] The membrane is one type of gas permeable solid polymer membranes. Data collected from the user manuals of AlphaSense products show t_{90} of longer than 10 seconds. The prolonged response time due to the presence of the membrane makes some sensors impractical for real-time monitoring as the change of sensing conditions can happen within seconds or less. Membrane dependent sensitivity is another issue. For example, work by Do et. al.[74] demonstrates that enhanced sensitivity was achieved by using conducting polymer membranes (polyaniline/Au/Nafion®) as working electrodes which not only reduces the need of a separate working electrode but also increases the sensitivity of nitrous oxide detection from 0.33 μA ppm^{-1}[75] to 2.28 μA ppm^{-1}.

Conventional solvents[76] used for gas detection are prone to evaporative losses, leading eventually to sensor failure [77]. Other sensing failures may be caused by high and low temperatures where solutions may be boiled or frozen in these environments. An electrochemical sensor normally has a lifetime of 24 months under standard conditions ($\sim$ 25 ^{0}C, $\sim$ 60 % RH, and within 20% of ambient pressure)[67]. H_2S, as a oil field gas, is one example that requires the sensor to be operated in extreme conditions (-60 to 60 ^{0}C)[78] [79] where shorter lifetimes may be expected.

The internal solution electrolyte of commercial sensors is often composed of H_2SO_4/ H_2O[80] as this electrolyte has a vapour pressure which most closely mirrors 'average ambient' conditions. However problems still remain as stated below. First the sensing range of the solution (-45 to 50 ^{0}C) is smaller than some real-world sensing conditions (-60 to 60 ^{0}C)[78]. Second losses of water result at humidity values lower than 60 % RH and gains of water at humidity values higher than this value. Experiments (by AlphaSense) in 5 M H_2SO_4 aqueous solution showed loss of the solution by ca. 50 % (by mass) at the temperature of 20 ^{0}C and at a humidity ranging from 0 % to 25 % RH over 2 days. At humidity values higher than 60 % RH, a 'flood' in the sensing chamber is caused where

the solution increased by around 100 % in mass, of water at the temperature of 20 ^{0}C and at a humidity of 95 % RH over 2 days[6]. Such changes to the solvent compositions result in the need for constant calibration of sensors. Further to this, the narrow electrochemical windows of H_2SO_4/H_2O (2 V) preclude useful electrochemical reactions of some gases to be observed in this media.[81, 82]

Other limitations may be ascribed to the nature of the electrochemical process used analytically. Due to the electron transfer process involved in the gas detection, the diffusion coefficient, the number of electrons transfer and the gas concentration are all sensitive to the environmental change. Therefore gas sensors typically are internally temperature and/or humidity compensated.[7] This is discussed in later sections.

Cross sensitivity[8] of non-target gases may result in a false reading of target gas concentrations. Taking an O_2 sensor as an example, an 6 % increase in signal is seen in the presence of 20 % CO_2. If more than 25 % CO_2 is present in the system, the O_2 sensor is damaged and an enhanced O_2 concentration is read, due to adsorption of CO_2 into the electrolyte($KC_2H_3O_2$)[9]. In addition, highly oxidising gases like chlorine, bromine, chlorine dioxide, and ozone can also interfere with oxygen sensing as electrons transferred during the oxygen reduction process can be possibly taken by those oxidising gases.[73] The next section focuses on overcoming some of the discussed limitations using recent advances.

2.3 Advances

Recognising the limitations of the traditional Clark type oxygen sensors as discussed in the previous section, we next discuss recent development aimed at overcoming these disadvantages. The following sections introduce recent advances for gas sensing systems

[6]please find more details in AlphaSense Application Note ANN 106
[7]See more details on Application notes for TGS2610 - Figaro
[8]The sensor responds to other gases that are not filtered out and can react on the electrode.
[9]Data collected from RAE Systems Inc Technical Note TN-152

from two respect: solvents and electrodes.

2.3.1 The Use of Ionic Liquids for Gas Sensing

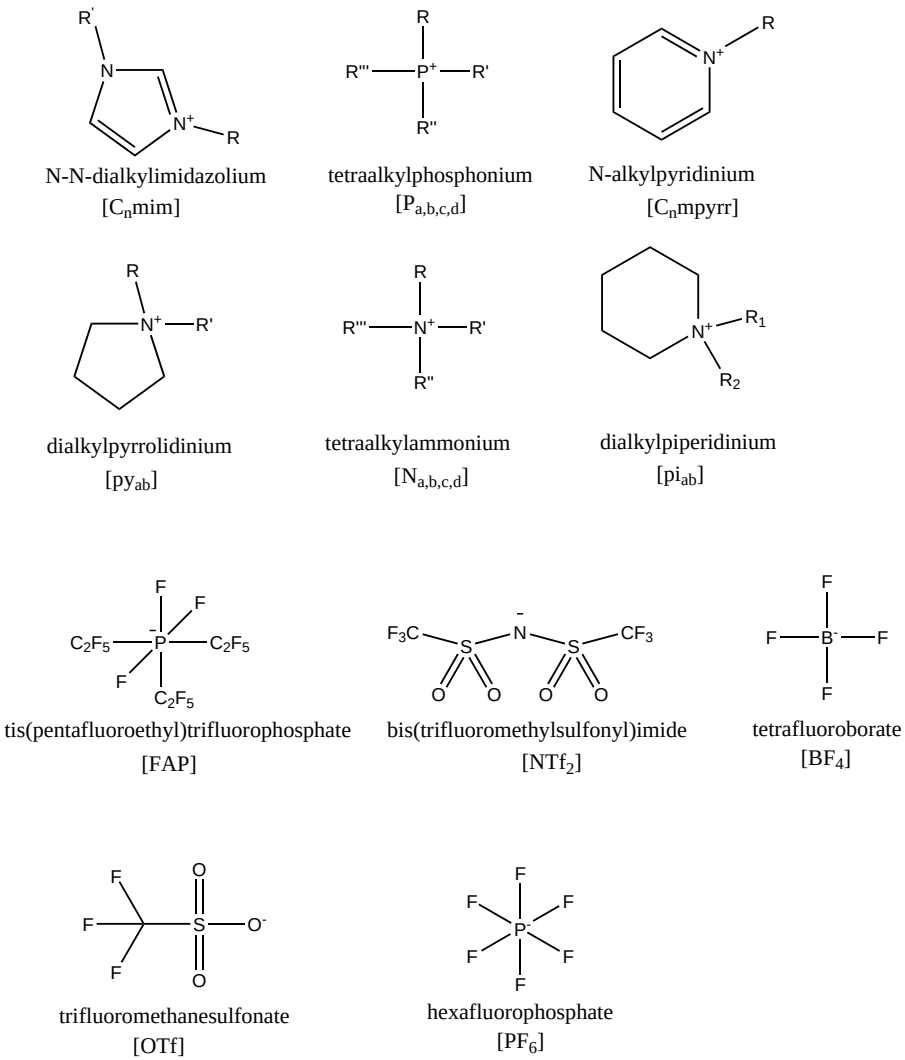

Figure 2.3: The structures, chemical names and usual abbreviations of the commonly used ionic components of RTILs

Room temperature ionic liquids (RTILs) are typically comprised of a bulky asymmetric organic cation and a small inorganic anion and exist as liquids at or below room temperature (298 K).[83] The main commercial suppliers of 'high purity' grade RTILs include Sigma-Aldrich[10], Merck[11] and BASF[12]. The purity of RTILs is frequently analysed[84]

[10]http://www.sigmaaldrich.com/chemistry/chemistry-products.html
[11]http://www.merckmillipore.co.uk/chemicals/ionic-liquids/
[12]http://www.intermediates.basf.com/chemicals/ionic-liquids/

using electrochemical techniques[76, 83, 85], high-performance liquid chromatography[86–88] and X-ray photo-electron spectroscopy[89–91]. Figure 2.3 shows some commonly used ionic cations and anions. The contrasting sizes of the ions result in poor coordination and therefore at room temperature the materials are liquids rather than solids like NaCl. RTILs have special properties which can offer an alternative to conventional solvents for use in gas sensors. The following sections focus on the possible beneficial properties of RTILs and their applications in gas detection.

Wide Electrochemical Windows

The width of the electrochemical window of a system is determined by the oxidation and reduction potential of the supporting electrolytes or the solvents. Wider electrochemical windows allow a greater range of molecules to be detected without masking from background currents. Water has a electrochemical window of 2.4 V and acetonitrile of 5 V. However, the oxidation or reduction potentials of the constituent ions are impossible to measure accurately as the commonly used reference electrodes in RTILs are Ag or Pt pseudo reference electrodes which may cause potential drifts (around 5 mV). To overcome this issue, either a stable $Ag/AgNTf_2$ external reference electrode is made[92] or an internal reference probe, normally ferrocene(Fc) or ferrocene derivatives, is dissolved in RTILs. The latter is commonly adopted for simplicity. The electrochemical windows are defined as the potential corresponding to a current density[13] of 1 mA cm^{-2}. A low current density is deliberately chosen since only small current is used in gas detection.[43, 45, 93, 94] A number of reports indicate that the oxidation and reduction potentials of ionic liquids are electrode material dependent[95–98]. The material dependence of electrochemical window was studied by Zhang and Bond at Au, glassy carbon (GC) and Pt working electrodes in $[C_4mim][BF_4]$. The magnitude of the electrochemical reduction window adhered to the

[13]Assuming macro-electrode behaviour (note that current density scales with the radius, not area, of micro-electrode)

electrode material sequence of Au ≈ GC > Pt while the oxidation window magnitude followed the order Au > GC ≈ Pt.

ionic liquid	EW (V)[77]	κ ($m\Omega^{-1}cm^{-1}$)[99]	thermal stability (K)
$[C_2mim][NTf_2]$	4.3	9.2[100]	455
$[C_4mim][NTf_2]$	4.8	4.0[101]	450
$[C_6mim][NTf_2]$	5.0	0.22[102]	428
$[C_6mim][FAP]$	5.3	0.17[103]	
$[C_4mpyrr][NTf_2]$	5.2	2.1[99]	
$[C_4mim][OTf_2]$	4.9	2.9[104]	
$[C_4mim][BF_4]$	4.7	0.36[102]	424
$[N_{6,2,2,2}][NTf_2]$	5.4	0.67[105]	
$[P_{14,6,6,6}][NTf_2]$	5.0	-	
$[P_{14,6,6,6}][FAP]$	5.6	1.1 (merck)	-
water	2.4	13 [106][a]	2273 K
acetonitrile	5.0	7.6 [106][b]	

a. 0.1 M KCl as supporting eletrolyte.

Table 2.4: Table of electrochemical window (EW), conductivity (κ) and thermal stability of vacuum dried aprotic ionic liquids at, unless stated, 298 K. Data are collected and summaried from the literatures

O'Mahony et al. compared the cathodic and anodic limits of some frequently used ionic liquids. To collect these data, the potentials were measured against the Fc/Fc^+ couple at 298 K and recorded at a Pt micro electrode. It was found that the anion followed the decreasing trend of stability[107]: $[NTf_2] \backsimeq [FAP] > [PF6] \backsimeq [BF4] > [OTf]$ > halides (Br^-, I^-). As the counter ion may also influence the oxidation potential of the anion, the cations were fixed to be $[C_4mim]$ in this study. The cathodic limits decreased as: $[C_4mprr] \backsimeq [P_{14,6,6,6}] \backsimeq [N_{6,2,2,2}] \backsimeq [C_6mim] > [C_4mim] \backsimeq [C_4dmim] > [C_2mim]$. Here the anions were selected to be $[NTf_2]$ for fair comparison. The electrochemical windows of RTILs typically range from 3 - 6 V. The widest electrochemical window is reported to be $[N_{6,2,2,2}][FAP]$(7.0 V)[97, 108]. Table 2.4 compares the electrochemical windows of some commonly used RTILs and the conventional solvents, water and acetonitrile.[77]

Apart from the chemical nature of RTILs, other factors also have a large impact on the electrochemical window. The study by O'Mahony et al. showed[109] that the width of the electrochemical window is subject to both the water content and temperature.

It was found that electrochemical window decreased in the following order of ionic liquid conditions: vacuum-dried > atmospheric > wet and 298 K > 318 K > 338 K. The temperature effect is because the electron transfer rate constant increases with the temperature. Hydrophobic RTILs may show less dependence on the width of electrochemical windows when exposed to atmospheric moisture as they uptake less water as compared to hydrophilic RTILs.[110] It was found by O'Mahony that the anion in particular affects the level of water uptake.[107] The hydrophobicity of the anions showed the following trend:[FAP] > [NTf_2] > [PF_6] > [BF_4] > halides. As for cations, long carbon chains enhance water repulsion in the solvent due to reduced polarity.[111]

Inherent Conductivity

Inherent conductivity is another important property of RTILs. It can be easily appreciated since RTILs are purely composed of ions. For RTILs, the extent of conductivity depends on the mobility of the ions composing the RTILs. The conductivity of RTILs near 298 K normally lies in the range of 0.12 - 8 $m\Omega^{-1}cm^{-1}$ which is comparable to organic solvents containing 0.1 M tetra-n-butylammonium perchlorate (TBAP) as supporting electrolyte where the values are within the range of 0.5 - 8 $m\Omega^{-1}cm^{-1}$. Table 2.4 lists the conductivities of RTILs, water (0.1 M KCl as supporting electrolyte) and acetonitrile (0.1 M TBAP as supporting electrolyte).

The large range of conductivities of RTILs reflects their structural differences. Bulky constituent ions usually show slower movement. This is exemplified by comparing the conductivity of [C_2mim][NTf_2], 9.2 $m\Omega^{-1}cm^{-1}$, and [C_6mim][NTf_2], 0.22 $m\Omega^{-1}cm^{-1}$. Here an order of magnitude drop is measured when the alkyl substituted group in the imidazolium changes from an ethyl to a hexyl group. Another cause of a decrease in mobility, hence conductivity, may be hydrogen bond formation.[112] The protic RTILs composed of fluoro- (F) or oxyl- (O) substituted anions generally show low conductivity ranging

from 0.14 to 1.3 $m\Omega^{-1}cm^{-1}$[98]. For the similar sized aprotic RTILs, the conductivities are above 4 $m\Omega^{-1}cm^{-1}$, except [[C_4mim][BF_4], where there may be some hydrogen bonds due to [BF_4].

The conductivity can also be changed due to the external environment. Influential factors include temperature and the presence of additives. The variation of RTILs conductivity with temperature follows the Vogel-Tammann-Fulcher(VTF) relationship with an empirical equation[113] being

$$\kappa = AT^{-\frac{1}{2}}exp[-B(T - T_0)] \tag{2.2}$$

From 258 K to 298 K, the conductivity of [C_2mim][NTf_2] increases from 1.5 to 9.2 $m\Omega^{-1}cm^{-1}$.[114] The higher conductivity at increased temperature reflects the increased mobility of the ions of RTILs. It was found that the addition of acetonitrile boosts the conductivity of imidazolium based RTILs where the conductivity of RTILs increases by more than 50 times with addition of just 15 % acetonitrile.[115] Similar observations were made with other co-solvents.[116–119] The use of organic co-solvent aims to decrease the solvent viscosity and hence to increase conductivity.

Low Volatility

The volatility of a solvent is measured by its vapour pressure. The pressure is measured when the gas phase of the solvent is in equilibrium with its liquid phase. This property reflects the applicability of a solvent under extreme conditions, notably high temperature and low pressure. High vapour pressure indicates the likelihood of solvent losses under extreme environmental conditions. Compared to almost all conventional solvents, RTILs have much lower volatility. This is evidenced by its capability for use in X-ray Photo-electron Spectroscopy(XPS).[120] XPS is generally not applicable to liquids since it employs ultra high vacuum (UHV) where conventional solvents evaporate. However

XPS is now regularly used to characterise RTILs.[121–126] The vapour pressure of pure water[127, 128] at 298 K is 3167.73 Pa whereas that of most ionic liquids is few mPa at 298 K[129]. This significant difference reflects the much stronger inter-molecular (ionic) forces in RTILs.

High Thermal Stability

The suitability of RTILs as solvents in gas sensing depends on the range of possible operation temperatures which is defined mostly by the melting point and decomposition temperature. Note, however, that a RTIL may also evaporate below its decomposition temperature. Maton et al.[130] thoroughly reviewed the factors that may affect the thermal stabilities, decomposition mechanisms and tools to analyse thermal decomposition for many RTILs.

As compared to conventional solvents, RTILs often exhibit high thermal stability. This is evidenced by the fact that RTILs remain as liquids over a large temperature range. For example, $[C_4mim][NTf_2]$ is liquid between 184 and 723 K as compared to the range of 273 K to 373 K for water at 1 atm.

The high thermal stability of RTILs is ascribed to their stable component organic and inorganic ion structures. Decomposition of RTILs follows various mechanisms[131, 132], including nucleophilic substitution (S_N1 and S_N2)[133], thermal rearrangement[134], alkene formation and dealkylation[129].

RTILs containing halides experience relatively low thermal stability as halides are good nucleophiles and in IL media, strongly basic in nature. It is possible for halides to react with the cations, leading to alkyl chain cleavage, at temperatures as low as 373 K. The thermal stability of RTILs decreases with increasing nucleophilicity of the constituent anion.

Stable products resulting from decomposition encourage thermal decomposition at

low temperatures.[111, 135] Long alkyl chains in the cation decreases thermal stability due to the favourable formation of stable carbon radicals. This is observed with basic anions, such as halides, [PF_6], [BF_4] and [NTf_2]. Because the conjugated radicals are stabilised through charge delocalisation, phenyl and allyl substituted cations show low thermal stability; decomposition via an S_N1 mechanism may take place.

Tunability

Another advantageous feature of RTILs is their 'tunability'. As RTILs consist of two ions, the composition of RTILs can be varied by altering either component and therefore they are frequently referred to as 'designer solvents'. By simply modifying the composition of RTILs, the physical and chemical properties can ideally be tailored for particular needs. This is exemplified with work by Xiong et al.[136] where ferrocene oxidation potentials can be shifted by changing the size of the anion of the ionic liquids. Three anions were studied (in the order of increasing size): [BF_4], [NTf_2] and [FAP] with the same counter ion, [C_4mim]. Figure 2.3 shows the abbreviations. It was found that the oxidation potential of ferrocene increases with decreasing size of anion as presumably the ferrocenium cation is stabilised with the presence of the smaller anion. This observation has the important implication that the oxidation potential of ferrocene, commonly used as an internal redox reference, can be tuned away from the potential of analytes of interest.

One method to tune the composition of RTILs is to simply mix two RTILs. This method has been used to optimise the solubility of CO_2[137] and SO_2[138–140]. This variation in the concentration of the RTILs leads to different intermolecular interactions and hence to a change in the gas capture activity.[138] Binary mixtures of ionic liquids are not rare[141] as mixed RTILs commonly combine merits of the different components. A study by Fox et al. [142] shows that the conductivity of a mixture of [$py_{1,5}$][NTf_2] and [$pi_{1,5}$][NTf_2] (see Figure 2.3 for abbreviations) remains unchanged but the viscosity

decreases as compared to the individual components.

Ionic Liquids and Gas Sensors

Gas	Reaction in RTILs
O_2	$O_2 + e \rightleftharpoons O_2^{\cdot -}$
NH_3	$4NH_3 \rightarrow 3NH_4^+ + \frac{1}{2}N_2(g) + 3e$
H_2S	$H_2S + e \rightarrow HS^- + H^{\cdot}$
SO_2	$SO_2 + e \rightleftharpoons SO_2^{\cdot -}$
NO_2	$NO_2 \rightleftharpoons NO_2^+ + e$

Table 2.5: Table of some electrochemical reactions of gas in RTILs.[76]

In the context of their use in electrochemical gas sensors, RTILs are of particular interest as this can address some of the problem caused by conventional solvents.[77] A wide diversity of gas detection has been studied in RTILs. Rogers et al.[76] reviewed the reaction mechanisms of various gases, including O_2, CO_2, H_2, NH_3, H_2S, SO_2 and NO_2, in RTILs. Some electrochemical reactions in RTILs are shown in Table 2.5. Examples of the use of RTILs for gas sensors include the application to CO_2 detection where the wide voltammetric window allows the electrochemical reduction of CO_2 to be observed. Also RTILs are deemed to be good solvents for electrochemical H_2S sensors where a very wide range of temperature is typically required. The benefits of applying RTILs as solvents for gas sensors are next summarised.

First, the wider electrochemical windows provided by RTILs as compared to those seen in aqueous/organic system suggests that many more gases may be detected electrochemically by using RTILs in comparison to conventional solvents. Also the wider potential window allows different reactions to be studied.

Second with the use of RTILs as solvents, membrane free electrodes can be realised as proposed by Huang et al..[143] This advance arises because of the RTIL low or zero volatility[144] which prevents their significant evaporation. As discussed in Section 2.2.3, the use of membranes largely limits the response times. The use of membrane free RTILs

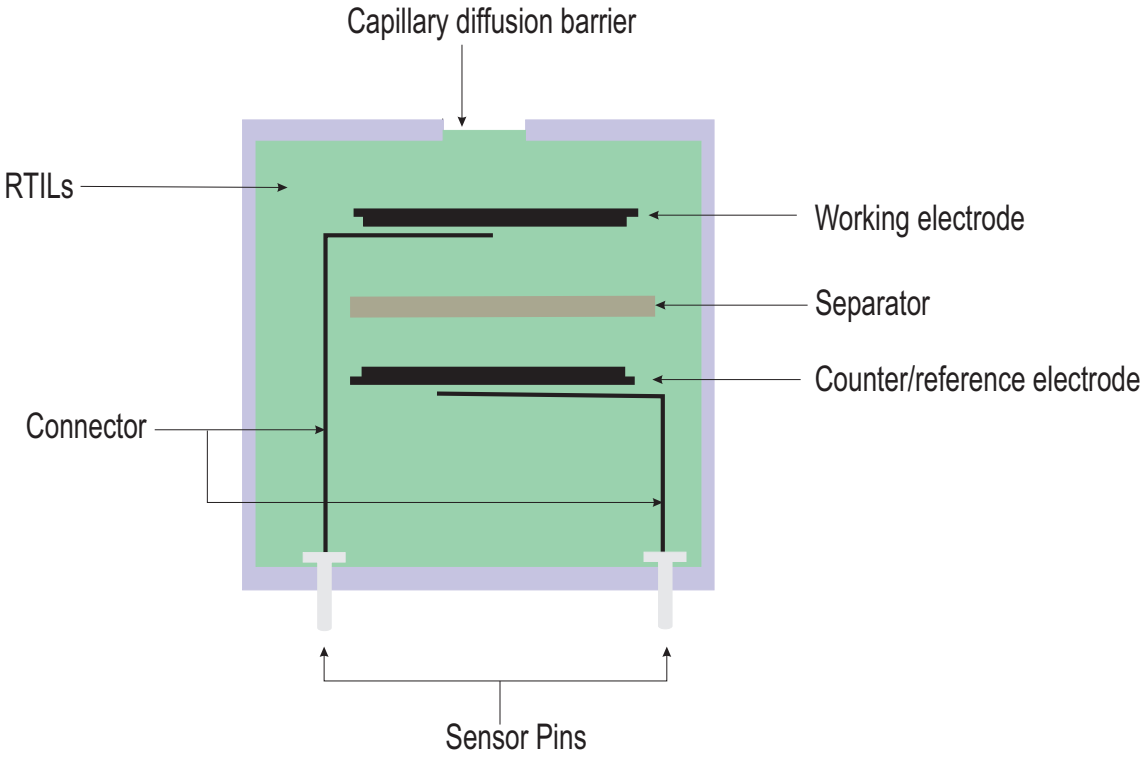

Figure 2.4: Proposed membrane-free gas detector

potentially eliminates rate determining gas diffusion through the membranes thus possibly allowing much more rapid response times. Figure 2.4 shows a schematic design for a membrane free gas sensor.

Third, in contrast to conventional solvents that are likely to dry out or decompose at extreme temperatures or pressures (see Section 2.2.3), the low volatility and high thermal stability of RTILs allow the sensors to function at extreme conditions (high/low temperature and pressures) without any losses in concentrations. This advantage not only ensures a longer lifetime of the gas sensors but also reduces the need of calibration.

Fourth, RTILs are comprised of ions and hence they are fully supported solvents which reduces the need of additional supporting electrolytes. The ions composing RTIL can be tuned so as to enable RTIL to possess desired chemical and physical properties.

Fifth, RTILs are usually suggested to be used in three-electrode sensors, or if a working micro-electrode is used then a two-electrode system can be employed. The various reference electrodes for use in RTILs have been reviewed[76] and a Ag/Ag^{+} electrode

developed by Meng et al.[92]. However ferrocene and its derivatives are often used as internal redox references. Ferrocene itself has a significant volatility in RTILs solvents so analytes such as decamethylferrocene has been proposed. The tuneability of RTILs solvents has the benefit that the reference signal can be shifted away from the target analyte if necessary.[145] RTIL solvents often show ohmic resistance approximating to those seen for organic solvents in electrochemistry and as such are best studied using micro-electrodes as working electrodes. These are discussed in the next section.

2.3.2 The Use of Micro-electrodes for Gas Sensing

A micro-electrode is defined as having at least one dimension on the micro-scale (10 to 100 μm). Due to the relatively low conductivity and high viscosity of RTILs as compared to conventional solutions, micro-electrodes are widely employed to compensate these undesired features. This is because micro-electrodes demonstrate higher mass transport rates, better signal-to-noise ratios and lower uncompensated resistances than macro-electrodes. These properties are detailed as below.

The diffusional regime (convergent or linear) is determined by the size of the electrode radius, r, relative to the diffusion layer thickness, d (see Equation 1.18).[50] Within the experimental time scale (in the regime of $r << d$), convergent diffusion dominates at a micro-disc electrode as the electro-active materials are driven not only onto the electrode surface but also to the edge of the electrode[146]. A macro-electrode, on the other hand, experiences less effective linear diffusion (as $r >> d$).

Here, D is the diffusion coefficient and t is the experimental time. Convergent diffusion dominates when $r << d$ and linear diffusion occurs when $r >> d$.

The use of micro-electrodes improves the signal-to-noise ratio since noise is proportional to the active electrode surface area whilst the signal depends on the total size of the diffusional field.[50, 147] A better signal-to-noise ratio leads a lower detection limit.[73]

In addition, as less current is generated with a smaller electrode area, less solution resistance is experienced by a micro-electrode as compared to a macro-electrode in the same solution. Therefore a simple two-electrode system can be exploited by using a micro-electrode.[50, 148]

An array of micro-electrodes[143, 149] provides merit over a single micro-electrode as the use of large numbers of micro-electrodes operating in parallel not only enhances the sensing signals but also offers insurance against the failure of a few individual electrodes.

From the manufacturing aspect, disposable electrode arrays not only should be made of low-cost materials but also be feasible to be produced in bulk scale. Therefore, the manufacturing process desirably avoids complex steps and uses accessible production equipment. Available fabrication methodologies including screen printing[150–153] and photo- or chemically etching[154–157]. Fabrication methods, along with the advantages and disadvantages of each method, have been extensively reviewed by Huang et al.[143]. Figures 2.5 a) and b) show two methods of micro-electrode array fabrication. Micro-electrode array suppliers include The Multi Channel Systems[14], NanoFlex[15], Micro Probe, Inc.[16] and AlphaOmega[17]. The choice of manufacturing method and electrode geometry dictate the usage and cost. Taking a 'well' electrode array as an example (see Figure 2.6), they are suitable for holding solvents inside the 3D well without the need of a separate cell.

In order to test the validity of arrays of different geometries, such as micro-disc, micro-band and micro-pillar as shown in Figure 2.6, various mass transport models were developed to characterise the responses of these electrode arrays.[158–160] Benefiting from these available theories, micro-electrode arrays were used as working probes for gas detections.[161–164] Griveau[162] has investigated the use of micro-disc arrays for amperometric NO monitoring which showed high selectivity and sensitivity. Further to this,

[14]http://shop.multichannelsystems.com/
[15]http://www.nanoflex.com/
[16]http://www.microprobes.com/
[17]http://www.alphaomega-eng.com/

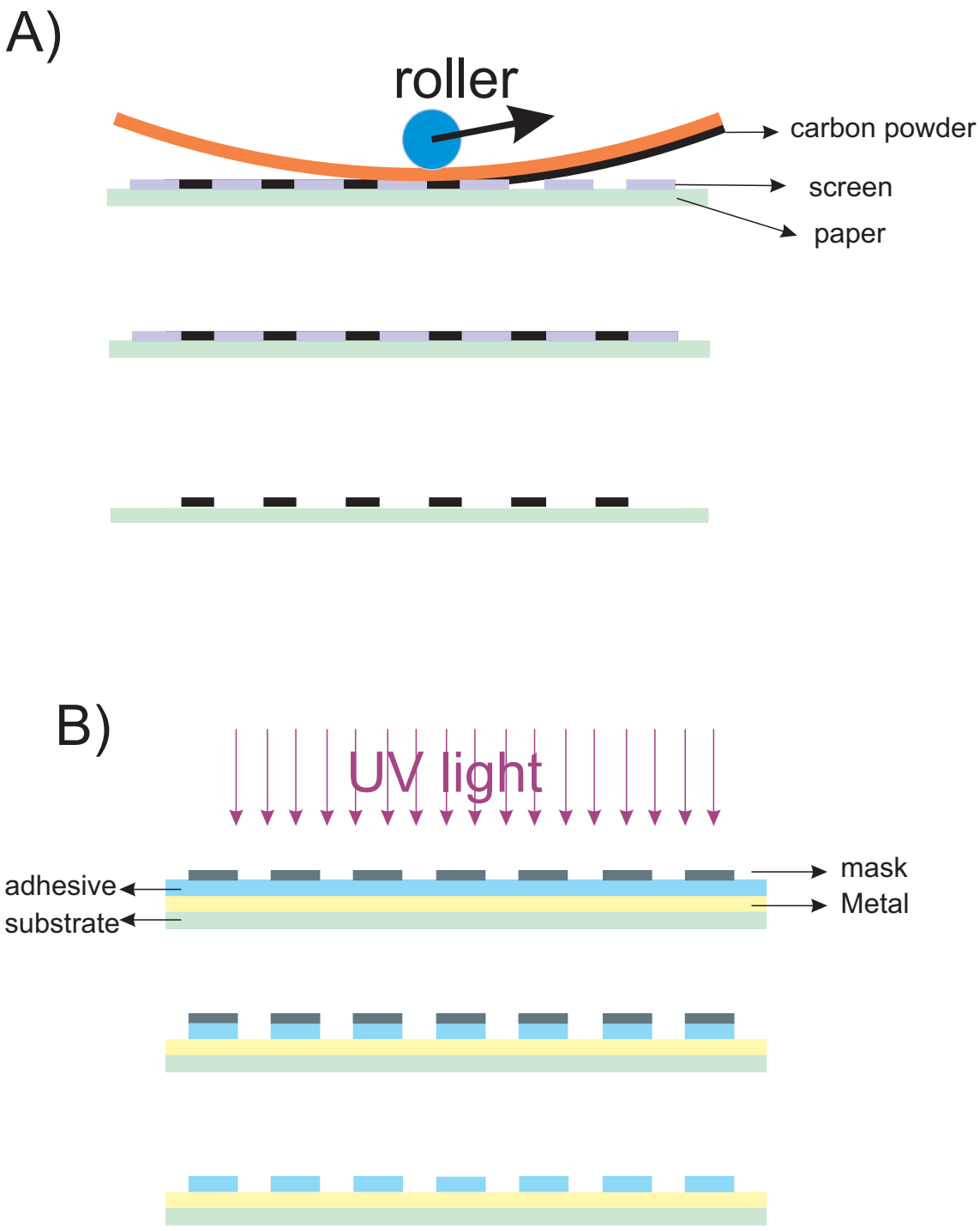

Figure 2.5: Schematic demonstration of micro-electrode fabrications. a) Screen printed method. b) photolithography.

simultaneous detection of NO and gases like CO_2 and O_2 has been developed.

Huang et al.[161] successfully developed a membrane free oxygen sensor using micro-electrode arrays as working electrodes and ionic liquids ($[P_{14,6,6,6}][FAP]$) as solvents. This

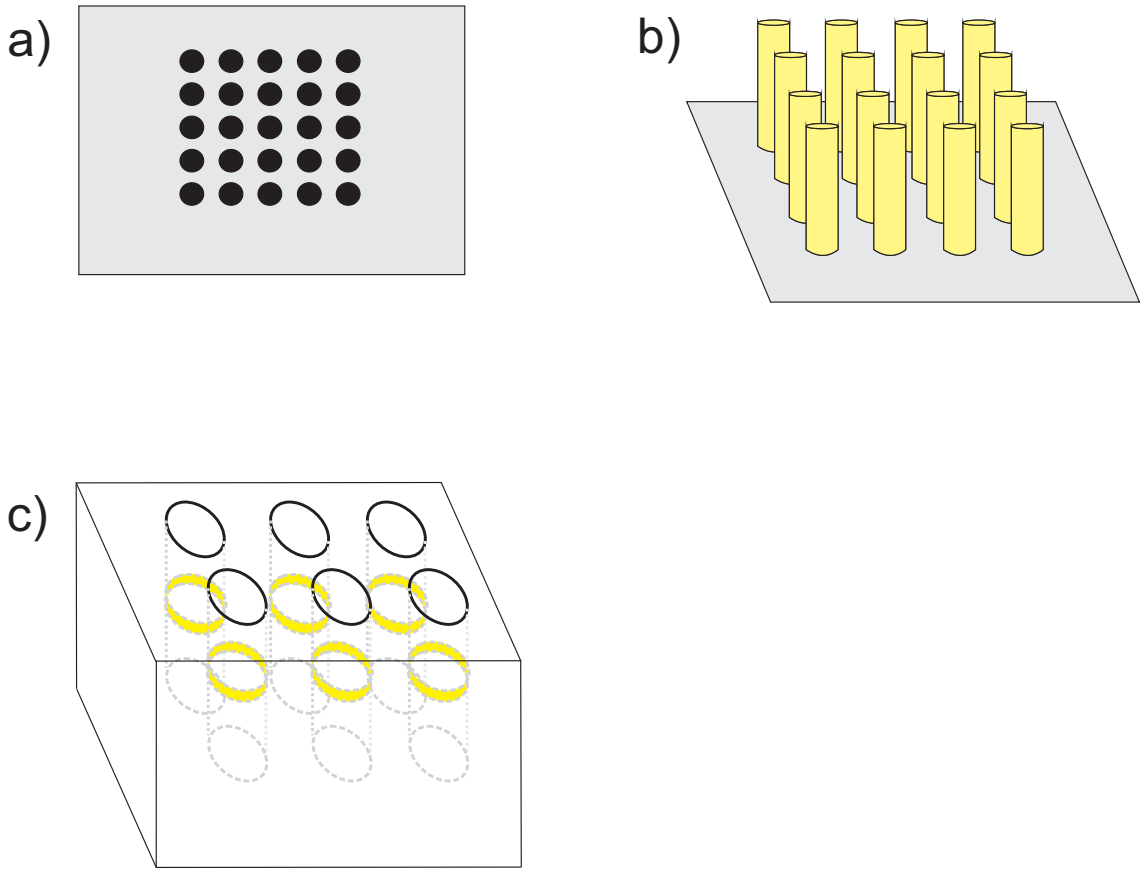

Figure 2.6: Different types of microarrays. a)A micro-disc electrode array. b)a micro-pillar electrode array. c)a micro-band array ('well' electrode array).

oxygen sensing system showed high sensitivity and most importantly, was freed from the problem caused by the use of membranes, especially frequent calibration.

2.4 Towards Intelligent Sensors

This section discusses some influential factors in the accurate measurement of gas concentration including the amperometric sensing techniques and environmental influences.

2.4.1 Micro-disc Electrode Chronoamperometry: Shoup and Szabo Analysis

Traditionally, the current generated by sensing (electrochemical) processes is used to reflect the concentrations of gas. However the current is not only dependent on concentration but also is a function of the number of electrons transferred during the electrochemical process and the diffusion coefficient of target molecules. An error in determining gas concentration may result from the change of any of these variables. This is not rare due to the fact that diffusion coefficients are sensitive to both temperature and humidity changes. Hence a method that allows simultaneous determination of concentrations and diffusion coefficients is advocated - specifically chronoamperometry has been used for this propose. In chronoamperometry, the potential steps from a potential where no current passes to a potential where the reaction of interest fully occurs in a diffusional controlled way. The current is recorded as a function of time. At the short time, the current response at a planar disc electrode follows Cottrellian behaviour (see Equation 1.20 in Chapter 1).

Whilst the current decays to zero for a macro-electrode, at longer time, a steady state current is seen at a micro-disc electrode(See Equation 1.30 in Chapter 1).

where r is the electrode radius and all other terms are defined as above. It is evident that at long time, current is a function of $ncD^{\frac{1}{2}}$ and at short time current is a product of ncD. Thus the parameters nc and D can be measured simultaneously through combining the current at short and long times.

Several models [165–168] have been proposed for simulating the current-time behaviour of chronoamperometry at micro-disc electrodes. Shoup and Szabo analysis is the most frequently used which describes chronoamperometric responses over all time values within an error of 0.5 % [167] (see Equation 4.1 in Chapter 4).

This equation is readily imported in data analysis software, such as Origin. Typically the value of electrode radius, r, is fixed as known and the software then automatically

implements a the fitting procedure. The values of c and D are iterated until the best fit (least difference between simulated and experimental current responses) is achieved.

Despite of the simple operation of this technique, the values of nc and D resulted from the Shoup and Szabo analysis at different transient times can be different[169]. This is because the Cottrellian current scales with $cD^{\frac{1}{2}}$ and the steady state current is a function of cD (for $n = 1$). At too short measured times, capacitative non-Faradaic currents lead to large error whilst at long times the steady state signal dominates and many pairs of c and D gives same steady state current. Hence, accurate values of c and D are only possible when a 'good' balance between the Cottrellian current and the steady state current is measured.

Chapter 4 investigates the optimisation of transient times for Shoup and Szabo analysis, exemplified by two systems, in order to achieve accurate results of gas systems.

2.4.2 Temperature and Humidity

Since the values of nc and D can be achieved accurately using chronoamperometry along with Shoup and Szabo analysis, it is essential to consider other external factors on the sensing accuracy. Due to the fact that an electrochemical gas sensor relies on the electron transfer process which is always highly sensitive to temperature and sometimes to humidity changes, the sensing accuracy is influenced by the change of environment. The affected parameters include the number of electron transfer, the concentration and the diffusion coefficient of solutes. How the environment plays part in these parameters is discussed below.

The following equilibrium is considered when a gaseous molecule is dissolved in a solution

$$A(g) \rightleftharpoons A(dis) \tag{2.3}$$

where $A_{(g)}$ is the analyte A in gas phase and $A_{(dis)}$ is dissolved A. Gas solubility and temperature normally exhibit a negative correlation[170] in ionic liquids as the Equilibrium 2.3 shifts to the gaseous phase at higher temperature. However this depends on the gases and solvents studied. CO_2 in [C_4mim][Ac] is one of the exceptional cases, where a possible chemical step is involved during CO_2 dissolution[171, 172]. The correlation between dissolved gas concentrations and temperature are determined by the Van't Hoff equation.

$$\frac{\partial ln K_{eq}}{\partial T} = \frac{\Delta H}{RT^2} \tag{2.4}$$

where K_{eq} is the equilibrium constant, ΔH is the standard enthalpy change and all other terms are defined as above.

The diffusion coefficient of a solute in ionic liquids generally increases with temperature. This correlation can often be predicted by the Arrhenius equation:

$$D = D_0 e^{-E_A/(RT)} \tag{2.5}$$

Here, D is the diffusion coefficient and E_A is the energy of activation and all other terms are defined as before.

The influence of humidity on the solubility is due to the solubility difference as water content of the ionic liquid changes. For example, for the pure solvents, the saturated solubility of oxygen in water is 1.2 mM and in [$P_{14,6,6,6}$][NTf_2] is 7.5 mM. The solubility of humidified oxygen in [$P_{14,6,6,6}$][NTf_2] ranges between these limits.[173]

The diffusion coefficient of a gas is affected by change of humidity for similar reasons. Dissolved molecules are normally more mobile in water as compared to that in ionic liquids. Hence humidified oxygen shows a higher diffusion coefficient than dry oxygen in ionic liquids[173]

One solution to the problem caused by changed temperature and humidity is to keep the detection system under a restrictedly stable environment where the temperature is thermostatted and gases are pre-dried before experiment. However this is not realistic outside of the laboratory in sensor applications. A more practical approach is to measure the temperature and humidity of the sensing environment and correct the sensor measurements accordingly. An independent temperature and humidity sensor is potentially implantable in gas sensing systems for monitoring the change of experimental conditions. Commercially a solid state independent temperature and humidity sensor is used to measure the temperature and humidity in sensing solutions.[174] However an external probe may be remote from the sensing system, leading to a decreased sensitivity of temperature and humidity measurement.

A built-in voltammetric temperature sensor incorporated into an amperometric oxygen sensor and a simultaneous temperature and humidity detector are shown in Chapter 6 and Chapter 7 respectively.

The reaction mechanism of dissolved molecules in ionic liquids may change with humidity. This is because dry protic ionic liquids are free from protons whereas water is a good source of protons. For example, the mechanism of dissolved oxygen (in ionic liquid) in the presence of moisture can vary from 1 and 4 electrons transferred[93, 175]. Note that the number of electron transferred also depends on the electrode materials. The mechanism undergone at different humidity is unpredictable thus resulting in difficult and inaccurate measurements.

In particular the Shoup and Szabo micro-disc electrode analysis advocated above assumes that the number, n, of electrons transferred is known and constant. Then c and D are functions of humidity and temperature which can be calculated through the simultaneous humidity and temperature sensor. However this approach is not applicable for mechanisms involving a slow chemical step. Taking an ECE mechanism (see Reaction

2.6 to 2.8) as an example, the number of electrons determined by chronoamperometry can vary between 1 and 2 depending on the rate of Reaction 2.8. This may be moisture sensitive and will certainly be temperature dependent.

$$A + e \longrightarrow A^- \tag{2.6}$$

$$A^- \longrightarrow B \tag{2.7}$$

$$B + e \longrightarrow B^- \tag{2.8}$$

An alternative approach to control the reaction at a known electron transfer stage is shown in Chapter 8.

2.5 Aim of the Thesis

This thesis aims at addressing the issues of current generation gas sensors, further developing intelligent gas sensors. The intelligent gas sensing systems will realise self-calibration against change of the sensing environment, such as humidity and temperature. Accurate measurement of gas concentration can therefore be achieved. This thesis also seeks the fabrication of low cost electrodes and investigates their suitability in electrochemical experiments.

References

[1] Xiong, L.; Compton, R. G. *Interntional Journal of Electrochemical Science* **2014**, *9*, 7152–7181.

[2] Gutmacher, D.; Foelmli, C.; Vollenweider, W.; Hoefer, U.; Wllenstein, J. *Procedia Engineering* **2011**, *25*, 1121 – 1124.

[3] Srivastava, S. C.; Jaiswal, R. J.; Sinha, S.; Singh, R. V. K.; Das, R. N. *Journal of Mines, Metals and Fuels* **1987**, *35*, 384–385.

[4] Sinha, A. K.; Rajwar, D. P.; Ghosh, A. K. *Journal of Mines, Metals and Fuels* **1987**, *35*, 365–367.

[5] Barnes, S.; Old, L. T. *Chemical Engineering Progress* **2009**, *105*, 51–56.

[6] Arasaradnam, R. P.; Covington, J. A.; Harmston, C.; Nwokolo, C. U. *Alimentary Pharmacology and Therapeutics* **2014**, *39*, 780–789.

[7] Buszewski, B.; Grzywinski, D.; Ligor, T.; Stacewicz, T.; Bielecki, Z.; Wojtas, J. *Bioanalysis* **2013**, *5*, 2287–2306.

[8] Biniecka, M.; Caroli, S. *TrAC - Trends in Analytical Chemistry* **2011**, *30*, 1756–1770.

[9] Angerosa, F. *European Journal of Lipid Science and Technology* **2002**, *104*, 639–660.

[10] Dorresteijn, R. C.; De Gooijer, C. D.; Tramper, J.; Beuvery, E. C. *Biotechnology and Bioengineering* **1994**, *43*, 149–154.

[11] Wolfbeis, O. *Analytical Chemistry* **2002**, *74*, 2663–2677.

[12] Lu, X.; Winnik, M. *Chemistry of Materials* **2001**, *13*, 3449–3463.

[13] Demas, J. N.; DeGraff, B. A.; Coleman, P. B. *Analytical Chemistry* **1999**, *71*, 793A–800A.

[14] Cheung, M. C.; Yung, K. Y.; Xu, H.; Kraut, N. D.; Liu, K.; Chodavarapu, V. P.; Cartwright, A. N.; Bright, F. V. *IEEE Journal on Selected Topics in Quantum Electronics* **2012**, *18*, 1147–1159.

[15] Chu, C.-S.; Lo, Y.-L.; Sung, T.-W. *Photonic Sensors* **2011**, *1*, 234–250.

[16] Rees, N. V.; Compton, R. G. *Energy and Environmental Science* **2011**, *4*, 403–408.

[17] Korotcenkov, G.; Han, S. D.; Stetter, J. R. *Chemical Reviews* **2009**, *109*, 1402–1433.

[18] Rahman, M.; Kumar, P.; Park, D.-S.; Shim, Y.-B. *Sensors* **2008**, *8*, 118–141.

[19] Stetter, J. R.; Li, J. *Chemical Reviews* **2008**, *108*, 352–366.

[20] Knake, R.; Jacquinot, P.; Hodgson, A. W. E.; Hauser, P. C. *Analytica Chimica Acta* **2005**, *549*, 1 – 9.

[21] Suresh, M.; Vasa, N. J.; Agarwal, V.; Chandapillai, J. *Sensors and Actuators, B: Chemical* **2014**, *195*, 44–51.

[22] Hori, H.; Ishimatsu, S.; Fueta, Y.; Hinoue, M.; Ishidao, T. *Journal of UOEH* **2013**, *34*, 363–368.

[23] Yin, C.; Liu, S.; Li, Y.; Chen, X. *Applied Mechanics and Materials* **2013**, *336-338*, 244–247.

[24] Chiorino, A.; Ghiotti, G.; Prinetto, F.; Carotta, M. C.; Gnani, D.; Martinelli, G. *Sensors and Actuators, B: Chemical* **1999**, *58*, 338–349.

[25] Golinelli, E.; Musazzi, S.; Perini, U.; Barberis, F. *Lecture Notes in Electrical Engineering* **2014**, *268*, 19–22.

[26] Dong, L.; Ma, W.; Zhang, L.; Yin, W.; Jia, S. *Guangxue Xuebao/Acta Optica Sinica* **2014**, *34*, Article number 0130002.

[27] Qiao, J.-P.; Qin, J.-M.; Yan, X.-Y.; Zhang, Z.-X. *Journal of Optoelectronics Laser* **2014**, *25*, 217–221.

[28] Li, C.; Shi, G. *Journal of Photochemistry and Photobiology C: Photochemistry Reviews* **2014**, *19*, 20–34.

[29] Kitiyanan, B.; Alvarez, W. E.; Harwell, J. H.; Resasco, D. E. *Chemical Physics Letters* **2000**, *317*, 497–503.

[30] Zhu, Q.; Aller, R. *Marine Chemistry* **2013**, *157*, 49–58.

[31] Jackson, R.; Oda, R. P.; Bhandari, R. K.; Mahon, S. B.; Brenner, M.; Rockwood, G. A.; Logue, B. A. *Analytical Chemistry* **2014**, *86*, 1845–1852.

[32] Zakrzewska, K. *Thin Solid Films* **2001**, *391*, 229–238.

[33] Vijayalakshmi, K.; Renitta, A.; Karthick, K. *Ceramics International* **2014**, *40*, 6171–6177.

[34] Gaman, V. I.; Sevast'yanov, Y. Y.; Maksimova, N. K.; Almaev, A. V.; Sergeichenko, N. S. *Russian Physics Journal* **2014**, *56*, pp 1427–1434.

[35] Patil, J. Y.; Nadargi, D. Y.; Gurav, J. L.; Mulla, I. S.; Suryavanshi, S. S. *Materials Letters* **2014**, *124*, 144–147.

[36] Qi, Q.; Wang, P.-P.; Zhao, J.; Feng, L.-L.; Zhou, L.-J.; Xuan, R.-F.; Liu, Y.-P.; Li, G.-D. *Sensors and Actuators, B: Chemical* **2014**, *194*, 440–446.

[37] Kaci, S.; Keffous, A.; Hakoum, S.; Trari, M.; Mansri, O.; Menari, H. *Applied Surface Science* **2014**, in press.

[38] Carotta, M. C.; Fioravanti, A.; Gherardi, S.; Malagu, C.; Sacerdoti, M.; Ghiotti, G.; Morandi, S. *Sensors and Actuators, B: Chemical* **2014**, *194*, 195–205.

[39] Gu, J.; Zhang, Y.; Jiang, J.; Li, S. *Chinese Journal of Scientific Instrument* **2014**, *35*, 350–359.

[40] Darmastuti, Z.; Bur, C.; Mller, P.; Rahlin, R.; Lindqvist, N.; Andersson, M.; Schtze, A.; Spetz, A. *Sensors and Actuators, B: Chemical* **2014**, *194*, 511–520.

[41] Somov, A.; Baranov, A.; Spirjakin, D. *Sensors and Actuators A: Physical* **2014**, *210*, 157 – 164.

[42] Karpova, E.; Mironov, S.; Suchkov, A.; Karelin, A.; Karpov, E.; Karpov, E. *Sensors and Actuators, B: Chemical* **2014**, *197*, 358–363.

[43] Xiong, L.; Batchelor-McAuley, C.; Goncalves, L. M.; Rodrigues, J. A.; Compton, R. G. *Biosensors and Bioelectronics* **2011**, *26*, 4198–4203.

[44] Husson-Borg, P.; Majer, V.; Costa Gomes, M. *Journal of Chemical and Engineering Data* **2003**, *48*, 480–485.

[45] Evans, R. G.; Klymenko, O. V.; Saddoughi, S. A.; Hardacre, C.; Compton, R. G. *Journal of Physical Chemistry B* **2004**, *108*, 7878–7886.

[46] Chen, W.-C.; Hsu, Y.-L.; Venkatesan, S.; Zen, J.-M. *Electroanalysis* **2014**, *26*, 565–572.

[47] Lawrence, N. S.; Davis, J.; Marken, F.; Jiang, L.; Jones, T. G. J.; Davies, S. N.; Compton, R. G. *Sensors and Actuators, B: Chemical* **2000**, *69*, 189–192.

[48] Lawrence, N. S.; Jiang, L.; Jones, T. G. J.; Compton, R. G. *Analytical Chemistry* **2003**, *75*, 2499–2503.

[49] Sekhar, P. K.; Subramaniyam, K. *ECS Electrochemistry Letters* **2014**, *3*, B1–B4.

[50] Compton, R. G.; Banks, C. E. *Understanding Voltammetry*; Imperial College Press, 2011, 2nd Edition.

[51] Maj-Zurawska, M.; Hulanicki, A. *Chemia Analityczna* **2009**, *54*, 1149–1167.

[52] Xie, X.; Bakker, E. *Analytical Chemistry* **2013**, *85*, 1332–1336.

[53] Severinghaus, J. W.; Bradley, A. F. *Journal of applied physiology* **1958**, *13*, 515–520.

[54] Caflisch, C. R.; Carter, N. W. *Analytical Biochemistry* **1974**, *60*, 252–257.

[55] Cai, W. J. *Analytical Chemistry* **1997**, *69*, 5052–5058.

[56] Beyenal, H.; Davis, C. C.; Lewandowski, Z. *Sensors and Actuators, B: Chemical* **2004**, *97*, 202–210.

[57] Mowery, M. D. *Analytical Chemistry* **1999**, *71*, 201–204.

[58] Ben Youssef, I.; Alem, H.; Sarry, F.; Elmazria, O.; Jimenez Rioboo, R.; Arnal-Hrault, C.; Jonquires, A. *Sensors and Actuators, B: Chemical* **2013**, *185*, 309–320.

[59] Fraticelli, Y. M.; Meyerhoff, M. E. *Analytical Chemistry* **1981**, *53*, 992–997.

[60] Meyerhoff, M. E.; Fraticelli, Y. M.; Greenberg, J. A.; Rosen, J.; Parks, S. J.; Opdycke, W. N. *Clinical Chemistry* **1982**, *28*, 1973–1978.

[61] Arnold, M. A. *Analytica Chimica Acta* **1983**, *154*, 33 – 39.

[62] Clark Jr., L. C.; Wolk, R.; Granger, D.; Talor, Z. *Journal of applied physiology* **1953**, *6*, 189–193.

[63] Compton, R. G.; Sanders, G. H. W. *Electrode Potentials*; OCP Series; OUP Oxford, 1996.

[64] Clark Jr., L. C.; Gollan, F.; Gupta, V. B. *Science* **1950**, *111*, 85–87.

[65] Danneel, H. L. *Zeitschrift Elektrochemie* **1897**, *4*, 227–242.

[66] Severinghaus, J. W.; Astrup, P. B. *Journal of Clinical Monitoring* **1986**, *2*, 125–139.

[67] Moseley, P.; Norris, J.; Williams, D. *Techniques and mechanisms in gas sensing*; The Adam Hilger series on sensors; Adam Hilger, 1991.

[68] Goswami, A.; Cooper, R. *Anaesthesia & Intensive Care Medicine* **2011**, *12*, 568 – 573.

[69] Cussler, E. L. *Diffusion: Mass Transfer in Fluid Systems*; Cambridge series in chemical engineering; Cambridge University Press, 1997.

[70] Evans, N. T. S.; Quinton, T. H. *Respiration Physiology* **1978**, *35*, 89 – 99.

[71] Haug, A. T.; White, R. E. *Journal of the Electrochemical Society* **2000**, *147*, 980–983.

[72] Hahn, C. *Analyst* **1998**, *123*, 57R–86R.

[73] Wang, J. *Analytical Electrochemistry*; Wiley, 2006.

[74] Do, J. S.; Chang, W. B. *Sensors and Actuators B: Chemical* **2001**, *72*, 101 – 107.

[75] Do, J.-S.; Shieh, R.-Y. *Sensors and Actuators B: Chemical* **1996**, *37*, 19 – 26.

[76] Rogers, E. I.; O'Mahony, A. M.; Aldous, L.; Compton, R. G. Amperometric gas detection using room temperature ionic liquid solvents. 2010.

[77] Barrosse-Antle, L. E.; Bond, A. M.; Compton, R. G.; O'Mahony, A. M.; Rogers, E. I.; Silvester, D. S. *Chemistry - An Asian Journal* **2010**, *5*, 202–230.

[78] O'Mahony, A. M.; Compton, R. G. *Electroanalysis* **2010**, *22*, 2313–2322.

[79] Koschel, D.; Coxam, J.-Y.; Majer, V. *Industrial and Engineering Chemistry Research* **2007**, *46*, 1421–1430.

[80] Silvester, D. S.; Compton, R. G. *Zeitschrift fur Physikalische Chemie* **2006**, *220*, 1247–1274.

[81] Najdeker, E.; Bishop, E. *Journal of Electroanalytical Chemistry* **1973**, *41*, 79–87.

[82] Ramasubramanian, N. *Journal of Electroanalytical Chemistry* **1975**, *64*, 21–37.

[83] Buzzeo, M. C.; Evans, R. G.; Compton, R. G. *ChemPhysChem* **2004**, *5*, 1106–1120.

[84] Stark, A.; Behrend, P.; Braun, O.; Muller, A.; Ranke, J.; Ondruschka, B.; Jastorff, B. *Green Chem.* **2008**, *10*, 1152–1161.

[85] Schroder, U.; Wadhawan, J.; Compton, R. G.; Marken, F.; Suarez, P. A. Z.; Consorti, C. S.; De Souza, R. F.; Dupont, J. *New Journal of Chemistry* **2000**, *24*, 1009–1015.

[86] Stepnowski, P.; Mller, A.; Behrend, P.; Ranke, J.; Hoffmann, J.; Jastorff, B. *Journal of Chromatography A* **2003**, *993*, 173–178.

[87] Stepnowski, P.; Nichthauser, J.; Mrozik, W.; Buszewski, B. *Analytical and Bioanalytical Chemistry* **2006**, *385*, 1483–1491.

[88] Le Rouzo, G.; Lamouroux, C.; Bresson, C.; Guichard, A.; Moisy, P.; Moutiers, G. *Journal of Chromatography A* **2007**, *1164*, 139–144.

[89] Kim, K.-S.; Choi, S.; Demberelnyamba, D.; Lee, H.; Oh, J.; Lee, B.-B.; Mun, S.-J. *Chemical Communications* **2004**, *10*, 828–829.

[90] Forsyth, S.; Golding, J.; MacFarlane, D.; Forsyth, M. *Electrochimica Acta* **2001**, *46*, 1753–1757.

[91] Matsumoto, H.; Kageyama, H.; Miyazaki, Y. *Chemistry Letters* **2001**, 182–183.

[92] Meng, Y.; Aldous, L.; Belding, S.; Compton, R. *Physical Chemistry Chemical Physics* **2012**, *14*, 5222–5228.

[93] Buzzeo, M. C.; Klymenko, O. V.; Wadhawan, J. D.; Hardacre, C.; Seddon, K. R.; Compton, R. G. *Journal of Physical Chemistry A* **2003**, *107*, 8872–8878.

[94] Huang, X. J.; Rogers, E. I.; Hardacre, C.; Compton, R. G. *The Journal of Physical Chemistry B* **2009**, *113*, 8953–8959.

[95] Rogers, E. I.; Sljukic, B.; Hardacre, C.; Compton, R. G. *Journal of Chemical and Engineering Data* **2009**, *54*, 2049–2053.

[96] Suarez, P.; Consorti, C.; De Souza, R.; Dupont, J.; Gonalves, R. *Journal of the Brazilian Chemical Society* **2002**, *13*, 106–109.

[97] Howlett, P. C.; Izgorodina, E. I.; Forsyth, M.; MacFarlane, D. R. *Zeitschrift fur Physikalische Chemie* **2006**, *220*, 1483–1498.

[98] Zhao, C.; Burrell, G.; Torriero, A.; Separovic, F.; Dunlop, N.; MacFarlane, D.; Bond, A. *Journal of Physical Chemistry B* **2008**, *112*, 6923–6936.

[99] Buzzeo, M. C.; Hardacre, C.; Compton, R. G. *Analytical Chemistry* **2004**, *76*, 4583–4588.

[100] Hui, N.; MinQiang, H.; QingQing, M.; YuanHui, L.; DeZhong, Y.; BuXing, H. *SCIENCE CHINA Chemistry* **2012**, *55*, 1509.

[101] Vranes, M.; Dozic, S.; Djeric, V.; Gadzuric, S. *Journal of Chemical & Engineering Data* **2012**, *57*, 1072–1077.

[102] Hunger, J.; Stoppa, A.; Schrdle, S.; Hefter, G.; Buchner, R. *ChemPhysChem* **2009**, *10*, 723–733.

[103] Li, J.-G.; Hu, Y.-F.; Ling, S.; Zhang, J.-Z. *Journal of Chemical & Engineering Data* **2011**, *56*, 3068–3072.

[104] Zech, O.; Stoppa, A.; Buchner, R.; Kunz, W. *Journal of Chemical & Engineering Data* **2010**, *55*, 1774–1778.

[105] Sun, J.; Forsyth, M.; MacFarlane, D. R. *The Journal of Physical Chemistry B* **1998**, *102*, 8858–8864.

[106] Lide, D. *CRC Handbook of Chemistry and Physics, 85th Edition*; CRC Handbook of Chemistry and Physics, 85th Ed; Taylor & Francis, 2004.

[107] O'Mahony, A. M.; Compton, R. G. *Electroanalysis* **2010**, *22*, 2313–2322.

[108] Ignat'ev, N.; Welz-Biermann, U.; Kucheryna, A.; Bissky, G.; Willner, H. *Journal of Fluorine Chemistry* **2005**, *126*, 1150–1159.

[109] O'Mahony, A. M.; Silvester, D. S.; Aldous, L.; Hardacre, C.; Compton, R. G. *Journal of Chemical and Engineering Data* **2008**, *53*, 2884–2891.

[110] Buzzeo, M. C.; Hardacre, C.; Compton, R. G. *ChemPhysChem* **2006**, *7*, 176–180.

[111] Clayden, J.; Greeves, N.; Warren, S. *Organic Chemistry, 2nd edition*; Oxford University Press, 2012.

[112] Miran, M. S.; Kinoshita, H.; Yasuda, T.; Susan, M. A. B. H.; Watanabe, M. *Chemical Communications* **2011**, *47*, 12676–12678.

[113] McFarlane, D. R.; Sun, J.; Golding, J.; Meakin, P.; Forsyth, M. *Electrochimica Acta* **2000**, *45*, 1271 – 1278.

[114] Schreiner, C.; Zugmann, S.; Hartl, R.; Gores, H. J. *Journal of Chemical & Engineering Data* **2010**, *55*, 1784–1788.

[115] Chaban, V. V.; Voroshylova, I. V.; Kalugin, O. N.; Prezhdo, O. V. *Journal of Physical Chemistry B* **2012**, *116*, 7719–7727.

[116] Wang, C.; Yan, P.; Xing, H.; Jin, C.; Xiao, J.-X. *Journal of Chemical & Engineering Data* **2010**, *55*, 1994–1999.

[117] Fitchett, B.; Knepp, T.; Conboy, J. *Journal of the Electrochemical Society* **2004**, *151*, E219–E225.

[118] Beter-Roga, M.; Hunger, J.; Stoppa, A.; Buchner, R. *Journal of Chemical and Engineering Data* **2010**, *55*, 1799–1803.

[119] Stoppa, A.; Hunger, J.; Buchner, R. *Journal of Chemical and Engineering Data* **2009**, *54*, 472–479.

[120] Silvester, D. S.; Broder, T. L.; Aldous, L.; Hardacre, C.; Crossley, A.; Compton, R. G. *The Analyst* **2007**, *132*, 196–198.

[121] Caporali, S.; Bardi, U.; Lavacchi, A. *Journal of Electron Spectroscopy and Related Phenomena* **2006**, *151*, 4–8.

[122] Fortunato, R.; Afonso, C.; Benavente, J.; Rodriguez-Castelln, E.; Crespo, J. *Journal of Membrane Science* **2005**, *256*, 216–223.

[123] Gottfried, J.; Maier, F.; Rossa, J.; Gerhard, D.; Schulz, P.; Wasserscheid, P.; Steinrck, H.-P. *Zeitschrift fur Physikalische Chemie* **2006**, *220*, 1439–1453.

[124] Hfft, O.; Bahr, S.; Himmerlich, M.; Krischok, S.; Schaefer, J. A.; Kempter, V. *Langmuir* **2006**, *22*, 7120–7123.

[125] Smith, E. F.; Rutten, F. J. M.; Villar-Garcia, I. J.; Briggs, D.; Licence, P. *Langmuir* **2006**, *22*, 9386–9392.

[126] Smith, E. F.; Villar Garcia, I. J.; Briggs, D.; Licence, P. *Chemical Communications* **2005**, 5633–5635.

[127] Tunnell, G. *World distribution of atmospheric water vapour pressure*; Geophysical memoirs; H.M. Stationery Office, 1958.

[128] Nesmeianov, A. N. *Vapor pressure of the chemical elements*; Elsevier Pub. Co., 1963.

[129] Chowdhury, A.; Thynell, S. T. *Thermochimica Acta* **2006**, *443*, 159 – 172.

[130] Maton, C.; De Vos, N.; Stevens, C. V. *Chemical Society Reviews* **2013**, *42*, 5963–5977.

[131] Pletcher, D.; of Chemistry (Great Britain), R. S. *A First Course in Electrode Processes*; A First Course in Electrode Processes; Royal Society of Chemistry, 2009.

[132] Rieger, P. H. *Electrochemistry*; Schaum's Outlines; Springer Netherlands, 1994.

[133] Chan, B. K. M.; Chang, N.; Grimmett, M. R. *Australian Journal of Chemistry* **1977**, *9*, 2005 – 2013.

[134] Dessiaterik, Y.; Baer, T.; Miller, R. E. *Journal of Physical Chemistry A* **2006**, *110*, 1500–1505.

[135] Atkins, P.; De Paula, J. *Atkins' Physical Chemistry*; Macmillan Higher Education, 2006.

[136] Xiong, L.; Fletcher, A. M.; Davies, S. G.; Norman, S. E.; Hardacre, C.; Compton, R. G. *Chemical Communications* **2012**, *48*, 5784–5786.

[137] Wang, C.; Guo, Y.; Zhu, X.; Cui, G.; Li, H.; Dai, S. *Chemical Communications* **2012**, *48*, 6526–6528.

[138] Cui, G.; Lin, W.; Ding, F.; Luo, X.; He, X.; Li, H.; Wang, C. *Green Chemistry* **2014**, *16*, 1211–1216.

[139] Cui, G.; Zheng, J.; Luo, X.; Lin, W.; Ding, F.; Li, H.; Wang, C. *Angewandte Chemie - International Edition* **2013**, *52*, 10620–10624.

[140] Wang, C.; Cui, G.; Luo, X.; Xu, Y.; Li, H.; Dai, S. *Journal of the American Chemical Society* **2011**, *133*, 11916–11919.

[141] Brussel, M.; Brehm, M.; Pensado, A. S.; Malberg, F.; Ramzan, M.; Stark, A.; Kirchner, B. *Phys. Chem. Chem. Phys.* **2012**, *14*, 13204–13215.

[142] Fox, E. T.; Paillard, E.; Borodin, O.; Henderson, W. A. *Journal of Physical Chemistry C* **2013**, *117*, 78–84.

[143] Huang, X.-J.; Aldous, L.; OMahony, A. M.; del Campo, F. J.; Compton, R. G. *Analytical Chemistry* **2010**, *82*, 5238–5245.

[144] Faridbod, F.; Mohammad Reza Ganjali, M. R.; Norouzi, P.; Riahi, S.; Rashedi, H. *Application of Room Temperature Ionic Liquids in Electrochemical Sensors and Biosensors*; InTech, 2011.

[145] Xiong, L.; Batchelor-Mcauley, C.; Ward, K. R.; Downing, C.; Hartshorne, R. S.; Lawrence, N. S.; Compton, R. G. *Journal of Electroanalytical Chemistry* **2011**, *661*, 144–149.

[146] Cope, D. K.; Tallman, D. E. *Journal of Electroanalytical Chemistry and Interfacial Electrochemistry* **1985**, *188*, 21 – 31.

[147] Weber, S. G. *Analytical Chemistry* **1989**, *61*, 295–302.

[148] Bard, A. J.; Faulkner, L. R. *Electrochemical Methods: Fundamentals and Applications*; Wiley, 2001.

[149] Ordeig, O.; Del Campo, J.; Munoz, F. X.; Banks, C. E.; Compton, R. G. *Electroanalysis* **2007**, *19*, 1973–1986.

[150] Dias, A. C. M. S.; Gomes-Filho, S. L. R.; Silva, M. M. S.; Dutra, R. F. *Biosens Bioelectron* **2013**, *44*, 216–221.

[151] Kanyong, P.; Pemberton, R. M.; Jackson, S. K.; Hart, J. P. *Anal. Biochem.* **2013**, *435*, 114–119.

[152] Xuan Viet, N.; Chikae, M.; Ukita, Y.; Maehashi, K.; Matsumoto, K.; Tamiya, E.; Hung Viet, P.; Takamura, Y. *Biosensors and Bioelectronics* **2013**, *42*, 592–597.

[153] Thiyagarajan, N.; Chang, J.-L.; Senthilkumar, K.; Zen, J.-M. *Electrochemistry Communications* **2014**, *38*, 86–90.

[154] Prehn, R.; Abad, L.; Snchez-Molas, D.; Duch, M.; Sabat, N.; Del Campo, F. J.; Muoz, F. X.; Compton, R. G. *Journal of Electroanalytical Chemistry* **2011**, *662*, 361–370.

[155] Wang, T.-J.; Huang, C.-F.; Wang, W.-S.; Wei, P.-K. *IEEE JOURNAL OF LIGHTWAVe TECHNOLOGY* **2004**, *22*, 1764–1771.

[156] Davies, T. J.; Ward-Jones, S.; Banks, C. E.; del Campo, J.; Mas, R.; Muoz, F. X.; Compton, R. G. *Journal of Electroanalytical Chemistry* **2005**, *585*, 51 – 62.

[157] Lee, H.; Shin, H.; Jeong, Y.; Moon, J.; Lee, M. *Appl. Phys. Lett.* **2009**, *95*, p. 071104–1 – p.071104–3.

[158] Sequeira, C. A. C.; Santos, D. M. F. *Zeitschrift fur Physikalische Chemie* **2010**, *224*, 1297–1336.

[159] Ward, K. R.; Xiong, L.; Lawrence, N. S.; Hartshorne, R. S.; Compton, R. G. *Journal of Electroanalytical Chemistry* **2013**, *702*, 15 – 24.

[160] Tomk, P. *Sensors (Switzerland)* **2013**, *13*, 13659–13684.

[161] Huang, X.-J.; Aldous, L.; OMahony, A. M.; del Campo, F. J.; Compton, R. G. *Analytical Chemistry* **2010**, *82*, 5238–5245.

[162] Griveau, S.; Bedioui, F. *Analytical and Bioanalytical Chemistry* **2013**, *405*, 3475–3488.

[163] Chen, R.; Li, Y.; Huo, K.; Chu, P. K. *RSC Adv.* **2013**, *3*, 18698–18715.

[164] George, P. M.; Muthuswamy, J.; Currie, J.; Thakor, N. V.; Paranjape, M. *Biomedical Microdevices* **2001**, *3*, 307–313.

[165] Fleischmann, M.; Pons, S. *Journal of Electroanalytical Chemistry* **1988**, *250*, 257–267.

[166] Klymenko, O. V.; Evans, R. G.; Hardacre, C.; Svir, I. B.; Compton, R. G. *Journal of Electroanalytical Chemistry* **2004**, *571*, 211–221.

[167] Shoup, D.; Szabo, A. *Journal of Electroanalytical Chemistry and Interfacial Electrochemistry* **1982**, *140*, 237 – 245.

[168] Heinze, J. *Journal of Electroanalytical Chemistry* **1981**, *124*, 73–86.

[169] Xiong, L.; Aldous, L.; Henstridge, M. C.; Compton, R. G. *Analytical Methods* **2012**, *4*, 371–376.

[170] Moore, J.; Stanitski, C.; Jurs, P. *Principles of Chemistry: The Molecular Science*; Available Titles OWL Series; Cengage Learning, 2009.

[171] Li, P.; Henstridge, M. C.; Xiong, L.; Compton, R. G. *Electroanalysis* **2013**, *25*, 2268–2274.

[172] Zhang, J.; Zhang, S.; Dong, K.; Zhang, Y.; Shen, Y.; Lv, X. *Chemistry - A European Journal* **2006**, *12*, 4021–4026.

[173] Xiong, L.; Barnes, E.; Compton, R. *Sensors and Actuators, B: Chemical* **2014**, *200*, 157–166.

[174] Courbat, J.; Kim, Y. B.; Briand, D.; De Rooij, N. F. Inkjet printing on paper for the realization of humidity and temperature sensors. 2011.

[175] Rogers, E. I.; Huang, X. J.; Dickinson, E. J. F.; Hardacre, C.; Compton, R. G. *Journal of Physical Chemistry C* **2009**, *113*, 17811–17823.

Chapter 3

Experimental Methods

This chapter outlines all chemical reagents and room temperature ionic liquids used throughout this thesis, and the general electrochemical cell set-ups together with their configurations. Details of individual experimental procedure are given in the relevant chapters.

3.1 Chemicals

The name and abbreviation of chemical used throughout the this thesis are listed in Table 3.1. 1-propyl-3-methylimidazolium bis(trifluoromethylsulfonyl)imide and 1-(2-methoxyethyl)-1-methylpyrrolidinium tris(pentafluoroethyl)trifluorophosphate were kindly donated by Dr. Sarah Norman and Prof. Christopher Hardacre from Queen's University Ionic Liquids Laboratory, Belfast. The synthesis methods were provided by Sarah. 1,2-diferrocenylethylene was synthesed by Dr. Ai Fletcher from Prof. Stephen Davies' Group. The method of synthesis was provided by Ai.

Chemical name	Formula/Abbreviation	Supplier	Purity
ferrocene	$Fe(C_5H_5)_2$/Fc	Aldrich	98 %
decamethylferrocene	$(Fe(C_{10}H_{15})_2$/DmFc	Fluka	95 %
1,2-diferrocenylethylene	$(Fe(C_5H_4))_2C_4H_6$/BisFc	synthesed	98 %
hexaaammineruthenium(III) chloride	$(Ru(NH_3)_6Cl_3$	Aldrich	98%
cobaltocenium hexafluorophosphate	$Co(C_5H_5)_2^+PF_6^-$/$Cc^+PF_6^-$	Acros Organics	98 %
N,N,N',N'-tetramethyl-p-phenylenediamine	TMPD	Aldrich	98 %
tetra-n-butylammonium perchlorate	TBAP	Fluka	99 %
distilled water	H_2O	Millipore	18.2 MΩ˙cm
acetonitrile	MeCN	Fischer Scientific	99 %
oxygen	O_2	BOC	>99.5 %
nitrogen	N_2	BOC	>99.998 %
1-propyl-3-methylimidazolium bis(trifluoromethylsulfonyl)imide	$[C_3mim][NTf_2]$	synthesed	-
1-(2-methoxyethyl)-1-methylpyrrolidinium tris(pentafluoroethyl)trifluorophosphate	[Moepyrr][FAP]	Merck	high purity
1-ethyl-3-methylimidazolium tetracyanoborate	$[C_2mim][TCB]$	Merck	high purity
trihexyltetradecylphosphonium bis(trifluoromethylsulfonyl)imide	$[P_{14,6,6,6}][NTf_2]$	Merck	high purity

Table 3.1: List of chemicals used throughout this thesis.

1,2-Diferrocenylethylene was synthesed using the following method: $TiCl_4$ (0.39 mL, 3.50 mmol) was added dropwise to anhydrous THF (10 mL) at 0^0C under N_2. A solution of

ferrocenecarboxaldehyde (500 mg, 2.34 mmol) in anhydrous THF (5 mL) and Zn powder (300 mg, 4.59 mmol) were sequentially added to the yellow solution at ^{0}C. The resultant black suspension was heated at reflux for four hours. After cooling, the mixture was poured onto ice water (50 mL), and sat. aq. $NaHCO_3$ (30 mL) was added. The resultant mixture was extracted with CH_2Cl_2 (3 $\times$ 30 mL). The organics were dried over $MgSO_4$ and concentrated in vacuo to give the title compound (340 mg, 73 %) as a dark orange solid; δ_H (400 MHz, $CDCl_3$) 4.18 (10H, s, Cp), 4.33 (4H, s, Cp), 4.55 (4H, s, Cp), 6.18 (2H, s, CH=CH).

Synthesis of 1-methyl-3-propylimidazolium chloride and 1-methyl-3-propylimidazolium bis(trifluoromethyl)sulfonylimide is provided as follow: N-methylimidazole (99 %) and 1-chloropropane (98 %) were purchased from Sigma-Aldrich. All solvents used were HPLC grade purchased from Riedel de Haën. Lithium bis-(trifluoromethyl)sulfonylimide was purchased from 3M.

Synthesis of 1-methyl-3-propylimidazolium chloride:

A mixture of 1-methylimidazole (99 % Sigma-Aldrich, 41.05 g, 0.5 mol) and 1-chloropropane (98 % Sigma-Aldrich 59.91 g, 0.75 mol) was placed in a Parr autoclave sealed reaction vessel along with 30 cm^3 of HPLC grade acetonitrile. The reaction mixture was heated up to 343 K and then held at this temperature for 24 h with stirring at 500 rpm. After cooling of the reaction mixture the acetonitrile was removed under vacuum. The highly viscous yellow product was recrystallised from acetonitrile/ethyl acetate mixture to afford an off-white solid, 78 % yield. The pure product was characterized by 1H NMR spectroscopy using a Bruker Avance machine

1H-NMR (300 MHz, DMSO-d_6): δ (ppm) = 0.83 (3H, t, J = 7.4 Hz, CH_3), 1.81 (2 H, m, CH_2), 3.86 (3H, s, N-CH_3), 4.18 (2H, t, J = 7.1 Hz, N-CH2), 7.75 (1 H, s), 7.83 (1 H, s), 9.32 (1 H, s);

Synthesis of 1-methyl-3-propylimidazolium bis(trifluoromethyl)sulfonylimide:

A solution of lithium bis(trifluoromethyl)sulfonylimide (143.55 g g, 0.5 mol) in distilled water (300 cm^3) was added drop-wise to a rapidly stirred solution of 1-Methyl-3-propylimidazolium chloride (78.4 g, 0.49 mmol) in dichloromethane (200 cm^3) and allowed to stir under ambient conditions overnight. The organic layer was then extracted and washed with distilled water (100 cm^3) repeatedly five times. The organic layer was then dried in vacuo to give the product as an off-white liquid in <98 % yield which was found to contain <0.10 wt% water, determined by Karl-Fischer analysis, and <15 ppm halide, determined by suppressed ion chromatography.[1]

1H-NMR (400 MHz, DMSO-d_6): δ (ppm) = 0.84 (3 H, t, J = 7.4 Hz, CH_3), 1.75 (2 H, m, CH_2), 3.79 (3 H, s, N-CH_3), 4.10 (2 H, t, J = 7.1 Hz, N-CH_2), 7.68 (1 H, s), 7.74 (1 H,s), 9.01 (1 H, s).

3.2 Instrumental

All electrochemical experiments were performed using a computer-controlled PGSTAT30-Autolab potentiostat (Eco-Chemie, Netherlands). For experiments in aqueous and organic systems, solutions were housed in a sealed glass vial, with a three-electrode arrangement consisting of a Pt working micro-disc electrode, a silver wire reference electrode and Pt coil wire counter electrode. The platinum microdisk working electrodes were polished on soft lapping pads (Kemet Ltd., UK) using alumina powders (Buehler, IL) of sizes 1.0, 0.3 mm and 0.05 mm. The electrode diameters were calibrated electrochemically by analysing the steady-state voltammetry of a 2 mM solution of ferrocene in MeCN containing 0.1 M TBAP, using a diffusion coefficient for ferrocene of 2.30×10^{-9} m^2 s^{-1}[2] at 298 K.(See more details in Chapter 4) For experiments with laminated electrodes (see Chapter 9 and Chapter 10) the sealed sample vial is used.

The experiments involving ionic liquids and micro-disc electtrodes were studied using a three-electrode arrangement, consisting of a platinum working electrode and two 0.5 mm

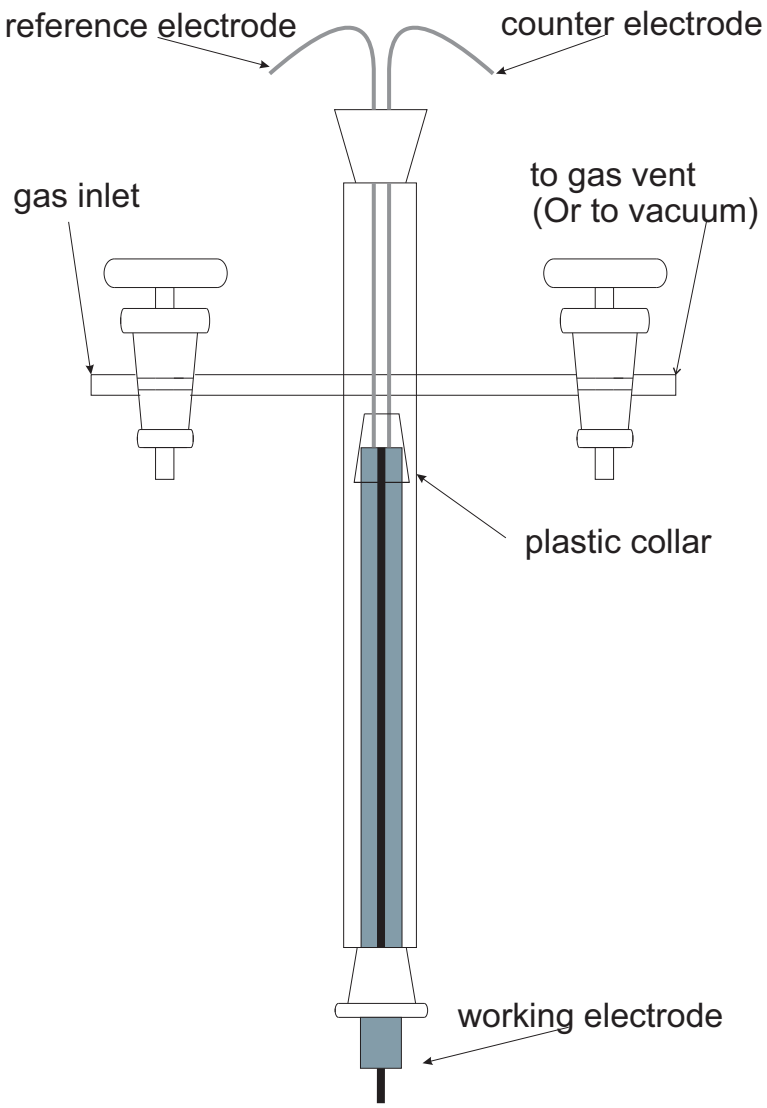

Figure 3.1: Scheme of T-Cell.

diameter silver wires acted as quasi-reference and counter electrode. The micro-electrode was modified with a small section of disposable pipette tip to form a cavity on the electrode surface into which microlitre quantities of RTIL were added. The electrodes were housed in a T-cell[3] (see Figure 3.2), specifically designed to allow samples to be studied under a controlled atmosphere. Prior to the addition of any gases, the whole system was degassed under vacuum for at least 2 hours to remove water.[4–6] For experiments involving dry gas, gas was pre-dried through a drying column either consisted of concentrated sulphuric acid and solid calcium or 4 Å molecular sieves and calcium chloride. The concentration of oxygen was tuned by changing the composition of oxygen and nitrogen in the mixed

gas. Before the gas measurements, gas was run for 30 minutes to ensure equilibrium was established. For experiments excluding gases, the ionic liquid was constantly purged under vacuum during experimental analysis. All experiments were performed inside a thermostatted box (previously described by Evans et al.)[3] which also functioned as a Faraday cage. The temperature was maintained at 298 (±0.5) K.

References

[1] Villagran, C.; Banks, C. E.; Hardacre, C.; Compton, R. G. *Analytical Chemistry* **2004**, *76*, 1998–2003.

[2] Rogers, E. I.; Silvester, D. S.; Poole, D. L.; Aldous, L.; Hardacre, C.; Compton, R. G. *Journal of Physical Chemistry C* **2008**, *112*, 2729–2735.

[3] Evans, R. G.; Klymenko, O. V.; Saddoughi, S. A.; Hardacre, C.; Compton, R. G. *J. Phys. Chem. B* **2004**, *108*, 7878–7886.

[4] Gavaghan, D. J.; Rollett, J. S. *Journal of Electroanalytical Chemistry* **1990**, *295*, 1–14.

[5] Fleischmann, M.; Pons, S. *Journal of Electroanalytical Chemistry* **1988**, *250*, 257–267.

[6] Aoki, K.; Osteryoung, J. *Journal of Electroanalytical Chemistry* **1984**, *160*, 335–339.

Chapter 4

Investigation of the optimal transient times for chronoamperometric analysis of diffusion coefficients and concentrations in non-aqueous solvents and ionic liquids

This chapter investigates the optimal transient times for chronoamperometric experiments in order to simultaneously determine accurate values of concentration (c) and diffusion coefficient (D), or alternatively the number of electrons passed (n) providing c is known. This is achieved by the analysis of the current-time transients resulting from potential steps for the oxidation of ferrocene in acetonitrile and the reduction of cobaltocenium in 1-ethyl-3-methylimidazolium bis(trifluoromethylsulfonyl)imide. The analysis is based upon Shoup and Szabo approximation, which has been reported to describe the current response over all time values to within an error of 0.5 % [D. Shoup and A. Szabo, Journal of Electroanalytical Chemistry, 1982, 140, 237-245]. The error is quantified by comparing the resulting chronoamperometric data with simulation at all transient times. In addition, an alternative simple approach to the simultaneous determination of nc and D values is proposed by independently investigating the short and long time regimes of chronoamperometric transients. The chronoamperometry of hydrazine is investigated as a multielectron example process. The work presented in this chapter has been published

in *Analytical Methods*[1].

4.1 Introduction

Electrochemistry is a powerful technique, by which a vast range of physical parameters can be extracted from the system of interest[2–4]. Arguably the simplest electro-analytical techniques are based on potential steps, where a system is stepped from a potential where no detectable Faradaic current is passing to a potential where the oxidation or reduction process of interest occurs, often under diffusion control. The potential is applied, current flows through the system and the resulting plot of current vs. time (or chronoamperometric transient) can be related to a range of physical parameters. This has been used to simultaneously measure concentration and diffusion coefficients,[2, 5–10] and is commonly used in electroanalytical investigations with the current measured during the standard addition of an analyte.[11] The current-time relationship resulting from potential step to a planar macro electrode described by the Cottrell equation (see Equation 1.32 in Chapter 1) where often up to three variables, n, c and D, involved in this equation are unknown when studying a redox reaction in an n-electron-transfer system. Therefore, it is beneficial to find an alternative approach that is able to determine (nc) and D values simultaneously. One simple approach utilises potential step chronoamperometry at a micro-electrode. Micro-electrodes are widely employed, and demonstrate high mass transport rates, good signal-to-noise ratios and low uncompensated resistances.[2, 3] These features are potentially beneficial when performing electrochemistry in non-aqueous environments, and especially when operating in room temperature ionic liquids (RTILs), due to the relatively low conductivity and high viscosity of these solvents when compared to aqueous systems.[12]

Several numerical models have been developed to describe the chronoamperometric responses (or current-time transients) observed at micro-electrodes.[6, 9, 13–18] The Shoup

and Szabo equation has been widely used, and has been reported to describe the current response over all time values to within an error of 0.5 %.[9] For an n electrons process, the chronoamperometric response at a micro-electrode can be described as

$$i = 4nFrDcf(t) \tag{4.1}$$

where

$$f(t) = 0.7854 + 0.8862\sqrt{\frac{r^2}{4Dt}} + 0.2146exp(-0.7823\sqrt{\frac{r^2}{4Dt}}) \tag{4.2}$$

Note that Equation 4.2 was derived using simulation and as such applies to all solvents regardless of their viscosity.

It has been demonstrated that combining experimental chronoamperometry with fitting of the results to the Shoup and Szabo equation results in a powerful electroanalytical technique, facilitating the simultaneous determination of both the product (nc) and the diffusion coefficient (D) of electroactive analytes.[5, 7] This is possible because at short times the response is Cottrellian and depends on $ncD^{\frac{1}{2}}$ whereas at long times the steady state current (see Equation 1.30 in Chapter 1) is recorded, which scales with ncD. Accordingly, it is possible to analyse the transient to give *(nc)* and D.

As noted above, at long transient times the current approaches a steady state value where ncD is constant.[10] Therefore attempts to simultaneously determine nc and D using chronoamperometric transients recorded over very large time ranges are likely to yield apparent acceptable agreement between experiment and simulation over a wide range of pairs of nc and D values; that is by using too long a measured time, a large error can be introduced during quantifications. Alternatively, transients recorded at very short time values will experience additional non-Faradaic current, e.g. from double layer charging and thus inflate estimates of D and nc. There therefore likely exists an optimal time range for chronoamperometric transients, resulting in the smallest combined error

for the simultaneous determination of nc and D. This chapter quantitatively investigates the effect of transient time on the analysis of chronoamperometric data using the Shoup and Szabo equation, focussing on experiments performed on ferrocene in acetonitrile and cobaltocenium in a room temperature ionic liquid. In addition, an alternative approach towards the simultaneous determination of nc and D values is explored by independently investigating the short-time transient and long-time transient and solving for nc and D using the resulting constants, using hydrazine as an example.

4.2 Chronoamprometric Experiments

Before chornoamperometry, a system was first characterised by cyclic voltammetry to find out the potential where the reaction fully occurs, which is noted by the peak at the cyclic voltammogram. In chronoamperometric experiment, chronoamperometric transients were measured using a sample time of 0.01 s. After pre-equilibration for 3 s, the potential was stepped from a position of zero current to a position where the reaction fully occurs at a diffusional controlled way, and the current was measured for 25 s. It is noted the first few data points demonstrate non-Cottrellian behaviour due to extensive double layer charging. Therefore data points before 10 ms for experiments in acetonitrile and before 20 ms for experiments in ionic liquid were discarded. Analysis was made for different parts of the transient using the Shoup and Szabo equation (Equation 4.1). The fitting is described below.

The platinum micro-electrode radius was electrochemically calibrated via analysis of the steady state voltammetry of a 2.19 $\pm$ 0.01 mM solution of ferrocene in MeCN containing 0.1 M TBAP at 25 ^{0}C, according to equation 4.1. An electrode radius was determined by using the known diffusion coefficient (2.3 $\times$ 10^{-9} m^2 s^{-1}, literature value for 298 K.)[2, 8, 19] and concentration of ferrocene (2.19 mM, by weight). The voltammetric response is shown in Figure 4.1, and which resulted in a steady state current of 9.9 $\times$ 10^{-9}

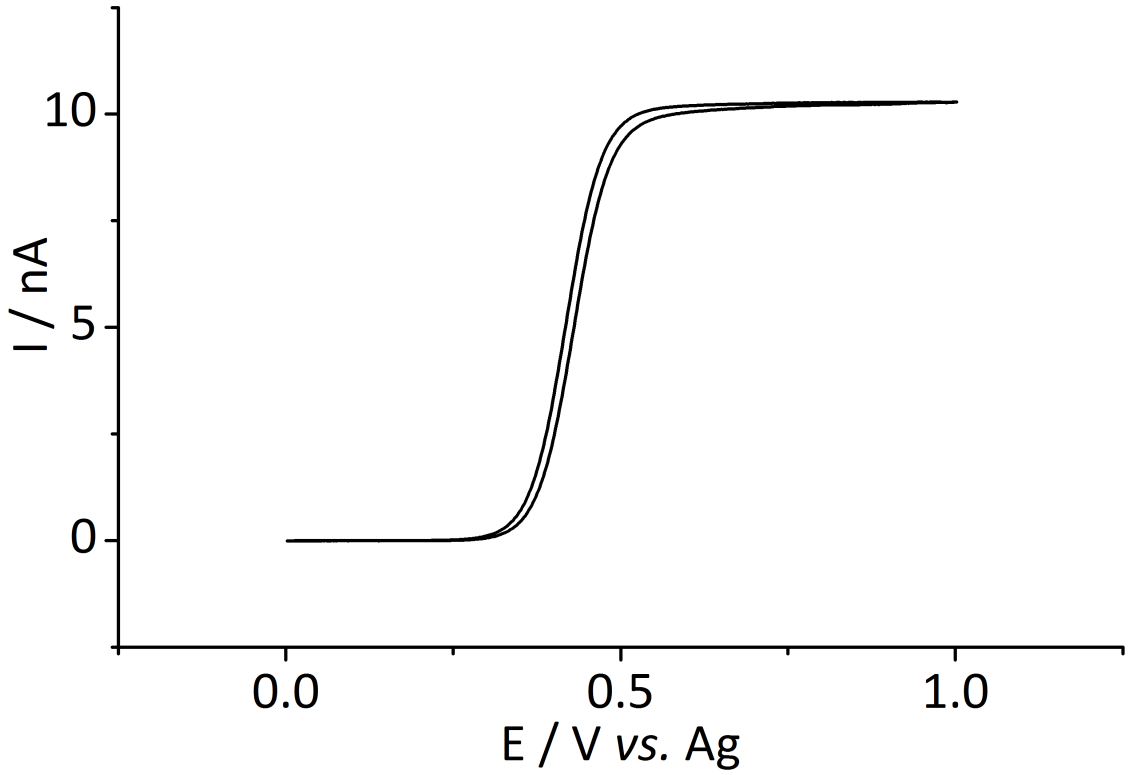

Figure 4.1: The voltammetric response of the oxidation of 2.19 mM ferrocene in acetonitrile at Pt micro electrode at a scan rate 10mV s^{-1}.

A. As a further test, a scan rate study was performed using scan rates over two orders of magnitude and the resulting voltammetry was simulated using the parameters quoted above. An excellent correlation was observed over all scan rates between experiment and simulation (not shown).

4.3 Results and Discussion

4.3.1 Determination of the Optimal Transient Time for Shoup and Szabo Analysis of the Oxidation of Ferrocene in Acetonitrile

Figures 4.2 a) - d) depict the chronoamperometric response for the one electron oxidation of 2.19 mM ferrocene in acetonitrile at transient times ranging from 0.5 seconds to 25

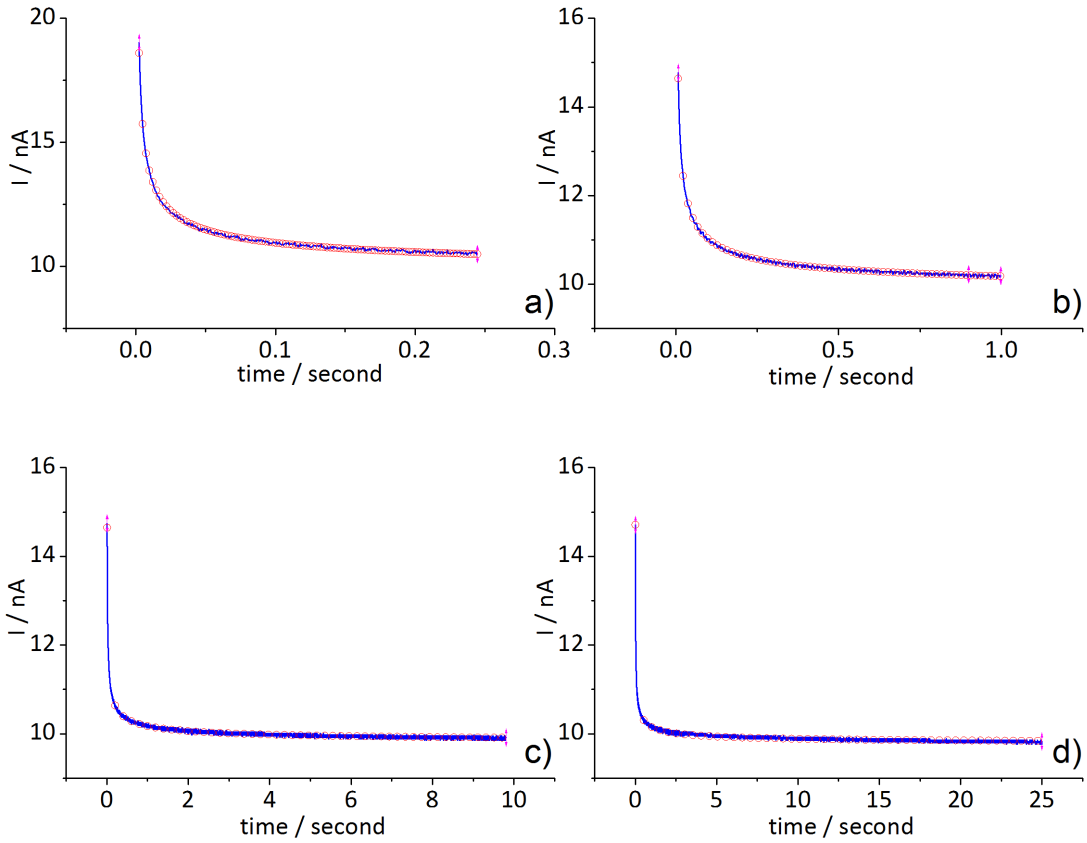

Figure 4.2: The chronoamperometric responses (blue solid line) of 2 mM ferrocene in acetonitrile at Pt electrode and corresponding line of best fit (red circles) derived from Shoup and Szabo equations at the transient time of a) 0.25 s, b) 1 s, c) 10 s and d) 25 s.

seconds (blue line), and the software package Origin 8.1 (Microcal Software Inc.) was used to fit the experimental data (red circles). The equations proposed by Shoup and Szabo (equation 4.1) were imported into the nonlinear curve fitting function, where the value for the radius of 5.05 μm (previously calibrated) was fixed, and values for the diffusion coefficient and concentration were obtained by fitting of the experimental data. The resulting simulated transients correspond to the fitting software reaching the defined level of correlation between the experimental data points and the corresponding simulated data points and then automatically ceasing the fitting procedure, yielding one value for c and one value for D that are within the fitting criteria.

In order to determine the exact values of concentration (c) and diffusion coefficient (D),

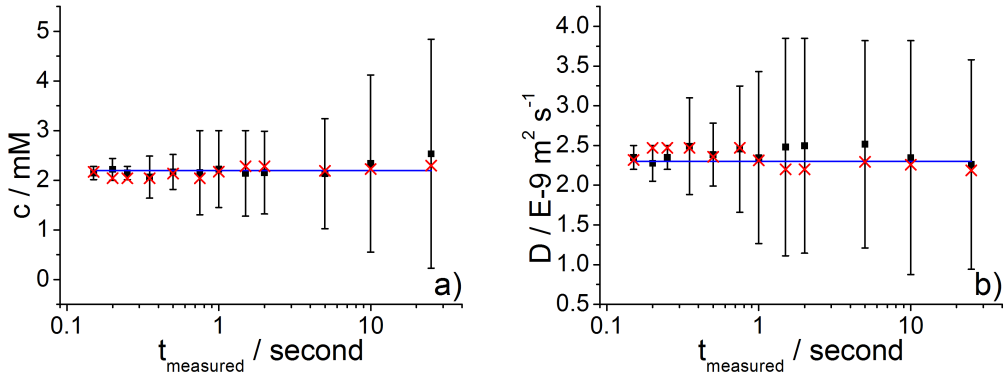

Figure 4.3: The plots of a) concentrations and b) diffusion coefficient as a function of transient time. Error bars: the range of values which have a MSAD < 0.5 %. Black square: the average value in this range. Red cross: the data point with the smallest MSAD value. Blue line: the known value for that system ($c = 2.19$ mM (by weight of ferrocene added) and $D = 2.3 \times 10^{-9}$ m^2 s^{-1} (literature value[2, 8, 19]).

chronoamperometric data was compared with the Shoup and Szabo equation. This was done systematically for a wide range of values for c and D using the following procedure; simulated chronoamperometric transients were generated using a wide range of c and D values, and then the current in each data point in the experimental transient was compared with current calculated using the Shoup and Szabo equation. The error was then quantified by the mean scaled absolute deviation (MSAD) to yield the average error per point over the entire chronoamperometric transients.

$$\%MSAD = \frac{1}{N}\Sigma N|\frac{I_{sim} - I_{exp}}{I_{exp}}| \times 100 \tag{4.3}$$

where N is the number of experimental data points, I_{exp} is the experimental current and I_{sim} is the current simulated using the Shoup and Szabo equation. This procedure was automated and repeated for a range of values for concentration and diffusion coefficient. The 'best' values of c and D are then those values which yield the lowest % MSAD.

Figures 4.3 a and b display the resulting data, where the error bars correspond to the range of c and D values which result in a % MSAD smaller than 0.5 % (e.g. within the

stated error of the Shoup and Szabo equation). The blue line corresponds to the known values for the system, where $c = 2.19$ mM and $D = 2.3 \times 10^{-9}$ m^2 s^{-1}.[8, 19] The black squares correspond to both the average value and the median value in the 0.5 % MSAD range, while the red crosses correspond to the value of c and D which resulted in the smallest measured % MSAD value.

The results demonstrate that the lowest values of % MSAD for all transient times correspond well to the known literature values of c and D, as would be expected. However, taking 0.5 % MSAD as a fitting criteria results in 'satisfactory' fits being obtained between experiment and simulation at long time values, despite the resulting c and D values being significantly different from the known values. The mean/median values of c and D are close to the real values, indicating the error bars are evenly spaced either side of the real values. This is a consequence of the linear relationship of c and D (cD = constant) at long time values, where one excessively large value and one excessively small value cancel to yield a satisfactory fit of the steady state section of the chronoamperometric transient. At short times the steady state contribution to the transient is minimised and satisfactory fits of the data can only be obtained close to the real c and D values.

At transient time values of less than 0.15 s, no fit could be obtained with an MSAD value less than 0.5 %, likely due to significant non-Faradaic contributions to the experimental data that are not considered in the Shoup and Szabo equation.[9] Therefore for the oxidation of ferrocene in acetonitrile at a micro-electrode, transient times between 0.15 s and 0.5 s will result in the closest fit between simulation and real values when using a basic non-linear fitting operation with defined fitting criteria. Alternatively, extensively simulation of the data to determine the lowest MSAD value over the entire range of possible c and D values can be used to extend the range of applicable transient times.

Figure 4.4 shows the 2D contour plot of MSAD from the chronoamperometric response of the oxidation of ferrocene at a transient time of 1 s, where the concentration diffusion

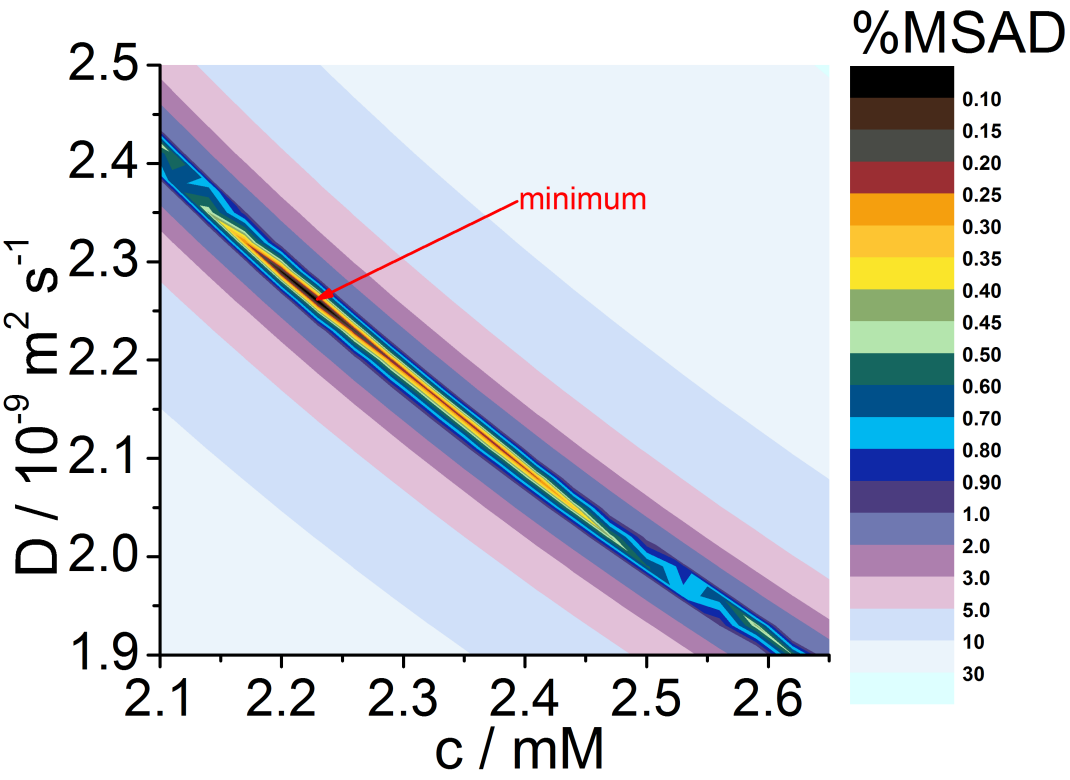

Figure 4.4: The 2D colour contour plots of MSAD, where the concentration and diffusion coefficient corresponding to the x and y axis respectively. The colour corresponding to the value of MSAD is listed on the right. This result is obtained from the chronoamperometry for the oxidation of ferrocene at a transient time of 1 second.

coefficient and diffusion coefficient concentration corresponding to the x and y axis respectively. The list of colour on the right indicates the values of MSAD in the contour plot. The lowest MSAD, where $c = 2.23$ mM and and $D = 2.26 \times 10^{-9}$ m^2 s^{-1}, corresponds to the black region of the graph whereas an increasing MSAD is radiated out from the black region. As can be seen, there is a wide range of c and D values giving a Shoup and Szabo chronoamperometry that satisfies the fitting criteria of MSAD less than 0.5 %.

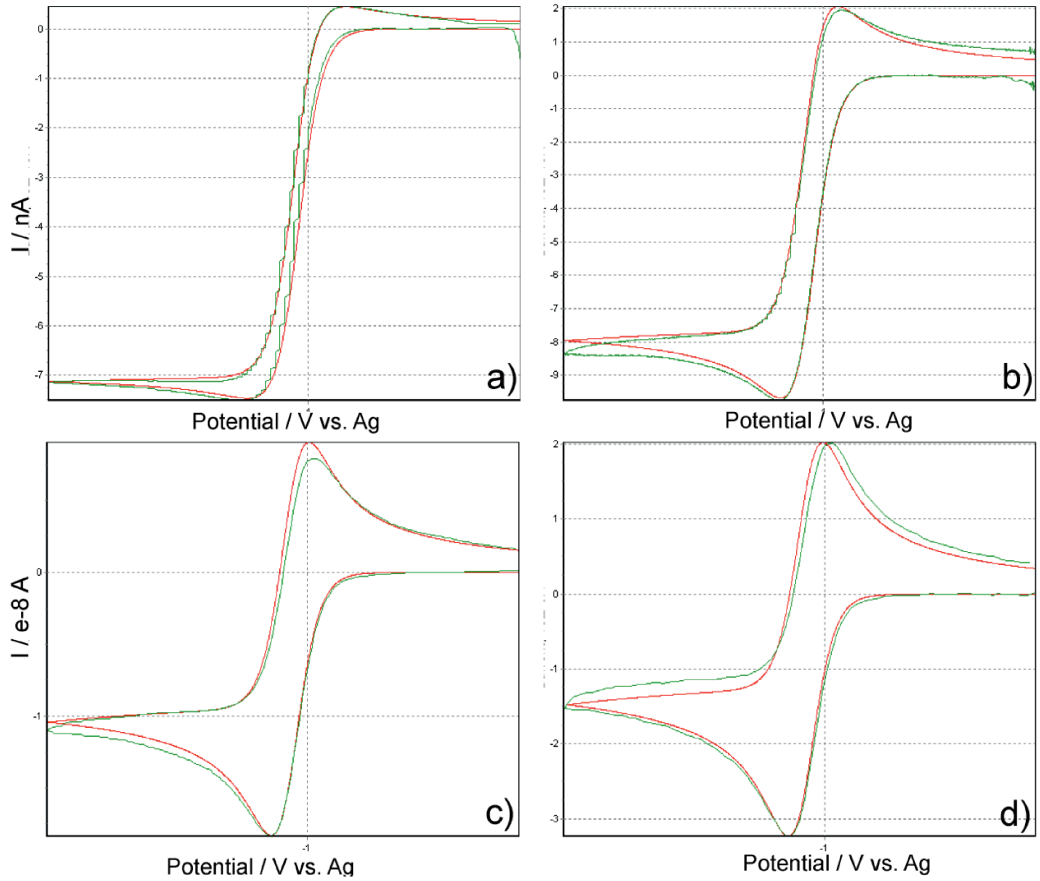

Figure 4.5: Comparison of simulated (red line) and experimental (green line) voltammetry for the reduction of $Cc^+PF_6^-$ in $[C_2mim][NTf_2]$ at a scan rate of a) 10 mV s^{-1}, b) 100 mV s^{-1}, c) 1 V s^{-1} and d) 4 V s^{-1}.

4.3.2 Optimal Transient Time for Shoup and Szabo Analysis of the Reduction of Cobaltocenium in 1-Ethyl-3-methylimidazolium Bis(trifluoromethylsulfonyl)imide

Further to the work in the conventional solvent, acetonitrile, analogous experiments were performed in the ionic liquid, 1-ethyl-3-methylimidazolium bis(trifluoromethylsulfony)-imide ($[C_2mim][NTf_2]$), containing cobaltocenium hexafluorophosphate ($Cc^+PF_6^-$). The diffusion coefficient of $Cc^+PF_6^-$, 3.2×10^{-11} m^2 s^{-1}, was obtained via a scan rate study. The resulting voltammetry was simulated using a fixed radius of 5.15 μm (previously calibrated) and concentration of 10.15 $\pm$ 0.01 mM (by weight). This simulation was per-

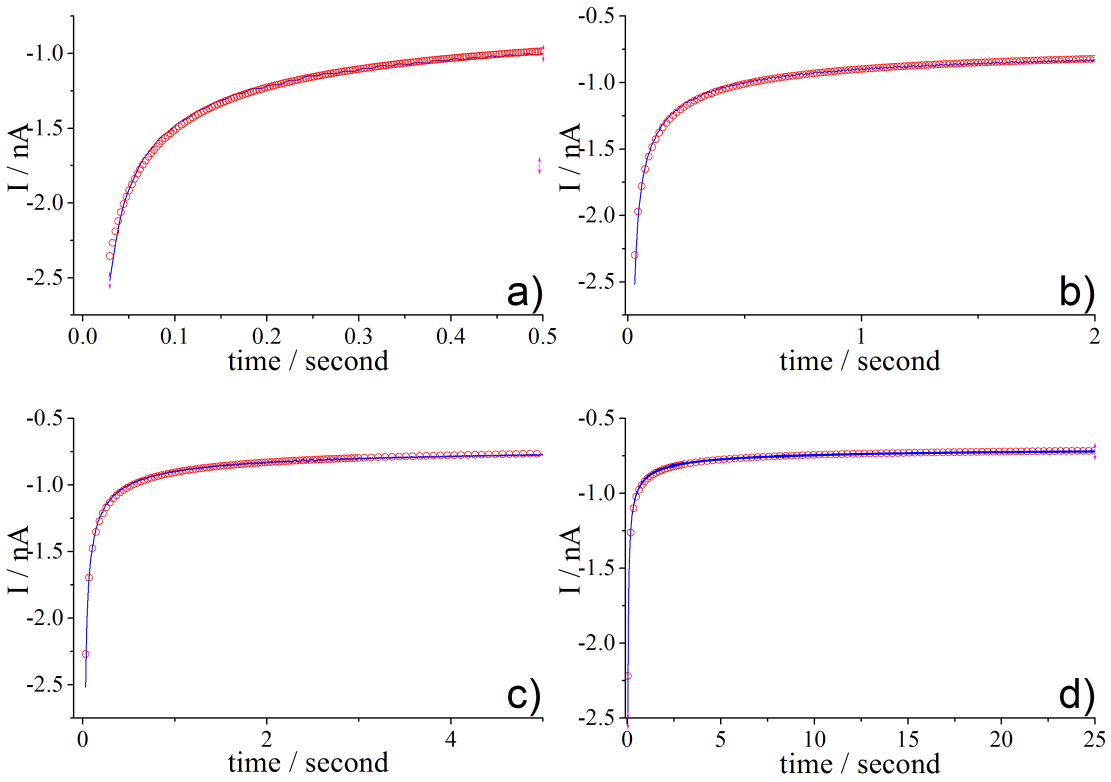

Figure 4.6: The chronoamperometric responses (blue solid line) for for the reduction of $Cc^+PF_6^-$ in $[C_2mim][NTf_2]$ at the transient time of a) 0.5 s, b) 2 s, c 5 s and d) 25 s.

formed using a model reported by Klymenko et al.[20] Figure 4.5 displays the experimental and simulated voltammetric response for the reduction of $Cc^+PF_6^-$ in $[C_2mim][NTf_2]$ at scan rates from 10 mV s^{-1} to 4 V s^{-1}, which shows a high correlation. The diffusion coefficient determined from this approach is virtually identical to the previously reported value[8] of 3.2×10^{-11} m^2 s^{-1}.

Figures 4.6 a) - d) show the chronoamperometric responses for 10.15 mM $Cc^+PF_6^-$ in $[C_2mim][NTf_2]$ at transient times ranging from 0.5 s to 25 s. The chronoamperometry was fitted using the same method as for the previous section. There is a good correlation found with the experimental and fitted chronoamperometry for $Cc^+PF_6^-$ in $[C_2mim][NTf_2]$ for all transient times. However, as in the case of ferrocene in acetonitrile, a range of c and D values could differ significantly from the correct values. This was investigated through calculating the MSAD for a range of values of c and D by comparing the simulated and

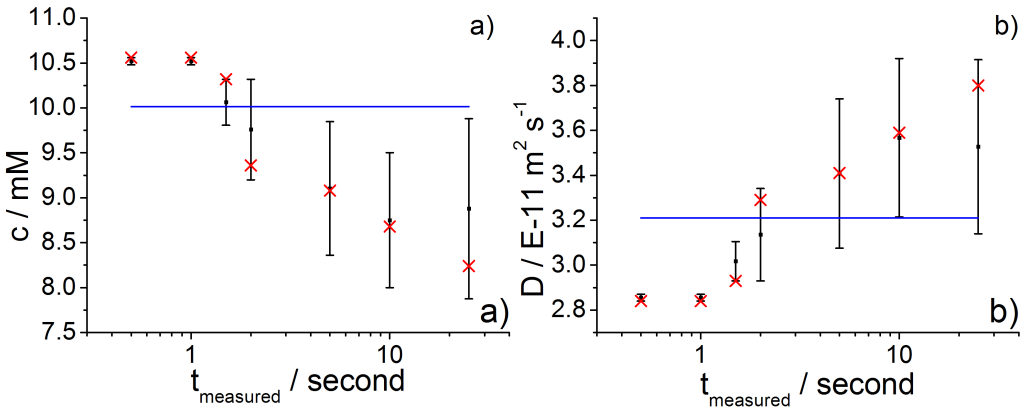

Figure 4.7: Plots of a) concentration and b) diffusion coefficient as a function of transient time. Error bars: the range of values which have a MSAD < 0.5 %. Black square: the average value in this range. Red cross: the data point with the smallest MSAD value. Blue line: the known value for that system ($c = 10.15$ mM [by weight of $Cc^+PF_6^-$ added] and $D = 3.2 \times 10^{-11}$ m^2 s^{-1}).

experimental data. The resulting c and D values are shown in Figures 4.7 a) and b), where the error bars indicate the range of c and D which satisfied the fitting criteria, i.e. MSAD ≤ 0.5 % , the black squares are the average values in the error range and the red cross correspond to the smallest MSAD. The blue lines are the expected values where $c = 10.15$ mM (by weight added) and $D = 3.2 \times 10^{-11}$ m^2 s^{-1} (from voltammetric simulation). It is also observed that a significant decrease in the error bars from long to short transient times. However, unlike experiments for ferrocene in acetonitrile, the values for c and D at shorter transient times do not give the real values. In particular, it should be noted that ionic liquids show larger double layer capacitances than those in acetonitrile,[21, 22] which may not be fully eliminated even if the first 20 ms of data is discarded. Therefore, as compared to the experiments in acetonitrile, a longer transient time may be more suitable for performing chronoamperometry in ionic liquid.

4.3.3 An Alternative Non-fitting Approach to Chronoamperometric Data to Simultaneously Yield Diffusion Coefficient and Concentration Values

The data presented in the previous two sections have highlighted the importance of obtaining a balance between 'short time' data (e.g. time scales relevant to analysis using the Cottrell equation) and 'long time' data (e.g. steady-state, diffusion-controlled data) when analysing entire transients. Alternatively, these two defined regimes observed during chronoamperometric experiments at micro-electrodes could be analysed separately, since the Cottrell equation (Equation 1.32 in Chapter 1) can be rearranged to give

$$cD^{\frac{1}{2}} = constant_1 \tag{4.4}$$

where constant$_1$ is a function of $nFA^{-\frac{1}{2}}$ and the gradient obtained by a plot of I vs $t^{\frac{1}{2}}$, while the steady state limiting current at long time values (Equation 1.30) can be rearranged to give

$$cD = constant_2 \tag{4.5}$$

and the two known constants can then be solved to yield

$$D^{\frac{1}{2}} = \frac{constant_2}{constant_1} \tag{4.6}$$

and ultimately give simultaneous quantification of both nc and D values.

As proof of principle, the data presented for the reduction of $Cc^+PF_6^-$ in $[C_2mim][NTf_2]$ was analysed using this technique. The Cottrell plot obtained for the chronoamperometric response of 10.15 mM cobaltocenium in $[C_2mim][NTf_2]$ at a 5.15 μm Pt micro-electrode gave a gradient of 2.62×10^{-10} A $s^{\frac{1}{2}}$. Solving the data by using the steady state current

(current at t = 5 s) and the gradient obtained by the Cottrell plot yielded a D value of 3.2 $\times$ 10^{-11} m^2 s^{-1}, which when substituted into either the Cottrell equation or the steady state current equation yielded a c value of 10.19 mM. These values are in good agreement with those obtained by the full simulation of the entire chronoamperometric transient using the Shoup and Szabo equation, which gave D = 3.2$\times$ 10^{-11} m^2 s^{-1} and c = 10.15 mM. The above data demonstrates the applicability of this technique towards the determination of c and D when $n = 1$. Alternatively, this technique should be applicable for multielectron processes, providing a sufficient overpotential is applied such that kinetic factors are not limiting. Hydrazine, N_2H_4, is well known to be oxidised in a four electron process[23], e.g.

$$N_2H_4 \rightarrow N_2 + 4H^+ + 4e^- \tag{4.7}$$

The voltammetry of hydrazine at Pt micro-electrodes has previously been described in detail.[23] Figure 4.8 displays a chronoamperogram recorded by stepping to + 1.0 V (vs. SCE) for 10.0 mM hydrazine in a 1 M sodium acetate buffer (pH 4.8) at a 13.8 μm radius Pt micro-electrode. The resulting Shoup and Szabo simulation (overlaid) gave D = 9.2 $\times$ 10^{-10} m^2 s^{-1} and nc = 38.1 mM (expected value 40.0 mM). Cottrell analysis of the chronoamperogram yielded a gradient of 3.92 $\times$ 10^{-8} A $s^{\frac{1}{2}}$, which when solved as above in combination with the steady state current recorded at t = 4 s (0.196 μA) gave D = 9.35 $\times$ 10^{-10} m^2 s^{-1} and nc = 39.4 mM, highlighting that both techniques are in good agreement with the expected values.

The above results therefore demonstrate that separately investigating the short and long time regimes of chronoamperometric transients obtained at micro-electrodes can yield simultaneous values of c and D, or alternatively number of electrons passed (a 'chronocoulometri' measurement) providing c is known. The data analysis involved is significantly more simple than the rigorous numerical analysis required for full analysis of

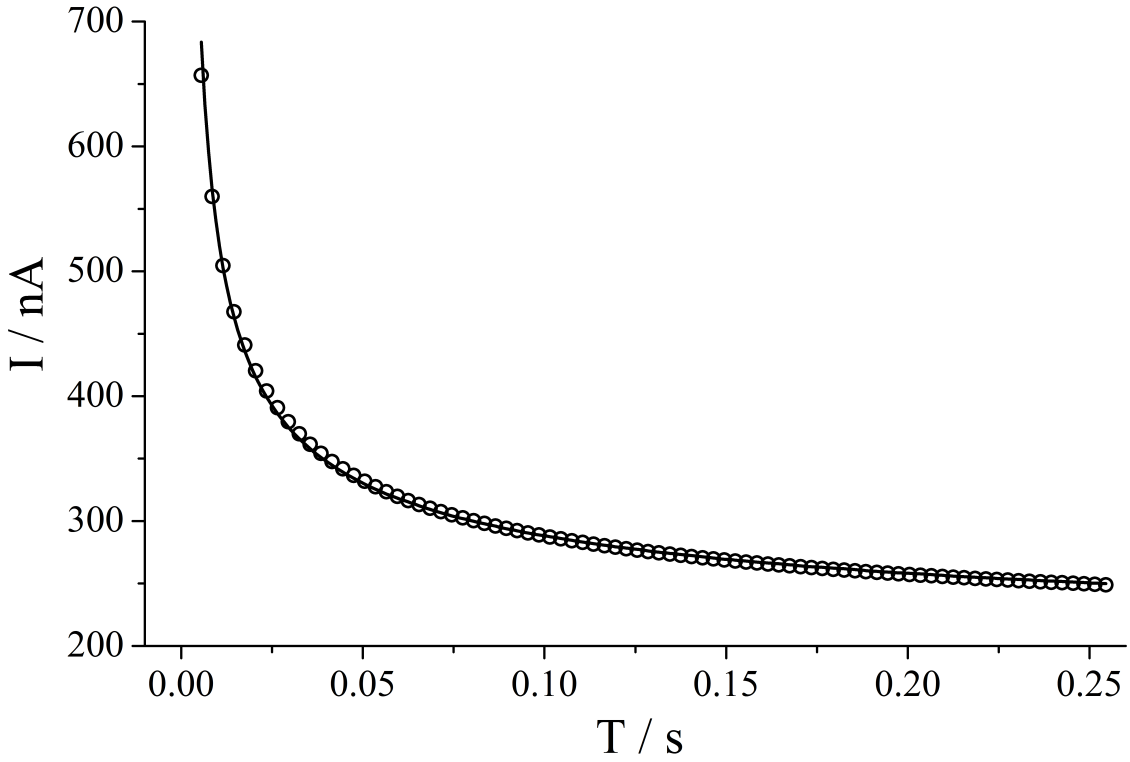

Figure 4.8: Experimental (-) and Shoup and Szabo simulated (∘) chronoamperometry for the oxidation of 10.0 mM hydrazine in 1 M sodium acetate buffer (pH 4.8) at a 13.8 μm radius Pt micro-disc electrode at + 1.0 V (vs. SCE)

a chronoamperometric transients by the Shoup and Szabo equation, and is therefore more suited to minaturised or low power consumption systems, such as remote electrochemical gas sensors.

4.4 Conclusions

This chapter highlighted the optimal chronoamperometric transient times for the determination of (nc) and D values using analysis based upon Shoup and Szabo equation via investigating the oxidation of ferrocene in acetonitrile and the reduction of the cobaltocenium cation in 1-ethyl-3-methylimidazolium bis(trifluoromethylsulfonyl)imide. The errors for (nc) and D values were investigated by comparing the simulated and experimental data and hence the values of (nc) and D within 0.5 % error of the Shoup and Szabo

equation were presented at all transient times. It was found that for the oxidation of ferrocene in acetonitrile the more promising results are given at transient times between 0.15 s and 0.5 s whereas for the experiments in ionic liquid a longer transient time is needed. In addition, a simple method to obtain (nc) and D values simultaneously using the analysis of long and short time regimes of chronoamperometric transients has been demonstrated, taking hydrazine as a multi-electron example. The next chapter looks into the tuneability property of RTILs through the study of how the formal potentials of ferrocene, a commonly used internal reference for RTILs, and its derivatives can be tuned by changing the composition of RTILs.

References

[1] Xiong, L.; Aldous, L.; Henstridge, M. C.; Compton, R. G. *Analytical Methods* **2012**, *4*, 371–376.

[2] Bard, A. J.; Faulkner, L. R. *Electrochemical Methods: Fundamentals and Applications*; Wiley, 2001.

[3] Compton, R. G.; Banks, C. E. *Understanding Voltammetry*; Imperial College Press, 2011, 2nd Edition.

[4] Wang, J. *Analytical Electrochemistry*; Wiley-VCH, New York, 1994.

[5] Paddon, C. A.; Silvester, D. S.; Bhatti, F. L.; Donohoe, T. J.; Compton, R. G. *Electroanalysis* **2007**, *19*, 11–22.

[6] Klymenko, O. V.; Evans, R. G.; Hardacre, C.; Svir, I. B.; Compton, R. G. *Journal of Electroanalytical Chemistry* **2004**, *571*, 211–221.

[7] Haruko, I. *Journal of Electroanalytical Chemistry* **2005**, *577*, 55–58.

[8] Rogers, E. I.; Silvester, D. S.; Poole, D. L.; Aldous, L.; Hardacre, C.; Compton, R. G. *Journal of Physical Chemistry C* **2008**, *112*, 2729–2735.

[9] Shoup, D.; Szabo, A. *Journal of Electroanalytical Chemistry* **1982**, *140*, 237–245.

[10] Evans, R. G.; Klymenko, O. V.; Hardacre, C.; Seddon, K. R.; Compton, R. G. *Journal of Electroanalytical Chemistry* **2003**, *556*, 179–188.

[11] Panchompoo, J.; Aldous, L.; Downing, C.; Crossley, A.; Compton, R. G. *Electroanalysis* **2011**, *23*, 1568–1578.

[12] Buzzeo, M. C.; Evans, R. G.; Compton, R. G. *ChemPhysChem* **2004**, *5*, 1106–1120.

[13] Heinze, J. *Journal of Electroanalytical Chemistry* **1981**, *124*, 73–86.

[14] Gavaghan, D. J.; Rollett, J. S. *Journal of Electroanalytical Chemistry* **1990**, *295*, 1–14.

[15] Oldham, K. B. *Journal of Electroanalytical Chemistry* **1981**, *122*, 1–17.

[16] Aoki, K.; Osteryoung, J. *Journal of Electroanalytical Chemistry* **1981**, *122*, 19–35.

[17] Aoki, K.; Osteryoung, J. *Journal of Electroanalytical Chemistry* **1984**, *160*, 335–339.

[18] Fleischmann, M.; Pons, S. *Journal of Electroanalytical Chemistry* **1988**, *250*, 257–267.

[19] Sharp, M. *Electrochimica Acta* **1983**, *28*, 301–308.

[20] Klymenko, O. V.; Gavaghan, D. J.; Harriman, K. E.; Compton, R. G. *Journal of Electroanalytical Chemistry* **2002**, *531*, 25–31.

[21] Yasui, Y.; Kitazumi, Y.; Mizunuma, H.; Nishi, N.; Kakiuchi, T. *Electrochemistry Communications* **2010**, *12*, 1479–1482.

[22] Fedorov, M. V.; Kornyshev, A. A. *Journal of Physical Chemistry B* **2008**, *112*, 11868–11872.

[23] Aldous, L.; Compton, R. G. *Physical Chemistry Chemical Physics* **2011**, *13*, 5279–5287.

Chapter 5

Tuning solute redox potentials by varying the anion component of room temperature ionic liquid

The electrode potentials for the two one electron oxidations of 1,2-diferrocenylethylene (BisFc) were studied relative to that of the one electrode oxidation of decamethylferrocene (DmFc) in a variety of RTILs. The difference in these potentials was found to be very sensitive to the anion component of the ionic liquid showing the scope of these solutes as 'designer media' to tune the thermodynamic properties of solutes dissolved in them. The work presented in this chapter has been published in *Chemical Communications*.[1]

5.1 Introduction

Chapter 2 introduces the advantageous properties of RTILs such as wide electrochemical window, high viscosity, low volatility, inherent conductivity and high thermal stability.[2] Due to all these properties and especially their low volatility, RTILs are considered as environmentally friendly solvents and are easy to recycle. Consequently, RTILs find increasing uses nowadays, ranging from fundamental studies to analytical applications.[3–5] As also shown in Chapter 2, RTILs can be also thought of as 'designer solvents' due to the fact that they consist of two components (anion and cation) which can be systematically varied and hence they can be tailored to possess different physical or chemical

properties.[6, 7] In this chapter we highlight how by changing the ionic liquid structure and composition of an ionic liquid mixture the reactivity can be tuned; this is explored in the context of the thermodynamics of the two redox centres localised on BisFc: BisFc/BisFc$^+$ and BisFc$^+$/BisFc^{2+}. Ferrocene and related species are widely used as electrode transfer mediators in, for example, glucose sensors and electrosynthesis as well as for the internal reference couple in a variety of electrochemical processes.[2, 8, 9] Thus, this 'tuneable' merit is meaningful beyond electrochemical analysis, although that is the aim here as well be used in Chapter 7.

5.2 Results and Discussion

As the potentials are recorded using a silver pseudo reference electrode, the oxidation potentials of BisFc are measured relative to a reference oxidative signal so as to avoid any potential drift. In this work, the voltammetric response of the oxidation of decamethylferrocene was used as the reference compound giving a well defined and reversible voltammetric response.[10] In addition, it is noted that decamethylferrocene exhibits only a weak solvent effect; it is less sensitive to the change of solvents, than ferrocene and bisferrocene which makes decamethylferrocene a very good reference candidate in order to study the anion effects.[9, 10] The ferrocenes (98 %, Aldrich) were pre-dissolved in acetonitrile (> 99 %, Aldrich) and the resulting solutions were transferred into ionic liquids. In order to remove the acetonitrile, water and other impurities such as organic solvents which may be used in the ionic liquid synthesis, the ionic liquids were degassed under vacuum for two hours at room temperature.[11–13] The ferrocenes dissolved in various ionic liquids, 1-butyl-3-methylimidazolium tetrafluoroborate ([C_4mim][BF_4]), 1-butyl-3-methylimidazolium bis(trifluoromethylsulfonyl)imide ([C_4mim][NTf_2]) and 1-butyl-3-methylimidazolium tris(pentafluoroethyl)trifluorophosphate ([C_4mim][FAP]), were characterised using cyclic voltammetry and square wave voltammetry. [C_4mim][BF_4] and [C_4mim][NTf_2]

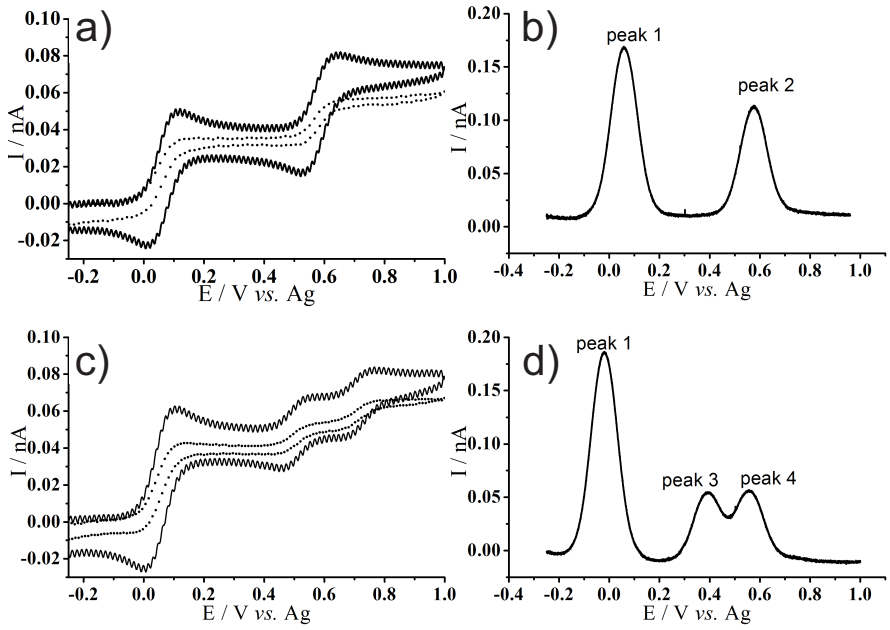

Figure 5.1: a). Cyclic voltammetric responses for the oxidation of 1 mM decamethylferrocene and 1 mM ferrocene in $[C_4mim][BF_4]$ at scan rates of 10 mV s^{-1} (dashed line) and 100 mVs^{-1} (solid line) at platinum micro-electrode. b) Square wave voltammetric response for the oxidation of the decamethylferrocene and ferrocene in $[C_4mim][BF_4]$ at a frequency of 50 Hz, step potential of 1 mV and an amplitude of 50 mV. c) Cyclic voltammetric response for the oxidation of the 1 mM decamethylferrocene and 1 mM bisferrocene in $[C_4mim][BF_4]$ at scan rates of 10 mV s^{-1} (dotted line) and 100 mVs^{-1} (solid line) at a platinum micro-electrode. d) Square wave voltammetric response for the oxidation of the decamethylferrocene and bisferrocene in $[C_4mim][BF_4]$ at a frequency of 50 Hz, step potential of 1 mV and an amplitude of 50 mV.

were synthesised in house from the corresponding bromide salt as reported previously.[14, 15]

Figure 5.1 a) shows the cyclic voltammogram of $[C_4mim][BF_4]$ containing 1 mM decamethylferrocene and 1 mM ferrocene at a platinum micro-disc electrode at scan rates of 10 mV s^{-1} and 100 mV s^{-1}. The peak at the most negative potential corresponds to the oxidation of decamethylferrocene and the second feature is due to the oxidation of ferrocene. The peak current response of ferrocene was low as ferrocene is volatile in most of the ionic liquids studied which leads to a reduction in concentration when treated under vacuum conditions.[16–18] The peak potential is obtained using square wave voltammetry

as this technique records the current in both reductive and oxidative directions at each potential step and hence the peak potential in square wave voltammetry is the mid way potential and very close to the formal potential of the redox couple studied.[19, 20] Figure 5.1 b) displays the square wave voltammetric response of the oxidation of decamethylferrocene (peak 1) and ferrocene (peak 2) in $[C_4mim][BF_4]$ at a frequency of 50 Hz, a step potential of 1 mV and an amplitude of 50 mV, where the reactions for peaks 1 (due to $DmFc/DmFc^+$) and 2 (due to Fc/Fc^+) correspond to Figure 5.2 a) and b) respectively.

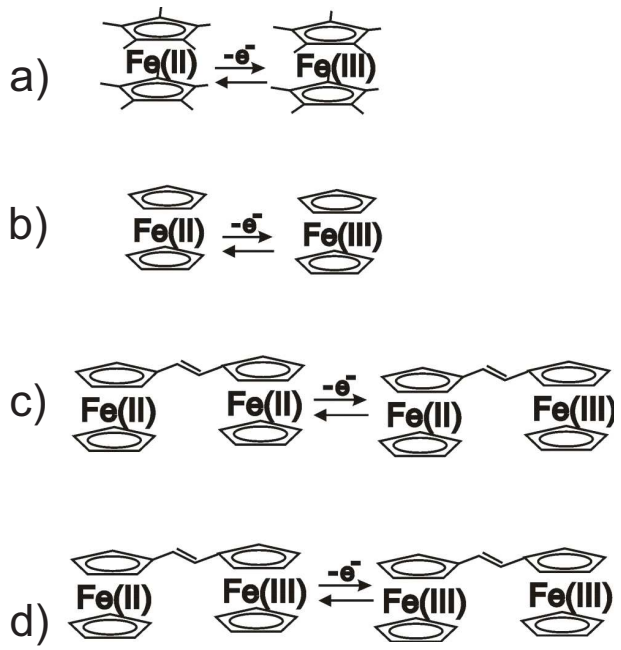

Figure 5.2: Reactions correspond a) oxidation of DmFc, b) oxidation of Fc c) the first and d) second oxidation of BisFc.

A similar experiment was carried out for the ionic liquid containing decamethylferrocene and bisferrocene (1,2-diferrocenylethylene). Figures 5.1 c) and d) display the cyclic voltammetric and square wave voltammetric responses of $[C_4mim][BF_4]$ containing 1 mM decamethylferrocene and 1 mM bisferrocene, where peaks 3 and 4 are due to the first and second oxidation of bisferrocene described by Figure 5.2 c) and d) respectively.

In order to compare the influence of the anion on the oxidation potentials, these two systems were examined in ionic liquids with the same cation but different anions, i.e.

[C_4mim][BF_4], [C_4mim][NTf_2] and [C_4mim][FAP]. In the following work the peak potential difference is measured as a function of the volume of the ionic liquid anion. The molecular volumes, V($[BF_4]^-$) = 0.089 nm^3, V($[NTf_2]^-$)= 0.262 nm^3 and V($[FAP]^-$)= 0.375 nm^3, were estimated using a group contribution model as a function of temperature.[21]

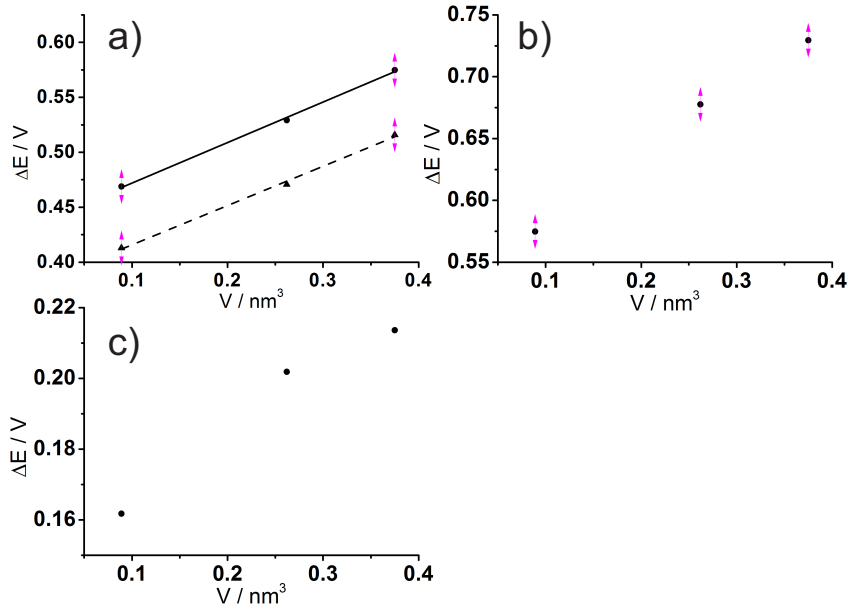

Figure 5.3: (a) Comparison of the plots of peak potential difference, ΔE of decamethylferrocene and ferrocene (solid line) with that of the oxidation of decamethylferrocene and first oxidation of bisferrocene (dashed line) against the molecular volume of the anion in the ionic liquid. (b) Peak potential difference of the oxidation of decamethylferrocene and second oxidation of bisferrocene as a function of molecular volume of ionic liquid anion. (c) Peak potential difference of oxidation of the first and second oxidation of bisferrocene as a function of molecular volume (V) of ionic liquid anion.

Figure 5.3 a) compares peak potential difference, ΔE, of peaks 1 and 2 with peaks 1 and 3 as a function of the molecular volume of ionic liquid anion, where clear linear correlations ($R_2 > 0.99$) were obtained. These peak potential differences between decamethylferrocene and ferrocene, 0.575, 0.528 and 0.469 V in [C_4mim][BF_4], [C_4mim][NTf_2] and [C_4mim][FAP] respectively, are comparable to those observed by Torriero et al., who reported potential differences of 0.575, 0.513 and 0.478 V for the same anions. As can be seen from both plots, the potential difference increases with the size of anion as the

ferrocenium cation is better stabilised by the smaller ionic liquid anion where the small anion produces larger coulombic interaction with ferrocenium cation. It is also observed that the peak potential difference for the oxidation of decamethylferrocene and ferrocene is c.a. 0.06 V higher than that of the oxidation of decamethylferrocene and first oxidation of bisferrocene for each ionic liquid. This is due to the fact that bisferrocene is easier to oxidise as bisferrocene is more electron rich than ferrocene. From this Figure, two lines of approximately similar gradient were seen which is reasonable since the charge of the single oxidised bisferrocene is localised in one ferrocene unit.[22, 23]

Figure 5.3 b) shows the peak potential difference of peak 1 and 4 dependence with the molecular volume of the anion in ionic liquid, which gave a non-linear correlation but increased with the size of anion as for the case of ferrocene alone. This is likely owing to the less efficient solvation of doubly charged bisferrocenium. A similar, again non-linear, trend is also shown in Figure 5.3 c) which depicts the correlation between the peak potential difference of the first and second oxidation of bisferrocene and the molecular volume of anion.

In order to further extend these this observations, a further experiment was conducted by adding ionic liquid composed of small anion, $[C_4mim][BF_4]$, into the one composed of larger anion, $[C_4mim][FAP]$. Figure 5.4 a) shows the plots of the peak separation of the oxidation of decamethylferrocene and ferrocene as a function of the percentage (by volume) of $[C_4mim][BF_4]$ in the ionic liquid mixture and a linear decrease in the peak potential difference is observed with increased percentage of $[C_4mim][BF_4]$. The observation can be rationalised as due to the large $[FAP]^-$ anion, which less effectively stabilises the oxidised ferrocene or bisferrocene, is gradually replaced by $[BF_4]^-$ as more $[C_4mim][BF_4]$ is mixed into $[C_4mim][FAP]$. As discussed above, the small anion stabilise the ferrocenium cation better as the Coulombic interaction between a smaller anion and ferrocenium is stronger, provided the charge of the anions are the same. Figure 5.4 b) displays the plot

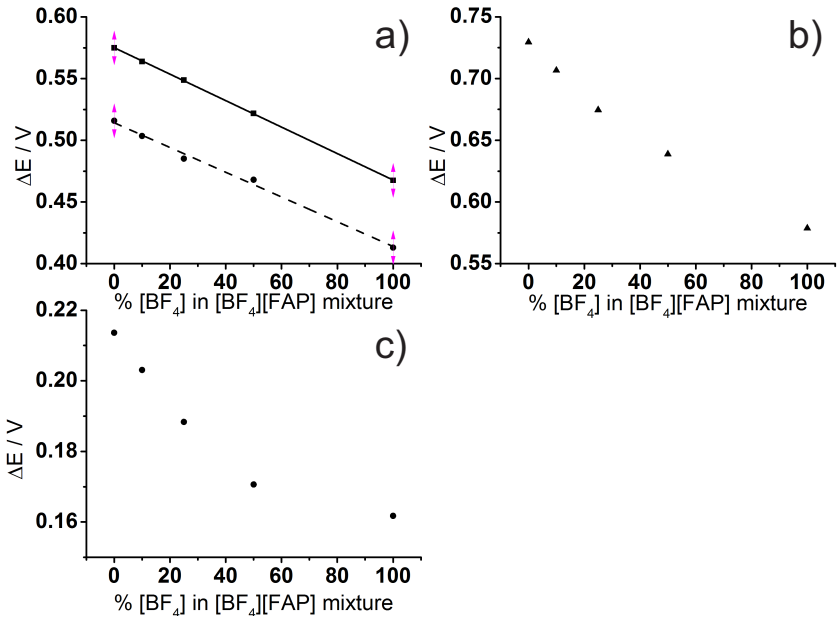

Figure 5.4: a) Comparison of the plots of peak potential difference, ΔE, of decamethylferrocene and ferrocene (solid line) with that of decamethylferrocene and first oxidation of bisferrocene (dashed line) against the percentage of $[C_4mim][BF_4]$ in the mixture of $[C_4mim][BF_4]$ and $[C_4mim][FAP]$. b) Peak potential difference of the oxidation of decamethylferrocene and second oxidation of bisferrocene as a function of the percentage of $[C_4mim][BF_4]$. (c) Peak potential difference of oxidation of the first and second oxidation of bisferrocene as a function of the percentage of $[C_4mim][BF_4]$.

of the peak potential difference of the oxidation of decamethylferrocene and second oxidation of bisferrocene against percentage of $[C_4mim][BF_4]$. A non-linear correlation is seen from Figure 5.4 b). This further illustrates that the second oxidised bisferrocene is solvated more poorly by the larger anion. A similar observation is found in Figure 5.4 c) which shows the peak potential difference of the first and second oxidation of bisferrocene dependence with the percentage of $[C_4mim][BF_4]$ in the ionic liquid mixture.

5.3 Conclusions

In conclusion, the oxidation potentials of ferrocene derivatives which reflect the thermodynamic oxidising power of the cation can be tuned by careful selection of the anion in the RTIL thereby using the RTILs as 'designer solvents' with tuneable properties. Based

upon fundamental studies on the analytical technique and the solvents property, electrochemical sensors and sensing electrodes were developed as discussed in the following chapters.

References

[1] Xiong, L.; Fletcher, A. M.; Davies, S. G.; Norman, S. E.; Hardacre, C.; Compton, R. G. *Chemical Communications* **2012**, *48*, 5784–5786.

[2] Barrosse-Antle, L. E.; Bond, A. M.; Compton, R. G.; O'Mahony, A. M.; Rogers, E. I.; Silvester, D. S. *Chemistry - An Asian Journal* **2010**, *5*, 202–230.

[3] Buzzeo, M. C.; Hardacre, C.; Compton, R. G. *Analytical Chemistry* **2004**, *76*, 4583–4588.

[4] Rogers, E. I.; Huang, X.-J.; Dickinson, E. J. F.; Hardacre, C.; Compton, R. G. *Journal of Physical Chemistry C* **2009**, *113*, 17811–17823.

[5] Cui, G.; Wang, C.; Zheng, J.; Guo, Y.; Luo, X.; Li, H. *Chemical Communications* **2012**, *48*, 2633–2635.

[6] Abbott, A. P.; Frisch, G.; Garrett, H.; Hartley, J. *Chemical Communications* **2011**, *47*, 11876–11878.

[7] Lee, S.-G. *Chemical Communications* **2006**, 1049–1063.

[8] Rogers, E. I.; Silvester, D. S.; Poole, D. L.; Aldous, L.; Hardacre, C.; Compton, R. G. *Journal of Physical Chemistry C* **2008**, *112*, 2729–2735.

[9] Torriero, A. A. J.; Howlett, P. C. *Electrochemistry Communications* **2012**, *16*, 84–87.

[10] Aranzaes, J. R.; Daniel, M.-C.; Astruc, D. *Canadian Journal of Chemistry* **2006**, *84*, 288–299.

[11] O'Mahony, A. M.; Silvester, D. S.; Aldous, L.; Hardacre, C.; Compton, R. G. *Journal of Chemical and Engineering Data* **2008**, *53*, 2884–2891.

[12] Seddon, K. R.; Stark, A.; Torres, M.-J. *Pure and Applied Chemistry* **2000**, *72*, 2275–2287.

[13] Buzzeo, M.; Evans, R. G.; Compton, R. G. *ChemPhysChem* **2004**, *5*, 1106–1120.

[14] Ngo, H. L.; LeCompte, K.; Hargens, L.; McEwen, A. B. *Thermochimica Acta* **2000**, *357-358*, 97–102.

[15] Bonhote, P.; Dias, A.-P.; Papageorgiou, N.; Kalyanasundaram, K.; Grtzel, M. *Inorganic Chemistry* **1996**, *35*, 1168–1178.

[16] Fu, C.; Aldous, L.; Dickinson, E. J. F.; Manan, N. S. A.; Compton, R. G. *Chemical Communications* **2011**, *47*, 7083–7085.

[17] Fu, C.; Aldous, L.; Dickinson, E. J. F.; Manan, N. S. A.; Compton, R. G. *New Journal of Chemistry* **2012**, *36*, 774–780.

[18] Fu, C.; Aldous, L.; Dickinson, E. J. F.; Manan, N. S. A.; Compton, R. G. *ChemPhysChem* **2011**, *12*, 1708–1713.

[19] Compton, R. G.; Banks, C. E. *Understanding Voltammetry*; Imperial College Press, 2011, 2nd Edition.

[20] Bard, A. J.; Faulkner, L. R. *Electrochemical Methods: Fundamentals and Applications*; Wiley, 2001.

[21] Jacquemin, J.; Ge, R.; Nancarrow, P.; Rooney, D. W.; Costa Gomes, M. F.; Padua, A. A. H.; Hardacre, C. *Journal of Chemical and Engineering Data* **2008**, *53*, 716–726.

[22] Zhang, Q.; Song, W.-L.; Showkot Hossain, A.; Liu, Z.-D.; Hu, G.-J.; Tian, Y.-P.; Wu, J.-Y.; Jin, B.-K.; Zhou, H.-P.; Yang, J.-X.; Zhang, S.-Y. *Dalton Transactions* **2011**, *40*, 3510–3516.

[23] Arima, V.; Iurlo, M.; Zoli, L.; Kumar, S.; Piacenza, M.; Della Sala, F.; Matino, F.; Maruccio, G.; Rinaldi, R.; Paolucci, F.; Marcaccio, M.; Cozzi, P. G.; Bramanti, A. P. *Nanoscale* **2012**, *4*, 813–823.

Chapter 6

An electrochemical thermometer: Voltammetric measurement of temperature and its application to amperometric gas sensing

Understanding the analytical technique and RTIL property is essential for improving sensor design. This chapter demonstrates a temperature sensing system incorporated into an amperometric oxygen sensor. In the first part of this work, we introduce temperature sensing systems based upon voltammetric responses of both single molecule (1,2-diferrocenylethhylene, bisferrocene, in 1-propyl-3-methylimidazolium bistrifluoromethylsulfonylimide) and two independent molecules (decamethylferrocene and N,N,N',N'-tetramethyl-p-phenylenediamine in 1-ethyl-3-methylimidazolium tetracyanoborate) respectively. In both systems, the difference of formal potentials of two redox centres was measured as a function of temperature. The former was recorded as the peak difference in square wave voltammetry with the peak potential difference increases linearly with the increasing temperature. In order to show proof-of-concept of voltammetric temperature measurement in relation to a gas sensor, the latter system was investigated in the presence of oxygen, where the concentration and diffusion coefficient of oxygen varied with temperature, as well as the peak difference discussed previously, were studied in the presence of pure oxy-

gen and dried air using chronoamperometry. A negligible variation of concentration of oxygen from both sources with temperature over the range 298 K to 318 K is demonstrated. These results obtained from pure oxygen and dried air were compared and a c.a. 79 % drop of cathodic signal from pure oxygen to dried air was found which is consistent with the percentage of oxygen in air. The diffusion coefficient of oxygen was related to temperature using an Arrhenius plot , yielding a linear graph with high correlation. All experiments gave a high reproducibility. The work presented here has been published in the *Analyst*[1].

6.1 Introduction

The attraction of electrochemical sensors is discussed in Chapter 2. For all types of electrochemical sensors, the detection depends on a Faradaic electron transfer event at a solute-electrode interface driven by an applied potential and the resulting current gives the sought analytical signal. Electrode processes are highly sensitive to temperature because of thermodynamic (formal potential) and kinetic (electrochemical rate constant, diffusion coefficient) features. The temperature dependent gas detection are detailed in Section 2.4.2 in Chapter 2. That said it is not always possible to deploy many practical amperometric sensors under thermostatted conditions. It is desirable in some situations to build-in a voltammetric measurement of the operating temperature - measured at the electrodes solution interface - so as to provide a validity and/or accuracy check. In this chapter we propose the use of a molecule containing two redox centres with different formal potentials which gives rise to two distinct voltammetric signals:

$$(A-B)-e^- \rightleftharpoons (A^+-B), \quad E^0_{f,a} \tag{6.1}$$

$$(A^+ - B) - e^- \rightleftharpoons (A^+ - B^+), \quad E^0_{f,b} \tag{6.2}$$

which may be oxidative (as above) or reductive in character. If the electron transfers are fast (relative to prevalent mass transport) then the observed voltammetry will be electrochemically reversible in character and the temperature dependence of the two formal potentials, $E_{f,a}$ and $E_{f,b}$, will be related to the entropy change associated with the electrochemical process via,

$$F\frac{(\partial E^0_f)}{\partial T} = \Delta S \tag{6.3}$$

If the temperature dependence of the two formal potentials is different then the two voltammetric peaks will not only appear at different potentials at two different temperatures but the difference in the potentials of the two peaks, $E_{f,a} - E_{f,b}$, for reversible electron transfer, will also vary with temperature. Accordingly the measurement of the difference of the two voltammetric peak potentials allows the measurement of temperature. In the following we will show that this difference can be measured with sufficient accuracy to realise the reliable measurement of temperature. In particular, we study the system

$$A - B \equiv Cp - Fe - C_5H_4 - (CH = CH) - H_4C_5 - Fe - Cp \tag{6.4}$$

on a room temperature ionic liquid solvent (RTIL) and show that the value of $(\partial E_{f,a}/\partial T - \partial E_{f,b}/\partial T) = 0.198 mV/K$ over the temperature range of 298 K to 318 K. Note that the benefits in the use of RTILs for solvents in gas sensing has been discussed elsewhere.[14] We further study a system where the different molecules, A and B are used for an equiv-

alent measurement,

$$A - e^- \rightleftharpoons A^+ \quad E^0_{f,a} \tag{6.5}$$

$$B - e^- \rightleftharpoons B^+ \quad E^0_{f,b} \tag{6.6}$$

and consider the molecules decamethylferrocene and N,N,N',N'-tetramethylphenylenediamine again in a room temperature ionic liquid solvent. In these cases much larger difference in the temperature coefficients of the peak potential are seen. The latter system is used to calibrate the temperature in a series of experiments in which the chronoamperometry of the one electron reduction of oxygen to superoxide in the RTIL,

$$O_2 + e^- \rightleftharpoons \dot{O_2^-} \tag{6.7}$$

is studied so as to find the solubility of the gas and the diffusion coefficient of O_2 as a function of temperature, thus providing proof-of-concept of measurement scenarios in amperometric gas sensors, and providing proof-of-concept of the use of a voltammetric thermometer.

6.2 Chronoamperometric Experiments

The chronoamperometric experiments adopted the methods described in Chapter 4 Section 4.2. Due to the fact that this experiment was carried out at different system, a longer pre-equilibration time, 300 s, is needed to reach oxygen saturation in ionic liquids. The following methods were applied. Chronoamperometric transients were recorded using a sample time of 0.001 s. The potential was stepped from 0 V vs. Ag to -2.0 V vs. Ag, and the current was measured for 0.5 s. To obtain concentration and diffusion coefficient of oxygen, the Shoup and Szabo equation (see Equation 4.1 in Chapter 4) was used to fit

the chronoamperometric responses of oxygen reduction. The calculations and parameters chosen behind this technique are discussed in detail in Chapter 4.[15–17]

Using this analysis, the diffusion coefficient and solubility of oxygen in ionic liquids can be simultaneously determined since n ($n = 1$) is known. The fit between experimental and simulated results was optimised by fixing the radius of the Pt micro-electrode, r, and allowing the software to iterate through various D and c values. All experiments were repeated at least three times and the variation of all results (i.e. peak potential, concentration and diffusion coefficient) for the same experiment was less than 0.15 %.

6.3 Results and Discussions

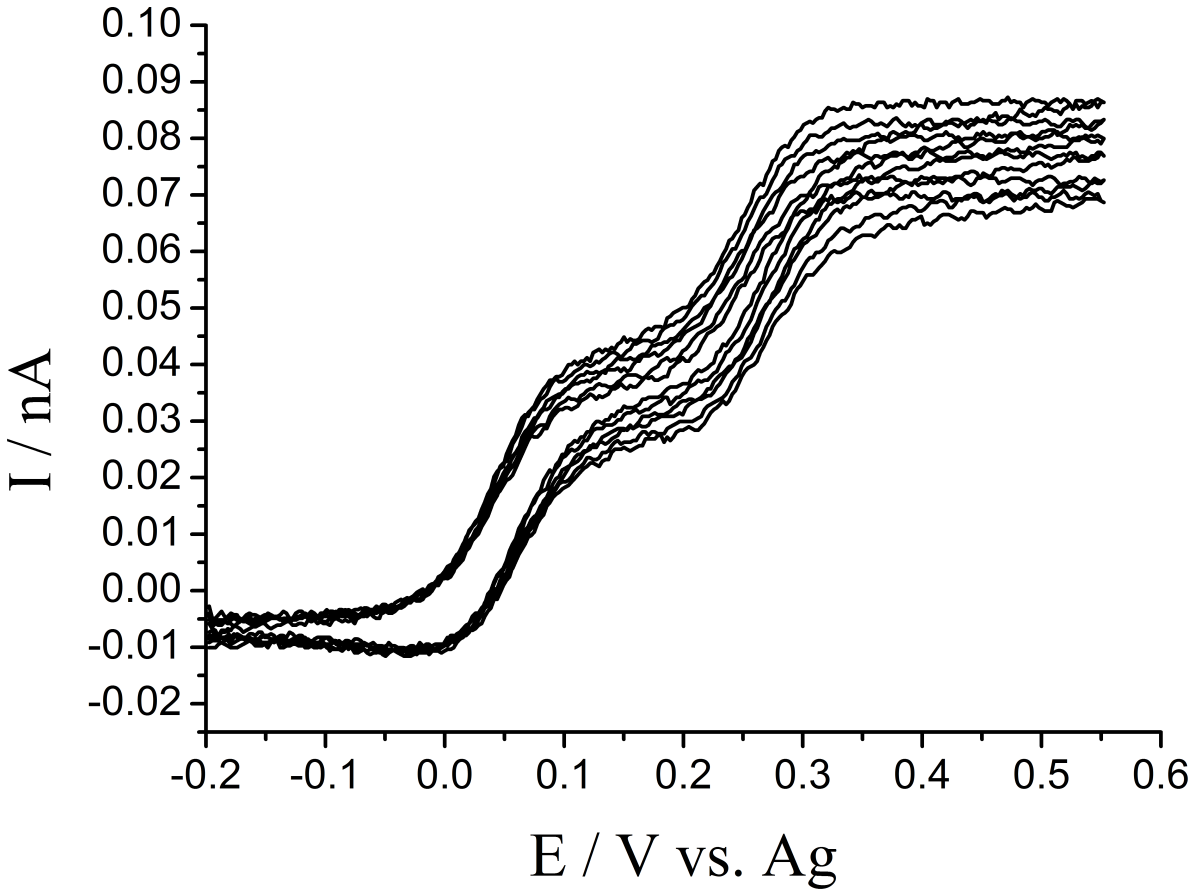

Figure 6.1: Cyclic voltammetry for the oxidation of bisferrocene in $[C_3mim][NTf_2]$ on a platinum microdisc electrode at 298 K over a period of 15 hours.

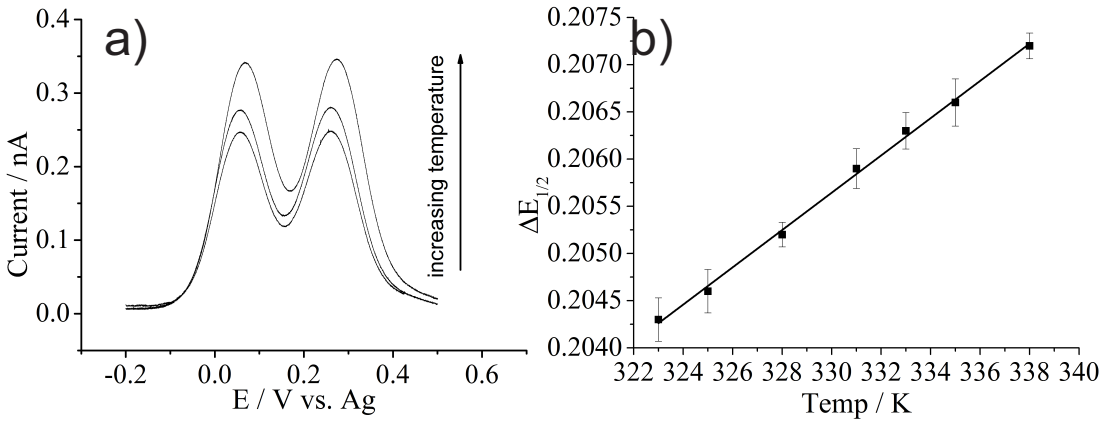

Figure 6.2: a) Square wave voltammetry of the oxidation of bisferrocene over a temperature range of 298 K to 313 K. b) Plot of the peak difference as a function of temperature.

As discussed in the introduction the study of the oxidation of bisferrocene allows the measurement of temperature since it contains two oxidisable centres; the voltammetric peaks as discussed below, are more than 200mV apart. Note that in the following the signals are measured against a Ag pseudo reference electrode. Whilst the potential of such electrodes is known to slightly drift,[18, 19] the difference between the two voltammetric signals will be insensitive to this drift since the latter is much slower than the time taken for a voltammetric scan. 1 mM bisferrocene was dissolved in $[C_3mim][NTf_2]$ and then the whole system was degassed under vacuum for 2 hours before experiment. Figure 6.1 shows successive cyclic voltammetric responses for the oxidation of bisferrocene in $[C_3mim][NTf_2]$ at a scan rate of 10 mV s^{-1} over a period of 15 hours and 2 hours interval between scans. A 6.9 % reduction of bisferrocene over 15 hours was found by analysis of the steady state current. This result indicates that bisferrocene remains in $[C_3mim][NTf_2]$ for a long period of time.

The formal potentials of redox couples can be readily evaluated using square wave voltammetry (SWV) as this records the current difference in the oxidative and reductive direction as a function of staircase potential.[20, 21] The peak potential in the square wave voltammetry is close to the formal potential of the redox couple studied.[22] Figure 6.2

a) shows the square wave voltammetry for the oxidation of bisferrocene in $[C_3mim][NTf_2]$ over temperature range of 298 to 318 K. The optimised experimental conditions for SWV were achieved using a frequency of 50 Hz, a step potential of 0.1 mV and amplitude of 25 mV. As can be seen from this figure, the peak height increases with increasing temperature. This is because the diffusion rates are greater at higher temperature which leads to an increase in the square wave voltammetric current. There are two oxidative peaks at c.a 0.06 V and c.a 0.26 V vs. Ag, which correspond to the first and second oxidation of BisFc (see Figure 5.2 c) and d) in Chapter 5).

The peak differences were measured via subtracting the peak potentials of these two oxidative waves in the square wave voltammetry at different temperatures. Figure 6.2 b) displays the plot of the temperature dependence of the peak difference, $\Delta E_{1/2}$. A linear correlation was obtained from the plot with R^2 of 0.997, gradient of 0.1976 ($\pm$ 0.0043) mV K^{-1} and an intercept of 0.1405 V. This correlation can be expressed as follows,

$$\Delta E_{1/2}(V) = 0.1405 + 0.198 \times 10^{-3} T \tag{6.8}$$

where T is the temperature in K.

6.3.1 Measurement of Temperature by A Decamethylferrocene - N,N,N',N'-tetramethyl-p-phenylenediamine (TMPD) System

In order to obtain a more sensitive detection of temperature, it is necessary to consider a system with a larger temperature coefficient of peak difference. TMPD and decamethylferrocene were used due to their long-term stabilities in $[C_2mim][TCB]$ which were investigated using successive cyclic voltammetry for the oxidation of these two species over a period of 15 hours where 5.1 % and 6.2 % decrease from the original currents were ob-

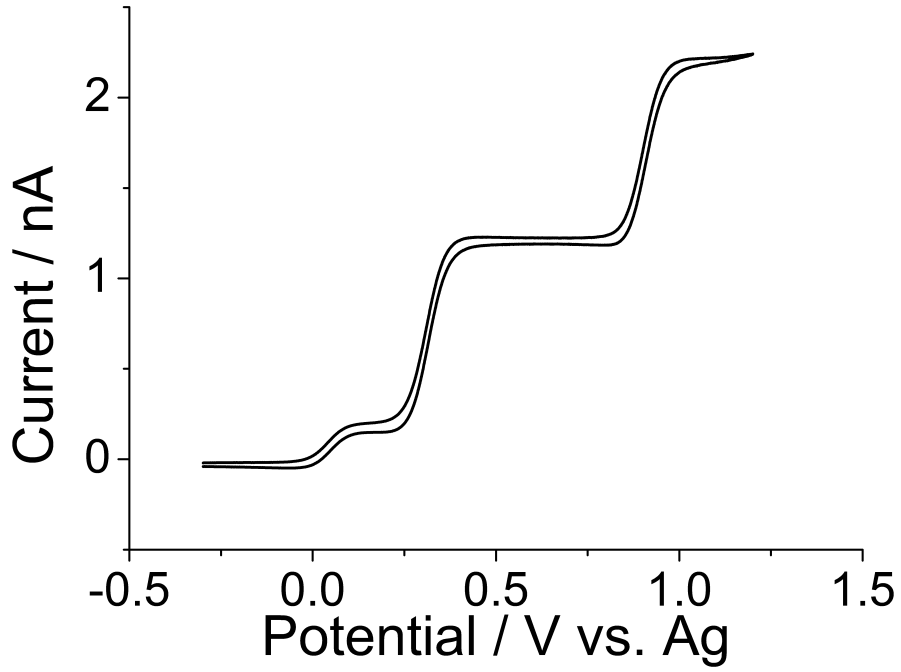

Figure 6.3: Cyclic voltammetry for the oxidation of decamethylferrocene and TMPD in $[C_2mim][TCB]$ on a platinum microdisc electrode at 298 K.

served respectively. TMPD, undergoing two electron transfers, together with decamethylferrocene acted as a temperature indicator where TMPD redox potential was recorded relative to the redox potential of decamethylferrocene at different temperatures. 1 mM decamethylferrocene and 5 mM TMPD were prepared in acetonitrile and 15 μL of each solution were then transferred into 15 μL $[C_2mim][TCB]$. In order to remove acetonitrile and other impurities from $[C_2mim][TCB]$, $[C_2mim][TCB]$, containing decamethylferrocene and TMPD, was purged under vacuum for two hours. Decamethylferrocene-TMPD system was characterised using cyclic voltammetry. Figure 6.3 shows the cyclic voltammetry of 1 mM Decamethylferrocene and 5 mM TMPD in $[C_2mim][TCB]$ recorded on a platinum electrode at 298 K over a potential range of - 0.3 V to 1.2 V vs. Ag and at a scan rate of 10 mV s^{-1}. The oxidation of DmFc (see Equation 5.2 in Chapter 5) occurs at ca. 0.05 V vs. Ag whilst the first and second oxidation of TMPD are at ca. 0.21 V and 0.92 V vs.

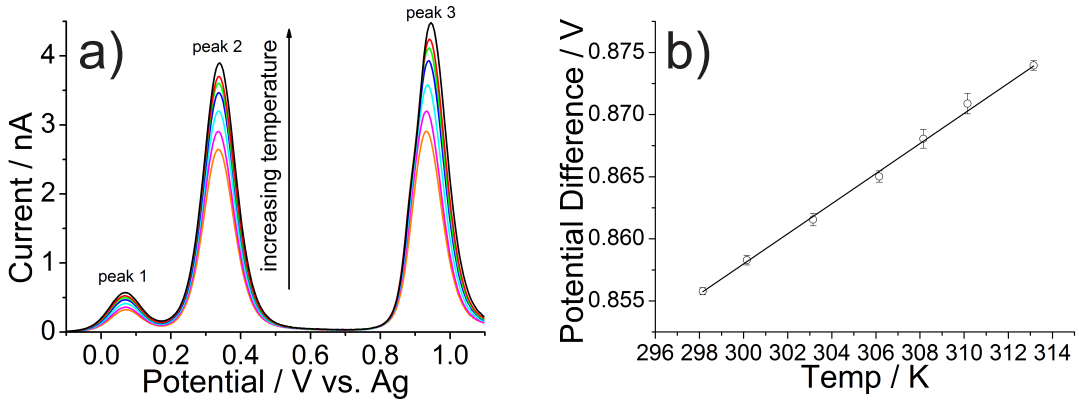

Figure 6.4: a) Square wave voltammetry of the oxidation of decamethyl ferrocene and TMPD over a temperature range of 298 K to 313 K. Peak 1 is due to the oxidation of decamethylferrocene, peak 2 and peak 3 are the first and second oxidation of TMPD respectively. b) Plot of the peak difference of peak 1 and 3 as a function of temperature for the experiment under vacuum.

Ag respectively. Reactions due to TMPD are as follows,

$$DmFc \rightleftharpoons DmFc^{+} + e^{-} \tag{6.9}$$

$$TMPD \rightleftharpoons TMPD^{+} + e^{-} \tag{6.10}$$

$$TMPD^{+} \rightleftharpoons TMPD^{2+} + e^{-} \tag{6.11}$$

Figure 6.4 a) displays square wave voltammetry for 1mM decamethylferrocene and 5 mM TMPD. In order to investigate the interactions between two redox couples, the system containing a single redox couple was voltammetrically compared with the system involving both compounds. The potential difference between the first and second oxidations of TMPD remained unchanged after the addition of decamethylferrocene. Figure 6.4 b) represents the peak difference plotted against the ambient temperature where the peak difference, $\Delta E_{1/3}$, was measured between peaks 1 and peak 3, and the temperature was

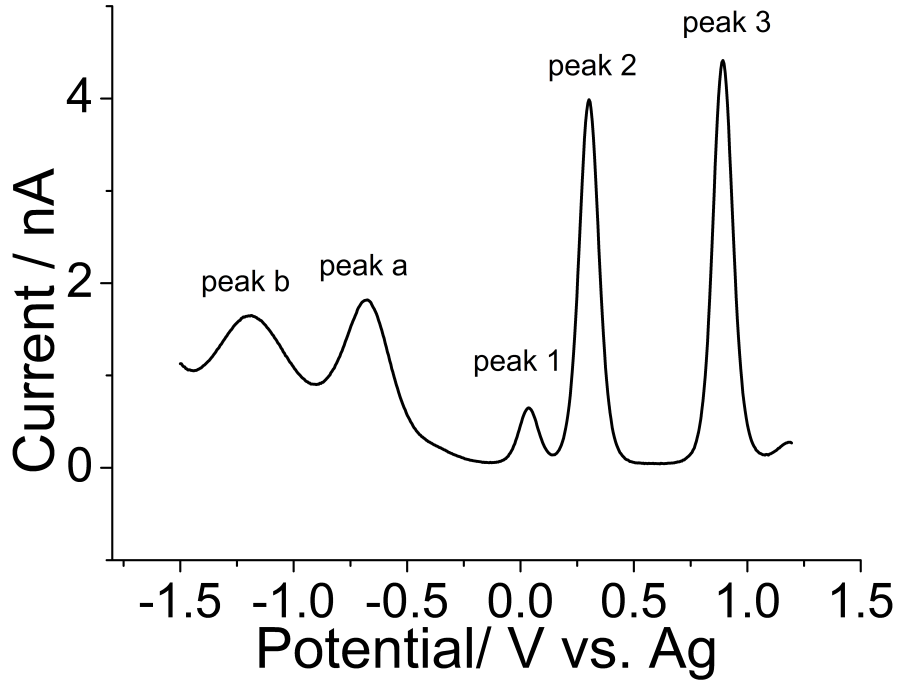

Figure 6.5: Square wave voltammetry for oxygen, decamethylferrocene and TMPD in [C_2mim][TCB] at 298 K. Peaks a and b are due to the first and second electron transfer of oxygen.

read from the thermostat. $\Delta E_{1/3}$ was measured instead of any other peak pairs due to the fact that among the potential difference of all peak pairs, peak difference of peaks 1 and 3 showed the largest change in peak difference versus the temperature change. The graph in Figure 6.4 b) yielded a gradient of 1.225 ± 0.027 mV/K and an intercept of 0.4906 ± 0.0082 V and the temperature can be related to the peak difference by the following equation:

$$\Delta E_{1/3}(V) = 0.4906 + 1.225 \times 10^{-3} T \tag{6.12}$$

6.3.2 Investigation of Oxygen under Pure Oxygen and Dried Air in the Decamethylferrocene-TMPD System

Next chronoamperometric measurements for the detection of oxygen were conducted at different temperatures using the voltammetric thermometer as a probe of the temper-

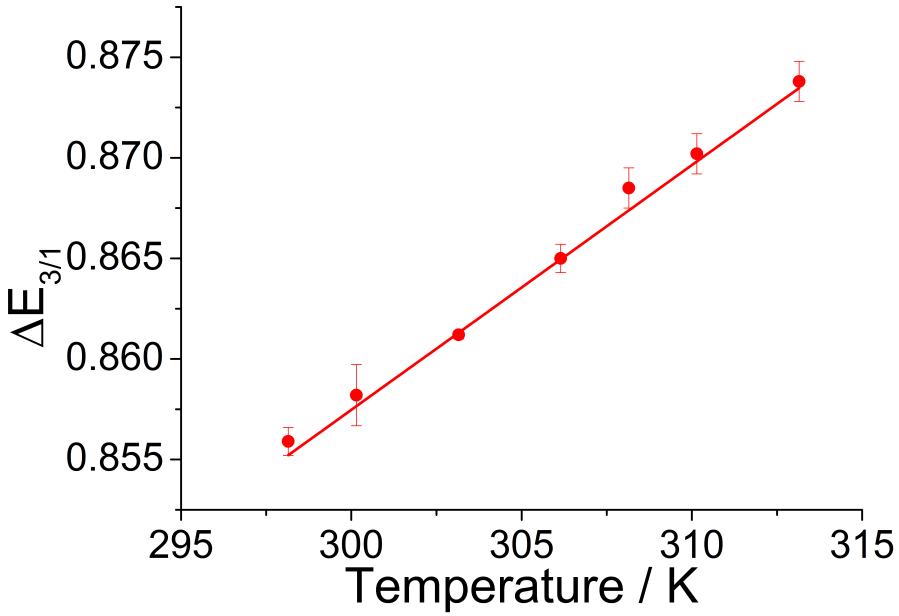

Figure 6.6: Plot of $\Delta E_{1/3}$ against temperature for the experiment in presence of dried pure oxygen.

ature. This experiment thus provides proof-of-concept of using the latter to calibrate amperometric sensors, for example of the Clark cell type. A system composed of decamethylferrocene and TMPD in presence of dried pure oxygen was also studied. It was observed that equilibrium was attained after passing oxygen through for 30 minutes. The decamethylferrocene-TMPD system under the dried oxygen was characterised using square wave voltammetry as shown in Figure 6.5. The first two peaks (a and b) at lower potential correspond to Reactions 6.13 and 6.14 as shown below, whereas the other peaks are defined as Reactions 6.9-6.11.

$$O_2 + e \rightleftharpoons O_2^{\cdot -} \tag{6.13}$$

$$O_2^{\cdot -} + e \rightleftharpoons O_2^{2-} \tag{6.14}$$

Figure 6.6 shows the change of the peak difference, measured between peak 1 and

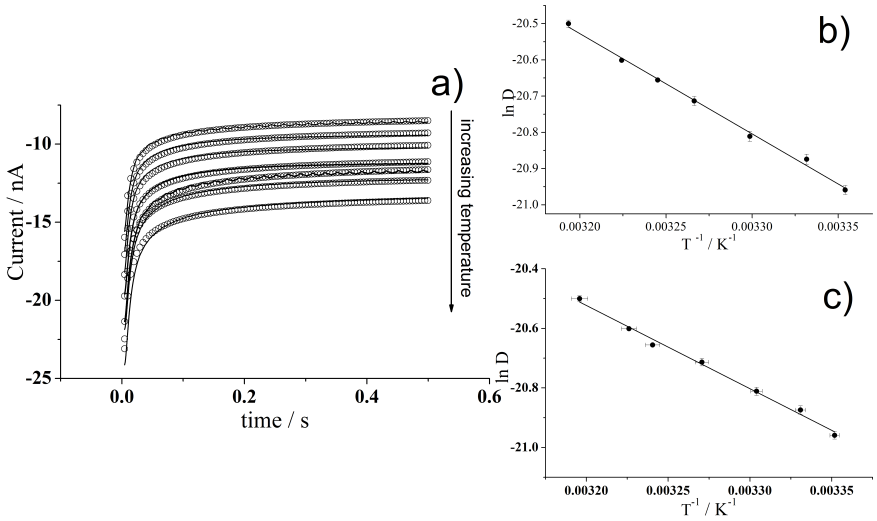

Figure 6.7: a) Experimental (solid line) and simulated (circles) chronoamperometry for the first reduction of pure oxygen in [C_2mim][TCB] over a temperature range of 298 K to 318 K. b) Plot of ln D vs 1/T for oxygen where T is the reading temperature obtained from the ther-mostat cage. c) Plot of ln D vs 1/T for oxygen where T is calculated from equation 6.12.

peak 3, with temperature, yielding a gradient of 1.220 ± 0.029 mV K^{-1} and an intercept of 0.4917 ± 0.0082 V, which is in good agreement with the results for the system in the absence of oxygen. The concentration and diffusion coefficient of oxygen in [C_2mim][TCB] at different temperatures were determined using potential step chronoamperometry which records the change of current as a function of time following a potential step from zero current to transport controlled currents. The current is initially very large due to the large concentration gradient in close vicinity to the electrode surface; then the faradaic current decreases and reaches the steady state due to depletion of the electro-active species near the electrode surface. Figure 6.7 a) shows the experimental and simulated chronoamperometric responses for the one electron reduction of oxygen in [C_2mim][TCB] containing decamethylferrocene and TMPD, where fittings of the experimental chronoamperometry were achieved using the Shoup and Szabo approximation which was imported into a non-linear function in the software package Origin 8.1 (Microcal Software Inc.), where the radius of the electrode of 5.05 μL was fixed (previously calibrated) and the values of con-

centration, c, and diffusion coefficient, D, of oxygen were obtained via constructing the software to iterate through all possible values of c and D. The concentrations of oxygen obtained from the Shoup and Szabo approximation over the temperature range studied are listed as follows: 5.16 mM (298K), 5.19 mM (300 K), 5.11 mM (303 K), 5.27 mM (306 K), 5.16 mM (308 K), 5.22 mM (310 K) and 5.23 mM (313 K). These results remained almost constant with change of temperature which gave an averaged value of 5.19 ± 0.01 mM. It is beneficial to have negligible variation of the solubility of oxygen with ambient temperature over the temperature range studied as the complexity of oxygen detection is largely minimised where the only variable changing with temperature is the diffusion coefficient of oxygen. The relationship of the diffusion coefficient and temperature is described by taking the nature logarithm of the Arrhenius Equation (see Equation 2.5 in Chapter 2),

$$lnD = constant - \frac{E_{a,D}}{RT} \tag{6.15}$$

where D is the diffusion coefficient of oxygen, D_∞ is the hypothetical diffusion coefficient at infinite temperature, $E_{a,D}$ is the diffusional activation energy of oxygen and all other constant are defined as above.

Figure 6.7 b) shows the Arrhenius plots of ln D with 1/T where T is the temperature read from the thermostat. In this plot, a line of best fit shows a high degree of correlation ($R_2 > 0.99$) and gives a gradient of -2760 ± 30 K. Combining this result and the Arrhenius equation (Equation 2.6), the activation energy of diffusion, $E_{a,D}$, of oxygen, 23.0 kJ mol^{-1}, is determined. This value is comparable to the results reported in the literatures, where the values of E_a of oxygen range from 20 kJ mol^{-1} to 35 kJ mol^{-1}, depending on the viscosity and nature of the ionic liquid.26 Temperature was also evaluated via the voltammetric thermometer by substituting the values of $\Delta E_{1/3}$ into Equation 2.5. Figure 6.7 c) displays the plot of ln D against 1/T where T is obtained from the peak difference,

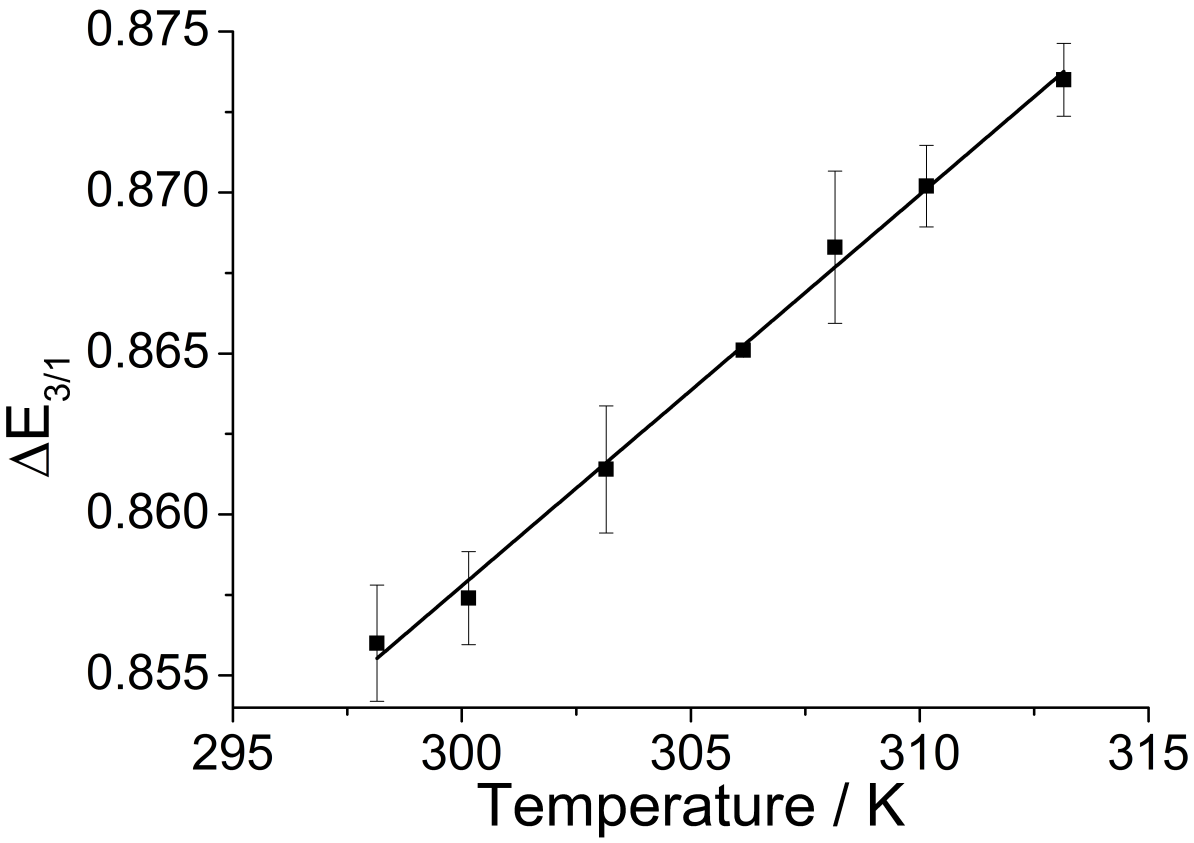

Figure 6.8: Plot of $\Delta E_{1/3}$ against temperature for the experiment in the presence of dried air.

$\Delta E_{1/3}$, yielding a gradient of -2790 ± 40 K (with $R^2 > 0.99$) and $E_{a,D}$ of 23.2 kJ mol^{-1} which is close to the value obtained in Figure 6.8 b). Hence it is concluded that the values of temperature calculated from $\Delta E_{1/3}$ and the voltammetric thermometer is reliable. A similar experiment was repeated under the dried air instead of dried pure oxygen. The system in presence of dried air is characterised using square wave voltammetry which shows a similar response as depicted in Figure 6.5. Peak difference, $\Delta E_{1/3}$, is measured between peak 1 and peak 3. The reliability of representing T by $\Delta E_{1/3}$ is examined by the plot shown in Figure 6.8, which gives a gradient of 1.215 ± 0.035 mV/K and an interception of 0.4923 ± 0.0072 V. This is in good agreement with the previous results (i.e. from Figure 6.4 and 6.6).

The diffusion coefficient and oxygen concentration were investigated using chronoam-

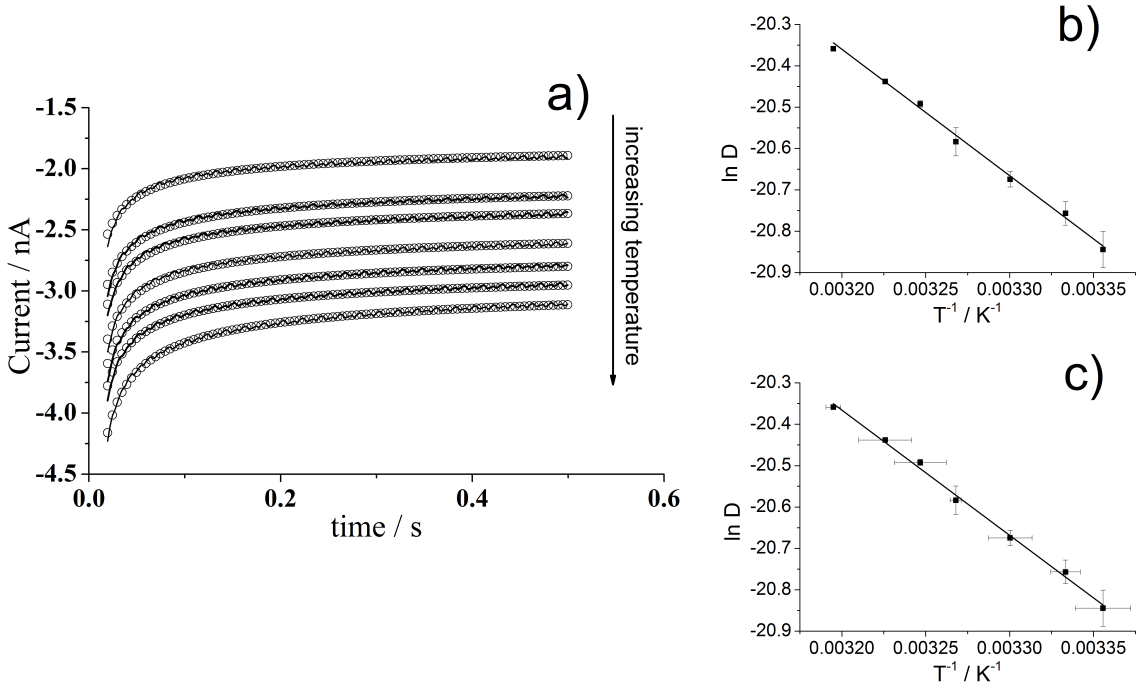

Figure 6.9: a) Experimental (solid line) and simulated (circles) Chronoamperometry for the first reduction of oxygen from the air in [C_2mim][TCB] over a temperature range of 298 K to 318 K. b) Plot of ln D vs 1/T for oxygen where T is the reading values obtained from the thermostat cage. c) Plot of ln D vs 1/T for oxygen where T is obtained from $\Delta E_{1/3}$ conversion.

perometry. Figure 6.9 a) compares the experimental and simulated chronoamperometry in the temperature range of 298 K to 313 K, where the fit between the simulated and experimental chronoamperometry all have a high correlation (R_2 is greater than 0.99). Figure 6.9 b) shows the plot of ln D against 1/T with T read from the thermostat, producing a gradient of 3060 $\pm$ 80 K which leads to a diffusional activation energy of 25.4 kJ mol^{-1}. This slightly higher activation energy of diffusion is probably due to a change in viscosity of [C_2mim][TCB] caused by other gaseous components in the air.[23] Figure 6.9 c) represents the Arrhenius plot of ln D with 1/T where T is obtained from Equation 2.5 by substituting the values of $\Delta E_{1/3}$. The line of best fit gave a gradient of 3050 $\pm$ 60 K, and consequently an activation energy, E_a of 25.3 kJ mol^{-1}.

Figure 6.10 compares the concentration of oxygen obtained from pure oxygen and the

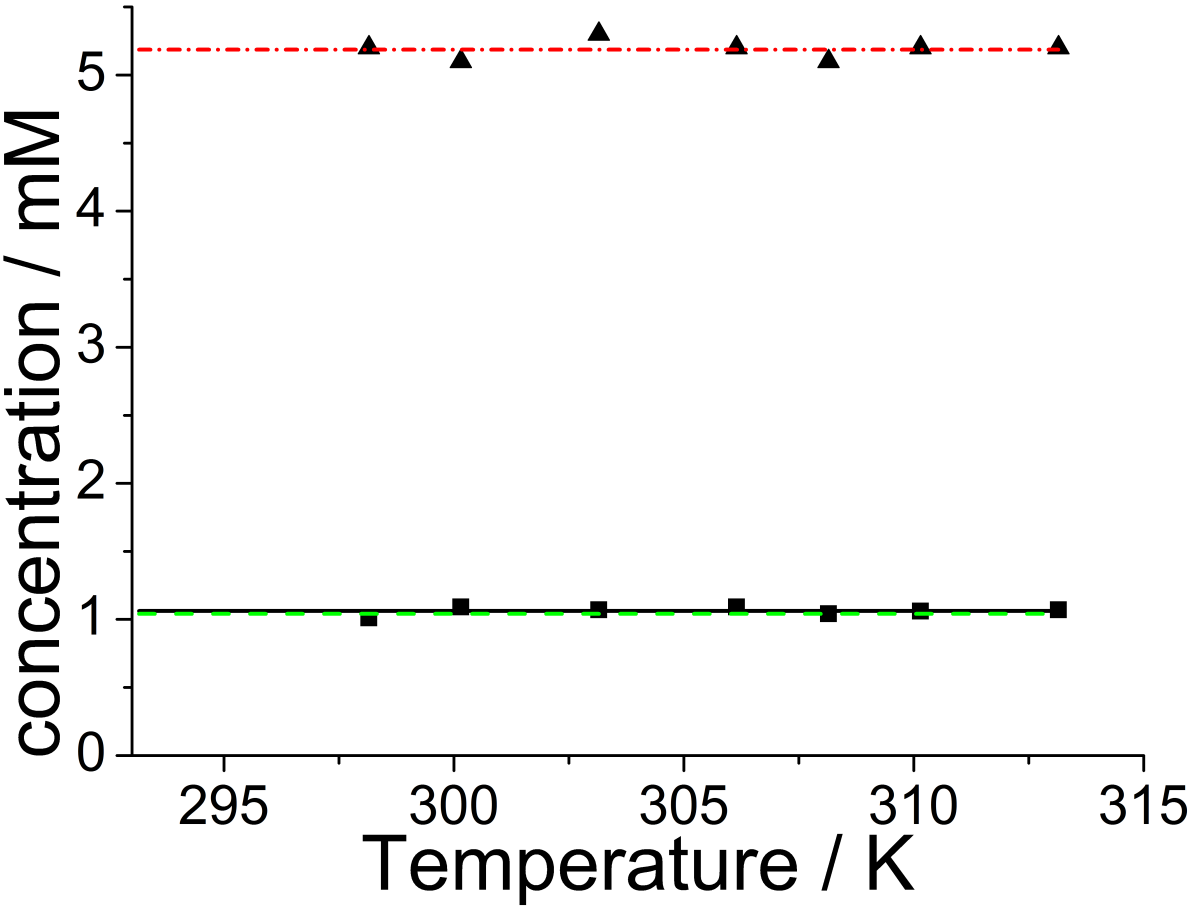

Figure 6.10: Plot of concentration of oxygen against temperature for experiments in pure oxygen (dotted line), in the dried air (solid line) and the theoretically predicted value for the oxygen concentration (dashed line). Triangles and squares are the experimental values obtained from Shoup and Szabo fittings.

dried air. It is known that dried air contains 21 % (by mole fraction)[24, 25] of oxygen and therefore an estimation of 79 % reduction in the oxygen concentration is expected. It was experimentally determined that there is 5.19 mM oxygen in [C_2mim][TCB] under pure oxygen and this dropped to 1.06 mM under the dried air, which is very close to the theoretical value predicted by the mole fraction of oxygen in air, 1.08 mM.

6.4 Conclusions

Through square wave voltammetric analysis of bisferrocene and decamethylferrocene-TMPD systems, this work has demonstrated the variation of difference in the peak po-

tentials for two redox centres with temperature, which showed temperature coefficients of 0.20 mV K^{-1} and 1.20 mV K^{-1} respectively. This temperature sensing system has been incorporated into a model oxygen sensor via investigating the latter system in the presence of oxygen either as pure oxygen or in dried air. It has been observed that the solubility of oxygen does not vary with temperature over the temperature range studied and c.a. 79 % reduction of oxygen concentration from pure oxygen to dried air is in close agreement with the oxygen composition in air. Diffusion coefficient of oxygen has been studied as a function of temperature via an Arrhenius plot, which can be further related to the peak difference discussed previously. All experiments have presented high reproducibility and a correlation of more than 0.99 has indicated a high sensitivity towards sensing temperature. Further to this design, the next chapter shows a simultaneous humidity and temperature sensor.

References

[1] Xiong, L.; Fletcher, A. M.; Ernst, S.; Davies, S. G.; Compton, R. G. *The Analyst* **2012**, *137*, 2567–2573.

[2] Hanrahan, G.; Patil, D.; Wang, J. *Journal of Environmental Monitoring* **2004**, *6*, 657–664.

[3] Wang, J. *Analytical Electrochemistry*; Wiley-VCH, New York, 1994.

[4] Metters, J.; Kadara, R.; Banks, C. *Analyst* **2011**, *136*, 1067–1076.

[5] Heller, A.; Feldman, B. *Chemical Reviews* **2008**, *108*, 2482–2505.

[6] Clark Jr., L. C.; Lyons, C. *Annals of the New York Academy of Sciences* **1962**, *102*, 29–45.

[7] Clark Jr., L. C. *Transactions - American Society for Artificial Internal Organs* **1956**, *2*, 41–48.

[8] Tierney, M. J.; Kim, H.-O. L. *Analytical Chemistry* **1993**, *65*, 3435–3440.

[9] Horn, J. J.; McCreedy, T.; Wadhawan, J. *Analytical Methods* **2010**, *2*, 1346–1354.

[10] Compton, R. G.; Northing, R. J. *Journal of the Chemical Society, Faraday Transactions* **1990**, *86*, 1077–1081.

[11] Nei, L.; Compton, R. G. *Sensors and Actuators, B: Chemical* **1996**, *30*, 83–87.

[12] Lawrence, N. S.; Jiang, L.; Jones, T. G. J.; Compton, R. G. *Analytical Chemistry* **2003**, *75*, 2499–2503.

[13] Chevallier, F. G.; Davies, T. J.; Klymenko, O. V.; Jiang, L.; Jones, T. G. J.; Compton, R. G. *Journal of Electroanalytical Chemistry* **2005**, *577*, 211–221.

[14] Buzzeo, M. C.; Evans, R. G.; Compton, R. G. *ChemPhysChem* **2004**, *5*, 1106–1120.

[15] Paddon, C. A.; Silvester, D. S.; Bhatti, F. L.; Donohoe, T. J.; Compton, R. G. *Electroanalysis* **2007**, *19*, 11–22.

[16] Xiong, L.; Aldous, L.; Henstridge, M. C.; Compton, R. G. *Analytical Methods* **2012**, *4*, 371–376.

[17] Klymenko, O. V.; Evans, R. G.; Hardacre, C.; Svir, I. B.; Compton, R. G. *Journal of Electroanalytical Chemistry* **2004**, *571*, 211–221.

[18] Rogers, E. I.; Silvester, D. S.; Poole, D. L.; Aldous, L.; Hardacre, C.; Compton, R. G. *Journal of Physical Chemistry C* **2008**, *112*, 2729–2735.

[19] Bott, A. W. *Current Separations* **1995**, *14*, 64–68.

[20] Compton, R. G.; Banks, C. E. *Understanding Voltammetry*; Imperial College Press, 2011, 2nd Edition.

[21] Bard, A. J.; Faulkner, L. R. *Electrochemical Methods: Fundamentals and Applications*; Wiley, 2001.

[22] Brett, C. M. A.; Brett, A. M. O. *Electrochemistry: Principles, Methods, and Applications*; Oxford Science Publications; Oxford University Press, Incorporated, 1993.

[23] Barrosse-Antle, L. E.; Aldous, L.; Hardacre, C.; Bond, A. M.; Compton, R. G. *Journal of Physical Chemistry C* **2009**, *113*, 7750–7754.

[24] Jacob, D. *Introduction to Atmospheric Chemistry*; Princeton University Press, 1999.

[25] Levine, I. N. *Physical Chemistry (Sie)*; McGraw-Hill Education (India) Pvt Limited, 2007.

Chapter 7

A simultaneous voltammetric temperature and humidity sensor

This chapter reports the simultaneous measurement of temperature and humidity by analysing the square wave voltammetric responses of two ferrocene derivatives, DmFc and BisFc in 1-(2-methoxyethyl)-1-methyl-pyrrolidinium tris(pentafluoroethyl)trifluorophosphate ([Moepyrr][FAP]). These two molecules produce three peaks in square wave voltammetry. Through study of the peak potentials of BisFc/BisFc$^+$ (vs. DmFc/DmFc$^+$) and BisFc$^+$/BisFc^{2+} (vs. DmFc/DmFc$^+$) over a temperature range of 298 K to 318 K and humidity range of 1 % to 50 % using square wave voltammetry, the temperature and humidity dependences of the relative peak potentials were investigated. A reliable method to calculate the humidity and temperature based on the voltammetric experiment is characterised and demonstrated. The work presented here has been published in the *Analyst*.[1]

7.1 Introduction

Chapter 6 demonstrated how temperature changes influence the sensing system and proposed an in situ voltammetric thermometer to accurately calibrate the local temperature at the electrode. Apart from the impact of temperature on the sensing system, the sensitivity and accuracy of electrochemical sensors may also be affected by humidity due to the nature of electron transfer and mass transport. Changes of the temperature or humidity

in the surroundings are important to monitor not only in their own right but also because they can indirectly influence the measurement of other properties including the quantification of chemical species. One approach to this problem is to build independent sensors to monitor the temperature and humidity into other analytical probes. The benefits of this approach are expected to be high in the area of gas sensing.

In this chapter, we propose a method to direct detect temperature and humidity at the electrode solution interface, providing electrochemical temperature and humidity sensing in their own right or, more likely, a sensing approach for immediate integration with other voltammetric sensing. This proposed sensor is voltammetrically based and measures the temperature and humidity via formal potentials. The formal potential dependence on temperature is related to the entropy change of the redox process in an electrochemical reaction,[2] and a temperature sensor has been developed according to this principle.[3] Building on our success in monitoring temperature using differences in formal potentials of two redox couples, we now develop this method in the current work to simultaneously measure the two quantities, temperature and humidity. This requires two independent formal potential measurements to be made. Furthermore, to simplify ease of measurement, efforts are made to select species such that the temperature dependent pair is humidity independent and vice versa. Chapter 5 has shown that change in solvation leads to changes in the formal potential,[4] in part under using DmFc and BisFc in a room temperature ionic liquid (RTIL). RTILs are purely composed of ions and exists as a liquid around room temperature; their benefits in electrochemistry have been frequently disscussed. Literature studies also demonstrate the influence of solvent humidity on solvation properties.[5, 6]

1-(2-Methoxyethyl)-1-methyl-pyrrolidinium tris(pentafluoroethyl)trifluorophosphate, is a highly viscous RTIL, and its conductivity and viscosity change dramatically with the humidity.[4] This is explored utilised in the work described below.

7.2 Experimental Methods

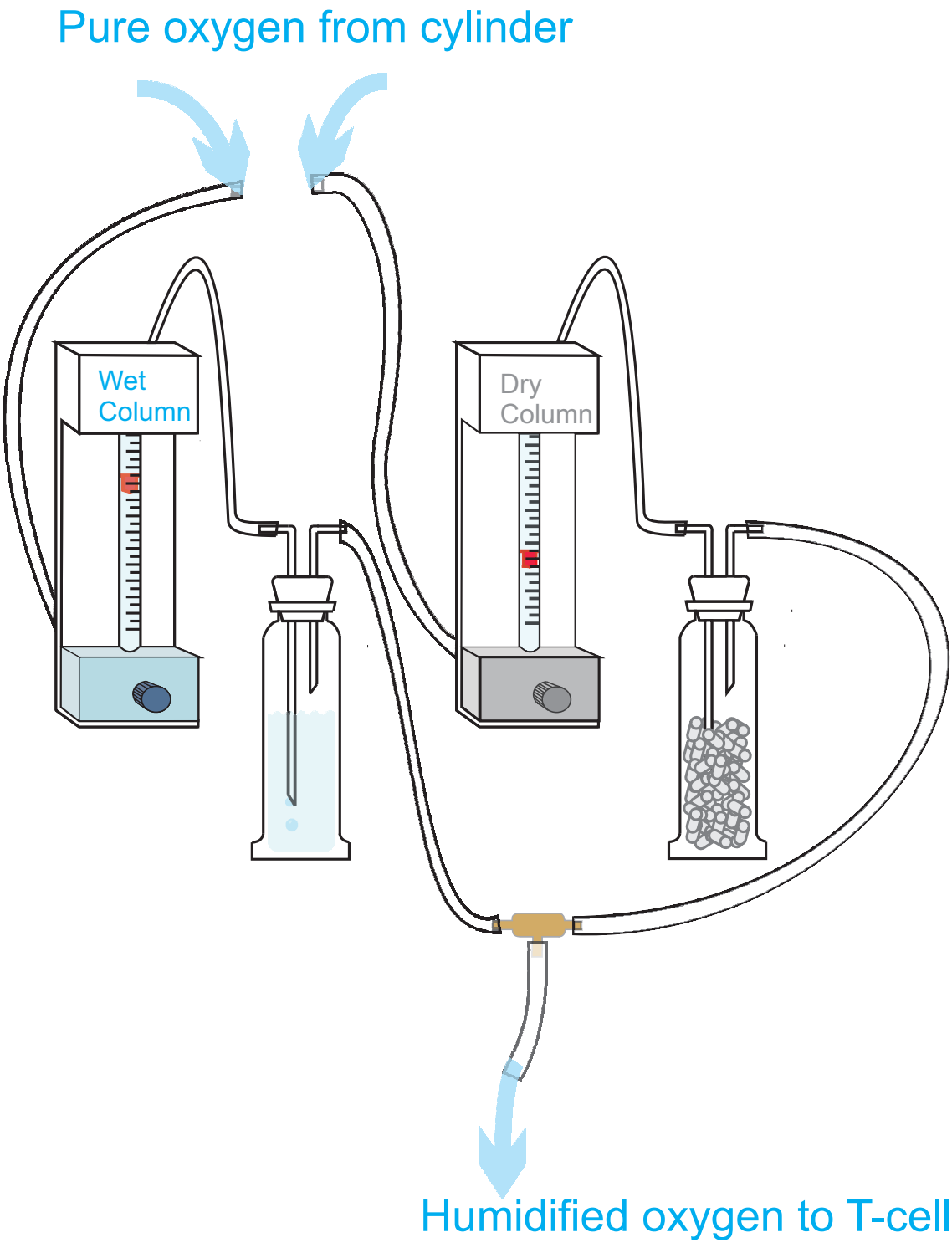

Figure 7.1: Scheme showing the gas line connections

The humidified air was realised via the following method: the inlet line of the gas is divided into two lines, with one connected to a drying column and another to a Dreschel

bottle which is filled with deionised water. These two lines then emerge into a common outlet line, which allows the gas to flow into the T-cell. The humidity is controlled by the flow meters in the dry and wet line respectively. The line connection is shown in Figure 7.1. The drying column consists of concentrated silica and solid calcium chloride. Before the electrochemical measurements, gas was run for at least 15 hours to ensure equilibrium was established. For experiments excluding gases, the ionic liquid was constantly purged under vacuum during experimental analysis. The values of humidity were recorded using an ADC-16 pico-logger (Honeywell, UK). The relative humidity, $RH\%$, is described using the equation below,[7]

$$RH(\%) = \frac{e_w}{e_w^*} \times 100 \tag{7.1}$$

where e_w is the partial pressure of water vapour (H_2O) in the mixture and e_w^* is the saturated vapour pressure of water at a prescribed temperature. The variation of humidity during an experiment was no more than 1 % RH. All experiments were repeated at least three times and the variation of all results (i.e. peak potential) for the same experiment was less than 3 mV which was calculated using standard deviations from at least three sets of experiments under the same experimental conditions.

7.3 Results and Discussion

7.3.1 Choice of Probes for Temperature and Humidity Measurements

In this paper, we study the following oxidative redox reactions in different ionic liquids.

$$DmFc \rightleftharpoons DmFc^+ + e \tag{7.2}$$

$$Cp-Fe-C_5H_4-(CH=CH)-H_4C_5-Fe-Cp \rightleftharpoons Cp-Fe^+-C_5H_4-(CH=CH)-H_4C_5-Fe-Cp+e \tag{7.3}$$

$$Cp-Fe^+-C_5H_4-(CH=CH)-H_4C_5-Fe-Cp \rightleftharpoons Cp-Fe^+-C_5H_4-(CH=CH)-H_4C_5-Fe^+-Cp+e \tag{7.4}$$

$$Fc \rightleftharpoons Fc^+ + e \tag{7.5}$$

where Fc is ferrocene, DmFc is DmFc and each redox reaction is associated with a formal potential $E_{f,1}$, $E_{f,2}$, $E_{f,3}$ and $E_{f,4}$ respectively. See also Figure 5.2 for structures. The following differences in formal potential are investigated adopting the notations given,

$$\Delta E_{1/2} = E_{f,2} - E_{f,1} \tag{7.6}$$

$$\Delta E_{1/3} = E_{f,3} - E_{f,1} \tag{7.7}$$

$$\Delta E_{2/3} = E_{f,3} - E_{f,2} \tag{7.8}$$

$$\Delta E_{1/4} = E_{f,4} - E_{f,1} \tag{7.9}$$

In the experiments to be reported, the peak potential difference of two redox centres is measured to avoid the need for a stable reference electrode[3] and hence the choice of redox probes is critical. DmFc shows many interesting electrochemical properties as compared to other ferrocene derivatives, one of which as being relative insensitive to solute composition makes it a very useful redox standard,[8] especially in the present humidity study. On the other hand, previous work indicates that the first and second oxidation potential of BisFc can be tuned by varying the anion component of ionic liquid.[4] As the change in humidity alters the composition of ionic liquid the peak potential differences of BisFc and DmFc may allow us to measure the humidity of air. These systems were accordingly

investigated in 1-2-methoxyethyl)-1-methyl-pyrrolidinium tris(penta-fluoroethyl)trifluorophosphate ([Moepyrr][FAP], see Figure 7.2) not only due to its very low melting point (223 K), high decomposition temperature (523 K) and negligible volatility which ensure that this system works over a large temperature and pressure range, but also because this ionic liquid is highly viscous and any additional water may dramatically change its physical properties and hence associated formal potentials.[9, 10] The volatility of DmFc and BisFc in [Moepyrr][FAP] under vacuum was tested using steady state voltammetry where only a slight reduction in the concentration was seen (no more than 5 %) in steady state current over a period of 20 hours. This shows that both DmFc and BisFc have a negligible volatility in the RTIL, in contrast to ferrocene.[11, 12]

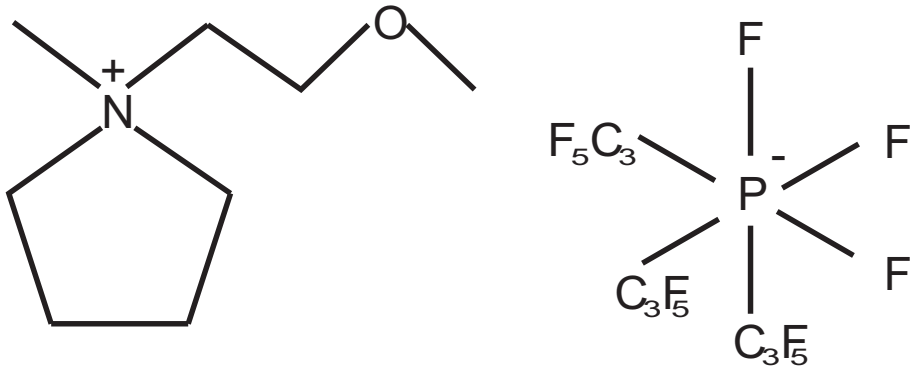

Figure 7.2: Structure of 1-(2-methoxyethyl)-1-methyl-pyrrolidinium tris(pentafluoroethyl)trifluorophosphate ([Moepyrr][FAP]).

1 mM DmFc and 1 mM BisFc in [Moepyrr][FAP] were then examined at different temperatures (in the range of 298 K to 318 K) under vacuum using square wave voltammetry at a potential range of -0.1 V to 1.0 V vs. Ag, where the redox reactions correspond to reaction 7.2 to 7.4. The formal potentials of redox couples were readily evaluated using square wave voltammetry (SWV) as this records the current difference in the oxidative and reductive direction as a function of staircase potential.[13–15] The peak potential in the square wave voltammetry is close to the formal potential of the redox couple studied.[16] The experimental conditions for SWV were optimised for maximum current

using a frequency of 50 Hz, a step potential of 0.1 mV and amplitude of 25 mV.

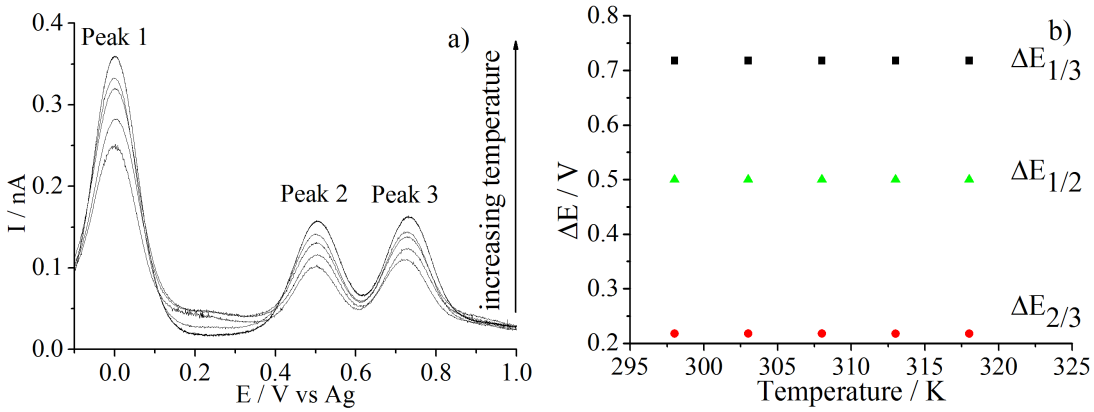

Figure 7.3: a) Square wave voltammetric responses for 1 mM DmFc and 1 mM BisFc in [Moepyrr][FAP] at a frequency of 50 Hz, a step potential of 0.1 mV, amplitude of 25 mV and over a temperature range of 298 - 318 K, b) From top to bottom: the corresponding plots of the peak difference of peaks 1 and 3, $\Delta E_{1/3}$, peaks 1 and 2, $\Delta E_{1/2}$ and peaks 2 and 3 $\Delta E_{2/3}$ against temperature.

Figure 7.3 a) shows the square wave voltammetric responses for the oxidation of 1.0 mM DmFc and 1.0 mM BisFc in [Moepyrr][FAP] over a temperature range of 298-318 K. The increase in the peak current with temperature is due to the fact that the diffusion is faster at higher temperature owing to the reduced solvent viscosity. The peaks in Figure 7.3 a) from negative to positive potential (marked with peaks 1, 2 and 3) are due to the reactions 1 to 3, respectively. The plots of $\Delta E_{1/3}$, $\Delta E_{2/3}$ and $\Delta E_{1/2}$ against temperature are depicted in Figure 7.3 b). It can be seen from these plots that the peak differences remain almost unchanged with the varying temperatures. This 'thermal insensitive' observation reflects that for a fast electron transfer reversible process, the temperature dependence of these two formal potentials is related to the entropy change associated with the electrochemical process via Equation 6.3

where E_f is the formal potential, T is the temperature, S is the entropy and F is the Faraday constant. The peak potential difference varies with temperature only if the tem-

Temperature / K	$\Delta E_{1/4}$ / V	
	(in [Moepyrr][FAP])	(in [C_2mim][TCB])
298	0.5737	0.5342
303	0.5737	0.5342
313	0.5736	0.5342

Table 7.1: Peak potential differences for DmFc and ferrocene in [Moepyrr][FAP] and [C_2mim][TCB] at 298 K, 303 K and 313 K. $\Delta E_{1/4}$ is defined as the difference between the redox potentials of DmFc and ferrocene, corresponding to Reactions 7.2 and 7.5.

perature dependence of the two formal potentials of two redox centres is different. There are basic structural similarities between decamethylferrocenium and the singly charged bisferrocenium (where the charge is located in one redox center of the bisferrocenium), as well as their unoxidised forms, which leads to the observed temperature independent peak difference ($\Delta E_{1/2}$). This is consistent with the observations in the square wave voltammetry for the oxidation of DmFc (Reaction 7.2) and ferrocene (Reaction 7.5) in [Moepyrr][FAP] and [C_2mim][TCB] over the temperature range reported. The results in the peak potential differences are shown in Table 7.1 which shows that the peak potential difference for the structurally similar DmFc and ferrocene is essentially temperature independent.

Temperature / K	$\Delta E_{2/3}$ / V		
	(in [Moepyrr][FAP])	(in [C_3mim][NTf2])	(in [C_2mim][TCB])
298	0.2202	0.2043	0.2077
303	0.2202	0.2052	0.2089
313	0.2202	0.2077	0.2110

Table 7.2: Peak potential differences for the first and second oxidation of BisFc in [Moepyrr][FAP] and [C_2mim][TCB] at 298, 303 and 313 K. $\Delta E_{2/3}$ is defined as the difference between the first and second oxidation potentials of BisFc (see Figures c) and d) in Chapter 5).

It is seen that $\Delta E_{1/3}$ and $\Delta E_{2/3}$ are both 'insensitive to temperature change. To investigate these observations further similar experiments were performed with BisFc in a range of ionic liquids. Table 7.2 shows the peak potential differences for the first and

second oxidation of BisFc in $[C_3mim][NTf_2]$, $[C_2mim][TCB]$ and [Moepyrr][FAP] over the temperature range of 298 - 313 K. It can be seen that all the peak differences increase with the temperature apart from in [Moepyrr][FAP]. Work by Barrosse-Antle et al. suggests that many dissolved gases, including N_2 the main component in air, may increase the diffusion coefficient of solutes in ionic liquids.[16] This observation implies that DmFc and BisFc in [Moepyrr][FAP] in air may show different temperature dependence of peak potential difference as compared to the experiments under vacuum. Further investigation was therefore carried out in dried air. Before conducting experiments, the system was purged into air for more than 15 hours in order to equilibrate the humidity between the ionic liquid and air.

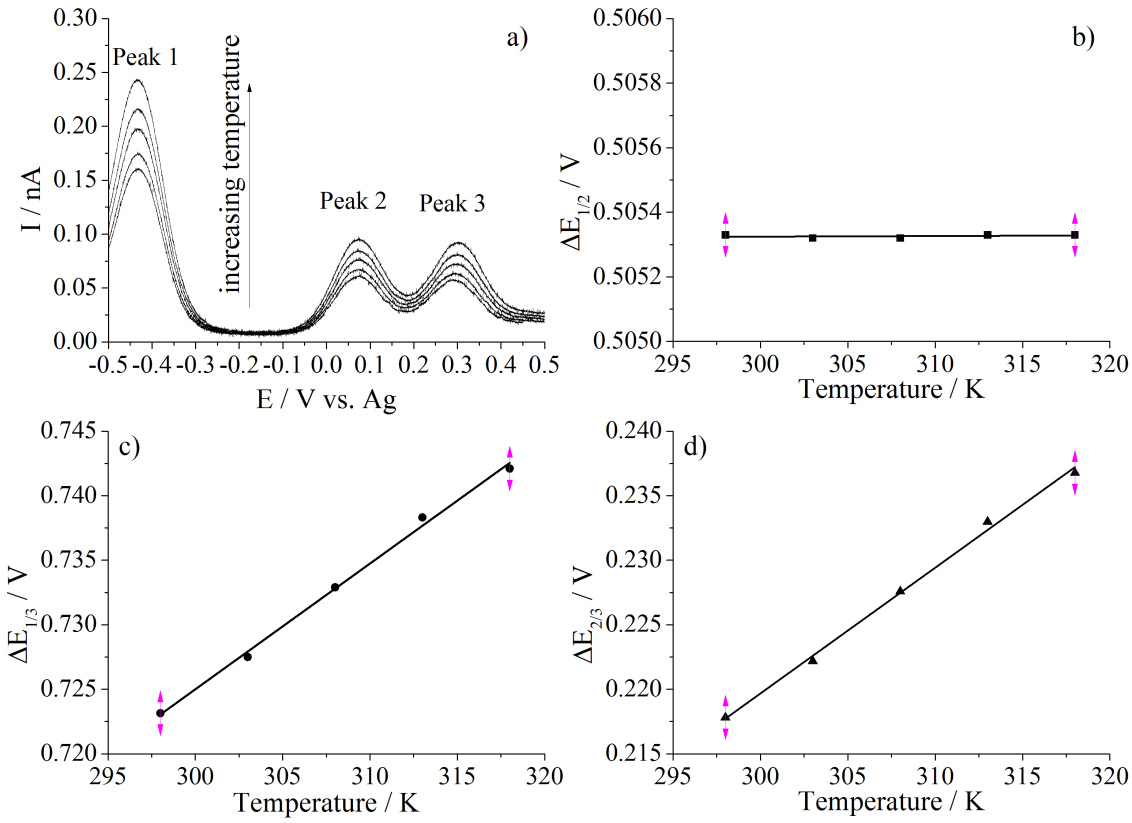

Figure 7.4: a) Square wave voltammetry for the oxidation of DmFc and BisFc in [Moepyrr][FAP] in the dried air (RH = 1 %) b)-d) the plots of the peak difference of peaks 1 and 2, $\Delta E_{1/2}$, peaks 1 and 3, $\Delta E_{1/3}$ and peaks 2 and 3, $\Delta E_{2/3}$ against temperature respectively.

Figure 7.4 a) shows the square wave voltammetry for the oxidation of DmFc (peak 1) and BisFc (peaks 2 and 3) in [Moepyrr][FAP] under dried air (RH = 1 %). The corresponding plot of peak potential difference against temperature, between peaks 1 and 2, $\Delta E_{1/2}$, is displayed in Figure 7.4 b). It is again observed that $\Delta E_{1/2}$ is insensitive to temperature change, where the equation for the line of best fit is given as below,

$$\Delta E_{1/2}(V) = 0.5053 + 2 \times 10^{-7} T \tag{7.10}$$

where, T is the temperature in K. Figure 7.4 c) depicts the peak potential difference $\Delta E_{1/3}$, measured between peak 1 and peak 3, as a function of temperature where a linear increase with temperature is seen. This temperature dependent peak potential difference can be described by the following equation,

$$\Delta E_{1/3}(V) = 0.4327 + 0.9744 \times 10^{-3} T \tag{7.11}$$

A similar observation is made with the temperature relationship of peak potential difference between peak 2 and peak 3, of $\Delta E_{2/3}$, which is shown in Figure 7.4 d). This linear relation is given below,

$$\Delta E_{2/3}(V) = -0.0726 + 0.9742 \times 10^{-3} T \tag{7.12}$$

Since $\Delta E_{1/3}$ has better defined peak to peak separations at each temperature, this term is used to measure temperature below.

7.3.2 Temperature and humidity calibration using DmFc and BisFc

Next we investigated the humidity effects as the temperature dependences of $\Delta E_{1/2}$ and $\Delta E_{1/3}$. The humidifier and its calibration were described in the experimental section. The humidity was controlled by carefully adjusting the wet and dry air flow rates. Before electrochemical analysis, humidified air was passed through the analytes for more than 15 hours to ensure that the humidity of the system has fully equilibrated. This was monitored by successive cyclic voltammetric scans for DmFc and BisFc in [Moepyrr][FAP] at a platinum micro electrode (a scan rate of 10 mV s^{-1} and an interval of 1 hour between scans) overnight. The variation in steady state current at different scans indicated whether the equilibrium has been reached. It was observed that the current in cyclic voltammetry reached a steady value after ca. 15 hours. The oxidation of DmFc and BisFc at different humidities was characterised using square wave voltammetry.

RH (%)	intercept (V)	gradient (mV)
1	0.6981	0.9744
12	0.7101	0.91313
25	0.70298	0.93313
35	0.7011	0.9090
50	0.7013	0.9196

Table 7.3: Gradients and intercepts of plots of $\Delta E_{1/3}$ vs. temperature at different RH. $\Delta E_{1/3}$ is the peak potential difference of the oxidation of DmFc and second oxidation of BisFc in [Moepyrr][FAP].

Figure 7.5 a) depicts the plot of $\Delta E_{1/2}$ vs. temperature over the RH range of 1 % to 50 %, where $\Delta E_{1/2}$ is independent of temperature over the temperature and humidity range studied (i.e. T = 298 - 318 K and RH = 1 % - 50 %). It can be seen that $\Delta E_{1/2}$ changes with humidity but not with temperature at a fixed humidity. Figure 7.5 b) shows $\Delta E_{1/3}$ as a function of temperature over the same humidity range. It can be seen that $\Delta E_{1/3}$

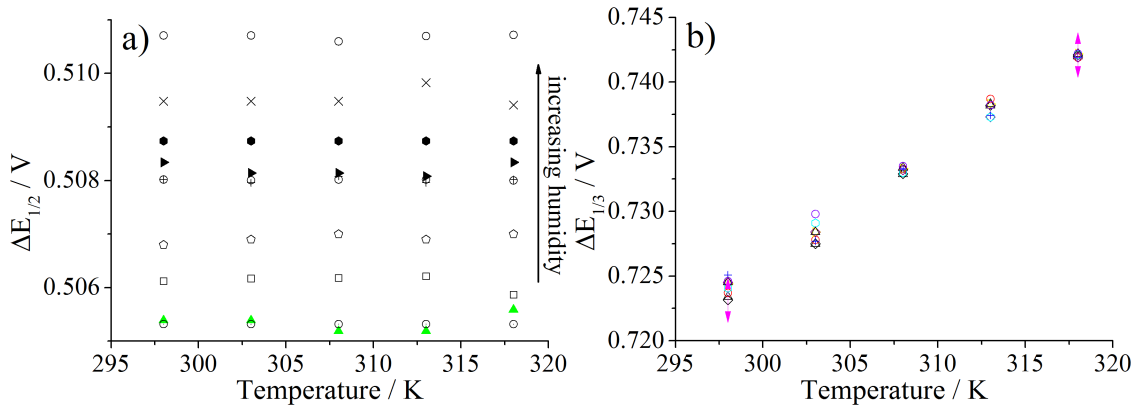

Figure 7.5: a) The plots of $\Delta E_{1/2}$ as a function of temperature over the RH range of 1 % to 50 %. b) The plots of $\Delta E_{1/3}$ as a function of temperature over the RH range of 1 % to 50 %.

in the humidity range studied is linearly dependent on temperature. Table 7.3 shows the temperature dependence of $\Delta E_{1/3}$ for five representative values of relative humidity. It is observed that the temperature dependency varies only slightly for different humidities. These slight variations observed are predominately due to the influence of different levels of moisture on the formal potentials of the BisFc/ $BisFc^+$ couples.

Figure 7.6 shows the square wave voltammetry for DmFc and BisFc over a range of humidity at 298 K, where the potential axis has been shifted to show the potential relative to the DmFc/$DmFc^+$ peak potential. The first oxidation and second oxidation of BisFc are enlarged and are shown in the inlays of Figure 7.6. A clear increase in the peak potential of BisFc/$BisFc^+$ couple with humidity is observed whereas the potential change for $BisFc^+$/$BisFc^{2+}$ with humidity is less significant.

Figure 7.7 shows the plot of $\Delta E_{1/2}$ vs. RH where the former is the average at a fixed temperature and error bars are assigned using standard deviation methods for each set of data. It shows that $\Delta E_{1/2}$ increases with RH (over a temperature range of 298 K to 318

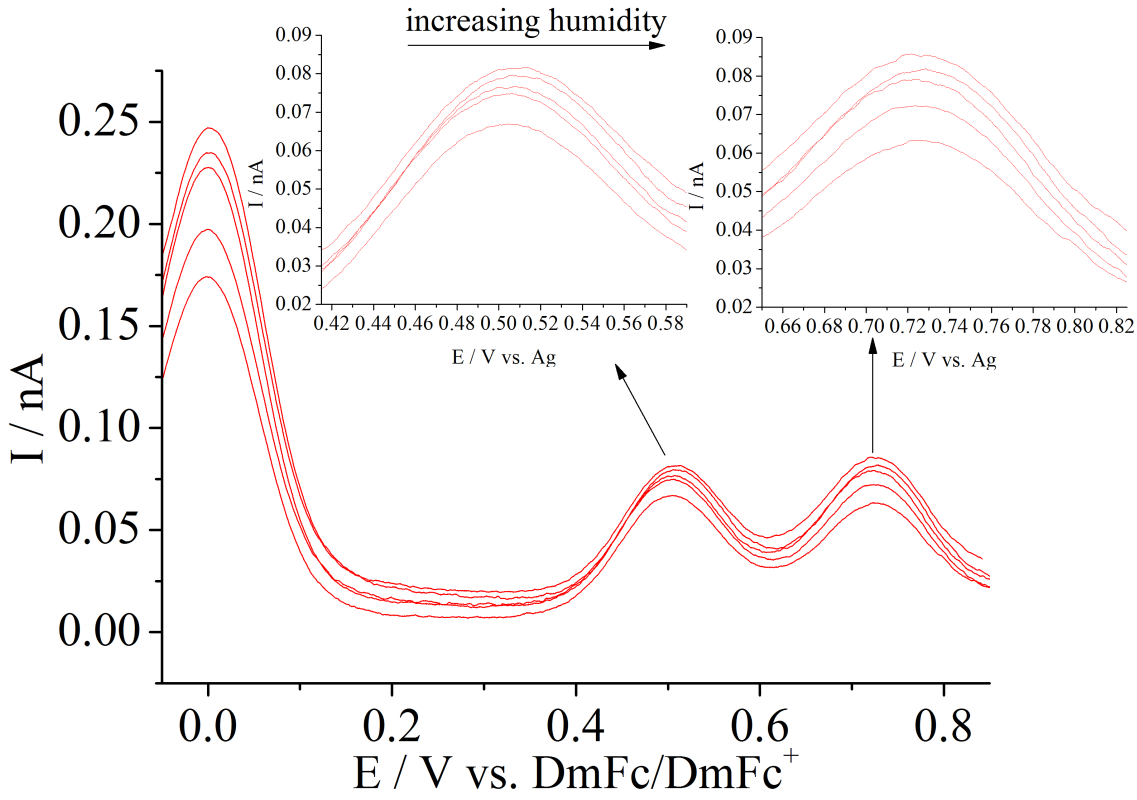

Figure 7.6: Square wave voltammetric responses for DmFc and BisFc in [Moepyrr][FAP] at RH of 1 %, 12 %, 28 %, 35 % and 50 % and temperature was fixed at 298K. The potential is measured relative to the peak potential for DmFc/DmFc$^+$. Inlays: The enlargements of the first (left) and second oxidation (right) of BisFc.

K) in a second order polynomial manner and the relation is described below,

$$\Delta E_{1/2} = 0.505 + 8.181 \times 10^{-5} RH + 5.997 \times 10^{-7} RH^2 \tag{7.13}$$

Figure 7.8 depicts the plots of $\Delta E_{1/3}$ versus RH at 298, 303, 308, 313 and 318 K. From this figure, it is seen that $\Delta E_{1/3}$ slightly increases with RH at 298 K and the difference between the maximum and minimum values is approximately 1.5 mV while at 303 K, this difference reduces to 0.9 mV. For temperature at and above 308 K, $\Delta E_{1/3}$ is almost independent of temperature.

The average value of $\Delta E_{1/3}$ is plotted against temperature in Figure 7.9. The bars in

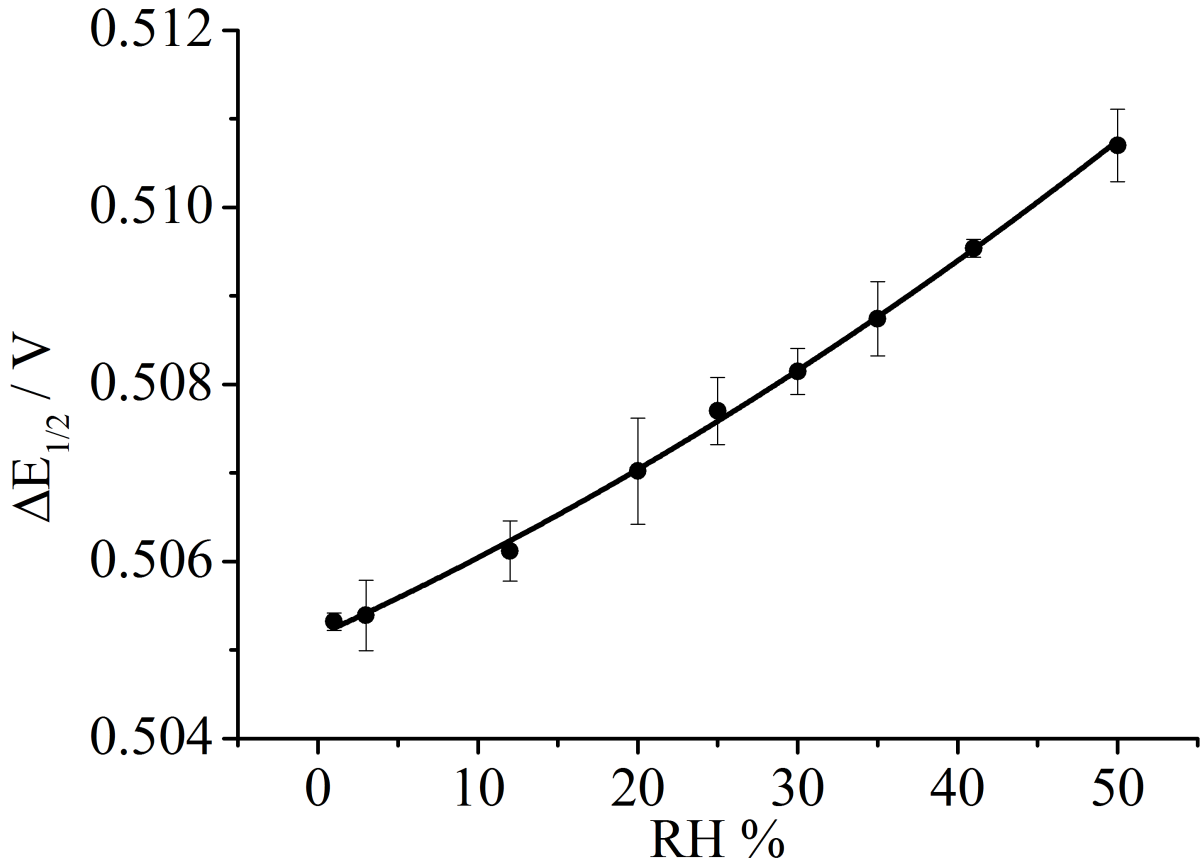

Figure 7.7: Dependence of $\Delta E_{1/2}$ on the value of RH.

the figure represent the uncertainty at each temperature.

$$\Delta E_{1/3}(V) = 0.31844 + 0.9181 \times 10^{-3} T \tag{7.14}$$

7.3.3 Simultaneous Determination of Temperature and Humidity

Figure 7.10 illustrates the proposed method for determining precise values of humidity and temperature simultaneously. First, $\Delta E_{1/3}$ can be read from square wave voltammetry and the temperature value can be roughly estimated by substituting the $\Delta E_{1/3}$ into Equation 7.14. For example, an uncertainty of 3 K is expected for temperature around

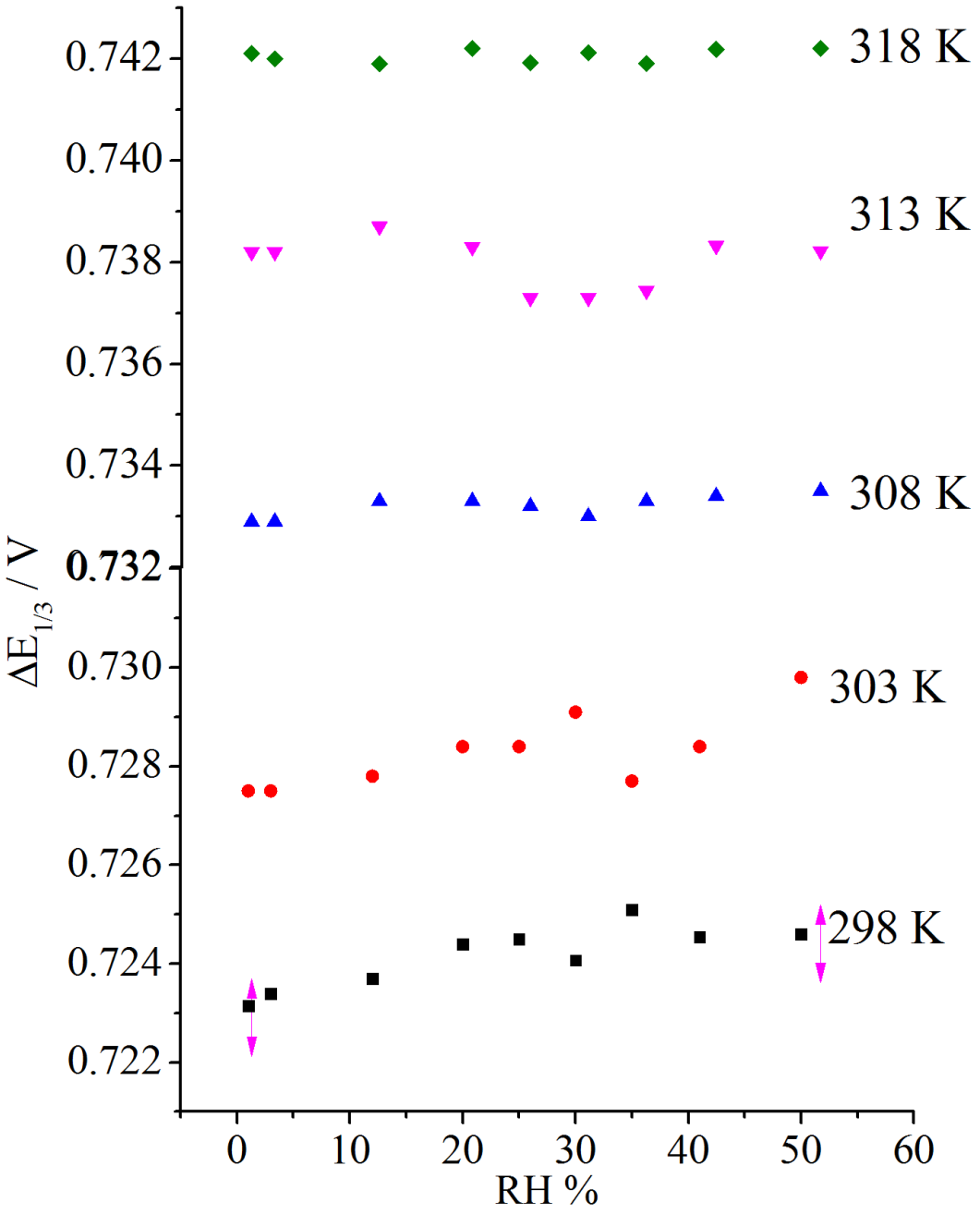

Figure 7.8: Dependence of $\Delta E_{1/3}$ on RH at 298 K, 303 K, 308 K, 313 K an 318 K.

298 K. Then the relative humidity can be estimated using $\Delta E_{1/2}$, the peak potential difference of peaks 1 and 2, and Equation 7.13 and an approximation of $\pm$ 2 % RH at each humidity value should be taken into account. Next, it is known that at a fixed

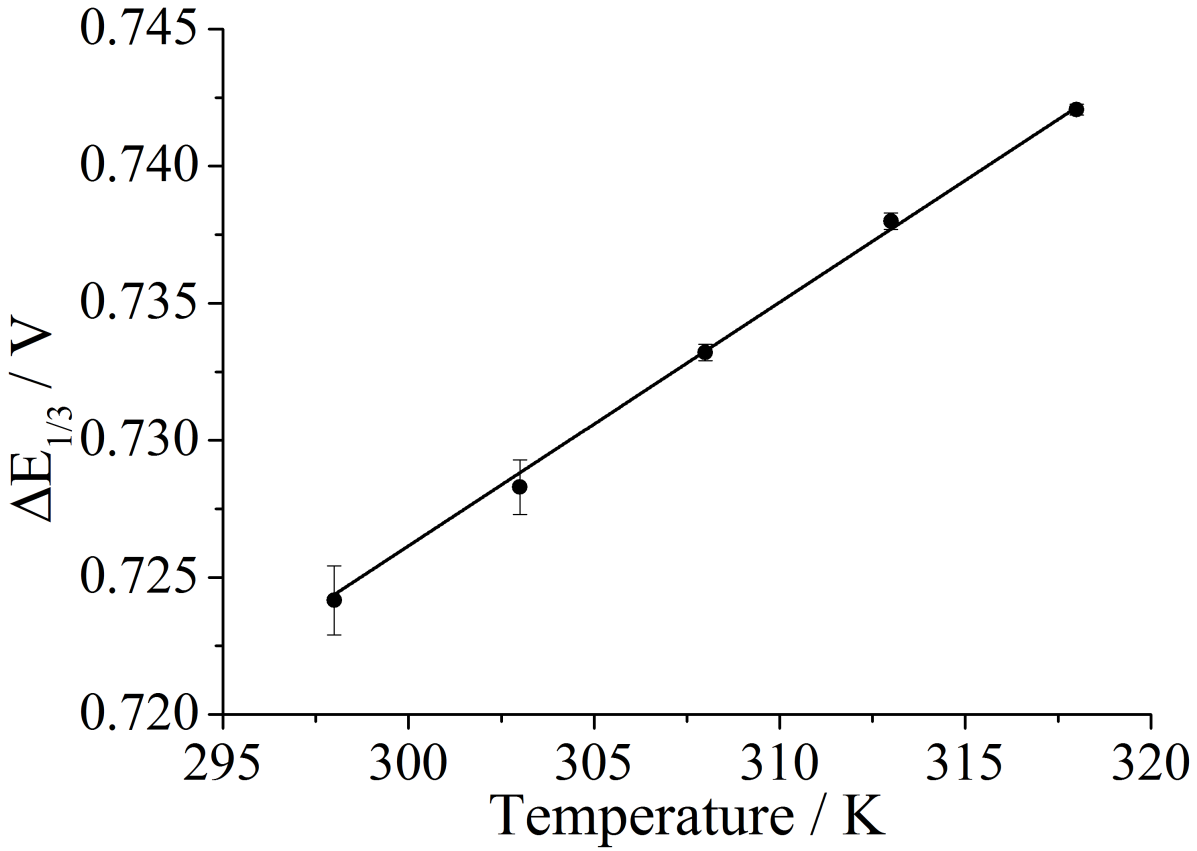

Figure 7.9: Dependence of average $\Delta E_{1/3}$ on the value of RH at 298 K, 303 K, 308 K, 313 K and 318 K.

humidity, the relationship of $\Delta E_{1/3}$ and temperature is one-to-one; hence a more precise value of temperature can be evaluated. Given a more accurate temperature value is known, a better estimate of the humidity can be made. Finally, the quality of the estimate is tested via the comparison of the new estimates of temperature and humidity with the old ones. If these two values are very close, it can be concluded that the estimates are representative of the actual temperature and humidity values; if not, the estimates can be further improved by repeating the same process iteratively until the estimates do not change by an appreciable amount.

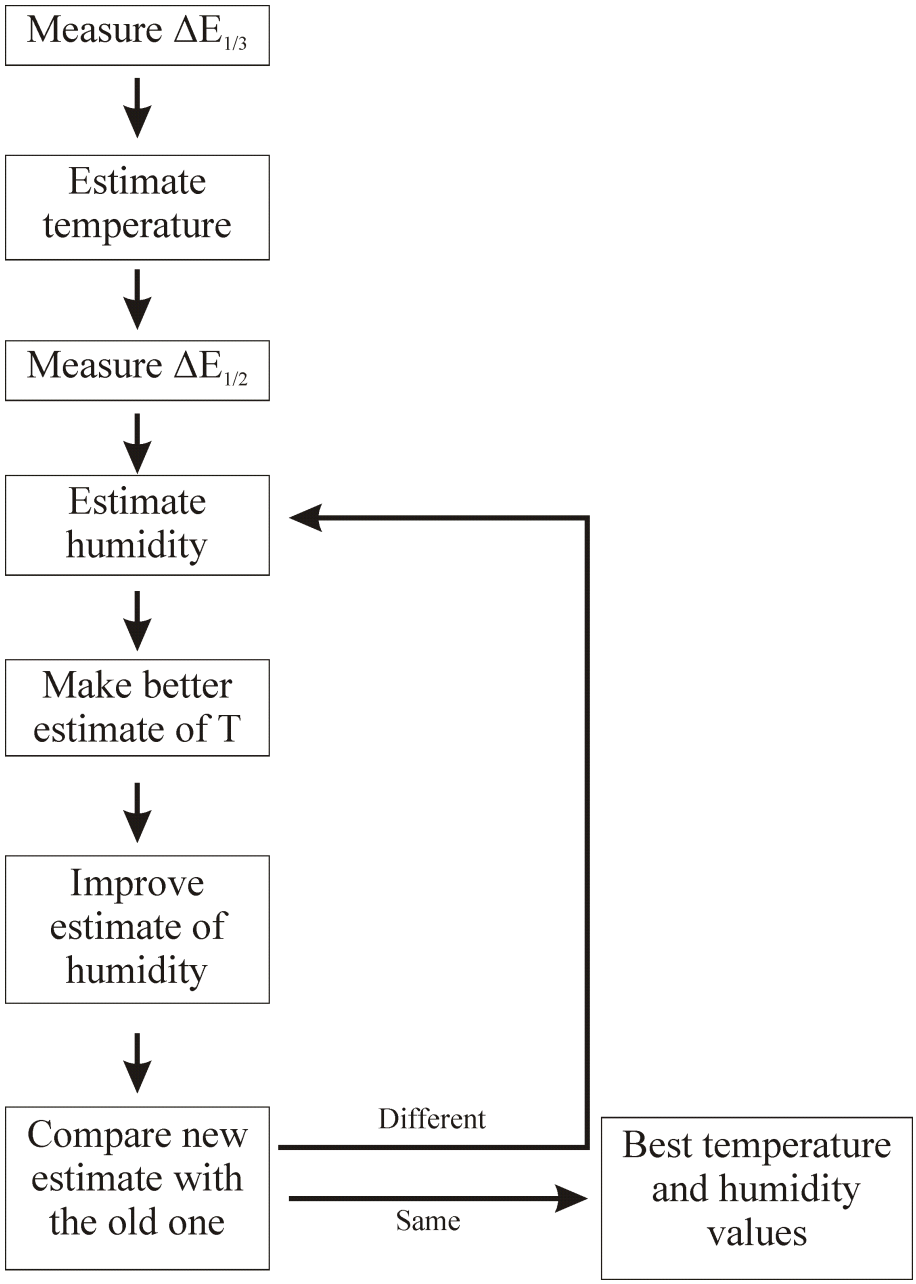

Figure 7.10: The proposed iterative method for determining temperature and humidity simultaneously.

7.4 Conclusions

Through square wave voltammetric analysis of BisFc and DmFc system, this work measured the temperature dependences of two independent peak potential differences, $\Delta E_{1/2}$ (i.e. the potential difference for oxidation of DmFc and first oxidation of BisFc) and $\Delta E_{1/3}$ (i.e. the potential difference for oxidation of DmFc and second oxidation of BisFc). The

former is temperature insensitive and the other has a temperature coefficient of 0.92 mV K^{-1}. The humidity effects of these two independent pairs over the temperature range of 298 K to 318 K have been investigated. It has observed that the peak potential difference between $DmFc/DmFc^+$ and $BisFc/BisFc^+$ is humidity dependent and the peak potential differences of other pairs are less influenced by humidity change. A method for finding accurate values of humidity and temperature has been proposed. Even it is possible to measure the humidity and temperature in the RTILs using the method introduced in this chapter, oxygen reduction mechanism in humid condition is complex and unpredictable. Next chapter introduces a method to 'trap' oxygen reduction at one electron stage.

References

[1] Xiong, L.; Fletcher, A. M.; Davies, S. G.; Norman, S. E.; Hardacre, C.; Compton, R. G. *The Analyst* **2012**, *137*, 4951–4957.

[2] Atkins, P.; De Paula, J. *Atkins' Physical Chemistry*; Macmillan Higher Education, 2006.

[3] Xiong, L.; Fletcher, A. M.; Ernst, S.; Davies, S. G.; Compton, R. G. *Analyst* **2012**, *137*, 2567–2573.

[4] Xiong, L.; Fletcher, A. M.; Davies, S. G.; Norman, S. E.; Hardacre, C.; Compton, R. G. *Chemical Communications* **2012**, *48*, 5784–5786.

[5] Buzzeo, M. C.; Evans, R. G.; Compton, R. G. *ChemPhysChem* **2004**, *5*, 1106–1120.

[6] Barrosse-Antle, L. E.; Bond, A. M.; Compton, R. G.; O'Mahony, A. M.; Rogers, E. I.; Silvester, D. S. *Chemistry - An Asian Journal* **2010**, *5*, 202–230.

[7] Green, D.; Perry, R. *Perry's Chemical Engineers' Handbook, Eighth Edition*; McGraw Hill professional; McGraw-Hill Education, 2007.

[8] Noviandri, I.; Brown, K. N.; Fleming, D. S.; Gulyas, P. T.; Lay, P. A.; Masters, A. F.; Phillips, L. *Journal of Physical Chemistry B* **1999**, *103*, 6713–6722.

[9] Ignat'ev, N.; Welz-Biermann, U.; Kucheryna, A.; Bissky, G.; Willner, H. *Journal of Fluorine Chemistry* **2005**, *126*, 1150–1159.

[10] Wang, Z.; Fu, L.; Xu, H.; Shang, Y.; Zhang, L.; Zhang, J. *Journal of Chemical and Engineering Data* **2012**, *57*, 1057–1063.

[11] Fu, C.; Aldous, L.; Dickinson, E.; Manan, N.; Compton, R. *ChemPhysChem* **2011**, *12*, 1708–1713.

[12] Fu, C.; Aldous, L.; Dickinson, E.; Manan, N.; Compton, R. *New Journal of Chemistry* **2012**, *36*, 774–780.

[13] Compton, R. G.; Banks, C. E. *Understanding Voltammetry*; Imperial College Press, 2011, 2nd Edition.

[14] Bard, A. J.; Faulkner, L. R. *Electrochemical Methods: Fundamentals and Applications*; Wiley, 2001.

[15] Molina, A.; Gonzalez, J.; Laborda, E.; Li, Q.; Batchelor-McAuley, C.; Compton, R. G. *Journal of Physical Chemistry C* **2012**, *116*, 1070–1079.

[16] Brett, C. M. A.; Brett, A. M. O. *Electrochemistry: Principles, Methods, and Applications*; Oxford Science Publications; Oxford University Press, Incorporated, 1993.

Chapter 8

Amperometric Detection of Oxygen Under Humid Conditions: The Use of A Chemically Reactive Room Temperature Ionic Liquid to 'Trap' Superoxide Ions and Ensure a Simple One Electron Reduction

Last two chapters showed the sensors to monitor temperature and humidity at electrode. However issues still remain under humid conditions as the mechanism of gas like oxygen are highly sensitive to the presence of water especially when the amperometric detection of oxygen via Clark cell type devices uses Room Temperature Ionic Liquids (RTILs) as electrochemical solvents. The number of electrons transferred in the electrode reaction varies between one and two as a function of the humidity. This chapter reports that the problem can be avoided through the use of phosphonium cation based ionic liquids in which the alkyl group of the phosphonium cation has acidic protons which are rapidly abstracted by superoxide ions. Thus the reduction of O_2 is to be trapped at the one electron level on the micro-electrode voltammetric timescale, allowing the amperometric detection of oxygen under humid conditions to be quantitatively viable. The work presented here has been published in the *Sensors and Actuators B.*[1]

8.1 Introduction

Chapter 7 demonstrated the design of the simultaneous humidity and temperature sensor which allows accurate measurements of temperature and humidity to be made at the local environment. Even though the temperature and humidity of the reaction at the electrode can be monitored, the mechanism of gas in RTILs may also change under various humidity. The changed mechanism is complex and hard to predict. The use of RTILs[2–7] as solvents for gas sensors is extensively discussed in Chapter 1 and 2.

In the context of Clark-cell measurements using ionic liquid solvents we have previously advocated the use of micro-electrodes or their arrays as opposed to macro-electrodes for gas sensing.[32] The benefits arise partly from the much reduced currents drawn such that cells can be designed such that at steady state any gas permeable membranes used to separate the electrolyte from the gas phase shows a negligible impact on the steady-state current in contrast to classical Clark cells using macroelectrodes[33]. Further Chapter 4 showed the merits of using transient current measurements using from potential step measurements at micro-electrodes. These lead to a changing diffusional region with time in which linear diffusion to the electrode precedes the convergent diffusion characterising the steady-state. Consequently the currents under the former, 'Cottrellian' conditions scale as $nD^{1/2}c$ where D is the diffusion coefficient of the target gases of interest of solubility c and n is the number of electrons transferred in the electrochemical process of interest. In contrast, the current scales with nDc under the latter steady-state conditions. Hence it is possible to extract values of D and (nc) from 'Shoup and Szabo analysis' of the current - time transients (see Chapter 4). This approach has been demonstrated to work very successfully for the measurement of oxygen under dry conditions. [17, 19, 35, 36]

As shown on Chapters 6 and 7, micro-electrodes measurements are additionally useful since they can be combined with simultaneous electrochemical measurements both of temperature and/or humidity [34, 37]. Thus by combining temperature and humidity

data with Shoup and Szabo analysis, the latter is able to provide reliable measurements of dissolved gas concentrations which, combined with the former parameters, allows gas phase concentrations to be inferred. This approach, of course, requires that the number of electrons, n, transferred in the electrochemical reaction used to probe the dissolved gas remains constant and independent of both temperature and humidity.

One case of considerable interest where variable humidity can alter an electrode reaction is that of oxygen reduction. In dry ionic liquids a one-electron (n = 1) reaction to form superoxide. (see Equation 6.7 in Chapter 6)

Under dry condition the superoxide is stable. However in the presence of water, protonation and futher electron transfer is possible leading to the overall formation of hydrogen peroxide for which n=2:

$$O_2 + 2H^+ + 2e^- \rightleftharpoons H_2O_2 \tag{8.1}$$

An example of this transition is shown for the reduction of O_2 in [Pmim][NTf_2] in Figure 8.1 where linear sweep voltammetric responses are shown for both 'wet' and 'dry' solvent. The former shows an increased current and the formation of H_2O_2.

Moreover for sufficiently 'wet' conditions, this reaction might take place on the time scale of micro-electrode voltammetry/chronoamperometry, thus complicating the 'Shoup and Szabo analysis' proposed above. In the present paper, we show how this problem can be overcome and the reduction can be 'trapped' at the one electron only stage by the use of an ionic liquid, which reacts very quickly with superoxide preventing its further reaction to hydrogen peroxide, not least since the ionic liquid is present in very high concentration relative to dissolved water resulting from ambient humidity.

In particular we use a phosphonium cation based ionic liquid using long chain alkyl groups as shown in Figure 8.2. It is known that the protons alpha to the phosphonium cation are acidic and are rapidly abstracted by superoxide ions [38]. Thus the use

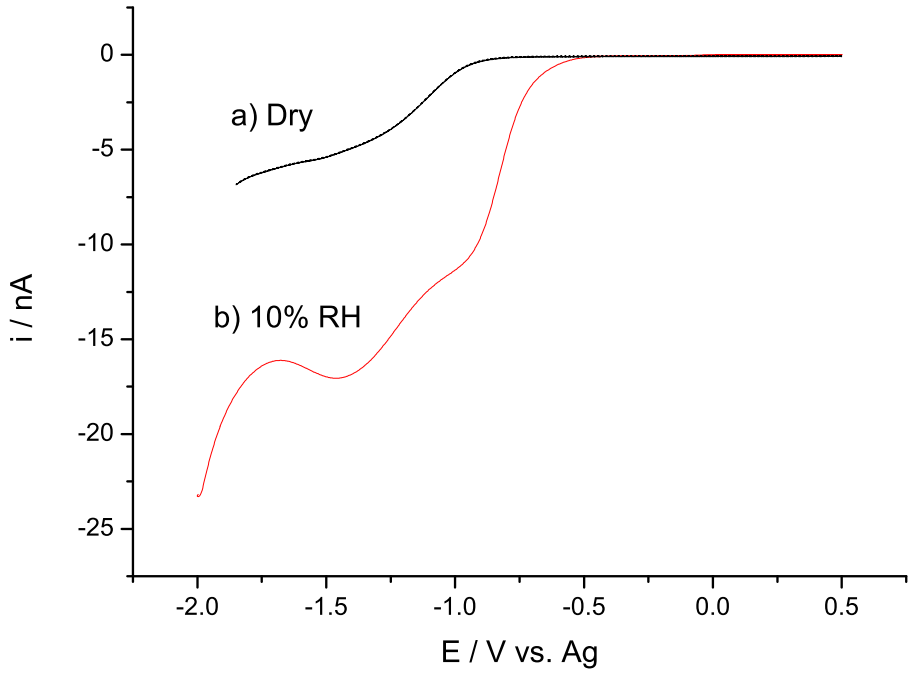

Figure 8.1: Comparison of liner sweep voltammetric responses of a) dry and b) 10 % RH O_2 in [Pmim][NTf_2] at a 5.4 μm Pt electrode at 298 K at a scan rate of 100 mV/s.

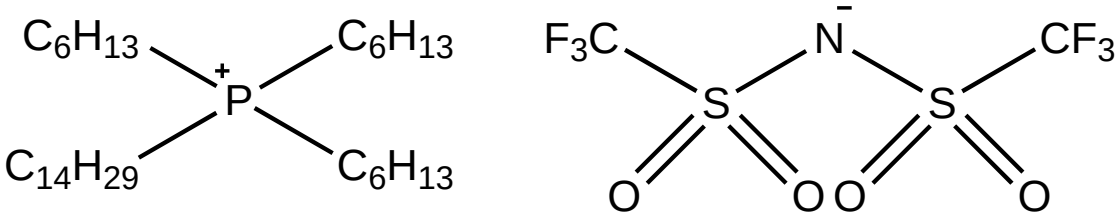

Figure 8.2: Structure of [$P_{14,6,6,6}$][NTf_2]

of Trihexyltetradecylphosphonium bis(trifluoro-methylsulfonyl)imide ([$P_{14,6,6,6}$][NTf_2] see Figure 8.2) for the reaction of O_2 aimed at gas sensing enables the latter to be stopped at the one electron stage,

$$PR_4^+ + O_2^{\dot{-}} \rightleftharpoons HO_2^{\cdot} + ylide \tag{8.2}$$

and the quantitative anlysis of O_2 via micro-electrode 'Shoup and Szabo Analysis' to be facilitated.

8.2 Experimental Section

The same line connection described in Section 7.2 was adopted to humidify oxygen for the work in this chapter. The relative humidity (RH %) of oxygen was also monitored using the method as previous chapter. The variation of humidity during an experiment was no more than 3% RH. Different RHs were achieved by tuning the flow rates of the dry column and a wet column. The flow rates corresponding to each RH are shown in Table 8.1. Water content was tested using a Karl-Fischer Titrator (Mettler-Toledo Ltd, Beaumont Leys Leicester, see Appendix for more details for the operational principal of Karl-Fischer Titrator). 100 μL of $[P_{14,6,6,6}][NTf_2]$ exposed to 36 % RH O_2 for three hours gave a concentration of H_2O of 6.7 mM (12 μg). A longer time was needed to reach O_2 saturation at higher RH. Therefore humidified O_2 was purged into $[P_{14,6,6,6}][NTf_2]$ for at least one hour before carrying any analysis to ensure the saturation was reached.

RH	Flow rate in Dry Column (cm^3 min^{-1})	Flow rate in Wet Column (cm^3 min^{-1})
8 %	600 ± 50	5 ± 2
25 %	600 ± 50	10 ± 1
36 %	600 ± 50	20 ± 5

Table 8.1: Flow rates used to achieve different RHs.

All experiments were performed inside a thermostatted box which was also used as a Faraday cage[36]. All temperature was controlled at 298.0 ± 0.5 K.

8.2.1 Theory

The work presented in this section was provided by Edward O. Barnes, a final year DPhil student in RGC group.

We simulate cyclic voltammetry at a micro-disc electrode with coupled homogeneous

kinetics according to the following mechanism:

$$\mathrm{A} + \mathrm{e}^- \rightleftharpoons \mathrm{B} \tag{8.3}$$

$$\mathrm{B} \rightarrow \mathrm{X} \tag{8.4}$$

$$\mathrm{X} - \mathrm{e}^- \rightleftharpoons \mathrm{Z} \tag{8.5}$$

The use of an ionic liquid solvent is assumed to suppress migration effect to ensure a diffusion only problem. The dependence of the three concentrations on time is given by:

$$\frac{\partial c_{\mathrm{A}}}{\partial t} = D_{\mathrm{A}} \left(\frac{\partial c_{\mathrm{A}}^2}{\partial r^2} + \frac{\partial c_{\mathrm{A}}^2}{\partial z^2} + \frac{1}{r} \frac{\partial c_{\mathrm{A}}}{\partial r} \right) \tag{8.6}$$

$$\frac{\partial c_{\mathrm{B}}}{\partial t} = D_{\mathrm{B}} \left(\frac{\partial c_{\mathrm{B}}^2}{\partial r^2} + \frac{\partial c_{\mathrm{B}}^2}{\partial z^2} + \frac{1}{r} \frac{\partial c_{\mathrm{B}}}{\partial r} \right) - k c_{\mathrm{B}} \tag{8.7}$$

$$\frac{\partial c_{\mathrm{X}}}{\partial t} = D_{\mathrm{X}} \left(\frac{\partial c_{\mathrm{X}}^2}{\partial r^2} + \frac{\partial c_{\mathrm{X}}^2}{\partial z^2} + \frac{1}{r} \frac{\partial c_{\mathrm{X}}}{\partial r} \right) + k c_{\mathrm{B}} \tag{8.8}$$

$$\frac{\partial c_{\mathrm{Z}}}{\partial t} = D_{\mathrm{Z}} \left(\frac{\partial c_{\mathrm{Z}}^2}{\partial r^2} + \frac{\partial c_{\mathrm{Z}}^2}{\partial z^2} + \frac{1}{r} \frac{\partial c_{\mathrm{Z}}}{\partial r} \right) \tag{8.9}$$

where k is the fastest rate constant for reaction 2.3. All symbols are defined in Table 8.2. The chemical step is assumed to be pseudo first order and irreversible. For the reaction of O_2^- via an ionic liquid solvent the ionic liquid cation is present in large excess so this is a good assumption. These mass transport equations are solved subject to boundary conditions at the electrode surface and in bulk solution. At the electrode surface, Butler-Volmer kinetics are employed. For each i/j couple (where i is the oxidised species):

$$D_{\mathrm{i}} \left(\frac{\partial c_{\mathrm{i}}}{\partial z} \right)_{z=0} = k^0 \left(c_{\mathrm{i}}^0 \exp \left[\frac{-\alpha \left(E - E_f^{\ominus} \right)}{RT} \right] - c_{\mathrm{j}}^0 \exp \left[\frac{\beta \left(E - E_f^{\ominus} \right)}{RT} \right] \right) \tag{8.10}$$

Parameter	Description	Units
α/β	Electron transfer coefficients	Unitless
c_{i}	Concentration of species i	mol m^{-3}
c_{i}^{*}	Bulk solution concentration of species i	mol m^{-3}
c_{i}^{0}	Electrode surface concentration of species i	mol m^{-3}
D_{i}	Diffusion coefficient of species i	m^2 s^{-1}
E	Applied potential	V
$E_{\mathrm{f}}^{\ominus}$	Formal potential	V
I	Current	A
k	Homogeneous rate constant	s^{-1}
k^0	Heterogeneous rate constant	m s^{-1}
r	Radial coordinate	m
r_e	Radius of electrode	m
t	Time	s
z	z coordinate	m

Table 8.2: Parameter definitions

Conservation of mass implies the flux of j at the electrode surface is equal and opposite to that of i.

The potential applied to the electrode, E, is defined by the start and vertex potential, and the scan rate:

$$E = |E_s - E_v - \nu t| + E_v \tag{8.11}$$

The bulk solution in both the r and z direction is set at $6\sqrt{D_{\max} t_{\max}}$ from the electrode surface, where $D_{\max}$ is the largest diffusion coefficient in the system, and $t_{\max}$ is the total time taken to carry out the experiment[39–41]. At these boundaries, as well as at the

symmetry boundary at $r = 0$, a zero flux condition is imposed.

The current is calculated by integrating the flux over the electrode surface:

$$I = -FD_{\mathrm{A}} \int_0^{2\pi} \int_0^{r_e} \frac{\partial c_{\mathrm{A}}}{\partial z} dr d\theta - FD_{\mathrm{Z}} \int_0^{2\pi} \int_0^{r_e} \frac{\partial c_{\mathrm{Z}}}{\partial z} dr d\theta \tag{8.12}$$

where i is the oxidised species of each redox couple.

Boundary	Dimensionless boundary condition
All R, all Z, $\tau < 0$	$C_{\mathrm{A}} = 1$
	$C_{\mathrm{i}\neq\mathrm{A}} = 0$
$R \leq 1$, $Z = 0$, $\tau \geq 0$	$D'_{\mathrm{i}} \frac{\partial C_{\mathrm{i}}}{\partial R} = K^0 \left[C^0_{\mathrm{i}} \mathrm{e}^{-\alpha\theta} - C^0_{\mathrm{j}} \mathrm{e}^{\beta\theta} \right]$
	$D'_{\mathrm{j}} \frac{\partial C_{\mathrm{j}}}{\partial R} = -D'_{\mathrm{i}} \frac{\partial C_{\mathrm{i}}}{\partial R}$
$R = 0$, all Z, $\tau \geq 0$	$\frac{\partial C_{\mathrm{i}}}{\partial R} = 0$
$R = 1 + 6\sqrt{D'_{\max}\tau_{\max}}$, all Z, $\tau \geq 0$	$\frac{\partial C_{\mathrm{i}}}{\partial R} = 0$
$R > 1$, $Z = 0$, $\tau \geq 0$	$\frac{\partial C_{\mathrm{i}}}{\partial R} = 0$
All R, $Z = 6\sqrt{D'_{\max}\tau_{\max}}$, $\tau \geq 0$	$\frac{\partial C_{\mathrm{i}}}{\partial R} = 0$

Table 8.3: Normalised boundary conditions for cyclic voltammetry at a micro-disc electrode

The model is normalised using dimensionless parameters listen in Table 8.4. The resultant boundary conditions are shown in Table 8.3. The mass transport equations and boundary conditions are solved using the Alternating Direction Implicit (ADI) method[42] in conjunction with the Thomas Algorithm[43]. Spatial and temporal grids are used as defined in previous work[44].

Normalised Parameter	Definition
C_{i}	$\frac{c_{\mathrm{i}}}{c^*_{\mathrm{A}}}$
D'_{i}	$\frac{D_{\mathrm{i}}}{D_{\mathrm{A}}}$
K	$\frac{r_e^2}{D_{\mathrm{A}}}k$
K^0	$\frac{r_{\mathrm{s}}}{D_{\mathrm{A}}}k^0$
R	$\frac{r}{r_{\mathrm{s}}}$
θ	$\frac{E-E^0_{\mathrm{f}}}{RT}$
τ	$\frac{D_{\mathrm{A}}}{r_s^2}t$
Z	$\frac{z}{r_{\mathrm{d}}}$

Table 8.4: Normalised parameter definitions

8.3 Results and Discussion

In order to subsequently compare the reduction of O_2 in both dry and wet conditions, experiments were first carried out in $[P_{14,6,6,6}][NTf_2]$ containing dry O_2 at 298 K. Previous work by Evans et al. demonstrated that O_2 reduction undergoes an EC mechanism in dry $[P_{14,6,6,6}][NTf_2]$ at a Pt electrode (308 K)[36]:

$$O_2 \rightarrow \dot{O_2^-} \tag{8.13}$$

$$\dot{O_2^-} + PR_4 \rightarrow X \tag{8.14}$$

where X is likely to be ·OOH at least initially but probably followed by further irreversible follow up chemistry such as disproportionation. However on the micro-electrode timescale a simple EC process is followed in which the C step is chemically irreversible[36].

How this EC mechanism benefits the detection of O_2 is demonstrated by experiments

and analysis in $[P_{14,6,6,6}][NTf_2]$ containing first dry O_2 (and later humidified O_2) at a Pt electrode (298 K). Experiments to confirm the purity and dryness of $[P_{14,6,6,6}][NTf_2]$ and the stability of dissolved O_2 were carried out, followed by the reduction of O_2 in $[P_{14,6,6,6}][NTf_2]$ which was analysed quantitatively by both chronoamperometry and cyclic voltammetry along with suitable simulation programs (see Theory section).

Prior to performing quantitative study for O_2 in $[P_{14,6,6,6}][NTf_2]$, it is essential to confirm the purity and dryness of the ionic liquids to avoid the possible interference between the analytes and impurities such as water or any organic solvents in the ionic liquids. Hence the following procedures were carried out. 1 mL of $[P_{14,6,6,6}][NTf_2]$ was placed under vacuum (4 mbar) overnight to remove impurities such as O_2, water and volatile organic compounds. This removal was confirmed by performing cyclic voltammetry over the range of +2 V to -3 V vs. Ag in the pure $[P_{14,6,6,6}][NTf_2]$ under nitrogen. No peak was shown in the solvent window, verifying that $[P_{14,6,6,6}][NTf_2]$ was analytically pure.

The stability and reproducibility of O_2 reduction were then investigated using the clean and dry $[P_{14,6,6,6}][NTf_2]$. To guarantee the whole system being dry, O_2 was predried in 4 Å molecular sieves before purging into $[P_{14,6,6,6}][NTf_2]$. A steady flow was achieved by maintaining the flow rate of O_2 at 300 cm^3 min^{-1} throughout the experiments. Cyclic voltammetry was carried out to find the time taken for O_2 saturation in dry $[P_{14,6,6,6}][NTf_2]$. Figure 8.3 compares two cyclic voltammetric responses for O_2 reduction in $[P_{14,6,6,6}][NTf_2]$ at the Pt electrode at a scan rate of 100 mV s^{-1} in an interval of 15 minutes where these almost exactly superimposed voltammograms suggest that a time interval of 15 minutes was the minimum amount of time required to reach maximum O_2 solubility in $[P_{14,6,6,6}][NTf_2]$. Peaks at ca. -2.0 V vs. Ag in the negative direction in Figure 8.3 correspond to the O_2 reduction and the immediate follow up chemical step (discussed later), while the peaks located at ca. -1.0 V vs. Ag relate to the oxidation of X.

The concentration and diffusion coefficient of O_2 in dry $[P_{14,6,6,6}][NTf_2]$ was evalu-

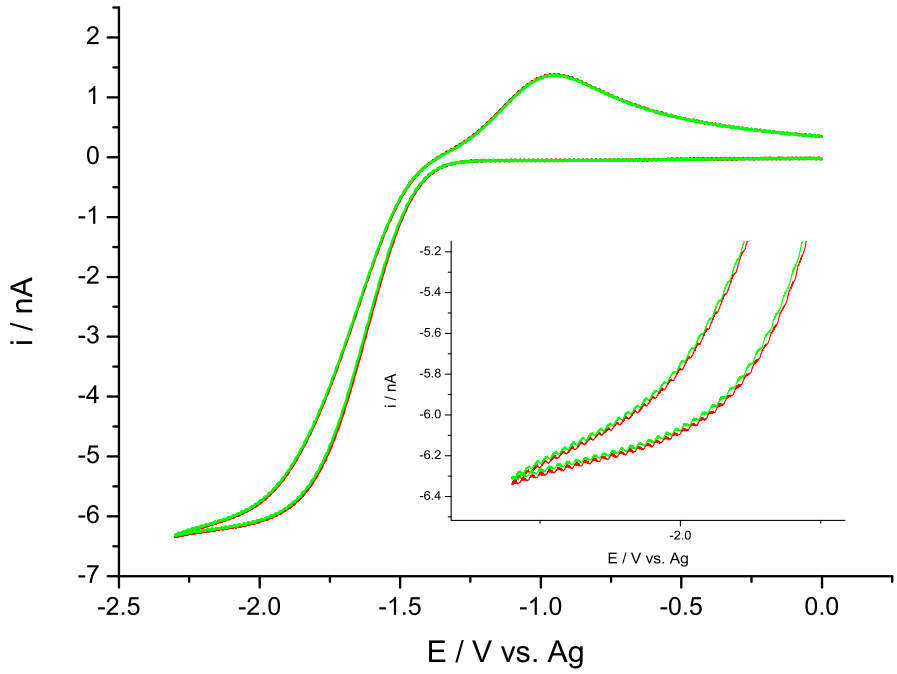

Figure 8.3: Comparison of cyclic voltammetric responses for saturated O_2 in $[P_{14,6,6,6}][NTf_2]$ at the 5.4 μm radius Pt microdisc electrode at a scan rate of 100 mV/s with a time interval of 15 min between scans. Inset: Enlargement of the reductive currents. It is seen that two voltammegrams are almost exactly superimposed.

ated using chronoamperometry. Chronoamperometry is a particularly useful technique in quantitative analysis of O_2 as discussed in the introduction. [45] In chronoamperometry, the potential is stepped from a value where no current passes to a value where the O_2 reduction is diffusion controlled. These values of potential were inferred from the cyclic voltammetric responses for O_2 saturated dry $[P_{14,6,6,6}][NTf_2]$ as seen in Figure 8.3 where there is no current more positive than 0 V vs. Ag and the current for O_2 reduction reaches steady state beyond -1.8 V vs. Ag. Hence, the following experimental procedure for chronoamperometry was adopted: the potential was initially held at 0 V vs. Ag for 20 second then stepped to -2.0 V vs. Ag. The resultant current along with the fitting based on Shoup and Szabo analysis[45] are plotted in Figure 8.4. Shoup and Szabo fitting is most commonly used to describe the chronoamperometry transient within an error of 0.6

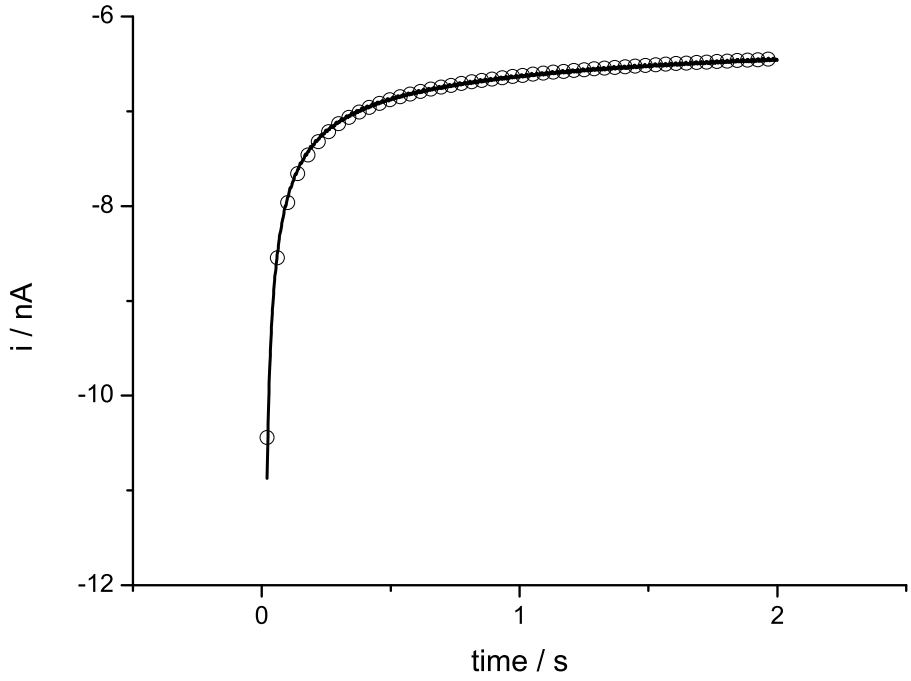

Figure 8.4: Simulated (circles) and experimental (solid line) chronoamperometric responses for saturated O_2 in $[P_{14,6,6,6}][NTf_2]$ at the 5.4 μm radius Pt microdisc electrode.

%. Chapter 4 details the fitting methods by using a readily imported Shoup and Szabo function in Origin 8.0 to find concentration and diffusion coefficient simultaneously by fixing the electrode radius.

By fixing the known measured value of electrode radius, 5.4 μm (previously calibrated using ferrocene in acetonitrile), the values of concentration and diffusion coefficient are iterated until the best fit is obtained which resulted in a O_2 concentration of 7.5 $\pm$ 0.1 mM and diffusion coefficient of 3.9 $\pm$ 0.1 $\times$ 10^{-10} m^2 s^{-1} at 298 K. The literature suggests a concentration of 6 mM and diffusion coefficient of 7.5 $\times$ 10^{-10} m^2 s^{-1} respectively in $[P_{14,6,6,6}][NTf_2]$ at 308 K[36]. The greater concentration of O_2 at higher temperature likely reflects negative enthalpy of dissolution for O_2 in $[P_{14,6,6,6}][NTf_2]$ which is observed for O_2 in most ionic liquids.[17] The lower diffusion coefficient at lower temperatures is expected because O_2 is less mobile at lower temperatures.[17]

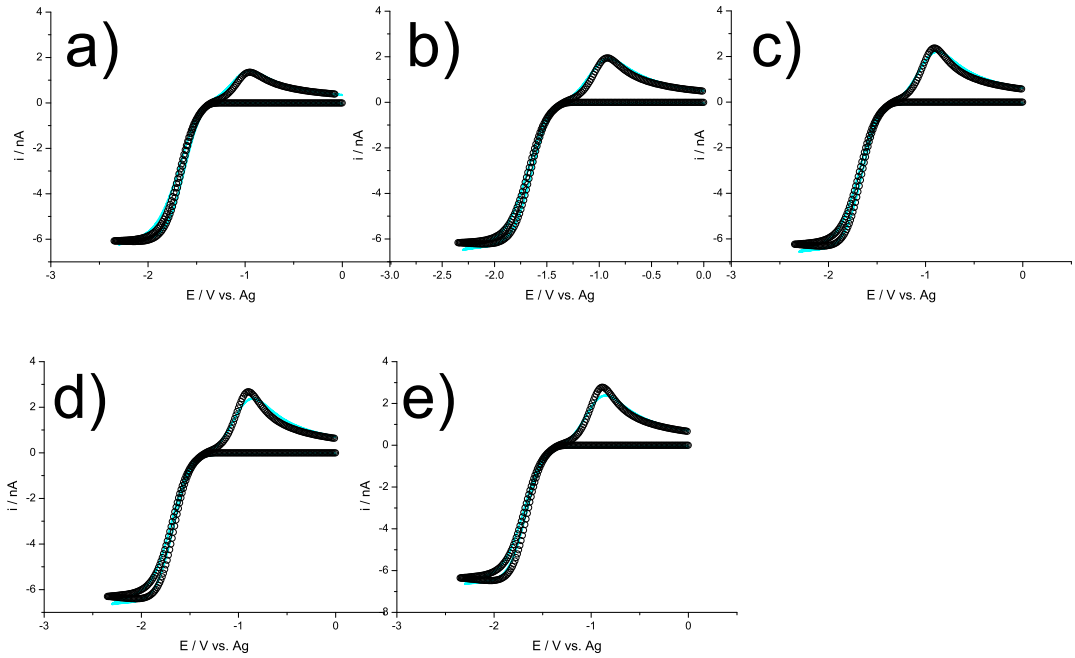

Figure 8.5: Simulated (circles) and experimental (solid lines) data for dry O_2 in $[P_{14,6,6,6}][NTf_2]$ at the 5.4 μm radius Pt microdisc electrode at 298 K at scan rates of a) 100 mV s^{-1}, b) 200 mV s^{-1}, c) 300 mV s^{-1}, d) 400 mV s^{-1} and e) 500 mV s^{-1}.

The values of concentration and diffusion coefficient of O_2 were further examined through simulating the cyclic voltammetry for O_2 in $[P_{14,6,6,6}][NTf_2]$ with the EC mechanism program reported alone. Figures 8.5 a) to e) show cyclic voltammetric responses for dry O_2 in $[P_{14,6,6,6}][NTf_2]$ over the scan rate range of 100 mV s^{-1} to 500 mV s^{-1} at 298 K. To simulate the back peak of the cyclic voltammetry, the oxidation of X is considered:

$$X - e \rightarrow product \tag{8.15}$$

which shows an excellent fit between the simulated and experimental data. Parameters used for simulation are listed in Table 8.5. Symbols are defined as follows: D is the diffusion coefficient; c is the concentration of oxygen; $k_{0,1}$ and $k_{0,2}$ are heterogeneous rate constant for the reductions 8.13 and 8.15 respectively; k is the homogeneous rate constant

RH	0 %	8 ± 2%	25 ± 1%	36 ± 3%
D_{O_2} ($\times$ 10^{-10} m^2 s^{-1})	4.0	5.2	6.2	7.6
c (mM)	7.3	6.6	5.1	4.4
α_1	0.31	0.35	0.31	0.29
$k_{0,1}$ (10^{-5} m s^{-1})	1	1	3	3
$D_{O_2^{\cdot}-}$ (10^{-10} m^2 s^{-1})	1.0	3.0	3.0	3.0
D_X (10^{-11} m^2 s^{-1})	3.0	8.0	9.0	30.0
$k_{0,2}$ (10^{-6} m s^{-1})	0.1	1	1	1
α_2	0.68	0.69	0.66	0.69
k (s^{-1})	1000	1000	1000	1000

Table 8.5: Table for the parameters used for simulating cyclic voltammetry of 100% oxygen dissolved in $[P_{14,6,6,6}][NTf_2]$ at the Pt microdisc electrode at 298 K.

for 8.14; α_1 and α_2 are transfer constants for the reactions 8.13 and 8.15 respectively.

Note that the diffusion coefficient of the product in Equation 8.15 is omitted since it plays no part in the simulation. The large homogeneous constant, 1000 s^{-1}, indicates a fast chemical step (Equation 8.18). To achieve optimised fits, the values of c and D_{O_2} obtained from chronoamperometry were used (less than 3 % of the Shoup and Szabo value). α_1 of 0.31 was obtained from Tafel analysis (see Equation 8.16 [15, 16]) of the oxygen reduction voltammogram by analysing the gradient of $ln\ I$ against E.

$$\alpha = -\frac{RT}{F}\frac{\partial ln|I|}{\partial E} \tag{8.16}$$

All other parameters were iterated until the best fit was seen.

The evaluated parameters are in good agreement with literature data[36], indicating O_2 reduction in $[P_{14,6,6,6}][NTf_2]$ at 298 K follows an EC mechanism with one-electron transfer which is summarised as follows:

$$O_2 + e \rightarrow O_2^{\cdot -} \tag{8.17}$$

$$O_2^{\cdot -} + [P_{14,6,6,6}]^+ \rightarrow X \tag{8.18}$$

$$X - e \rightarrow product \tag{8.19}$$

The above mechanism was selected in the light of the full mechanistic study reported in Reference 35. Note that a simple ECE process in which the reverse peak is attributed to the re-oxidation of $O_2^{\cdot-}$ was found to be incompatible with experimental data, a finding reproduced in the present study. The key observation is that the transfer coefficients ($\alpha + \beta$) measured experimentally for the reduction and oxidation waves are such that the usual expected $\alpha + \beta = 1$ is far from being met (vide infra). Thus modelling the voltammetry under the Butler - Volmer formalism clearly indicates that oxidation wave (oxidation of X) is not due to superoxide re-oxidation.

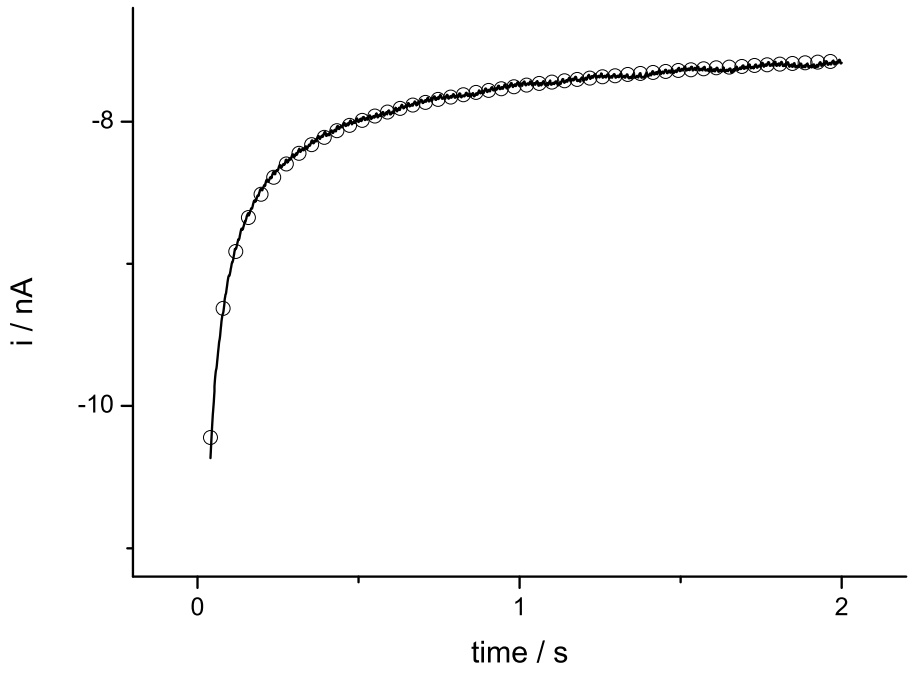

Figure 8.6: Simulated (circles) and experimental (solid line) chronoamperometric responses for O_2 in $[P_{14,6,6,6}][NTf_2]$ at the 5.4 μm radius Pt microdisc electrode recorded at RH of 8% and temperature of 298 K.

Next, similar experiments were carried out for the reduction of O_2 of 8%, 25% and

35% RH in $[P_{14,6,6,6}][NTf_2]$ at 298 K. Concentrations and diffusion coefficients of O_2 were again determined by fitting chronoamperometry with Shoup and Szabo analysis. Figure 8.6 shows the simulated (circles) and experimental (solid line) chronoamperometry for O_2 (8% RH) in $[P_{14,6,6,6}][NTf_2]$ where the current was sampled at -1.5 V vs. Ag for 2 seconds. The concentration and diffusion coefficient were determined to be 5.5 mM and 6.2×10^{-10} m^2 s^{-1} respectively, assuming n = 1.

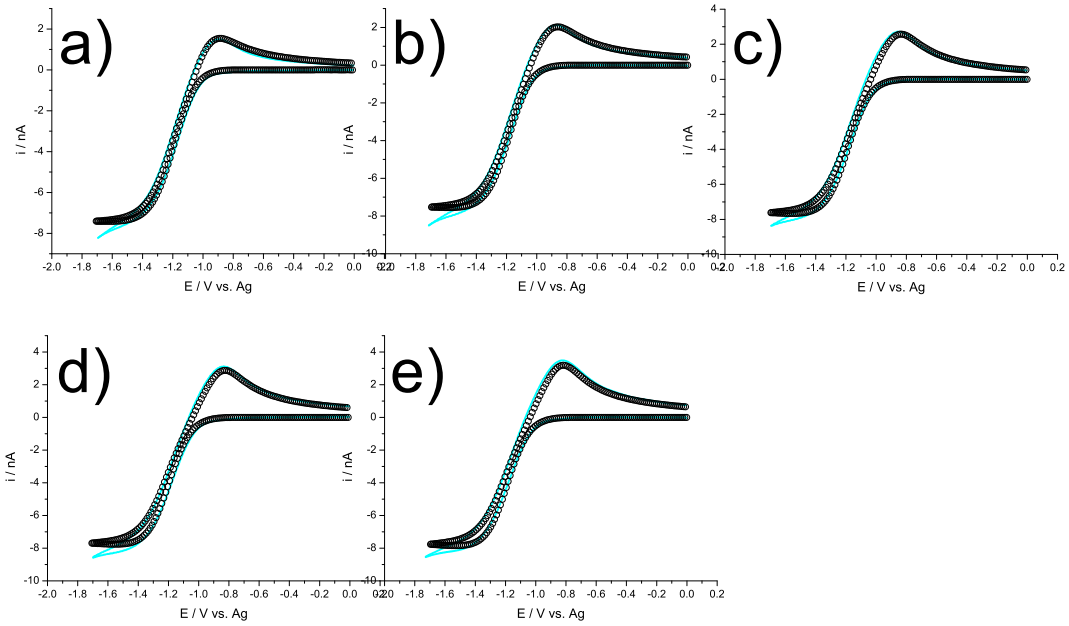

Figure 8.7: Simulated (circles) and experimental (solid lines) data for 8% RH O_2 in $[P_{14,6,6,6}][NTf_2]$ at the 5.4 μm radius Pt microdisc electrode at 298 K and at scan rates of a) 100 mV s^{-1}, b) 200 mV s^{-1}, c) 300 mV s^{-1}, d) 400 mV s^{-1} and e) 500 mV s^{-1}.

To validate whether the reduction of humidified O_2 follows a one electron reduction mechanism, cyclic voltammograms for humidified O_2 were fitted with the simulation program for an EC mechanism. Figures 8.7 a) to e) depict the cyclic voltammograms (solid lines), along with the EC simulations (circles), for O_2 in $[P_{14,6,6,6}][NTf_2]$ at RH of 8% and temperature of 298 K over the scan rate range of 100 mV s^{-1} to 500 mV s^{-1}. Parameters determined by simulation are listed in Table 8.5. It is seen that the concentration

and diffusion coefficient determined in cyclic voltammetry are in close agreement to those obtained from chronoamperometry. Compared with the experiments in dry condition, all species diffuse faster at RH of 8 %. Furthermore, a higher $k_{0,2}$ observed may be due to a change of reaction environment.

The excellent fit between simulated and experimental cyclic voltammograms suggests that O_2 at RH of 8 % reacts with $[P_{14,6,6,6}]^+$ instead of H_2O, resulting in the same EC mechanism where n=1.

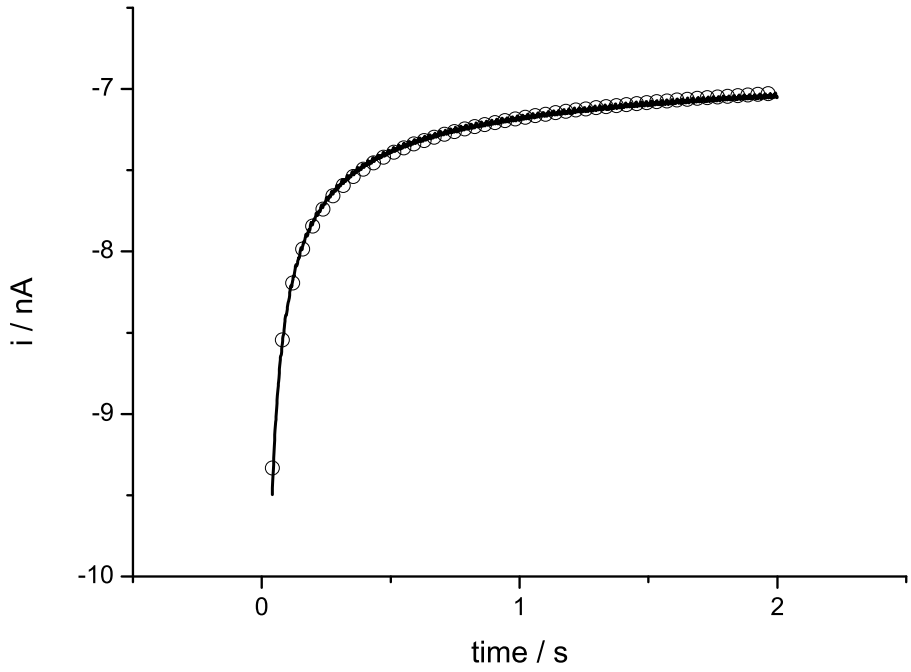

Figure 8.8: Simulated (circles) and experimental (solid line) chronoamperometric responses for O_2 in $[P_{14,6,6,6}][NTf_2]$ at the 5.4 μm radius Pt microdisc electrode recorded at RH of 25% and temperature of 298 K.

Similar experiments and analysis were then repeated at higher RH, 25 % and 36%. Figures 8.8 and 8.9 depict the chronoamperometric responses (solid line) with the corresponding simulation based on Shoup and Szabo analysis (circles) for O_2 reduction at RH of 25 % and 35 % respectively. At 25 % RH, the values of the concentration and diffusion coefficient were found to be 5.1 mM and 6.3 $\times$ 10^{-10} m^2 s^{-1} whereas at 36 %

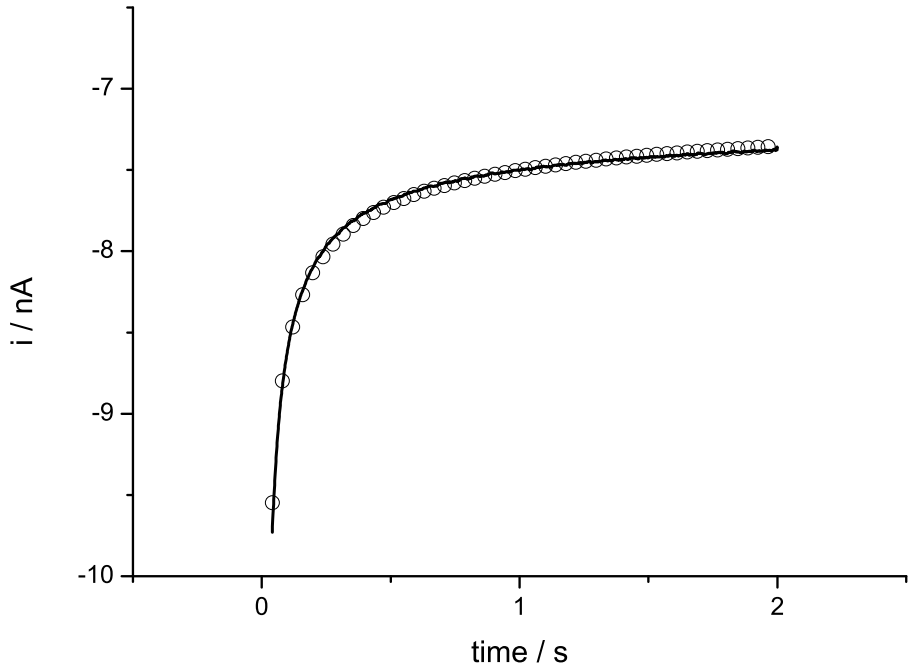

Figure 8.9: Simulated (circles) and experimental (solid line) chronoamperometric responses for O_2 in $[P_{14,6,6,6}][NTf_2]$ at the 5.4 μm radius Pt microdisc electrode recorded at RH of 36% and temperature of 298 K.

RH, the concentration and diffusion coefficient of O_2 were determined to be 4.4 mM and 7.6×10^{-10} m^2 s^{-1}. Values obtained via analysing chronoamperometry are summarised in Table 8.6 for clarity. These values were substituted in to EC CV simulation program to investigate the suitability of the EC mechanism in describing the O_2 reduction at higher humidity.

Figure 8.10 shows experimental (solid line) and simulated cyclic voltametric (circles) responses for oxygen reduction at 25 % RH at scan rates in the range of 100 mV s^{-1} to 500 mV s^{-1}. At all scan rates, simulated and experimental data show good correlation. Excellent agreement is also seen in the reverse scans except at the slow scan rate of 100 mV s^{-1} where the experimental current in the oxidation direction decays a little faster than the simulation expected. This is likely a result of a further, unmodelled reaction taking place in the oxidation direction in the presence of high water level. This additional

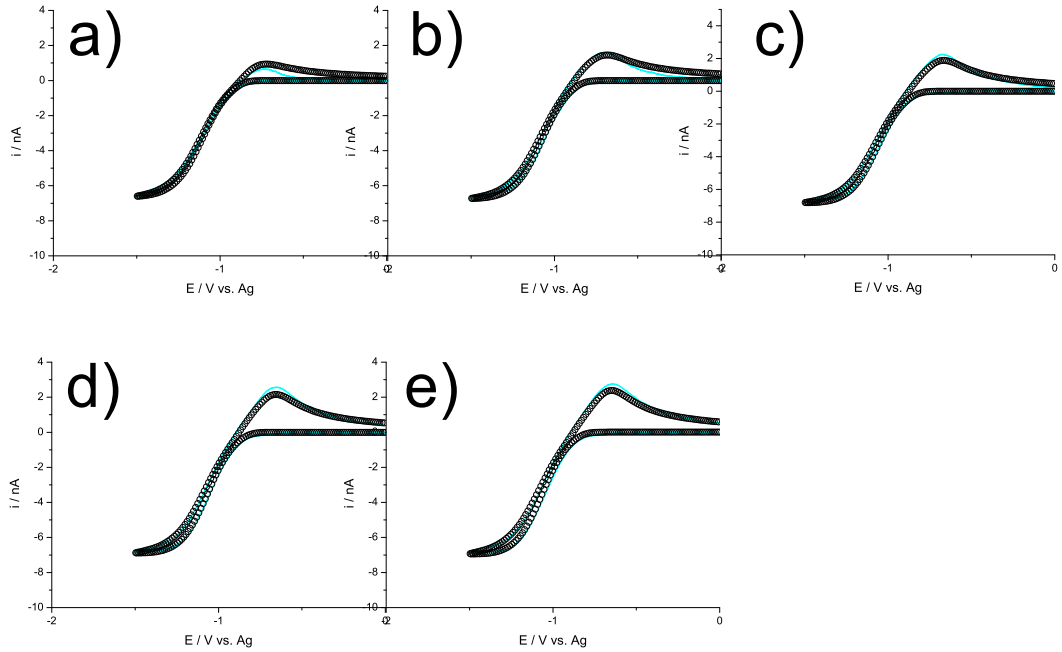

Figure 8.10: Simulated (circles) and experimental (solid lines) data for 25% RH O_2 in $[P_{14,6,6,6}][NTf_2]$ at the 5.4 μm radius Pt microdisc electrode at 298 K at scan rates of a) 100 mV s^{-1}, b) 200 mV s^{-1}, c) 300 mV s^{-1}, d) 400 mV s^{-1} and e) 500 mV s^{-1}.

reaction has more impact at a slow scan rate since a longer voltammetric timescale allows the reaction to begin to be visible. However this reaction only affects the oxidation of X. It does not impact the chronoamperometric results which would be used to measure the concentration and diffusion coefficient of O_2.

RH	0 %	8 ± 2 %	25 ± 1 %	36 ± 3 %
D_{O_2} (10^{-10} m^2 s^{-1})	3.9±0.1	5.5±0.2	6.3±0.7	7.6±0.1
c (mM)	7.5±0.1	6.2±0.3	5.1±0.4	4.4±0.1

Table 8.6: Table of the concentrations and the diffusion coefficients of pure oxygen dissolved in $[P_{14,6,6,6}][NTf_2]$ at a Pt microdisc electrode at 298 K. All data were collected from fitting of chronoamperometry with Shoup and Szabo analysis.

Analysing simulation of cyclic voltammetry was also carried out at 36 % RH to investigate the influence of higher concentration of water on the measurement of concentration

and diffusion coefficient of O_2. Figure 8.11 shows the cyclic voltammetric responses (solid lines), with the corresponding simulations (circles), for O_2 reduction in $[P_{14,6,6,6}][NTf_2]$ at 36 % RH.

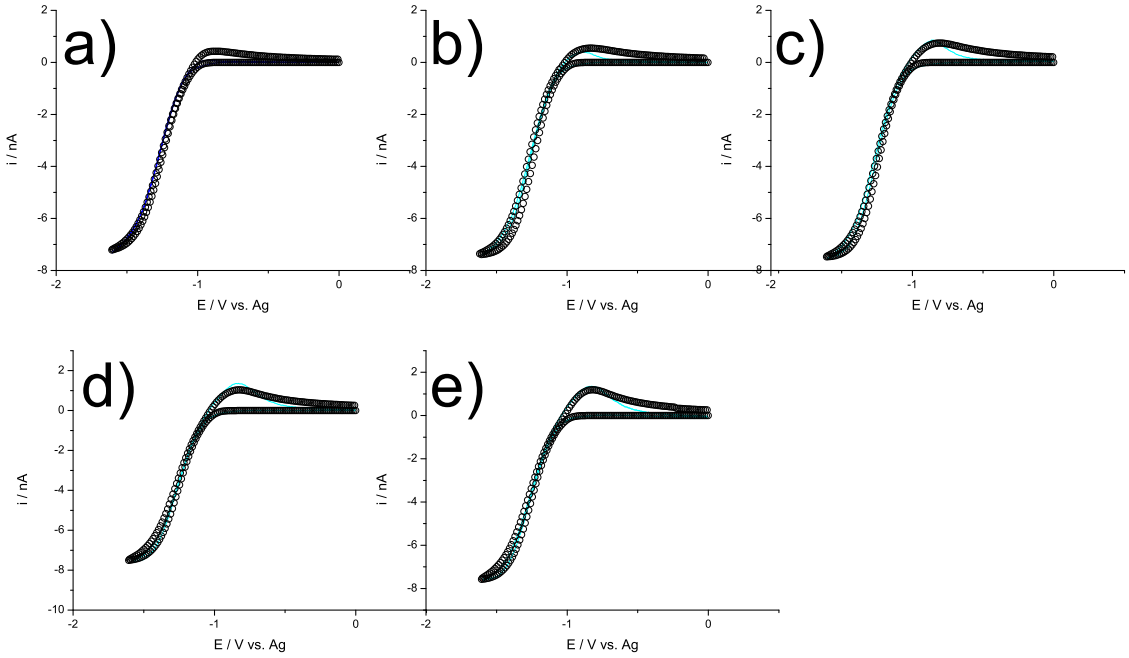

Figure 8.11: Simulated (circles) and experimental (solid lines) data for 36% RH O_2 in $[P_{14,6,6,6}][NTf_2]$ at the 5.4 μm radius Pt microdisc electrode at 298 K at scan rates of a) 100 mV s^{-1}, b) 200 mV s^{-1}, c) 300 mV s^{-1}, d) 400 mV s^{-1} and e) 500 mV s^{-1}.

Excellent fits are observed in the reduction responses although the fitting of the peak corresponding to the oxidation of X is approximate. This is again likely a result of the competitive reaction in the presence of water which has a more significant influence at higher concentrations of H_2O. Parameters used for this simulation are shown in Table 8.5. The values for concentration and diffusion coefficient agree well with those obtained from chronoamperometry. This again indicates that the reduction of O_2 at higher RH undertakes the same reduction mechanism. Most importantly, the addition of H_2O in the system does not affect the quantitative analysis of concentration and diffusion coefficient of O_2. This is because H_2O does not participate in the reaction with $O_2^{\cdot-}$, as supported by

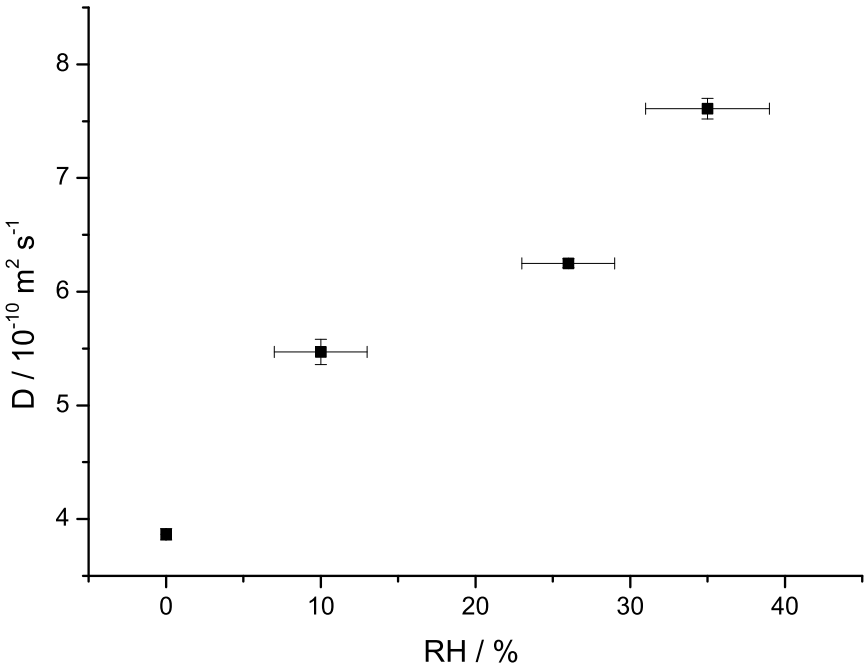

Figure 8.12: Plot of the oxygen diffusion coefficient against RH.

the simulations; rather the superoxide is 'trapped' via reaction with the solvent. Therefore at different RH, the parameters, which emerge from Shoup and Szabo analysis, are the concentration and diffusion coefficient of O_2, since the number of electron transferred remains constant throughout the RH range studied.

The change of diffusion coefficient of O_2 with RH was studied. Figure 8.12 shows the plot of diffusion coefficient against RH over the RH range of 0% to 36%. The positive correlation reflects that O_2 becomes more mobile at higher RH which can be understood by the fact that the viscosity of H_2O (1 cP) is much less than that of $[P_{14,6,6,6}][NTf_2]$ (450 cP) [46]. H_2O 'lubricates' $[P_{14,6,6,6}][NTf_2]$ and hence O_2 is more mobile in $[P_{14,6,6,6}][NTf_2]$ containing higher content of H_2O. The value of D can be used as an indicator for the % RH.

The relation between O_2 solubility and RH was also investigated. This is shown in Figure 8.13, where the concentration of O_2 is inversely proportional to increasing RH.

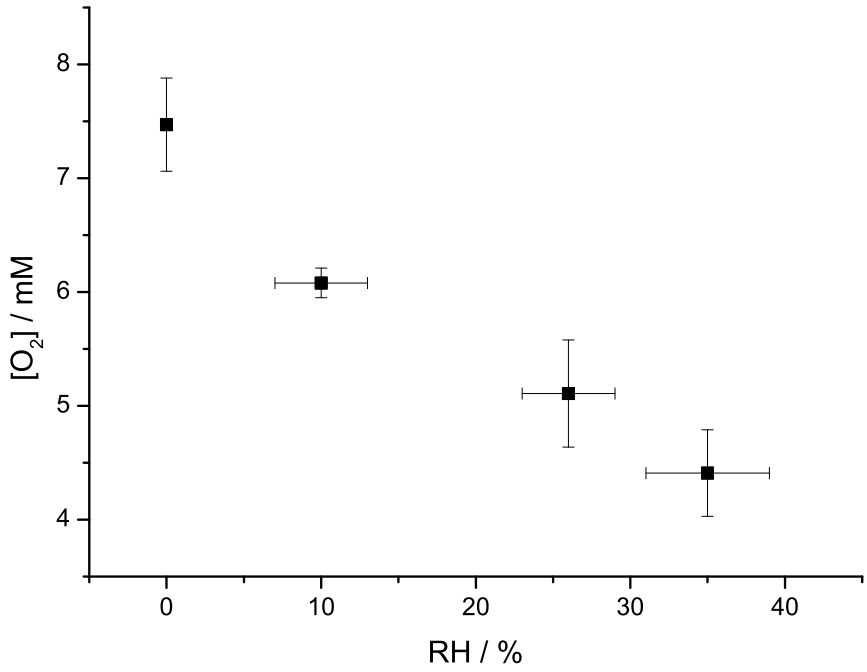

Figure 8.13: Plot of the oxygen concentration against RH.

This is due to the observation that O_2 is more soluble in $[P_{14,6,6,6}][NTf_2]$ (7.5 mM, from this work) than it is in water (1.2 mM[47]). Therefore, O_2 concentration is between 1.2 mM to 7.5 mM in $[P_{14,6,6,6}][NTf_2]$ depending on the RH of the gaseous oxygen.

Because O_2 is 'trapped' by $[P_{14,6,6,6}]^+$ even in the presence of water, it is unlikely that the reduction of O_2 experiences a change of mechanism at different % RH. In this way, O_2 detection using amperometry can be largely simplified. The method of determining gaseous O_2 at various RH may be proposed as follows: First, the RH is read by measurement of diffusion coefficient of dissolved O_2 in $[P_{14,6,6,6}][NTf_2]$ using chronoamperometry and Shoup and Szabo analysis. Then the concentration of dissolved O_2 is determined by chronoamperometry and related to the saturated O_2 concentration at that RH.

8.4 Conclusions

The reduction of O_2 in $[P_{14,6,6,6}][NTf_2]$ over the RH range of 0 % to 36 % has been demonstrated. The concentrations and diffusion coefficients of O_2 at different RHs have been determined by fitting chronoamperometry with Shoup and Szabo analysis. Cyclic voltammetry showed that the reduction of O_2 follows a simple one electron EC mechanism over the RH range of 0 % to 36 % where the superoxide is 'trapped' via reaction with the phosphonium cation. In addition to gas sensor development described in Chapter 6 to Chapter 8 for providing more accurate results by monitoring the local environment for gas detection and simplifying sensing reactions, Chapters 9 and 10 demonstrate low cost home-made electrodes for both general electrochemical reactions and gas sensing systems.

References

[1] Xiong, L.; Barnes, E. O.; Compton, R. G. *Sensors and Actuators, B: Chemical* **2014**, *200*, 157–166.

[2] Silvester, D. *Analyst* **2011**, *136*, 4871–4882.

[3] Shiddiky, M.; Torriero, A. *Biosensors and Bioelectronics* **2011**, *26*, 1775–1787.

[4] Hasanzadeh, M.; Shadjou, N.; Eskandani, M.; Guardia, M. *TrAC - Trends in Analytical Chemistry* **2012**, *41*, 58–74.

[5] Faridbod, F.; Mohammad Reza Ganjali, M. R.; Norouzi, P.; Riahi, S.; Rashedi, H. *Application of Room Temperature Ionic Liquids in Electrochemical Sensors and Biosensors*; InTech, 2011.

[6] Evans, R. G.; Klymenko, O. V.; Price, P. D.; Davies, S. G.; Hardacre, C.; Compton, R. G. *ChemPhysChem* **2005**, *6*, 526–533.

[7] Silvester, D. S.; Compton, R. G. *Zeitschrift fur Physikalische Chemie* **2006**, *220*, 1247–1274.

[8] Clark Jr., L.; Wolk, R.; Granger, D.; Talor, Z. *Journal of applied physiology* **1953**, *6*, 189–193.

[9] Barrosse-Antle, L. E.; Bond, A. M.; Compton, R. G.; O'Mahony, A. M.; Rogers, E. I.; Silvester, D. S. *Chemistry - An Asian Journal* **2010**, *5*, 202–230.

[10] Huang, X.-J.; Aldous, L.; OMahony, A. M.; del Campo, F. J.; Compton, R. G. *Analytical Chemistry* **2010**, *82*, 5238–5245.

[11] Matsumoto, K.; Hagiwara, R.; Ito, Y. *Electrochemical and Solid-State Letters* **2004**, *7*, E41–E44.

[12] Buzzeo, M. C.; Hardacre, C.; Compton, R. G. *ChemPhysChem* **2006**, *7*, 176–180.

[13] Zein El Abedin, S.; Endres, F. *ChemPhysChem* **2006**, *7*, 58–61.

[14] Lipsztajn, M.; Osteryoung, R. A. *Journal of the Electrochemical Society* **1983**, *130*, 11–13.

[15] Compton, R. G.; Banks, C. E. *Understanding Voltammetry*; Imperial College Press, 2011, 2nd Edition.

[16] Bard, A. J.; Faulkner, L. R. *Electrochemical Methods: Fundamentals and Applications*; Wiley, 2001.

[17] Huang, X. J.; Rogers, E. I.; Hardacre, C.; Compton, R. G. *The Journal of Physical Chemistry B* **2009**, *113*, 8953–8959.

[18] Xiong, L.; Lowinsohn, D.; Ward, K. R.; Compton, R. G. *Analyst* **2013**, *138*, 5444–5452.

[19] Xiong, L.; Fletcher, A. M.; Ernst, S.; Davies, S. G.; Compton, R. G. *Analyst* **2012**, *137*, 2567–2573.

[20] Wang, Z.; Lin, P.; Baker, G. A.; Stetter, J.; Zeng, X. *Analytical Chemistry* **2011**, *83*, 7066–7073.

[21] Barnes, A. S.; Rogers, E. I.; Streeter, I.; Aldous, L.; Hardacre, C.; Wildgoose, G. G.; Compton, R. G. *The Journal of Physical Chemistry C* **2008**, *112*, 13709–13715.

[22] Zhao, C.; Bond, A. M.; Compton, R. G.; O'Mahony, A. M.; Rogers, E. I. *Analytical Chemistry* **2010**, *82*, 3856–3861.

[23] Murakawa, Y.; Hara, M.; Oguchi, H.; Hamate, Y.; Kuwano, H. *Microsystem Technologies* **2013**, *19*, 1255–1259.

[24] Jalili, A. H.; Rahmati-Rostami, M.; Ghotbi, C.; Hosseini-Jenab, M.; Ahmadi, A. N. *Journal of Chemical & Engineering Data* **2009**, *54*, 1844–1849.

[25] O'Mahony, A. M.; Compton, R. G. *Electroanalysis* **2010**, *22*, 2313–2322.

[26] Villagran, C.; Banks, C. E.; Hardacre, C.; Compton, R. G. *Anal. Chem.* **2004**, *76*, 1998–2003.

[27] Ng, S. R.; Guo, C. X.; Li, C. M. *Electroanalysis* **2011**, *23*, 442–448.

[28] Peng, Y.; Ji, Y.; Zheng, D.; Hu, S. *Sensors and Actuators B: Chemical* **2009**, *137*, 656 – 661.

[29] Toniolo, R.; Dossi, N.; Pizzariello, A.; Doherty, A. P.; Bontempelli, G. *Electroanalysis* **2012**, *24*, 865–871.

[30] Silvester, D. S.; Ward, K. R.; Aldous, L.; Hardacre, C.; Compton, R. G. *Journal of Electroanalytical Chemistry* **2008**, *618*, 53–60.

[31] Ji, X.; Banks, C. E.; Silvester, D. S.; Aldous, L.; Hardacre, C.; Compton, R. G. *Electroanalysis* **2007**, *19*, 2194–2201.

[32] Buzzeo, M. C.; Hardacre, C.; Compton, R. G. *Anal. Chem.* **2004**, *76*, 4583–4588.

[33] Kudera, M.; Hill, H. A. O.; Dobson, P. J.; Leigh, P. A.; McIntire, W. S. *Sensors* **2001**, *1*, 18–28.

[34] Xiong, L.; Fletcher, A. M.; Davies, S. G.; Norman, S. E.; Hardacre, C.; Compton, R. G. *The Analyst* **2012**, *137*, 4951–4957.

[35] Buzzeo, M. C.; Klymenko, O. V.; Wadhawan, J. D.; Hardacre, C.; Seddon, K. R.; Compton, R. G. *Journal of Physical Chemistry A* **2003**, *107*, 8872–8878.

[36] Evans, R. G.; Klymenko, O. V.; Saddoughi, S. A.; Hardacre, C.; Compton, R. G. *J. Phys. Chem. B* **2004**, *108*, 7878–7886.

[37] Xiong, L.; Aldous, L.; Henstridge, M. C.; Compton, R. G. *Analytical Methods* **2012**, *4*, 371–376.

[38] Clayden, J.; Greeves, N.; Warren, S. *Organic Chemistry, 2nd edition*; Oxford University Press, 2012.

[39] Gavaghan, D. J. *J. Electroanal. Chem.* **1998**, *456*, 1–12.

[40] Gavaghan, D. J. *J. Electroanal. Chem.* **1998**, *456*, 13–23.

[41] Gavaghan, D. J. *J. Electroanal. Chem.* **1998**, *456*, 25–35.

[42] Britz, D. *Digital Simulation in Electrochemistry*; Springer-Verlag: Heidelberg, 2005.

[43] Press, W. H., Teukolsky, S. A., Vetterling, W. T., Flannery, B. P., Eds. *Numerical Recipes: The Art of Scientific Computing*; Cambridge University Press, 2007.

[44] Molina, A.; Gonzalez, J.; Barnes, E. O.; Compton, R. G. *J. Phys. Chem. C* **2014**, *118*, 346–356.

[45] Shoup, D.; Szabo, A. *Journal of Electroanalytical Chemistry and Interfacial Electrochemistry* **1982**, *140*, 237 – 245.

[46] Del Sesto, R.; Corley, C.; Robertson, A.; Wilkes, J. *Journal of Organometallic Chemistry* **2005**, *690*, 2536–2542.

[47] Association, A. P. H. *Standard methods for the examination of water and wastewater, 18th ed*; American Public Health Association (APHA), American Water Works Association (AWWA) & Water Environment Federation (WEF), 2001.

Chapter 9

Fabrication of Disposable Gold Macro-disc and Platinum Micro-band Electrodes for Use in Room-Temperature Ionic Liquids

The last two chapters focus on electrode development. This chapter introduces a simple and facile methodology for constructing gold macro-disc and platinum micro-band for use in room temperature ionic liquids(RTILs). To validate the use of gold macro-disc electrodes, the voltammetry of $Ru(NH_3)_6^{3+}$ is studied in 0.1 M aqueous KCl. The Randles-Ševčík equation is used to calculate the diffusion coefficient of $Ru(NH_3)_6^{3+}$, giving excellent agreement with literature values, suggesting the gold macro-disc electrode is capable of performing quantitative electroanalysis in aqueous media. Gold macro-disc electrodes are used to study oxidation of ferrocene in N-butyl-N-methylpyrrolidinium bis(fluoromethylsulfonyl)imide ($[C_4mpyrr][NTf_2]$) using cyclic voltammetry. A diffusion coefficient of ferrocene, $(2.43 \pm 0.07) \times 10^{-11}$ m^2 s^{-1}, is obtained. This value is very close to the literature value, indicating the good performance of gold electrode in RTILs. Platinum micro-bands electrodes are tested in 1-propyl-3-methylimidazolium bis-trifluoromethylsulfonylimide ($[C_3mim][NTf_2]$) containing DmFc. Diffusion coefficients and electron transfer rate are obtained by fitting relevant simulations into the experimental data. For comparison, analogous experiments and analysis are performed on a commercial plat-

inum micro-disc, where the results obtained from both micro-disc and micro-band agree well, further suggesting the platinum micro-band electrode is suitable to be used in RTILs. Last gold macro-disc and platinum micro-disc electrodes are used for oxygen detection. Gold macro-disc electrodes are used to find the peak currents of oxygen at each volume percentage analysed. Platinum micro-band electrodes showed steady-state currents of different volumes of oxygen. These two results are compared which resulted in excellent agreement. This is further confirmed by studying Henry's law constants obtained from both electrodes. The excellent behaviour of these two fabricated electrodes suggests they are suitable for quantitative measurements and practicable for real world applications. The work presented here has been published in the *Analyst*.[1]

9.1 Introduction

Work on the improvement of gas detection accuracy under various thermal and humid condition is shown in Chapters 6 to 8, based upon the fundamental studies of the analytical techniques in Chapter 4 and the interesting property of room temperature ionic liquids in Chapter 5. Beside optimisation of accuracy of the gas sensing systems, gas sensors to be produced in the manufacture, especially in large scale production, requires low cost and high reproducibility. Hence low cost and easily fabricated disposable electrodes are desired which is the main focus in the following chapters.

From literatures, not only have electrodes of different geometries and materials been investigated, but also methods of construction have been developed. The most important examples include screen printed[2–4], photo- or chemically etched[5–8] and glass sealed electrodes[9–12]. Despite the success in the manufacture of various electrodes, numerous challenges still exist. The cost of fabrication processes is normally high arising from the use of expensive machines or insulators. The electrode surface may result in unreliable voltammetric responses since the surface may only be partially exposed in

some cases. Welford et al. have developed inexpensive methods for the construction of micro-electrodes, based upon thermal lamination of metal foils, which largely solves the concerns discussed above.[13] This chapter extends this approach to fabrication methods of electrodes to both macro- and micro- geometries and, in particular, demonstrates electrochemical analysis on the fabricated electrodes in aqueous RTILs as well as in aqueous solutions, where three commonly used systems, aqueous $Ru(NH_3)_6^{3+}$, ferrocene in N-butyl-N-methylpyrrolidinium bis(fluoromethylsulfonyl)imide ($[C_4mpyrr][NTf_2]$) and DmFc in 1-propyl-3-methylimidazolium bis-(trifluoromethylsulfonyl)imide ($[C_3mim][NTf_2]$), are exemplified. Further to this, oxygen detection using these two types of fabricated electrodes is illustrated as an example of real-world application.

9.2 Experimental

9.2.1 Fabrication processes

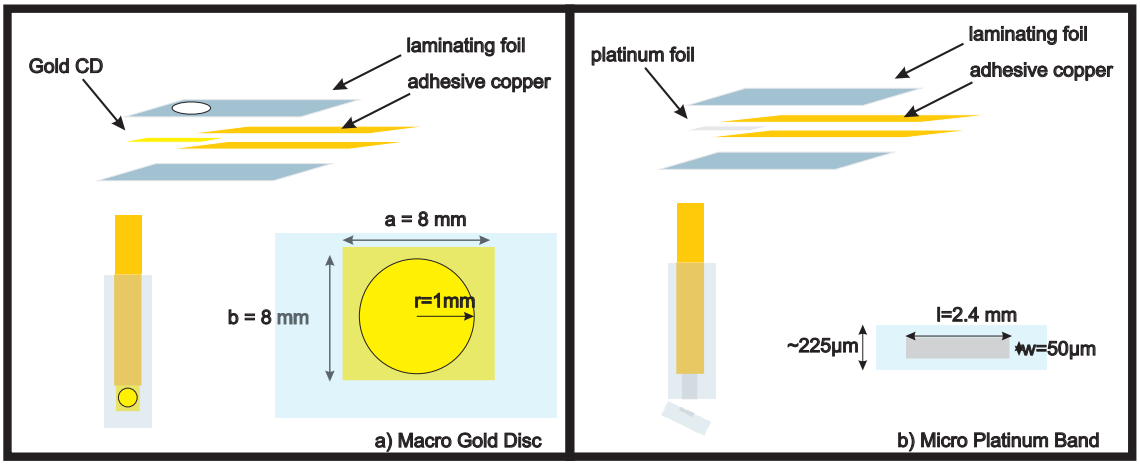

Figure 9.1: Schematic illustration of a) a gold macro-disc and b) a platinum micro-band electrode fabricated. a and b are the length and width of the cut CD. r is the radius of the macro-disc electrode. l and w refer to the length and width of the micro-band electrode.

Gold disposable macro-disc electrodes were made from recordable compact discs (CDs, EmTec®, Germany). To expose the gold surface, the polymer layers on the CDs were removed with concentrated HNO_3 ($\sim$ 16 M). Note this step was to prevent the gold

surface from distortion when cutting which happens if the polymer is not removed. Figure 9.1 shows the schemes of electrode fabrication[14]. Both gold macro-disc electrodes and platinum micro-band electrodes were prepared by thermal lamination of a piece of CD (width × length = 8 mm × 8 mm) or platinum foil (width = 50 μm, Buckbee Mears Co., St. Paul, US). Electrical connection to the foil is previously established by using a piece of copper foil with a conductive adhesive on one side (3 M Scotch brand electrical tape No. 1739-7). Gold macro-disc electrodes were exposed by punching a hole (r = 1 mm) on one page of laminating foil prior to lamination and platinum micro-band electrode surfaces were exposed by simply cutting the lamination normal to the foil with scissors[13].

The fabricated electrodes showed high stability over a period of three months by repeatedly performing experiments (at least 30 scans per day) of $Ru(NH_3)_6^{3+}$ in water or DmFc in $[C_3mim][NTf_2]$ over a period of one month; only a slight change in peak current, ca. 3 %, was seen. These fabricated electrodes can be stored in a dry place and can be reused straight away once needed. The variation of different fabricated gold macro-disc or platinum micro-band electrodes was less than ± 2.5 %.

Experimental results were collected from more than five different gold macro-disc or platinum micro-band electrodes, where the variations in peak current of cyclic voltammetry analysed for the same experiment at different electrodes were not more than ± 2.5 % (analysed by standard deviation). This chapter shows representative results.

9.2.2 Simulation

All simulated results presented herein were generated by simulation packages developed in-house by Dr. Kristopher Ward, fomally a PhD student in RGC group. Simulations of micro electrodes use a well established model developed by Klymenko et al.[15].Simulations of micro-band electrodes use the 2D alternating direction implicit method.[16]

9.3 Results and Discussion

This section starts with investigating the suitability of fabricated electrodes used in aqueous solution and ionic liquid. Three systems are reported: $Ru(NH_3)_6^{3+}$ reduction at the gold macro-disc electrodes, ferrocene oxidation in $[C_4mpyrr][NTf_2]$ recorded on the gold macro-disc electrode and DmFc oxidation in $[C_3mim][NTf_2]$ at the platinum micro-band electrode. Mass transport for the experiments involving gold macro-disc electrodes was studied by cyclic voltammetry and a Randles-Ševčík plot (peak current against square root of scan rate) whereas experiments performed at platinum micro-band electrodes were analysed by simulations of chronoamperometric and cyclic voltammetric responses via a home-made program (by Kristopher Ward). All values are compared with literature. Further to this, oxygen quantitative detection using gold macro-disc and platinum micro-band electrode is demonstrated where the concentrations are determined at different percentage by volume of oxygen using relevant theory. The Henry's law constant for oxygen was also found with good consistency between the two electrode types.

9.3.1 Reproducibility of Gold Macro-disc Electrodes

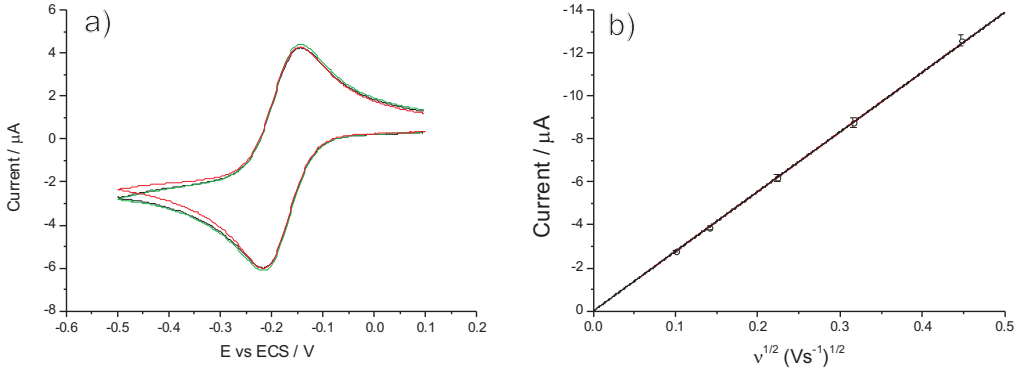

Figure 9.2: a)Cyclic voltammetric responses for 2.0 mM $Ru(NH_3)_6Cl_3$ (0.1 M KCl was used as supporting electrolyte) at a scan rate of 50 mV s^{-1} on three different gold macro disc electrodes of the same radius (1.0 mm). b)Plot of peak current against root square of scan rate for cyclic voltammetric response of 2.0 mM $Ru(NH_3)_6^{3+}$ (0.1 M KCl was used as supporting electrolyte) on the gold macrodisc electrode.

In order to investigate the electrochemical behaviour and reproducibility of the fabricated gold electrodes, experiments were performed in aqueous 2.0 mM $Ru(NH_3)_6^{3+}$ with 0.1 M KCl as supporting electrolyte. This system has been frequently used in calibrating both micro-disc and macro-disc electrodes since its diffusion coefficient is well known.[17–19] Experiments were performed on three different gold electrodes (radius = 1 mm), fabricated according to the procedure in section 9.2.1. Figure 9.2 a) shows cyclic voltammetric responses for the reduction of $Ru(NH_3)_6^{3+}$ on these electrodes at 50 mV s^{-1}. The peaks at -0.19 V vs. SCE correspond to $Ru(NH_3)_6^{3+}$ reduction [20] where excellent agreement between all three responses suggest a high level of reproducibility. This was quantitatively studied by comparing the peak currents at scan rates ranging from 0.01 to 0.2 V s^{-1} on these three electrodes, as shown in table 9.1, where a standard deviation of 2% was measured. This confirms that all three electrodes have very similar surface areas.

Scan rate (V s^{-1})	I_p at electrode 1 (μA)	I_p at electrode 2 (μA)	I_p at electrode 3 (μA)
0.01	-2.7	-2.8	-2.7
0.02	-3.8	-4.0	-3.8
0.05	-6.1	-6.4	-6.1
0.1	-8.6	-9.0	-8.7
0.2	-12.4	-12.8	-12.6

Table 9.1: Table of peak currents of the reduction of $Ru(NH_3)_6^{3+}$ on three different gold macro-disc electrodes over a scan rate range of 0.01 to 0.2 V s^{-1}.

The peak current, I_p of the forward sweep of a cyclic voltammogram for a fully reversible one electron transfer at a planar flat macro-electrode is given by the Randles-Ševčík equation[21, 22]. (Equation 1.28 in Chapter 1)

where A is the geometric area of the flat surface and ν is the scan rate. Figure 9.2 b) compares the plots of I_p versus $\nu^{\frac{1}{2}}$ for aqueous 2.0 mM $Ru(NH_3)Cl_6^{3+}$ at the gold macro-disc electrode, which gave a diffusion coefficient of $(8.58 \pm 0.06) \times 10^{-10}$ m^2 s^{-1}. Table 9.2 compares diffusion coefficients obtained from Equation 1.28 on fabricated gold electrodes with those from the literature. The value from this work is very close to those previously

Diffusion coefficient (m^2 s^{-1})	Author
$(8.58 \pm 0.06) \times 10^{-10}$	this work
$(8.43 \pm 0.03) \times 10^{-10}$	Wang. et al [17]
$(8.80 \pm 1.30) \times 10^{-10}$	Rees et al [18]
9.1×10^{-10}	Marken et al [19]

Table 9.2: Diffusion coefficients of $Ru(NH_3)_6^{3+}$ from different works where the supporting electrolytes for all listed works were 0.1 M KCl (298 K).

found, which suggests that the fabricated electrodes are able to produce accurate and quantitative analytical results.

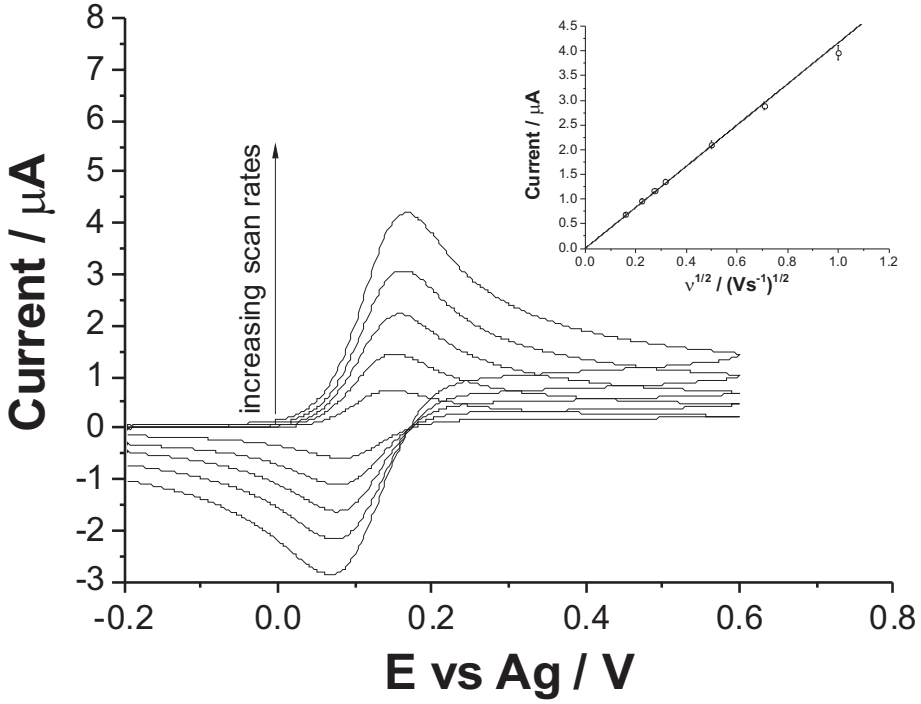

Figure 9.3: Cyclic voltammograms of the oxidation of 1.0 mM ferrocene in $[C_4mpyrr][NTf_2]$ on the gold electrode over a scan rate range of 0.025 - 1.0 V s^{-1}. Inlay: Plots of peak current against root square of scan rate for cyclic voltammetric response of 1.0 mM ferrocene in $[C_4mpyrr][NTf_2]$ on the gold macro disc electrode. Solid line shows results predicted by Randles-Ševčík equation.

9.3.2 The Oxidation of Ferrocene on the Gold Macro-disc Electrode Studies Using $[C_4mpyrr][NTf_2]$ as Solvent

The performance of the gold macro-disc electrode was evaluated by analysing 1.0 mM ferrocene in $[C_4mpyrr][NTf_2]$. Figure 9.3 shows the cyclic voltammograms of the oxidation of ferrocene in $[C_4mpyrr][NTf_2]$ on the gold electrode over a scan rate range of 0.025 - 1 V s^{-1}. The peak at ca. + 0.15 V vs. Ag corresponds to the oxidation of ferrocene. Inlay of Figure 9.3 demonstrates the corresponding Randles-Ševčík plots, where a diffusion coefficient of (2.43 $\pm$0.07) $\times 10^{-11}$ m^2 s^{-1} was found. This result is very close to the literature value of 2.55 $\times$ 10^{-11} m^2 s^{-1}. [23]

9.3.3 The Platinum Micro-band Electrode in $[C_3mim][NTf_2]$

To validate the fabricated platinum micro-band electrode, experimental and simulated voltammetric and chronoamperometric responses of this electrode in 2.0 mM DmFc in $[C_3mim][NTf_2]$ were compared.

Decamethylferrocene (DmFc) is a frequently used internal reference alternative to ferrocene[24]. As compared to ferrocene for use in ionic liquids[25, 26], DmFc is more suitable since it is more resistant to evaporation under vacuum or high temperature from the ionic liquid[27].

Diffusion coefficients of DmFc and $DmFc^+$ in $[C_3mim][NTf_2]$ were first determined using a well established program[15] of double step chronoamperometry on a commercially available platinum micro-disc electrode (radius = 5.0 μm) . Figure 9.4 shows the fitting of simulated and experimental data which resulted in diffusion coefficients for DmFc and $DmFc^+$ of (2.5 $\pm$ 0.1) $\times$ 10^{-11} m^2 s^{-1} and (9.7 $\pm$ 0.2) $\times$ 10^{-11} m^2 s^{-1} at 298K respectively. For comparison, the diffusion coefficients of DmFc and $DmFc^+$ in $[C_3mim][NTf_2]$ have been found to be (2.49 $\pm$ 0.2) $\times$ 10^{-11} m^2 s^{-1} and (9.57 $\pm$ 0.06) 10^{-12} m^2 s^{-1}.[28] Thus the value determined in this work is consistent with the literature value. [28]

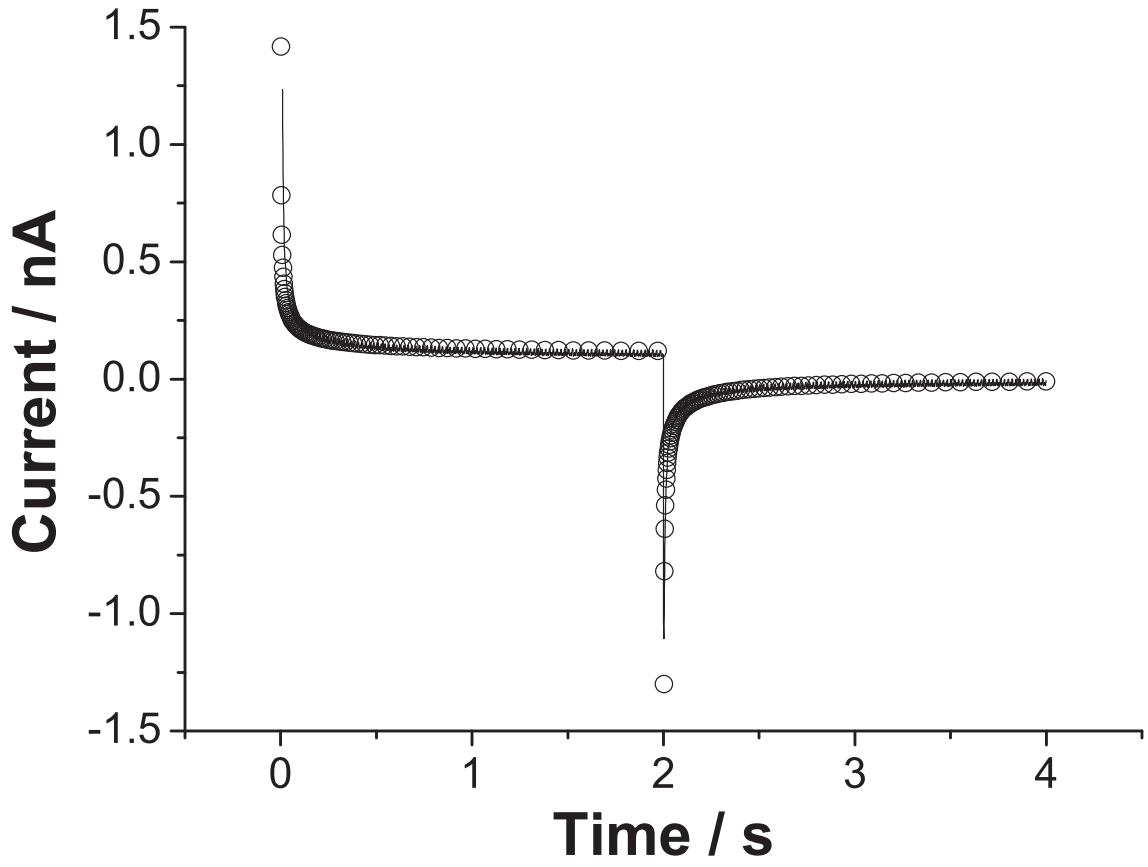

Figure 9.4: Double step chronoamperometric response (solid line) of 2 mM DmFc in $[C_3mim][NTf_2]$ at 298 K on a 5.0 μm platinum micro disc and corresponding line of best fit (circles) using homemade program.

The values of the two diffusion coefficients were used to fit the cyclic voltammetry simulation of the same system in order to find the value of the heterogeneous electron transfer rate constant, k_0, $(7 \pm 1) \times 10^{-6}$ m s^{-1}. Figure 9.5 compares simulated and experimental voltammetry for 2.0 mM DmFc in $[C_3mim][NTf_2]$ on platinum micro-disc electrode at scan rates ranging from 50 to 400 mV s^{-1}, where a high correlation is observed between simulated and experimental data.

Similar experiments were performed on the platinum micro-band electrodes (width = 50 μm and length = 2.45 mm). The simulation program described in section 9.2.2 was used to fit the experimental data. Figure 9.6 a) compares simulated and experimental chronoamperometry for oxidation of DmFc on the platinum micro-band electrode, using the diffusion coefficient for DmFc of $(2.49 \pm 0.02) \times 10^{-11}$ m^2 s^{-1}, where good agreement

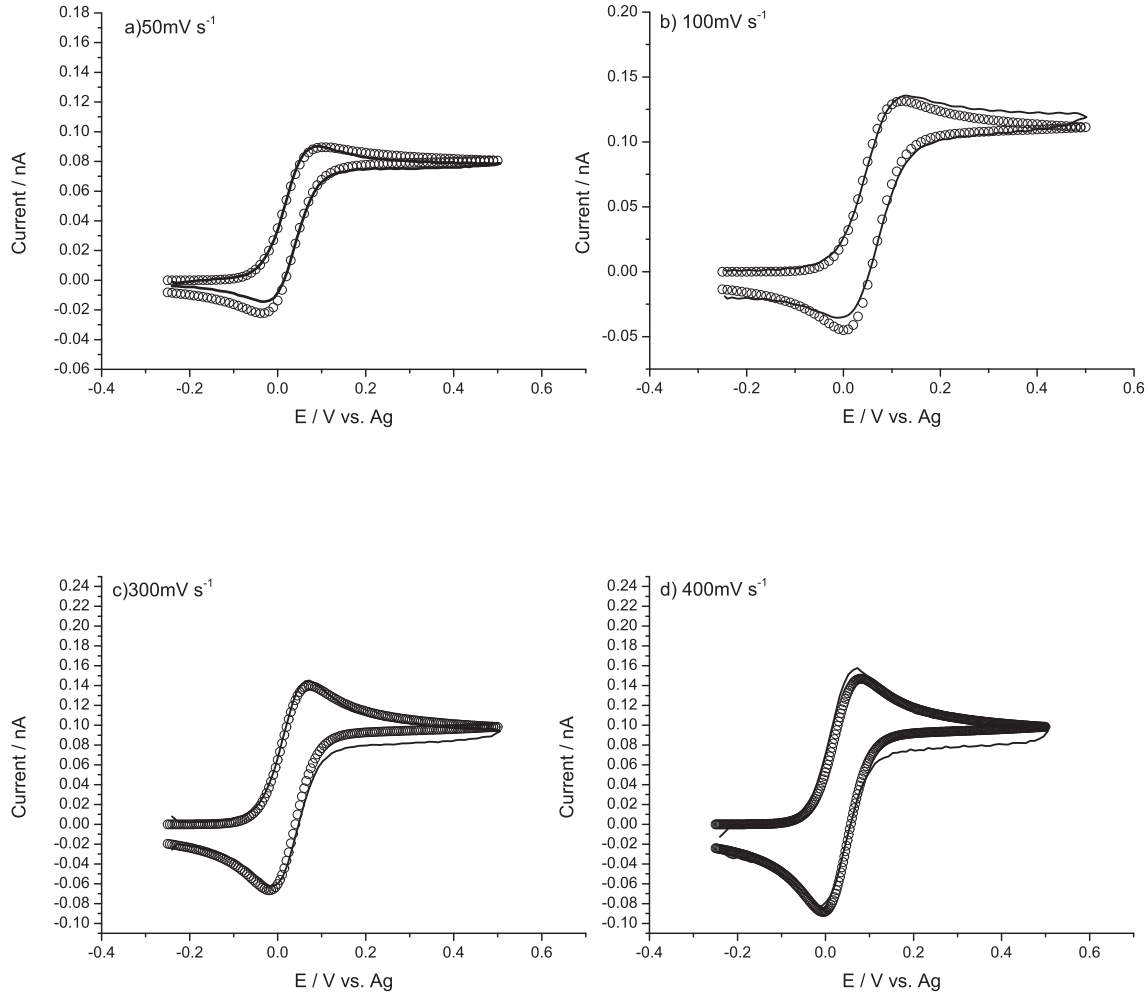

Figure 9.5: Comparison of simulated (circles) and experimental (solid line) voltammetry for DmFc in C_3mimNTF on 5.0 μm platinum micro disc at a scan rate of a) 50 mV s^{-1}, b) 100 mV s^{-1}, c) 300 mV s^{-1} and d) 400 mV s^{-1}.

is seen.

The reproducibility of the system was investigated via performing chronoamperometry at different platinum micro-band electrodes over a duration of 15 days in 2.0 ($\pm$0.15) DmFc in [C_3mim][NTf_2]. Figure 9.6 b) compares the chronoamperometric responses for 2.0 ($\pm$0.15) mM DmFc in [C_3mim][NTf_2] at three different electrodes over 15 days where gives a current variation of 4.3 %. The reproducibility is high enough to allow quantitative analysis.

Figure 9.7 shows the fittings of the voltammetric responses of the platinum micro-band electrode at scan rates ranging from 50 mV s^{-1} to 400 mV s^{-1} where diffusion coefficients

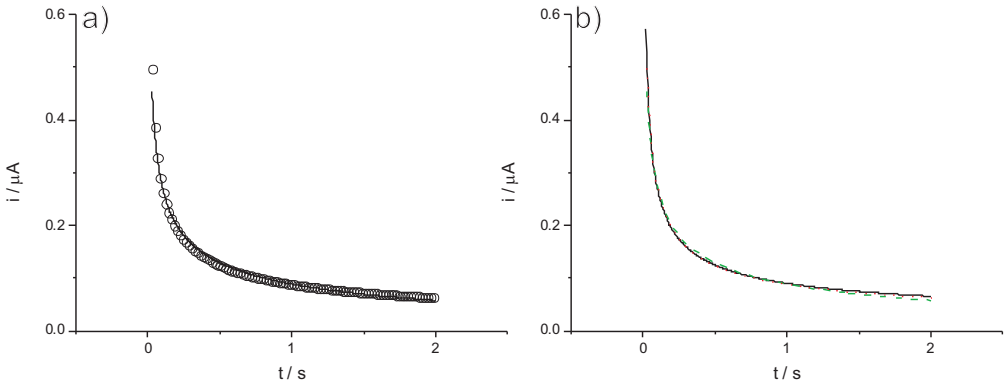

Figure 9.6: a)Chronoamperometric response (solid line) of 2.0 mM DmFc in $[C_3mim][NTf_2]$ at 298 K on the platinum micro-band electrode (l=6.28 mm, w=50 μm) and corresponding simulated data (circles). b)Comparison of chronoamperometric responses of 2.0 (*pm* 0.15) mM DmFc in $[C_3mim][NTf_2]$ at 298 K on three different platinum micro-band electrodes (l=2.45 ($\pm$ 0.10) mm, w=50 μm) over a period of 15 days.

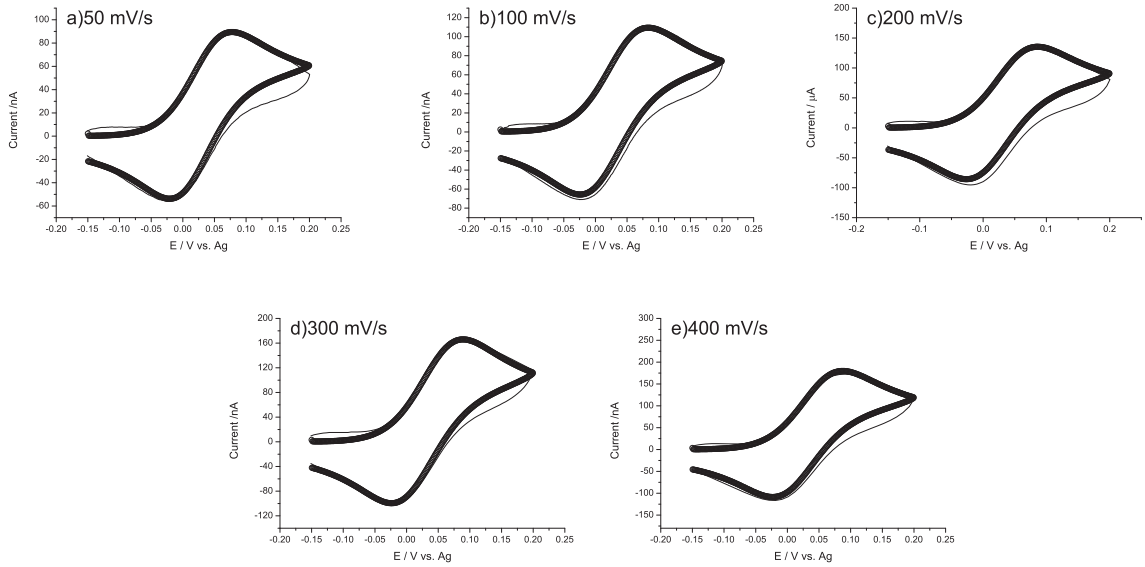

Figure 9.7: Comparison of simulated (circles) and experimental (solid line) voltammetry for DmFc in C_3mimNTF on a platinum micro-band (l = 6.28 mm, w = 50 μm) at a scan rate of a) 50 mV s^{-1}, b) 100 mV s^{-1}, c) 200 mV s^{-1} , d) 300 mV s^{-1} and e) 400 mV s^{-1}.

for DmFc and $DmFc^+$ of 2.49 $\times$ 10^{-11} m^2 s^{-1} and 9.50 $\times$ 10^{-11} m^2 s^{-1} and k_0 of 7 $\times$ 10^{-6} m s^{-1} were found. Again good agreement between the commercial Pt micro-disc electrode and fabricated Pt micro-band electrode indicates that the fabrication method is successful and that quantitative electrochemistry is possible with the latter.

9.3.4 Oxygen Reduction in RTILs at Gold Macro-disc and Platinum Micro-band Electrode

In this section oxygen gas detection is used as an example to demonstrate the suitability of the gold macro-disc and platinum micro-band electrodes for real world application. The volume percentage of O_2 was tuned by changing the composition of N_2 and O_2 in the gas mixture. $[C_3mim][NTf_2]$ was saturated with the gas mixture by passing over the gas mixture for more than 30 min.

The one electron reduction of O_2 in ionic liquids has been abundantly reported in literature[23, 29–31] and also in the previous chapters (see Reaction 6.7 in Chapter 6).

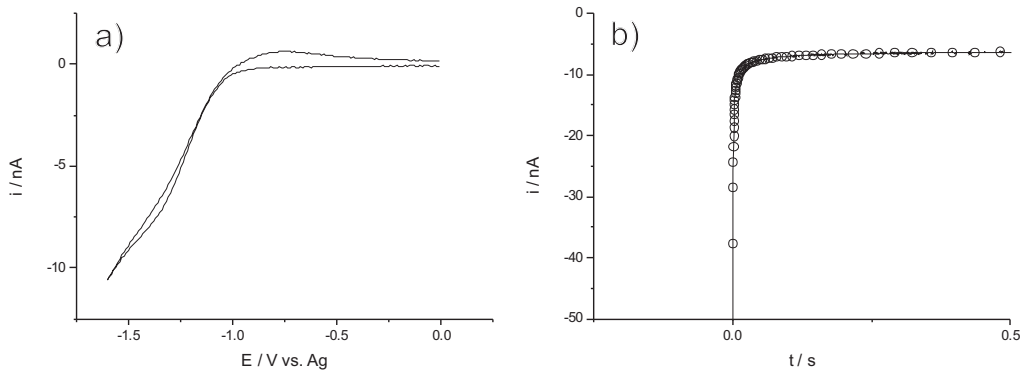

Figure 9.8: a)Cyclic voltammetry and b) chronoamperometry for pure oxygen in $[C_3min][NTf_2]$ at 5.0 μm micro-disc platinum micro-disc electrode using 0.05 V s^{-1}.

In order to obtain the diffusion coefficient of O_2 in $[C_3mim][NTf_2]$ and in addition to compare the concentrations of pure O_2 for fabricated electrodes, the values of diffusion coefficient and concentration of pure oxygen in $[C_3mim][NTf_2]$ were first determined by simulating the chronoamperometric response for oxygen at a commercial platinum electrode of known size. To determine the step potential for chronoamperometry of the first oxygen reduction, cyclic voltammetry was carried out. Figure 9.8 a) shows cyclic voltammetry of O_2 in $[C_3mim][NTf_2]$ at 0.05 V s^{-1}. It is observed that no current passes at 0.0 V vs. Ag and reduction is fully driven at 1.5 V vs. Ag. Therefore the following

chronoamperometry procedure is used: the potential was first held at 0.0 V for 20 seconds then stepped to 1.5 V for 2 seconds. Figure 9.8 b) shows the fitting of chronoamperometric response for O_2 in $[C_3mim][NTf_2]$ on 5.0 μm radius platinum electrode at 298 K. An oxygen concentration of 5.65 mM and a diffusion coefficient of 8.0×10^{-10} m^2 s^{-1} were determined.

Cyclic voltammetry was carried out for analysing $[C_3mim][NTf_2]$ containing different percentage by volume of oxygen at gold macro-disc electrode at 298 K. Figure 9.9 a) shows the cyclic voltammetry of 100 %, 75 %, 50 % and 25 % O_2 in $[C_3mim][NTf_2]$ at gold macro-disc electtrode at 0.01 V s^{-1} at 298 K. Each cyclic voltammetry gives a well defined peak at c.a. 1.2 V vs. Ag. Peak current, i_p, is related to concentration, c, by applying the equation for a one-electron transfer irreversible reduction.[32, 33](Equation 1.29 in Chapter 1)

Here, α is the transfer coefficient and others are all as defined above. α was determined to be 0.35 via analysing the gradient of Tafel plot(Equation 1.12 in Chapter 1), which was simply done by plotting natural logarithm of current against potential in cyclic voltammetry.

Given the diffusion coefficient, 8.0×10^{-10} m^2 s^{-1}, the transfer coefficient, 0.35 and the surface area were known, the concentrations of oxygen at each percentage by volume of O_2 were calculated: 5.99 ($\pm$ 0.35) mM; 100 % O_2, 4.34 ($\pm$ 0.27) mM; 75 % O_2, 3.00 ($\pm$ 0.26) mM; 50 % O_2 and 1.64 ($\pm$ 0.26) 25 % O_2. The concentrations of 100 % O_2 at the commercial platinum micro-disc electrode and the home-made gold macro-disc electrode are in close agreement.

To mimic the classic Clark type O_2 sensor using a platinum micro-band electrode, steady state current was used to analyse the concentrations of different percentage by volume of O_2. To obtain steady state current, the potential was stepped to 1.5 V for 2 seconds. Steady state currents were reached after ca. 1 second and the data over first

second were discarded to simplify analysis. Figure 9.9 b) shows the steady state currents at different percentage by volume of O_2 at 298 K. The currents were fitted by previous discussed simulation program (see Section 9.2.2) and the concentrations of O_2 at different percentage by volume were evaluated: 5.70 ($\pm$ 0.20) mM; 100 % O_2, 4.25 ($\pm$ 0.15) mM; 75 % O_2, 2.90 ($\pm$ 0.16) mM; 50 % O_2 and 1.55 ($\pm$ 0.21) 25 % O_2. Values of the O_2 concentration measured at the platinum micro-band electrode are consistent to that at platinum micro-disc electrode with a difference of 2 %.

Figure 9.9 c) compares the plots of O_2 concentration against O_2 % at gold macro-disc and platinum micro-band electrodes in [C_3mim][NTf_2] at 298 K which results in gradients of 0.059 and 0.057 for gold macro-disc and platinum micro-band respectively where the corresponding percentage difference was less than 4 %. This indicates these two types of electrodes are suitable to be used in O_2 detection. The gradient in this plot can then be used to calculate the Henry's law constant. Henry's law relates the solubility of oxygen to the partial pressure and is described as below,

$$p = k_H \times x \tag{9.1}$$

Here, p(/bar) is the partial pressure of O_2 , x is the mole fraction of gas in solution (dimensionless) and k_H(/bar) is the Henry's law constant. To calculate the Henry's law constant, the total pressure of the gas mixture is taken to be 1 bar and the mole fraction of pure oxygen dissolved in [C_3mim][NTf_2] is 3.7×10^{-3}. These values lead to a Henry's law constant of 621 $\pm$ 11 bar for the gold macro-disc electrode and 637 $\pm$ 8 bar for the platinum micro-band electrode respectively which again are in good agreement.

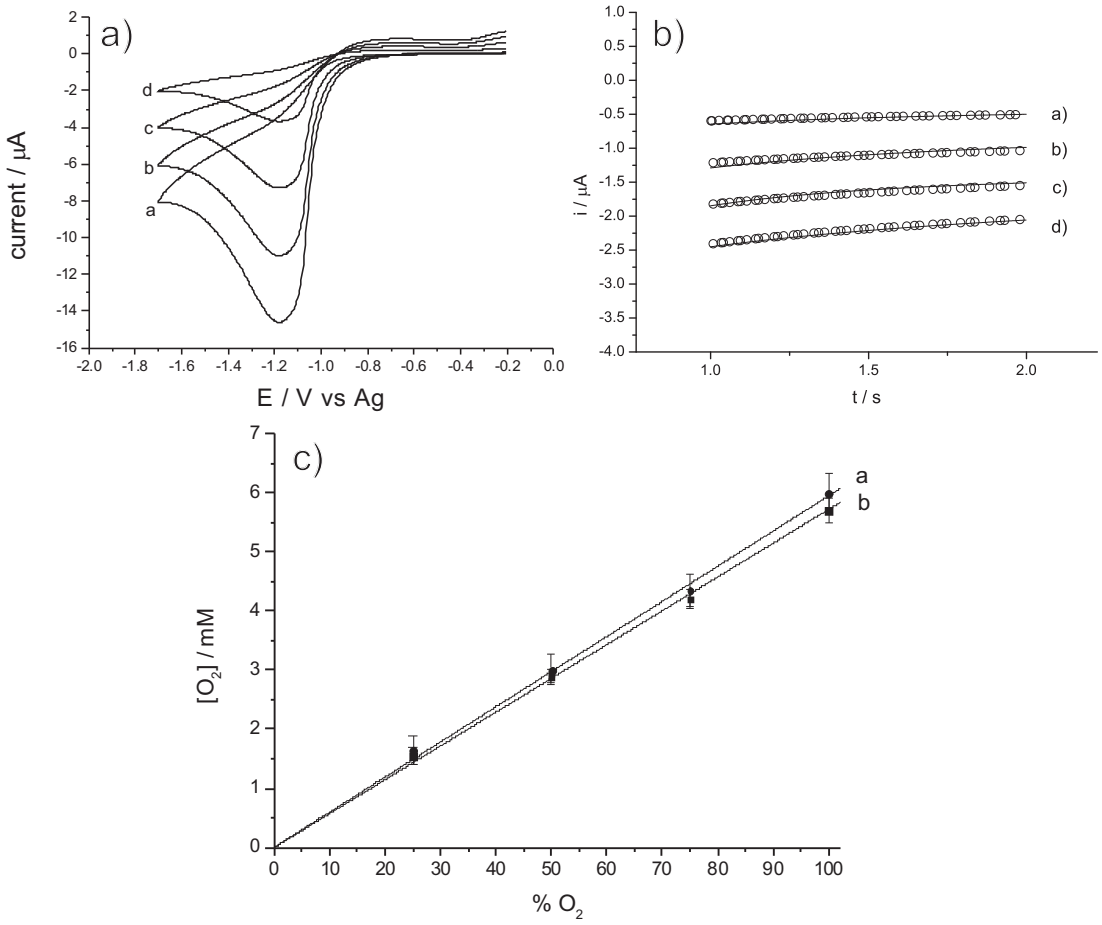

Figure 9.9: a) Cyclic voltammetric responses for oxygen of a) 100 %, b) 75 %, c) 50 % and d) 25 % (by volume) in [Pmin][NTf_2] at a gold macro-disc electrode using a scan rate of 0.01 V s^{-1}. b) The fittings of steady state current for a) 100 %, b) 75 %, c) 50 % and d) 25 % (by volume) O_2 in [Pmin][NTf_2] at the platinum micro-band electrode. c) The fittings of steady state current for (a) 100 %, (b) 75 %, (c) 50 % and (d) 25 % (by volume) O_2 in [Pmin][NTf_2] at the platinum micro-band electrode. Plots of O_2 concentration against percentage by volume of oxygen determined from a) gold macro-disc electrode and b) platinum micro-band electrode.

9.4 Conclusions

A simple and inexpensive method of manufacturing cheap disposable electrodes of different materials and shapes has been described. The method, based on laminating the electrodes, is effective for the fabrication of disposable electrodes. These home-made electrodes have been analysed in three commonly used systems, aqueous $(Ru(NH_3)_6^{3+}$, ferrocene in [C_4mpyrr][NTf_2] and DmFc in [C_3mim][NTf_2]. Diffusion coefficients for ana-

lytes at each experiment have been evaluated using relevant theory or simulations. These values have been either compared with literature values, or values collected from an commercially available electrode of known size. In all cases, very good agreement has been found. This suggests the home made electrodes are suitable for use in both ionic liquids and aqueous solution, and may be made to both macro and micro scale. Further these two types of electrode have been studied for use in oxygen detection. Values of dissolved pure oxygen concentrations in $[C_3mim][NTf_2]$ at a commercial platinum micro-disc electrode has been compared and good agreement found. The concentrations of oxygen have been determined at different % (by volume) at both gold macro-disc and platinum micro-band electrodes. Less than 4 % difference in oxygen concentration has been found, suggesting both electrodes are suitable for use in oxygen detection. In addition, the Henry's law constants of oxygen obtained from both electrodes agree very well.

References

[1] Xiong, L.; Lowinsohn, D.; Ward, K. R.; Compton, R. G. *Analyst* **2013**, *138*, 5444–5452.

[2] Dias, A. C. M. S.; Gomes-Filho, S. L. R.; Silva, M. M. S.; Dutra, R. F. *Biosensors and Bioelectronics* **2013**, *44*, 216–221.

[3] Kanyong, P.; Pemberton, R. M.; Jackson, S. K.; Hart, J. P. *Analytical Biochemistry* **2013**, *435*, 114–119, cited By (since 1996) 0; Article in Press.

[4] Xuan Viet, N.; Chikae, M.; Ukita, Y.; Maehashi, K.; Matsumoto, K.; Tamiya, E.; Hung Viet, P.; Takamura, Y. *Biosensors and Bioelectronics* **2013**, *42*, 592–597, cited B.

[5] Prehn, R.; Abad, L.; Snchez-Molas, D.; Duch, M.; Sabat, N.; Del Campo, F. J.; Muoz, F. X.; Compton, R. G. *Journal of Electroanalytical Chemistry* **2011**, *662*, 361–370.

[6] Wang, T.-J.; Huang, C.-F.; Wang, W.-S.; Wei, P.-K. *IEEE JOURNAL OF LIGHTWAVE TECHNOLOGY* **2004**, *22*, 1764–1771.

[7] Davies, T. J.; Ward-Jones, S.; Banks, C. E.; del Campo, J.; Mas, R.; Muoz, F. X.; Compton, R. G. *Journal of Electroanalytical Chemistry* **2005**, *585*, 51 – 62.

[8] Lee, H.; Shin, H.; Jeong, Y.; Moon, J.; Lee, M. *Applied Physics Letters* **2009**, *95*, p071104.

[9] Koppenol, M.; Cooper, J. B.; Bond, A. M. *American Laboratory* **1994**, *26*, 25–29.

[10] Shao, Y.; Mirkin, M.; Fish, G.; Kokotov, S.; Palanker, D.; Lewis, A. *Analytical Chemistry* **1997**, *69*, 1627–1634.

[11] Kovach, P. M.; Caudill, W. L.; Peters, D. G.; Wightman, R. M. *Journal of Electroanalytical Chemistry* **1985**, *185*, 285–295.

[12] Shea, T. V.; Bard, A. J. *Analytical Chemistry* **1987**, *59*, 2101–2111.

[13] Welford, P. J.; Freeman, J.; Wilkins, S. J.; Wadhawan, J. D.; Hahn, C. E. W.; Compton, R. G. *Analytical Chemistry* **2001**, *73*, 6088–6092.

[14] Angnes, L.; Richter, E. M.; Augelli, M. A.; Kume, G. H. *Analytical Chemistry* **2000**, *72*, 5503–5506.

[15] Klymenko, O. V.; Evans, R. G.; Hardacre, C.; Svir, I. B.; Compton, R. G. *Journal of Electroanalytical Chemistry* **2004**, *571*, 211–221.

[16] Alden, J. A.; Compton, R. G. *Journal of Electroanalytical Chemistry* **1996**, *402*, 1–10.

[17] Wang, Y.; Limon-Petersen, J. G.; Compton, R. G. *Journal of Electroanalytical Chemistry* **2011**, *652*, 13–17.

[18] Banks, C. E.; Rees, N. V.; Compton, R. G. *Journal of Electroanalytical Chemistry* **2002**, *535*, 41–47.

[19] Marken, F.; Eklund, J. C.; Compton, R. G. *Journal of Electroanalytical Chemistry* **1995**, *395*, 335–339.

[20] Banks, C. E.; Compton, R. G.; Fisher, A. C.; Henley, I. E. *Physical Chemistry Chemical Physics* **2004**, *6*, 3147–3152.

[21] Randles, J. E. B. *Transactions of the Faraday Society* **1948**, *44*, 327–338.

[22] Sevcik, A. *Collection of Czechoslovak Chemical Communications* **1948**, *13*, 349–377.

[23] Rogers, E. I.; Silvester, D. S.; Poole, D. L.; Aldous, L.; Hardacre, C.; Compton, R. G. *Journal of Physical Chemistry C* **2008**, *112*, 2729–2735.

[24] Noviandri, I.; Brown, K. N.; Fleming, D. S.; Gulyas, P. T.; Lay, P. A.; Masters, A. F.; Phillips, L. *The Journal of Physical Chemistry B* **1999**, *103*, 6713–6722.

[25] Fu, C.; Aldous, L.; Dickinson, E. J. F.; Manan, N. S. A.; Compton, R. G. *ChemPhysChem* **2011**, *12*, 1708–1713.

[26] Vorotyntsev, M. A.; Zinovyeva, V. A.; Konev, D. V.; Picquet, M.; Gaillon, L.; Rizzi, C. *Journal of Physical Chemistry B* **2009**, *113*, 1085–1099.

[27] Xiong, L.; Fletcher, A. M.; Davies, S. G.; Norman, S. E.; Hardacre, C.; Compton, R. G. *Analyst* **2012**, *137*, 4951–4957.

[28] Barnes, E. O.; Xiong, L.; Ward, K. R.; Compton, R. G. *Journal of Electroanalytical Chemistry* **2013**, –.

[29] Evans, R. G.; Klymenko, O. V.; Saddoughi, S. A.; Hardacre, C.; Compton, R. G. *Journal of Physical Chemistry B* **2004**, *108*, 7878–7886.

[30] Huang, X. J.; Rogers, E. I.; Hardacre, C.; Compton, R. G. *The Journal of Physical Chemistry B* **2009**, *113*, 8953–8959.

[31] Switzer, E. E.; Zeller, R.; Chen, Q.; Sieradzki, K.; Buttry, D. A.; Friesen, C. *The Journal of Physical Chemistry C* **2013**, *117*, 8683–8690.

[32] Compton, R. G.; Banks, C. E. *Understanding Voltammetry*; Imperial College Press, 2011, 2nd Edition.

[33] Bard, A.; Faulkner, L. *Electrochemical Methods: Fundamentals and Applications*; Wiley, 2001.

Chapter 10

Evaluation of A Simple Disposable micro-band electrode Device for Amperometric Gas Sensing

Following the success of previous work on the use of laminated macro-disc and micro-band electrodes for electrochemical experiments, including in aqueous, non-aqueous and RTIL systems, this chapter further demonstrates the home-made laminated Pt (6.3 mm $\times$ 50 μm) and Cu (6.3 mm $\times$ 30 μm) annular micro-band electrodes for use in room temperature ionic liquids (RTILs) and proposes their use for amperometric gas sensing. The suitability of micro-band electrodes for use in electrochemical analysis was examined in experiments on two systems. The first system studied to validate the electrochemical responses of the annular micro-band electrode was decamethylferrocene (DmFc), as a stable internal reference probe commonly used in ionic liquids, in $[C_3mim][NTf_2]$, where the diffusion coefficients of DmFc and $DmFc^+$ and the standard electron rate constant for the $DmFc/DmFc^+$ couple were determined through fitting chronoamperometric and cyclic voltammetric responses with relevant simulations.These values are independently compared with those collected from a commercially available Pt microdisc electrode with excellent agreement. The second system focuses on O_2 reduction in $[C_3mim][NTf_2]$, which is used as a model for gas sensing. The diffusion coefficients of O_2 and $O_2^{\cdot-}$ and the electron transfer rate constant were again obtained using chronoamperometry and cyclic

voltammetry, along with simulations. Results determined from the micro-bands are again consistent to those evaluated from the Pt microdisc electrode when compared these results from home-made micro-band and commercially available microdisc electrodes. These observations indicate that the fabricated annular micro-band electrodes are suitable for quantitative measurements. Further the successful use of the Cu electrodes in the O_2 system suggests a cheap disposable sensor for gas detection. This work has been published in *Sensors and Actuators B.*[1]

10.1 Introduction

The previous chapter discussed the use of laminated electrodes as working electrodes in electrochemical experiments in various solvent media. This chapter is concerned with the home-made electrode in room temperature ionic liquids. The benefits of RTILs as solvents for gas sensors as compared to conventional solvents have been discussed earlier in the thesis. Chapter 2 introduced the possible design of membrane free gas sensors through combining room temperature ionic liquids as solvents and laminated electrodes as sensing probes. Huang et al.[1] successfully developed a membrane free oxygen sensor using micro-electrode arrays as working electrodes and ionic liquids($[P_{14,6,6,6}][FAP]$) as solvents. This oxygen sensing system showed high sensitivity and most importantly, was freed from the problem caused by the use of membranes, especially frequent calibration.

In this chapter a design for a gas sensor is proposed which utilises micro-band electrodes and RTIL solvents. The aim of this work is to validate the use of such electrodes for gas sensing in RTIL media and to show that such electrodes are easily fabricated to the extent that practical disposable electrodes could be readily envisaged.

The use of chronoamperometry to measure gas concentrations and diffusion coefficients in this type of electrode is established by conducting O_2 detection using the RTIL $[C_3mim][NTf_2]$. Two additional observations to be reported are first that the solubility of

O_2 in this RTIL is essentially independent of temperature and second that Cu metal may be used as a satisfactory but cheap cathode material for O_2 sensing.

10.2 Electrode Fabrication

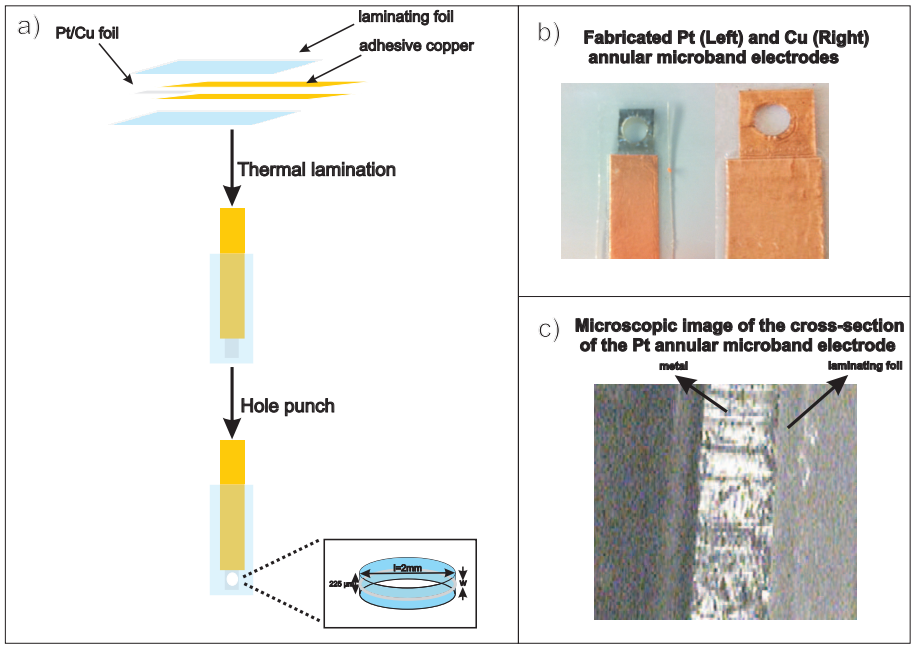

Figure 10.1: a) Schematic illustration of electrode fabrication. l and w refer to the diameter of the circle and width of the annular band electrodes respectively. b) Final appearance of fabricated electrodes. c) Microscopic image of the cross-section of Pt annular microband electrode.

The approach to the electrode preparations for platinum and copper annular band electrodes are summarised schematically in Figure 10.1 a). Both Pt and Cu annular band electrodes were fabricated by thermal lamination[36] of a piece of Pt (width = 50 μm, Buckbee Mears Co., St. Paul, US) or Cu foil (width = 30 μm, Buckbee Mears Co., St. Paul, US). Electrical connection to the foil is established prior to lamination by using a piece of copper foil with a conductive adhesive on one side (3 M Scotch brand electrical tape No. 1739-7).[36] The copper foil was then thermally sandwiched between two layers of polyester/polyethylene (in a 4:1 mass ratio) laminating foil (Murodigital, Weston Super Mare, Somerset U.K., thickness = 225 μm) which was found to be resistant to most

organic solvents and water.[36] Lamination was carried out at the temperature pre-set by the laminator and under standard pressure (1 bar). Note the thermal lamination step may be repeated several times to ensure a thorough sealing of the electrodes. The annular micro-band surfaces were revealed by simply punching the lamination normal to the foil with a hole punch (Weaver Leather, USA). The annular micro-band electrode was in the wall of the lamination. The circumference of the band was calculated to be 6.28 ($\pm$ 0.09) mm by directly measuring the diameter (diameter = 2 $\pm$ 0.3) mm of the punching head with callipers. Figure 10.1 b) shows the final appearance of Pt and Cu annular micro-band electrodes. A microscopic image was taken to present the structure of the micro-band electrode. Figure 10.1 c) shows the corresponding cross-sectional microscopic image of the Pt annular micro-band electrode. The electrode dimensions as inferred from the size of the foils used, and microscopically, are quantitatively consistent with all the electrochemical characterisation reported later in this chapter. More than 20 electrodes were made and each electrode performed more than 50 scans per day. The variation for the same experiment at different electrodes was no more than 5 % which was evaluating by standard deviation of the steady state currents.

10.3 Results and Discussion

In this section, two experimental systems are reported: decamethylferrocene (DmFc) oxidation and O_2 reduction in $[C_3mim][NTf_2]$. Mass transport and electron transfer were studied using cyclic voltammetry and chronoamperometry, along with simulations. In each experiment, data was first collected at a commercially available Pt microdisc electrode of 5.0 μm radius. These results are then compared with those obtained from Pt and Cu micro-band electrodes in order to validate the electrochemical application of the home-made micro-band electrodes and their use in gas sensing.

10.3.1 Oxidation of Decamethylferrocene in $[C_3mim][NTf_2]$

The first analysis was performed in $[C_3mim][NTf_2]$ containing decamethylferrocene at Pt microdisc electrodes, Cu and Pt micro-band electrodes.

Decamethylferrocene (DmFc) undergoes a one-electron oxidation at c.a. +0.15 V vs. Ag in $[C_3mim][NTf_2]$. The oxidation is described below [16, 18],

$$DmFc \rightleftharpoons DmFc^{+} + e^{-} \tag{10.1}$$

Chronoamperometry and cyclic voltammetry were carried out to analyse the oxidation. Results were first collected from a 5.0 μm radius Pt microdisc electrode which were then compared with those determined from Pt and Cu annular micro-band electrodes in order to investigate the capability of such micro-band electrodes as working electrodes for electrochemical analysis.

Analysis of DmFc at Pt Micro-disc Electrodes

The diffusion coefficients of DmFc (D_{DmFc}) and $DmFc^{+}$ ($D_{DmFc^{+}}$) at the Pt microdisc electrode were determined using double step chronoamperometry. In double step chronoamperometry, the potential is first stepped from a potential where no current passes to a potential where the reaction rate is controlled by diffusion. In the second step, the electrode is returned to the original potential (or another) to reverse the process occurring during the first step.

To identify two suitable potentials, the DmFc oxidation at the Pt microdisc electrode was characterised by cyclic voltammetry. Figure 10.2 a) shows cyclic voltammetric response for 2.0 mM DmFc in $[C_3mim][NTf_2]$ at 50 mV s^{-1}. It is seen from this cyclic voltammetry that there is no current passing at c.a. -0.2 V vs. Ag and the oxidation is fully driven when the potential is more positive than c.a. 0.15 V vs. Ag. Therefore,

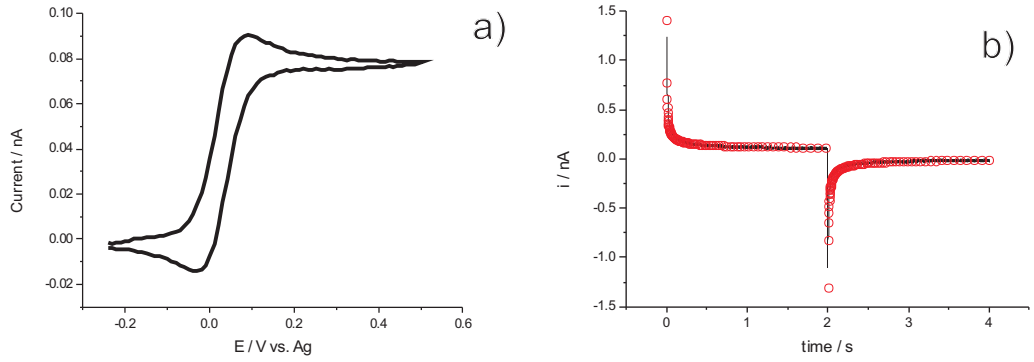

Figure 10.2: a) Cyclic voltammetry for 2.0 mM DmFc in $[C_3mim][NTf_2]$ at the 5.0 μm radius Pt microdisc electrode at 50 mV s^{-1}.b) Simulated and experimental data of double step chronoamperometric responses for 2.0 mM DmFc in $[C_3mim][NTf_2]$ at the 5.0 μm radius Pt microdisc electrode.

the following experimental procedure of double step chronoamperometry for DmFc was adopted throughout section 10.3.1: the potential was first held at -0.25 V vs. Ag for 20 s, after which the potential was stepped to +0.20 V vs. Ag for 2 s and back to -0.25 V vs. Ag for 2 s.

This experimental data was simulated via a simulation program for double potential step chronoamperometry at a microdisc electrode developed by Klymenko et al. [37] D_{DmFc} and D_{DmFc^+} were obtained through fixing the previously calibrated radius of the Pt microdisc electrode, 5.0 μm, and the known concentration of DmFc of 2.0 mM. The program initially simulated the first step where the value of D_{DmFc} was determined from Shoup and Szabo analysis of the first step.[38] D_{DmFc^+} was then deduced by inputting the determined D_{DmFc} into the simulation program.[37]

Figure 10.2 b) shows the simulated and experimental data for the chronoamperometric response of 2.0 mM DmFc in $[C_3mim][NTf_2]$ at the Pt microdisc electrode at 298 K. Excellent correlation between the experimental result and simulation is seen. The diffusion coefficients of DmFc and $DmFc^+$ were determined to be (2.49 $\pm$0.2) $\times$ 10^{-11} m^2 s^{-1} and (0.96 $\pm$0.6) $\times$ 10^{-11} m^2 s^{-1} respectively in $[C_3mim][NTf_2]$.

Next quantitative cyclic voltammetry was carried out at the Pt microdisc electrode.

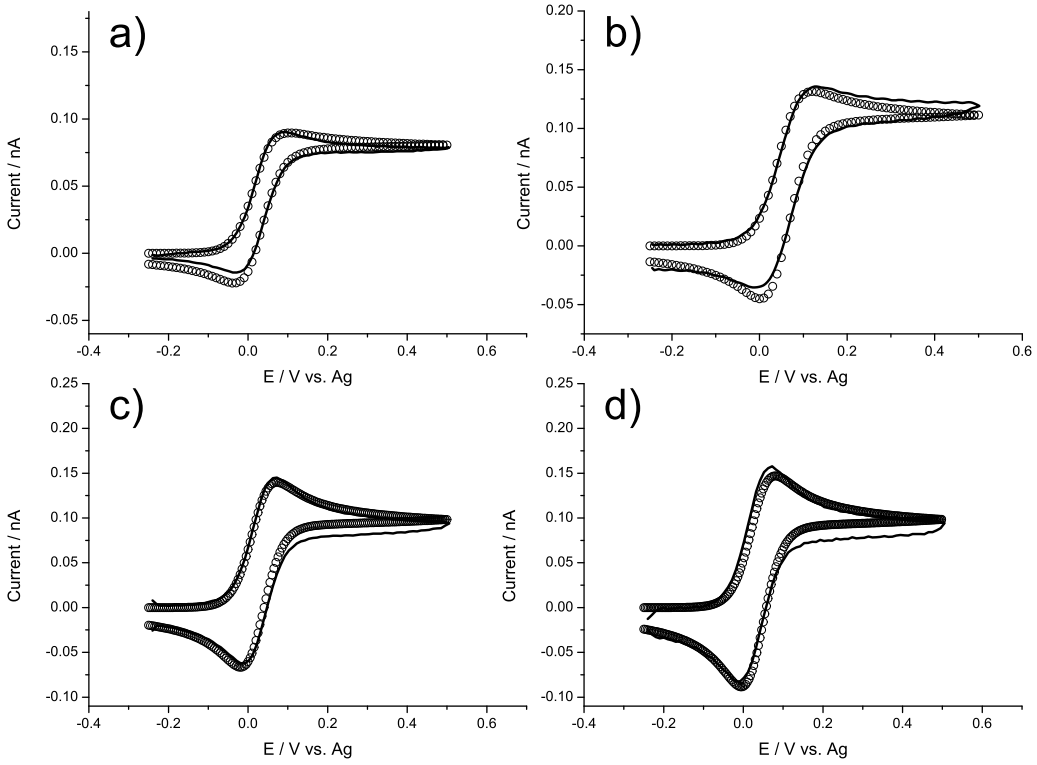

Figure 10.3: Simulated and experimental data of cyclic voltammetric responses for 2.0 mM DmFc in $[C_3mim][NTf_2]$ at the Pt microdisc electrode at scan rates of a) 50 mV/s, b) 100 mV/s c) 300 mV/s and d) 400 mV/s

Figures 10.3 a) to d) depict the simulated and experimental data for the cyclic voltammetry of DmFc oxidation in $[C_3mim][NTf_2]$ over a scan rate range of 50 mV s^{-1} to 400 mV s^{-1} over a potential range of -0.35 V to -0.3 V vs. Ag, giving the standard electrochemical rate constant, k_0, of $(7 \pm 1) \times 10^{-6}$ m s^{-1} and diffusion coefficients of DmFc and $DmFc^+$ of $(2.45 \pm 0.08) \times 10^{-11}$ m^2 s^{-1} and $(1.1 \pm 0.2) \times 10^{-11}$ m^2 s^{-1} respectively. The transfer coefficient, α, was determined to be 0.50 $\pm$ 0.08 prior to simulations via analysing the gradient of Tafel plot(Equation 1.12 in Chapter 1), which was simply done by plotting natural logarithm of current, I, against potential, E, in cyclic voltammetry. These results are in good agreement with those obtained from chronoamperomentry.

where R is the universal gas constant, F is the Faraday constant, I is the current, E is the step potential and T is the temperature.

For comparison, the diffusion coefficients of decamethylferrocene and decamethylfer-

rocenium in $[C_3mim][NTf_2]$ have been found to be (2.49 ± 0.2) × 10^{-11} m^2 s^{-1} and (9.57 ± 0.06).[39] D_{DmFc} and D_{DmFc^+} obtained from this work are consistent with the literature values.

Analysis of DmFc at Pt Annular Micro-band Electrodes

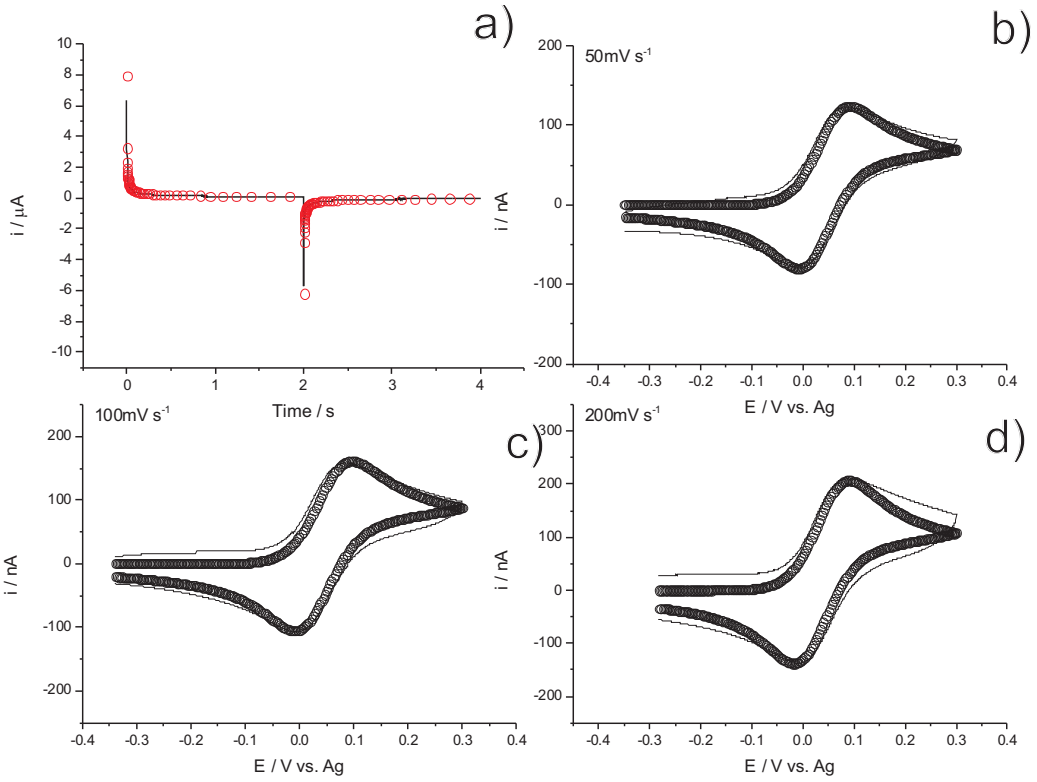

Figure 10.4: a) Double step chronoamperometric responses for 2.0 mM DmFc in $[C_3mim][NTf_2]$ at the Pt band electrode. b)-d) Simulated and experimental data of cyclic voltammetric responses for 2.0 mM DmFc in $[C_3mim][NTf_2]$ at the 5.0 μm radius Pt micro-band electrode at scan rates of b) 50 mV/s, c) 100 mV/s and d) 200 mV/s.

Similar experiments and analysis were performed on Pt annular micro-band electrodes. The simulated and experimental results for chronoamperometry and cyclic voltammetry of DmFc in pure $[C_3mim][NTf_2]$ are shown in Figure 10.4. The diffusion coefficients were found to be (2.43 ±0.15) × 10^{-11} m^2 s^{-1} for DmFc and (1.10 ±0.25) × 10^{-11} m^2 s^{-1} for $DmFc^+$ and the value of k_0 was again (7 ± 1) × 10^{-6} m s^{-1}. The value of α of 0.50 (± 0.05) was again evaluated using Tafel plot before simulations. These values are in

excellent agreement with those found with the platinum microdisc electrode, suggesting Pt micro-band electrodes can be *quantitatively* used as working electrodes in electrochemical analysis.

Analysis of DmFc at Cu Annular Micro-band Electrodes

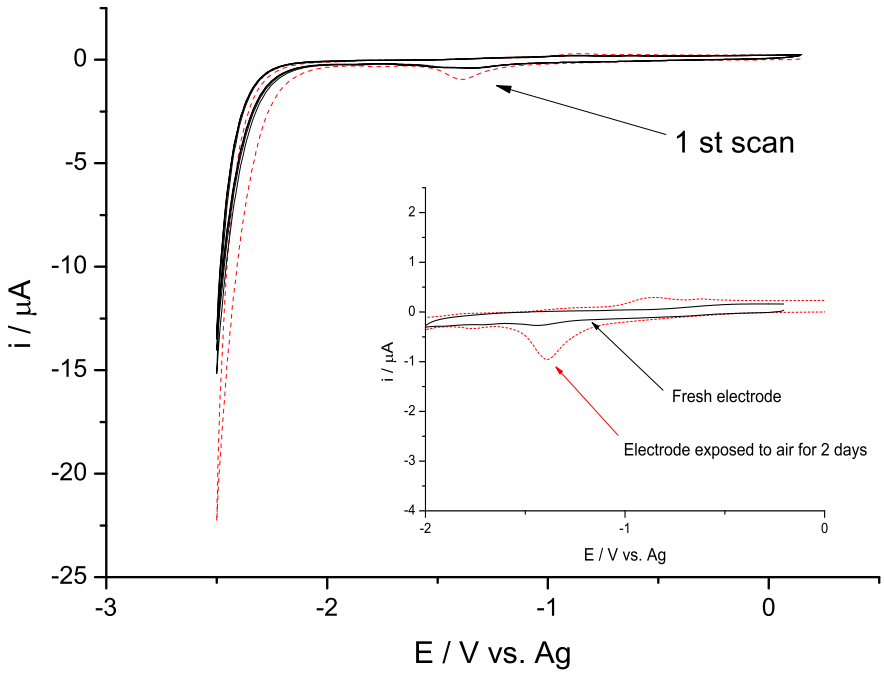

Figure 10.5: Successive cycles of cyclic voltammetric responses for the Cu band electrode in $[C_3mim][NTf_2]$. Insert: Comparison of the first scan of a Cu micro-band which was exposed to air for 2 days and a new Cu band.

Before carrying out any experiments on Cu annular micro-band electrodes, these electrodes were electrochemically activated by repetitive potential cycling from a start potential of c.a. 0 V vs. Ag to a potential more negative than c.a. -1.2 V vs. Ag in $[C_3mim][NTf_2]$ under dry N_2[40]. Figure 10.5 shows the successive cyclic voltammetric scans of the Cu micro-band electrodes in $[C_3mim][NTf_2]$ under dry N_2 between 0.15 V and -2.5 V vs. Ag at 100 mV s^{-1}. It is seen that a peak at c.a. -1.2 V vs. Ag visible on the first scan does not appear in the following scans. The insert in Figure 10.5 compares

[DmFc] (mM)	2.0	1.0	0.5
D_{DmFc} ($\times$ 10^{-11} m^2 s^{-1})	2.48 ($\pm$ 0.2)	2.48 ($\pm$ 0.1)	2.52 ($\pm$ 0.1)
D_{DmFc^+} ($\times$ 10^{-11} m^2 s^{-1})	0.90 ($\pm$ 0.5)	0.90 ($\pm$ 0.3)	1.10 ($\pm$ 0.5)

Table 10.1: Table of diffusion coefficients for DmFc and $DmFc^+$ at different concentrations of DmFc at the Cu annular band in $[C_3mim][NTf_2]$.

the first cyclic voltammetric scan at a Cu annular micro-band electrode exposed to air for 2 days with that at a new Cu annular micro-band electrode in pure $[C_3mim][NTf_2]$ under dry N_2. The peak at c.a. -1.2 V vs. Ag is much smaller at the new electrode. Such observations suggest that the peak at the first scan is likely due to the reduction of native copper oxide(s). Note the electrode surface may be partially 'blocked', which may lead to reduced voltammetric signals, if it is not activated.

Cu annular micro-band electrodes were investigated using the following approaches. First the Cu micro-band electrodes were studied in different concentrations of DmFc (2.0 mM, 1.0 mM and 0.5 mM) in $[C_3mim][NTf_2]$ at 298 K under dry nitrogen. The values of diffusion coefficient of DmFc and $DmFc^+$ were determined via simulations of the experimental results using a written in-house simulation program for double potential step chronoamperometry at a micro-band electrode developed by Barnes et al.[39] Figure 10.6 compares the simulated and experimental data for the chronoamperometric responses of 2.0 mM, 1.0 mM and 0.5 mM DmFc in $[C_3mim][NTf_2]$ under dry nitrogen. Table 10.1 shows the values of D_{DmFc} and D_{DmFc^+} tested in all concentrations of DmFc. The diffusion coefficients are in good agreement with the values determined from the Pt microdisc and the Pt annular micro-band electrodes.

Oxidations of 2.0 mM and 1.0 mM DmFc in $[C_3mim][NTf_2]$ at Cu annular micro-band electrodes were then analysed using cyclic voltammetry. The experimental data were fitted by a simulation program for cyclic voltammetry at a micro-band electrode developed by Ward et al.[41] Figure 10.7 shows simulations for the cyclic voltammetry of 2.0 mM and 1.0 mM DmFc in $[C_3mim][NTf_2]$ at scan rates of 100 mV s^{-1} and 50 mV s^{-1} at 298 K.

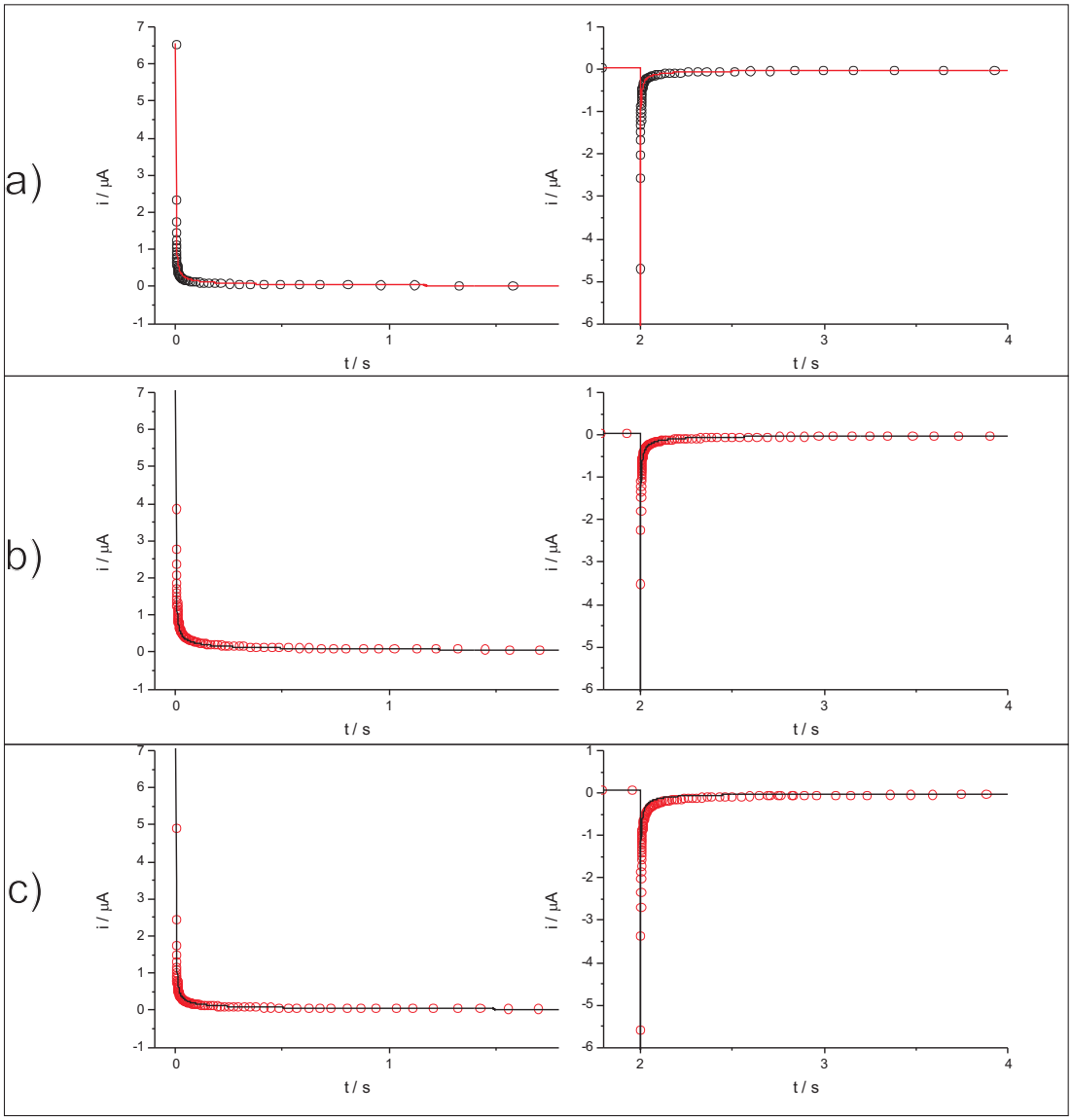

Figure 10.6: The first and second steps of double step chronoamperometry for a) 2.0 mM DmFc, b) 1.0 mM DmFc and c) 0.5 mM DmFc in $[C_3mim][NTf_2]$ at the Cu band electrode.

Via fitting the experimental data with the simulations, the diffusion coefficients of DmFc of 2.40 ($\pm$0.2) $\times$ 10^{-11} m^2 s^{-1} was found in 2.0 mM DmFc and that of (2.42 $\pm$0.2) $\times$ 10^{-11} m^2 s^{-1} was determined in 1 mM DmFc whilst the values of diffusion coefficient of its oxidised form were found to be (1.10 $\pm$0.15) $\times$ 10^{-11} m^2 s^{-1} with both concentrations. The value of α was evaluated to be 0.5 ($\pm$ 0.05) using a Tafel plot. These values were again in reasonable agreement to those found above. This indicates that both Pt and Cu

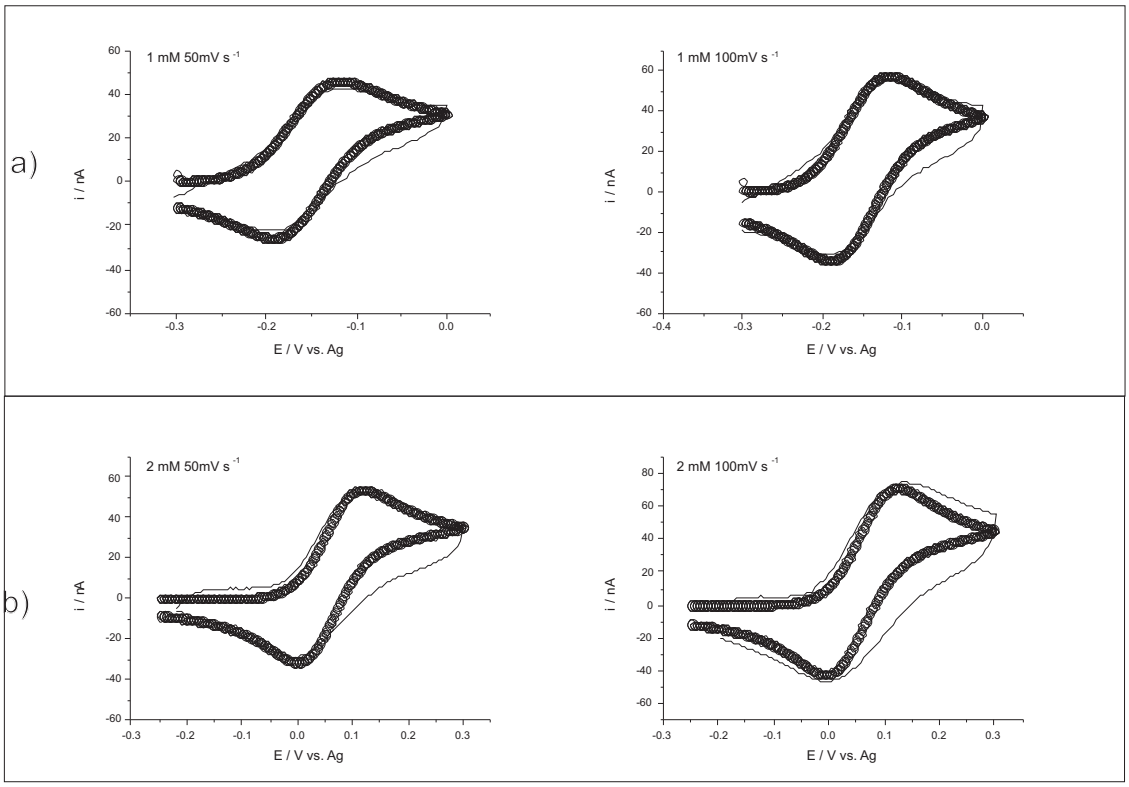

Figure 10.7: Simulated and experimental data of cyclic voltammetric responses for a) 1.0 mM DmFc and b) 2.0 mM DmFc in $[C_3mim][NTf_2]$ at the Cu band electrode at scan rates of 50 mV s^{-1} (left) and 100 mV s^{-1} (right).

micro-band electrodes can be able to be used to generate accurate results. The standard electrochemical rate constant for the $DmFc/DmFc^+$ couple was determined to be (5 $\pm$1) $\times$ 10^{-5} m s^{-1} and the same value was obtained at all concentrations. This higher rate constant of DmFc at Cu micro-band electrode indicates a faster electron-transfer rate of DmFc oxidation on Cu as compared to that on Pt.

10.3.2 Oxygen Reduction in $[C_3mim][NTf_2]$

The second set of analyses was conducted for the reduction of dissolved oxygen in $[C_3mim][NTf_2]$ over the temperature range of 298 K - 313 K on the Pt microdisc, Pt micro-band and Cu micro-band electrodes. The oxygen was passed through $[C_3mim][NTf_2]$ for more than 30 min to reach equilibrium and then the following reduction was studied[42, 43],

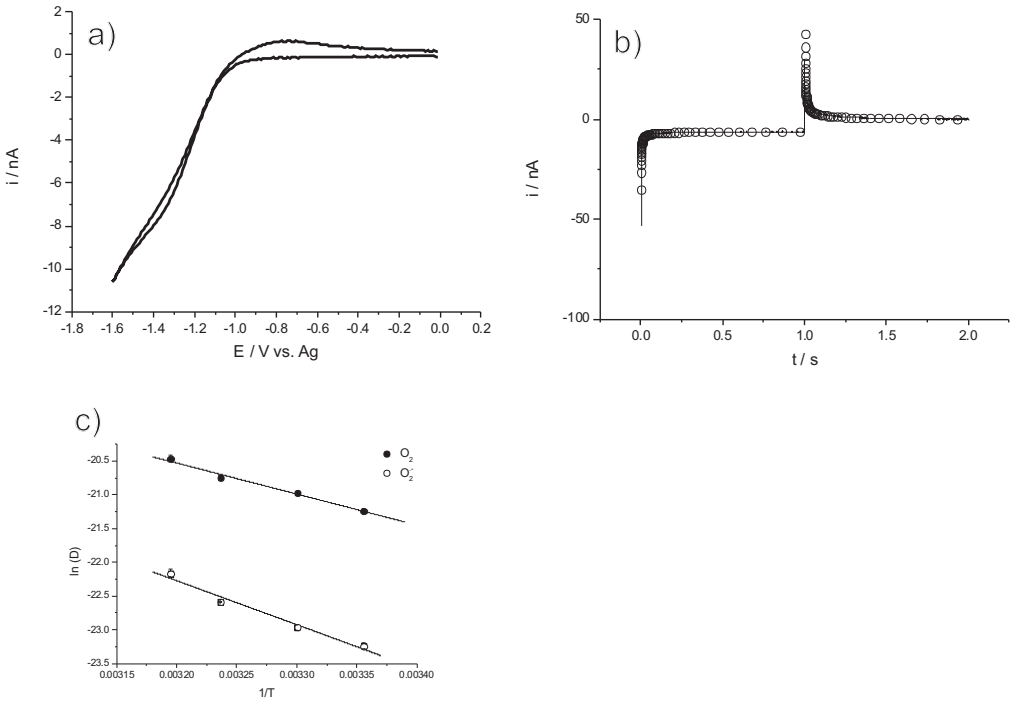

Figure 10.8: a) Cyclic voltammetry for 100% O_2 in [C_3mim][NTf_2] at the 5.0 μm radius Pt microdisc electrode at 100 mV s^{-1}. b) Simulated and experimental data of double step chronoamperometric responses for 100% O_2 in [C_3mim][NTf_2] at the 5.0 μm radius Pt microdisc electrode. c) Plot of *ln D* vs T^{-1} for 100% O_2 in [C_3mim][NTf_2] over 298 K to 313 K.

$$O_2 + e^- \rightleftharpoons O_2^{\cdot -} \tag{10.2}$$

The one electron reduction of oxygen to superoxide in RTIL media is well established[44, 45]. This experiment was again investigated using cyclic voltammetry and chronoamperometry, along with simulations, at the Pt microdisc, Pt micro-band and Cu micro-band electrodes. Data was also first obtained from the Pt microdisc electrode to compare those collected from the Pt and Cu micro-band electrodes for the purpose of investigating the suitability of Pt and Cu disposable micro-band electrodes used for gas (O_2) sensing.

Analysis of O_2 at Pt Micro-disc Electrodes

To collect data at the Pt microdisc electrode, O_2 reduction was performed in $[C_3mim][NTf_2]$. Diffusion coefficients and concentrations of oxygen were again found using chronoamperometry. Cyclic voltammetry was used first to investigate the potentials for performing chronoamperometry. Figure 10.8 a) depicts cyclic voltammetric response for 100% O_2 in $[C_3mim][NTf_2]$ at 100 mV s^{-1} which shows zero current at -0.2 V vs. Ag and a limiting current occurred at -1.5 V vs. Ag. Note that there is a small back peak showing the stability of superoxide in the media studied. According to this observation, the following procedure was used to perform double potential step chronoamperometry for O_2 reduction: the potential was initially held at -0.2 V vs. Ag for 20 s before stepping to -1.50 V vs. Ag for 1 s then to -0.2 V for 1 s. Figures 10.8 b) shows typical fitting for the double potential chronoamperometric response for oxygen reduction at Pt microdisc electrode. From simulations, the concentrations and diffusion coefficients at temperatures of 298 K, 303 K, 308 K and 313 K were determined and are summarised in table 10.2. The diffusion coefficients are similar to values from literature for other ionic liquids.[18, 42, 43] It is seen that the solubility of oxygen is essentially independent of temperature which could significantly benefit gas detection since the only temperature dependent variables controlling the current would be the O_2 and diffusion coefficient.

	Temperature (K)	298	303	308	313
Pt Disc	$[O_2]$ (mM)	5.20	5.20	5.10	5.40
	D_{O_2} ($\times 10^{-10}$ m^2 s^{-1})	5.97	7.75	9.71	12.90
	$D_{O_2^{\cdot-}}$ ($\times 10^{-11}$ m^2 s^{-1})	8.06	10.06	15.50	23.70
Pt Band	$[O_2]$ (mM)	5.30	5.20	5.10	5.40
	D_{O_2} ($\times 10^{-10}$ m^2 s^{-1})	6.20	8.00	10.00	13.00
	$D_{O_2^{\cdot-}}$ ($\times 10^{-11}$ m^2 s^{-1})	7.50	10.00	15.00	21.50
Cu Band	$[O_2]$ (mM)	5.40	5.30	5.30	5.40
	D_{O_2} ($\times 10^{-10}$ m^2 s^{-1})	6.60	8.00	10.00	14.00

Table 10.2: Summary of the concentrations of 100% O_2 and the diffusion coefficients of O_2 and $O_2^{\cdot-}$ in $[C_3mim][NTf_2]$ collected at the Pt microdisc, Pt annular band and Cu annular band over a temperature range of 298 K to 313 K.

The diffusion coefficient is related to temperature by the Arrhenius equation[46–48]

$$lnD = constant - \frac{E_{D,a}}{RT} \tag{10.3}$$

where D is the diffusion coefficient, $E_{D,a}$ is the activation energy of diffusion in J mol^{-1}, R is the universal gas constant, 8.31 J K^{-1} mol^{-1}, and T is the temperature in K.

Figure 10.8 c) shows Arrhrenius plots of O_2 (squares) and $O_2^{\cdot-}$ (circles) over 298 K to 313 K, which give the diffusion activation energies ($E_{D,a}$) of (38.2 ±0.6) kJ mol^{-1} and (54 ± 1) kJ mol^{-1} for O_2 and $O_2^{\cdot-}$ respectively. The larger activation energy for $O_2^{\cdot-}$ as compared to that for O_2 is due to the fact that charged species are harder to diffuse through ionic solvents than the neutral ones because of their coulombic interaction with other ions.

Analysis of O_2 at Pt Annular Micro-band Electrodes

The same analysis was repeated with Pt annular micro-band electrodes. Typical double potential step chronoamperometric responses, along with simulations, for oxygen reduction at the Pt annular micro-band electrode are shown in Figures 10.9 a) and b). A good fit is observed between the simulated and experimental data. The corresponding Arrhenius plots for O_2 and $O_2^{\cdot-}$ are shown in figure 10.9 c). Diffusion activation energies of (37.9 ± 0.9) kJ mol^{-1} and (53 ± 5) kJ mol^{-1} for O_2 and $O_2^{\cdot-}$ respectively were determined. These values are very close to what were found on the Pt microdisc electrode, suggesting that Pt micro-band electrodes again have performed excellently for gas sensing.

Analysis of O_2 at Cu annular micro-band electrodes

To validate the use of Cu electrodes for oxygen detection, experiments were performed in 100%, 50% and 25% O_2 (by volume). The other part of the gas mixture was N_2. To fully dissolve(saturate) the gas mixture in [C_3mim][NTf_2], the gas was passed over

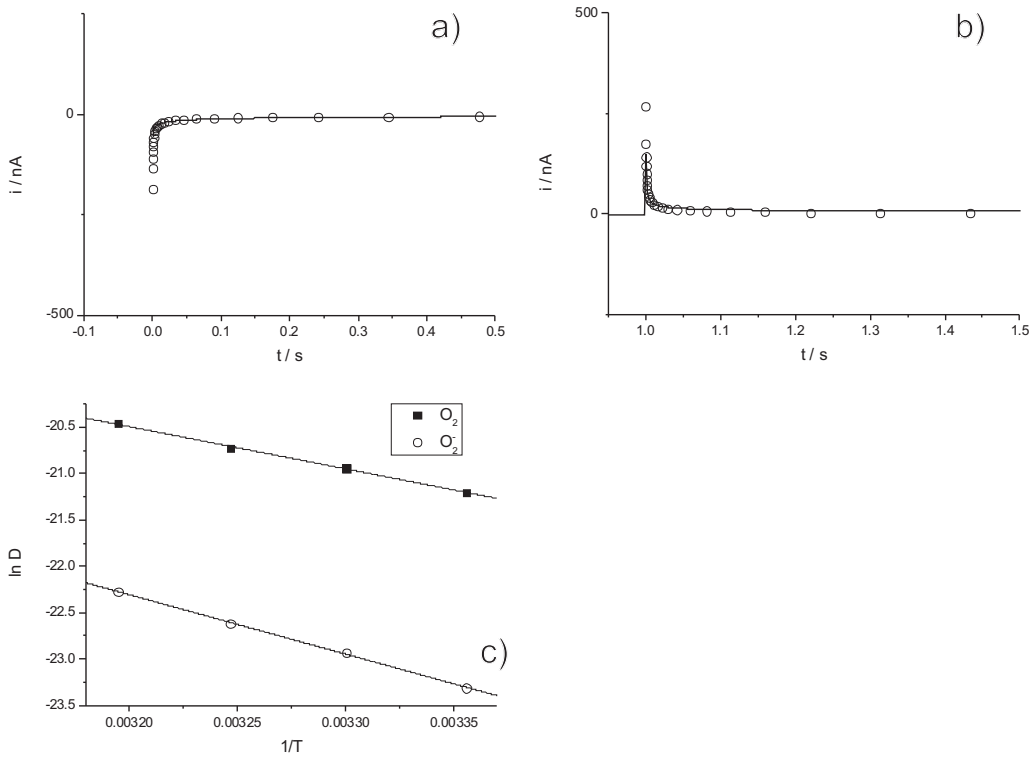

Figure 10.9: Simulated and experimental data of a) first step and b) second step of double step chronoamperometric responses for 100% O_2 in [C_3mim][NTf_2] at the Pt micro-band. c) Plot of ln D vs T^{-1} for 100% O_2 in [C_3mim][NTf_2] over 298 K to 313 K.

[C_3mim][NTf_2] for more than 30 min. Prior to experiments, the Cu annular micro-band electrodes were activated using the methods described in Section 10.3.1. Single potential step chronoamperometry was used to analyse the oxygen reduction where the potential was initially held at -0.25 V vs. Ag for 20 s and then stepped to -1.55 V vs. Ag.

Figure 10.10 a) shows the fittings of chronoamperometric responses for 100% oxygen in [C_3mim][NTf_2] at 298 K recorded on a Cu annular band. This was repeated at temperatures of 303 K, 308 K and 313 K. The concentrations and diffusion coefficients of oxygen were obtained by fitting simulations to the experimental data. The results are summarised in Table 10.3. Arrhenius plots were again applied to find out the activation energy, as shown in Figure 10.10 b), resulting in diffusion activation energies of (38.4 $\pm$ 0.8) kJ mol^{-1}. This analysis was also carried out for 50 % and 25 % oxygen which lead

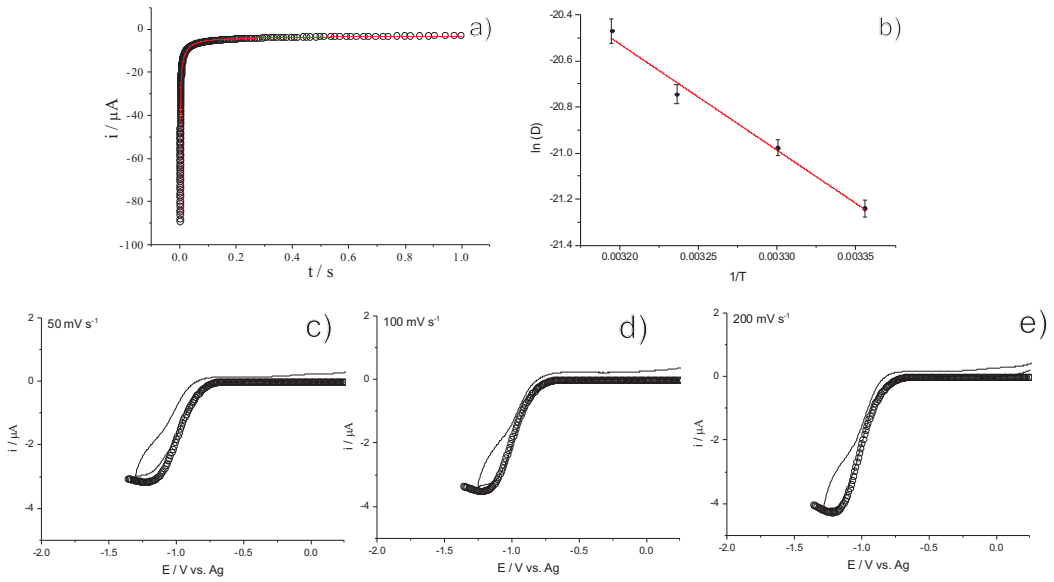

Figure 10.10: a)Simulated and experimental data of chronoamperometric responses for 100% O_2 in [C_3mim][NTf_2] at the Cu micro-band. b)Plot of ln D vs T^{-1} for 100% O_2 in [C_3mim][NTf_2] over 298 K to 313 K.c)- e) Cyclic voltammetry for 100% O_2 at 303 K on the Cu annular micro-band electrode in [C_3mim][NTf_2].

	Temperature (K)	298	303	308	313
100% O_2	[O_2] (mM)	5.40	5.30	5.30	5.40
	D_{O_2} ($\times 10^{-10}$ m^2 s^{-1})	6.60	8.00	10.00	14.00
50% O_2, 50% N_2	[O_2] (mM)	2.70	2.80	2.60	2.70
	D_{O_2} ($\times 10^{-10}$ m^2 s^{-1})	6.30	8.30	10.00	13.00
25% O_2, 75% N_2	[O_2] (mM)	1.4	1.30	1.30	1.50
	D_{O_2} ($\times 10^{-10}$ m^2 s^{-1})	6.40	8.00	10.00	13.50

Table 10.3: Table of the concentrations and the diffusion coefficients of 100%, 50% and 25% oxygen dissolved in [C_3mim][NTf_2] at the Cu band electrode over 298 K to 313 K.

to activation energies of (37.6 ± 0.5) kJ mol^{-1} and (38.1 ± 0.7) kJ mol^{-1} respectively. These again agree very well with the results obtained above.

To further validate the use of Cu micro-band electrodes for oxygen sensing, the experiments in 100 % O_2 at 303 K on the Cu annular band were also analysed using cyclic voltammetry. Figures 10.10 c), d) and e) show the cyclic voltammetry for 100 % O_2 in [C_3mim][NTf_2] at scan rates of 50 mV s^{-1}, 100 mV s^{-1} and 200 mV s^{-1} at the Cu annular band. The temperature was controlled at 303 K. The simulations were performed which resulted in the concentration of 5.4 mM, the diffusion coefficient of (7.8 ± 0.6) × 10^{-10}

m^2 s^{-1} and the value of the standard electrochemical rate constant, k_0, of 5 $\times$ 10^{-7} m s^{-1}. A value of α was determined to be 0.35 $\pm$ 0.15 using Tafel analysis (Equation 1.12).

Ionic liquid	k_H (bar)	Authors	Method
$[C_6mim][Ntf_2]$	254	Kumelan et al.[49]	microbalance
$[C_4mim][BF_4]$	1552	Jacquemin et al.[50]	microbalance
$[C_4mim][BF_4]$	378	Husson-Borg et al.[51]	microbalance
$[C_4C_6mim]$[Acetate]	1080	Afzal et al.[52]	inert gas stripping
$[C_4C_6mim]$[Acetate]	1210	Azal et al.[52]	microbalance
$[C_4mim][PF_6]$	8000	Anthony et al.[53]	microbalance
$[C_4mim][PF_6]$	513	Kumelan et al.[54]	microbalance
$[C_3mim][Ntf_2]$	694	this work	electrochemistry

Table 10.4: List of the Henry's law constants of oxygen in different ionic liquids (298 K).

The concentration of oxygen was studied as a function of oxygen percentage volume over 3 % to 100 %. The solubility of oxygen is expected to be directly proportional to the partial pressure via Henry's Law,

$$p = k_H \times x \tag{10.4}$$

Here, p is the partial pressure of O_2 in bar, x is the mole fraction of gas in solution (dimensionless) and k_H is the Henry's law constant measured in bar. Figure 10.11 shows the plot of p against x at 298 K which gives a linear dependency and leads to k_H of 667 bar. The result obtained in this work is within the range of a selection of ionic liquids in the literature. Table 10.4 lists the values of k_H of oxygen in different ionic liquids from literatures and the result obtained in this work is within the range. The limit of detection of 0.5 % was analysed using three sigma method.

For experiments in 100% oxygen, the values of oxygen solubility at all three electrodes (Pt disc, Pt band and Cu band) are in good agreement. The diffusion coefficients and activation energies of oxygen are also found to be very close for all experiments with a difference no more than 1.5%. The diffusion coefficients and diffusion activation energies

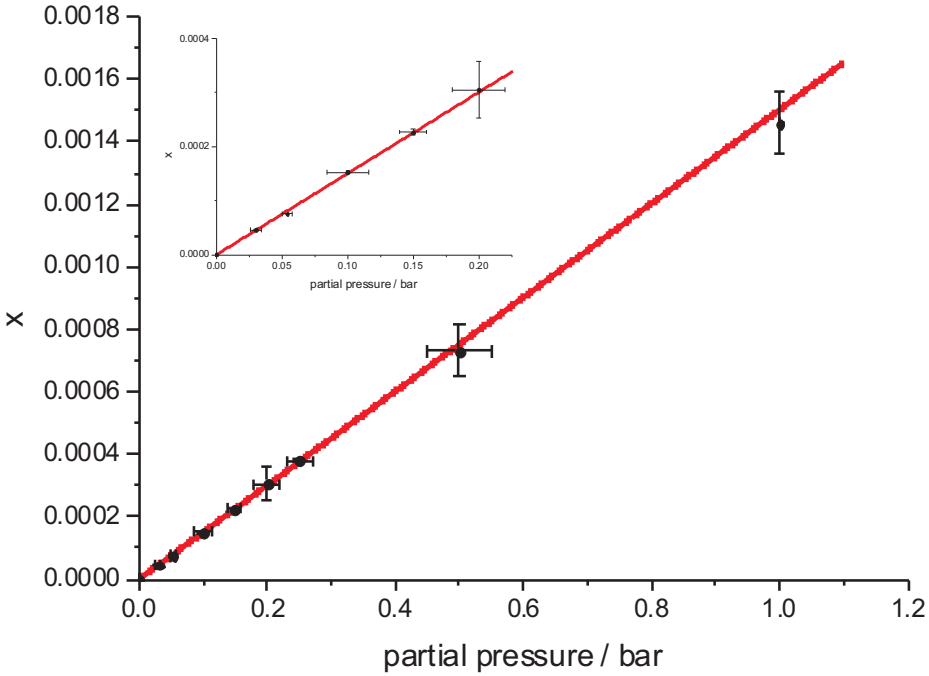

Figure 10.11: Plot of mole fraction, x, against partial pressure, p for O_2 dissolved in $[C_3mim][NTf_2]$. Insert: Enlargement in the region of oxygen percentage volume from 3% to 20 %.

of $O_2^{\cdot-}$ at the Pt annular band and the Pt microdisc electrode are in excellent agreement. These observations imply that these laminated annular bands can be used as working electrodes for oxygen sensing.

10.4 Conclusions

A facile methodology of fabricating Pt and Cu disposable annular micro-band electrodes has been demonstrated. The functionality of these electrodes has been investigated by analysing the experiments of DmFc oxidation and O_2 reduction in $[C_3mim][NTf_2]$ using cyclic voltammetry and chronoamperometry. The results at Pt and Cu micro-band electrodes have been compared with values determined from the same experiments performed at a commercially available Pt microdisc electrode, showing excellent agreement. These

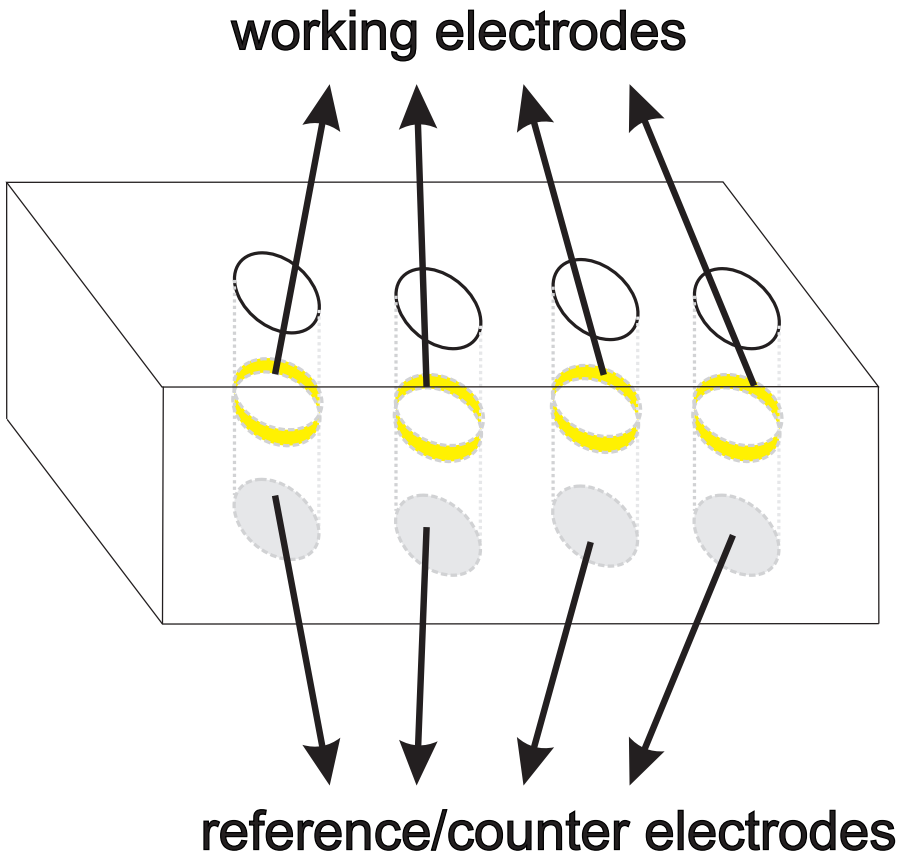

Figure 10.12: Scheme of a proposed micro-band array.

two types of home-made annular micro-band electrode have been proved to be suitable for performing electrochemical gas sensing. We conclude that annular micro-band electrodes be used with RTILs for gas sensing and that they are readily and cheaply constructed not only for Pt but also for Cu, the latter giving satisfactory voltammetry in RTIL media. It would be possible to extend the present one electrode design into an array of annular micro-band electrodes (see Figure 10.12 for the potential design). The array consists of a grid of circular holes at the base of which is a reference/counter electrode. In the walls of each of the cylindrical pores, is a circular (annular) micro-band electrode.

References

[1] Xiong, L.; Goodrich, P.; Hardacre, C.; Compton, R. *Sensors and Actuators, B: Chemical* **2013**, *188*, 978–987.

[2] Clark Jr., L. C.; Wolk, R.; Granger, D.; Talor, Z. *Journal of applied physiology* **1953**, *6*, 189–193.

[3] Bakker, E.; Telting-Diaz, M. *Analytical Chemistry* **2002**, *74*, 2781–2800.

[4] Knake, R.; Guchardi, R.; Hauser, P. *Analytica Chimica Acta* **2003**, *475*, 17–25.

[5] Hammond, M.; Johnson, K.; Rose-Pehrsson, S.; Ziegler, J.; Walker, H.; Caudy, K.; Gary, D.; Tillett, D. *Sensors and Actuators, B: Chemical* **2006**, *116*, 135–144.

[6] Kealy, J.; Bennett, R.; Lowry, J. *Journal of Neuroscience Methods* **2013**, *215*, 110–120.

[7] Roberts, T. J.; Braban, C. F.; Oppenheimer, C.; Martin, R. S.; Freshwater, R. A.; Dawson, D. H.; Griffiths, P. T.; Cox, R. A.; Saffell, J. R.; Jones, R. L. *Chemical Geology* **2012**, *332-333*, 74–91.

[8] Al-Heuseen, K.; Hashim, M. R. *Sensors and Actuators, B: Chemical* **2012**, *163*, 159–164.

[9] Lawrence, N. S.; Jiang, L.; Jones, T. G. J.; Compton, R. G. *Analytical Chemistry* **2003**, *75*, 2499–2503.

[10] Lawrence, N. S.; Jiang, L.; Jones, T. G. J.; Compton, R. G. *Analytical Chemistry* **2003**, *75*, 2054–2059.

[11] Buzzeo, M. C.; Hardacre, C.; Compton, R. G. *Analytical Chemistry* **2004**, *76*, 4583–4588.

[12] Buzzeo, M. C.; Evans, R. G.; Compton, R. G. *ChemPhysChem* **2004**, *5*, 1106–1120.

[13] Silvester, D. S.; Compton, R. G. *Zeitschrift fur Physikalische Chemie* **2006**, *220*, 1247–1274.

[14] Faridbod, F.; Mohammad Reza Ganjali, M. R.; Norouzi, P.; Riahi, S.; Rashedi, H. *Application of Room Temperature Ionic Liquids in Electrochemical Sensors and Biosensors*; InTech, 2011.

[15] Barrosse-Antle, L. E.; Bond, A. M.; Compton, R. G.; O'Mahony, A. M.; Rogers, E. I.; Silvester, D. S. *Chemistry - An Asian Journal* **2010**, *5*, 202–230.

[16] Xiong, L.; Fletcher, A. M.; Ernst, S.; Davies, S. G.; Compton, R. G. *The Analyst* **2012**, *137*, 2567–2573.

[17] Xiong, L.; Fletcher, A. M.; Davies, S. G.; Norman, S. E.; Hardacre, C.; Compton, R. G. *The Analyst* **2012**, *137*, 4951–4957.

[18] Buzzeo, M. C.; Klymenko, O. V.; Wadhawan, J. D.; Hardacre, C.; Seddon, K. R.; Compton, R. G. *Journal of Physical Chemistry A* **2003**, *107*, 8872–8878.

[19] Dias, A. C. M. S.; Gomes-Filho, S. L. R.; Silva, M. M. S.; Dutra, R. F. *Biosens Bioelectron* **2013**, *44*, 216–221.

[20] Kanyong, P.; Pemberton, R. M.; Jackson, S. K.; Hart, J. P. *Anal. Biochem.* **2013**, *435*, 114–119.

[21] Xuan Viet, N.; Chikae, M.; Ukita, Y.; Maehashi, K.; Matsumoto, K.; Tamiya, E.; Hung Viet, P.; Takamura, Y. *Biosensors and Bioelectronics* **2013**, *42*, 592–597.

[22] Prehn, R.; Abad, L.; Snchez-Molas, D.; Duch, M.; Sabat, N.; Del Campo, F. J.; Muoz, F. X.; Compton, R. G. *Journal of Electroanalytical Chemistry* **2011**, *662*, 361–370.

[23] Wang, T.-J.; Huang, C.-F.; Wang, W.-S.; Wei, P.-K. *IEEE JOURNAL OF LIGHTWAVe TECHNOLOGY* **2004**, *22*, 1764–1771.

[24] Davies, T. J.; Ward-Jones, S.; Banks, C. E.; del Campo, J.; Mas, R.; Muoz, F. X.; Compton, R. G. *Journal of Electroanalytical Chemistry* **2005**, *585*, 51 – 62.

[25] Lee, H.; Shin, H.; Jeong, Y.; Moon, J.; Lee, M. *Appl. Phys. Lett.* **2009**, *95*, p. 071104–1 – p.071104–3.

[26] Koppenol, M.; Cooper, J. B.; Bond, A. M. *American Laboratory* **1994**, *26*, 25–29.

[27] Shao, Y.; Mirkin, M.; Fish, G.; Kokotov, S.; Palanker, D.; Lewis, A. *Analytical Chemistry* **1997**, *69*, 1627–1634.

[28] Kovach, P. M.; Caudill, W. L.; Peters, D. G.; Wightman, R. M. *Journal of Electroanalytical Chemistry* **1985**, *185*, 285–295.

[29] Shea, T. V.; Bard, A. J. *Analytical Chemistry* **1987**, *59*, 2101–2111.

[30] Rajantie, H.; Strutwolf, J.; Williams, D. *Journal of Electroanalytical Chemistry* **2001**, *500*, 108–120.

[31] Tomk, P.; Jursa, S.; Bustin, D.; Tvaroek, V. *Chemicke Listy* **1998**, *92*, 631–632.

[32] Freeman, N.; Sultana, R.; Reza, N.; Woodvine, H.; Terry, J.; Walton, A.; Brady, C.; Schmueser, I.; Mount, A. *Physical Chemistry Chemical Physics* **2013**, *15*, 8112–8118.

[33] Tsunozaki, K.; Einaga, Y.; Rao, T.; Fujishima, A. *Chemistry Letters* **2002**, 502–503.

[34] Farrington, A.; Jagota, N.; Slater, J. *Analyst* **1994**, *119*, 233–238.

[35] Guiseppi-Elie, A.; Brahim, S.; Slaughter, G.; Ward, K. *IEEE Sensors Journal* **2005**, *5*, 345–355.

[36] Welford, P. J.; Freeman, J.; Wilkins, S. J.; Wadhawan, J. D.; Hahn, C. E. W.; Compton, R. G. *Analytical Chemistry* **2001**, *73*, 6088–6092.

[37] Klymenko, O. V.; Evans, R. G.; Hardacre, C.; Svir, I. B.; Compton, R. G. *Journal of Electroanalytical Chemistry* **2004**, *571*, 211–221.

[38] Shoup, D.; Szabo, A. *Journal of Electroanalytical Chemistry and Interfacial Electrochemistry* **1982**, *140*, 237 – 245.

[39] Barnes, E. O.; Xiong, L.; Ward, K. R.; Compton, R. G. *Journal of Electroanalytical Chemistry* **2013**, *701*, 59 – 68.

[40] Reyter, D.; Odziemkowski, M.; B'langer, D.; Ro, L. *Journal of the Electrochemical Society* **2007**, *154*, 36 – 44.

[41] Ward, K. R.; Xiong, L.; Lawrence, N. S.; Hartshorne, R. S.; Compton, R. G. *Journal of Electroanalytical Chemistry* **2013**, *702*, 15 – 24.

[42] Rogers, E. I.; Huang, X. J.; Dickinson, E. J. F.; Hardacre, C.; Compton, R. G. *Journal of Physical Chemistry C* **2009**, *113*, 17811–17823.

[43] Huang, X. J.; Rogers, E. I.; Hardacre, C.; Compton, R. G. *The Journal of Physical Chemistry B* **2009**, *113*, 8953–8959.

[44] Switzer, E. E.; Zeller, R.; Chen, Q.; Sieradzki, K.; Buttry, D. A.; Friesen, C. *The Journal of Physical Chemistry C* **2013**, *117*, 8683–8690.

[45] Evans, R. G.; Klymenko, O. V.; Saddoughi, S. A.; Hardacre, C.; Compton, R. G. *J. Phys. Chem. B* **2004**, *108*, 7878–7886.

[46] Compton, R. G.; Banks, C. E. *Understanding Voltammetry*; Imperial College Press, 2011, 2nd Edition.

[47] Bard, A. J.; Faulkner, L. R. *Electrochemical Methods: Fundamentals and Applications*; Wiley, 2001.

[48] Russell, J.; Cohn, R. *Arrhenius Equation*; Book on Demand, 2012.

[49] Kumelan, J.; Kamps, . P. S.; Tuma, D.; Maurer, G. *Journal of Chemical and Engineering Data* **2009**, *54*, 966–971.

[50] Jacquemin, J.; Gomes, M. F. C.; Husson, P.; Majer, V. *The Journal of Chemical Thermodynamics* **2006**, *38*, 490 – 502.

[51] Husson-Borg, P.; Majer, V.; Costa Gomes, M. *Journal of Chemical and Engineering Data* **2003**, *48*, 480–485.

[52] Afzal, W.; Yoo, B.; Prausnitz, J. *Industrial and Engineering Chemistry Research* **2012**, *51*, 4433–4439.

[53] Anthony, J. L.; Maginn, E. J.; Brennecke, J. F. *Journal of Physical Chemistry B* **2002**, *106*, 7315–7320.

[54] Kumelan, J.; Kamps, A. P.-S.; Urukova, I.; Tuma, D.; Maurer, G. *The Journal of Chemical Thermodynamics* **2005**, *37*, 595 – 602.

Chapter 11

Conclusions

This thesis aimed at improving present generation gas sensors. As discussed in Chapter 2 these suffer from some significant limitations. First the lifetime of the sensor is limited by solution evaporation as the sensor is normally exposed to different humidity levels with electrolyte loss under dry conditions. Second the solvents in the sensor provide restrictions to the high and low temperature and pressure limits on the range of operation. Third the presence of a membrane to retain the electrolyte increases the response time of the sensor. Finally, calibration of gas sensors against temperature and humidity is required.

To address the problems due to the use of conventional solvents, RTILs were employed throughout the thesis. The benefits of RTILs were discussed in Chapter 2. To compensate some undesired features of RTILs, like high viscosity and low conductivity, micro-electrodes were used as working probes.

To improve the accuracy of gas detection, a method to obtain optimised chronoamperometry for Shoup and Szabo analysis was reported in Chapter 4. The 'best' transient times were found to be dependent on the electrochemical systems. This work enabled the simultaneous and accurate determination of the concentration and diffusion coefficient of analyte, improved the accuracy of gas sensors and underpinned all the subsequent work.

The properties of RTILs have been further investigated in Chapter 5 where the tuneability of RTILs was studied. Control of the oxidation potential of ferrocene was realised by changing the size of the anion of the ionic liquids. This observation has important

implications for sensors in that the oxidation potential of ferrocene, commonly used as an internal redox reference, can be tuned away from the potential of analytes of interest. Further, work in this chapter provided a key basis for Chapter 7.

Two self-calibrating ('intelligent') systems have been developed to eliminate the need of constant calibration of gas sensors against temperature and humidity. Work presented in Chapter 6 proposed a built-in voltammetric temperature sensor incorporated into an amperometric oxygen sensor. This patented sensor was shown to be capable of providing a real-time temperature for amperometric oxygen sensing systems at the electrode surface for both air and dry oxygen analytes.

A simultaneous temperature and humidity sensor has also been designed. This sensor provides a simple measurement towards humidity and temperature, giving humidity insensitive temperature measurement and vice versa. An iterative scheme to determine simultaneous values of temperature and humidity was proposed (see Figure 7.10 in Chapter 7) and again patented.

Gas detection under wet conditions may undergo complicated redox mechanism which cannot be resolved by Shoup and Szabo analysis. Chapter 8 demonstrated a method to prevent the influence of water on the mechanism of oxygen reduction by 'trapping' superoxide ions using a phosphonium based ionic liquid. This method largely simplifies oxygen detection through forcing oxygen reduction to stop at the one electron transfer stage which allows the Shoup and Szabo analysis to determine the concentration and diffusion coefficient of oxygen.

A methodology for the reliable fabrication of cheap disposable electrodes of different geometries and materials was validated. The suitability of these electrodes to be used as working electrodes for electrochemical experiments in water, acetonitrile and ionic liquid media was shown. The electrodes demonstrated high capability toward oxygen sensing with high reproducibility. The cheap laminated annular micro-band electrodes may be

potentially used as both electrodes and solvent containers for gas detection.

Overall this thesis has shown that RTILs can offer many advantages in gas sensors and reports developments which go a long way towards the realisation of intelligent gas sensors.